

**STUDY OF LASER DRIVEN PLASMA BASED ELECTRON
ACCELERATION AND BREMSSTRAHLUNG RADIATION
EMISSION USING ULTRA-HIGH INTENSITY LASER PULSES**

By
SANYASI RAO BOBBILI
PHYS 03 2008 04 002

Raja Ramanna Centre for Advanced Technology, Indore

A thesis submitted to the
Board of Studies in Physical Sciences
In partial fulfilment of requirements
for the Degree of
DOCTOR OF PHILOSOPHY
of
HOMI BHABHA NATIONAL INSTITUTE




August, 2013


Homi Bhabha National Institute

Recommendations of the Viva Voce Board

As members of the Viva Voce Board, we certify that we have read the dissertation prepared by *Shri Sanyasi Rao Bobbili* entitled "*Study of laser driven plasma based electron acceleration and bremsstrahlung radiation emission using ultra-high intensity laser pulses*" and recommend that it may be accepted as fulfilling the dissertation requirement for the Degree of Doctor of Philosophy.


Chairman – Prof. L. M. Kukreja

Date: 25.2.2014.


Guide – Prof. P. D. Gupta

Date: 25-3-2014


Co-Guide: Prof. P. A. Naik


Date: 25/3/2014

Co-Guide: Prof. P. A. Naik


Member – Prof. S. Krishnagopal

Date: 25/3/2014

Member – Prof. S. Krishnagopal


External Examiner - Prof. G. Ravindra Kumar


Date: 25 March 2014

External Examiner - Prof. G. Ravindra Kumar

Final approval and acceptance of this dissertation is contingent upon the candidate's submission of the final copies of the dissertation to HBNI.

I hereby certify that I have read this dissertation prepared under my direction and recommend that it may be accepted as fulfilling the dissertation requirement.

Date: March 25, 2014


Guide: 
(Prof. P. D. Gupta)

Place: RRCAT, Indore

STATEMENT BY AUTHOR

This dissertation has been submitted in partial fulfilment of requirements for an advanced degree at Homi Bhabha National Institute (HBNI) and is deposited in the Library to be made available to borrowers under rules of the HBNI.

Brief quotations from this dissertation are allowable without special permission, provided that accurate acknowledgement of source is made. Requests for permission for extended quotation from or reproduction of this manuscript in whole or in part may be granted by the Competent Authority of HBNI when in his or her judgment the proposed use of the material is in the interests of scholarship. In all other instances, however, permission must be obtained from the author.

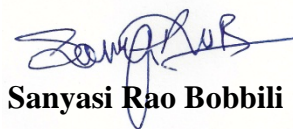


Sanyasi Rao Bobbili

DECLARATION

I, hereby declare that the investigation presented in the thesis has been carried out by me.

The work is original and has not been submitted earlier as a whole or in part for a degree / diploma at this or any other Institution / University.



Sanyasi Rao Bobbili

List of Publications arising from the thesis

Journals

1. “Stable and high quality electron beams from laser wakefield acceleration in high density plasma”, **B. S. Rao**, A. Moorti, R. Rathore, J. A. Chakera, P. A. Naik, and P. D. Gupta, Physical Review Special Topics – Accelerators and Beams **2014**, Vol. 17, p. 011301(6 pages).
2. “Effect of chirp on self-modulation and laser wakefield electron acceleration in the regime of quasi-monoenergetic electron beam generation”, **B. S. Rao**, A. Moorti, R. Rathore, P. A. Naik, J. A. Chakera, and P. D. Gupta, Physical Review Special Topics – Accelerators and Beams **2013**, Vol. 16, p. 091301(6 pages).
3. “Highly collimated quasi-monoenergetic electron beam from laser wakefield acceleration in laser produced plasma plume”, **B. S. Rao**, A. Moorti, P. A. Naik, and P. D. Gupta, Applied Physics Letters **2013**, Vol. 102, p. 231108(5 pages).
4. “Study of fast electron jet produced from interaction of intense laser beam with solid target at oblique incidence”, **B. S. Rao**, V. Arora, P. A. Naik, and P. D. Gupta, Physics of Plasmas **2012**, Vol. 19, p. 113118(6 pages).
5. “Laser wakefield acceleration in pre-formed plasma channel created by pre-pulse pedestal of terawatt laser pulse”, **B. S. Rao**, J. A. Chakera, P. A. Naik, M. Kumar, and P. D. Gupta, Physics of Plasmas **2011**, Vol. 18, 093104(9).
6. “Generation of highly collimated, mono-energetic electron beam from laser-driven plasma-based acceleration”, **B. S. Rao**, A. Moorti, P. A. Naik, and P. D. Gupta, New Journal of Physics **2010**, Vol. 12, p. 045011(9 pages).
7. “Initial experiments on laser-based electron acceleration at RRCAT, Indore”, **B.S. Rao**, P. A. Naik, V. Arora, H. Singhal, U. Chakravarty, R. A. Khan, P. D. Gupta, K. Nakajima, and T. Kameshima, IEEE Transactions on Plasma Science **2008**, Vol. 36, p. 1694 (5 pages).
8. “Angular distribution and dose measurements of hard x-ray emission from intense laser-plasma interaction”, **B. S. Rao**, V. Arora, P. A. Naik, and P. D. Gupta, Journal of Applied Physics **2007**, Vol. 102, p. 063307(4 pages).
9. “Multi-MeV quasi-monoenergetic electron beam from relativistically intense laser interaction with solid target at grazing incidence”, **B. S. Rao et al.**, Manuscript under preparation.
10. “Stable high charge electron beam from laser wakefield acceleration using nitrogen gas jet target”, **B. S. Rao et al.**, Manuscript under preparation.

Conferences (Selected Papers)

1. “Laser wakefield acceleration in high-Z gas jets”, **B. S. Rao**, A. Moorti, R. A. Khan, J. A. Chakera, P. A. Naik, and P. D. Gupta, 28th National Symposium on Plasma Science and Technology, Bhubaneshwar, Dec. 3 - 6, **2013**.

Received Best Poster Award from the Plasma Society of India

2. “High-quality stable electron beam generation by interaction of 10 TW, 45 fs laser pulses with gas-jet and plasma plume targets”, A. Moorti, **B. S. Rao**, R. Rathore, J. A. Chakera, P. A. Naik, and P. D. Gupta, Laser and Plasma Accelerators Workshop, Goa, India, Sep. 2 - 6, **2013**.
3. “Highly-collimated quasi-mono-energetic electron beam by laser wakefield acceleration in laser produced solid target plasma plume”, **B. S. Rao**, A. Moorti, R. Rathore, J. A. Chakera, P. A. Naik, and P. D. Gupta, 4th Asian Forum for Accelerators and Detectors, BINP, Novosibirsk, Russia, Feb. 25 - 26, **2013**.
4. “Highly collimated relativistic electron beam from intense femtosecond laser interaction at grazing incidence with solid target”, **B. S. Rao**, A. Moorti, G. Pathak, R. Rathore, J. A. Chakera, P. A. Naik, and P. D. Gupta, 21st DAE-BRNS National Laser Symposium, BARC, Mumbai, Feb. 6 - 9, **2013**.
5. “Laser wakefield acceleration in laser produced plasma plume target”, **B. S. Rao**, A. Moorti, J. A. Chakera, P. A. Naik, and P. D. Gupta, 27th National Symposium on Plasma Science and Technology, Puducherry, Dec. 10-13, **2012**.

Received Best Poster Award from the Plasma Society of India

6. “Progress on experimental studies on laser-driven plasma based electron acceleration at RRCAT, India”, A. Moorti, **B. S. Rao**, Chakera J. A. Chakera, P. A. Naik, and P. D. Gupta, International Committee on Ultra-High Intensity Lasers, Mamia, Romania, Sep. 16 – 21, **2012**.
7. “Generation of stable electron beam from laser wakefield acceleration”, **B. S. Rao**, P. A. Naik, J. A. Chakera, R. A. Khan, and P. D. Gupta, 26th National Symposium on Plasma Science and Technology, BIT Mesra, Patna, Dec. 20 – 23, **2011**.
8. “Laser-driven plasma based charged particle acceleration and associated radiation safety aspects”, A. Moorti, **B. S. Rao**, J. A. Chakera, P. A. Naik, and P. D. Gupta, Conference on Accelerators and Radiation Safety, BARC, Mumbai, Nov. 16 - 18, **2011**.
9. “Advanced Acceleration Schemes”, P. A. Naik, **B. S. Rao**, and P. D. Gupta, 2nd International Particle Accelerator Conference, San Sebastian, Spain, Sep. 4 – 9, **2011**.
10. “Study of high energy electron beam stability in laser-driven plasma-based acceleration”, **B. S. Rao**, M. Kumar, J. A. Chakera, P. A. Naik, and P. D. Gupta, Indian Particle Accelerator Conference, IUAC, Delhi, Feb. 15-18, **2011**.
11. “Generation of 50 MeV electron beam from sub-mm size laser-driven accelerator”, **B. S. Rao**, J. A. Chakera, P. A. Naik, M. Kumar, and P. D. Gupta, 18th DAE-BRNS National Laser Symposium, RRCAT, Indore, Dec. 1-4, **2010**.
12. “Update on the activity on laser plasma interaction with ultrashort laser pulses at RRCAT, India”, P. A. Naik, **B. S. Rao**, H. Singhal, M. Tayyab, Y. B. S. R. Prasad, S. Barnwal, J. A. Chakera, and P. D. Gupta, 2nd International

Committee Meeting & Symposium of the Asian Laser Centre at APRI, Gwangju, Korea, Nov., 4-5, **2010**.

13. “Experimental studies on laser-driven plasma-based electron acceleration: Status in India”, **B. S. Rao**, A. Moorti, P. A. Naik, J. A. Chakera, and P. D. Gupta, 7th Asia-Pacific Laser Symposium, Jeju Island, S. Korea, May 11 – 14, **2010**.
14. “Electron acceleration in self-modulation regime using 10 TW, 45 fs Ti:sapphire laser beam”, J. A. Chakera, **B. S. Rao**, P. A. Naik, M. Kumar, and P. D. Gupta, International Symposium on Waves, Coherent Structures & Turbulence in Plasmas, IPR, Gandhi Nagar, Jan. 12 – 15, **2010**.
15. “Forward Raman scattering driven self-modulation of ultra-short, intense laser pulse and relativistic electron beam generation from under-dense plasma”, **B. S. Rao**, A. Moorti, P. A. Naik, R. K. Bhat, and P. D. Gupta, 24th National Symposium on Plasma Science and Technology, NIT, Hamirpur, Himachal Pradesh, Dec. 8 – 11, **2009**.

Received Best Poster Award from the Plasma Society of India

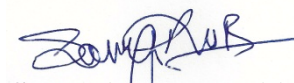
16. “Ultra-intense laser plasma interaction: A table-top source of energetic electrons, protons and γ -rays”, **B. S. Rao**, H. Singhal, V. Arora, U. Chakravarty, J. A. Chakera, P. A. Naik, and P. D. Gupta, International Conference on Peaceful Uses of Atomic Energy, Vigyan Bhavan, New Delhi, Sep. 29 – Oct. 1, **2009**.
17. “Highly collimated and monoenergetic electron beam from laser wakefield electron acceleration”, **B. S. Rao**, A. Moorti, P. A. Naik, R. K. Bhat, and P. D. Gupta, 17th DAE-BRNS National Laser Symposium, LASTEC, Delhi, Jan. 7 – 10, **2009**.

Received Best Poster Award from the Plasma Society of India

18. “Experimental study on self-modulated laser wakefield electron acceleration”, A. Moorti, **B. S. Rao**, P. A. Naik, and P. D. Gupta, 3rd Asian Summer School on Laser Plasma Acceleration and Radiations, GIST, Gwangju, Korea, Jul. 21-25, **2008**.

Received Best Poster Award from the organizers

19. “Energy spectrum measurement of fast electrons produced in ultra-intense laser solid interaction”, **B. S. Rao**, V. Arora, P. A. Naik, and P. D. Gupta, 22nd National Symposium on Plasma Science and Technology, Ahmedabad, Dec. 7-11, **2007**.
20. “Initial experiments on laser based electron acceleration at RRCAT, Indore”, **B. S. Rao**, P. A. Naik, H. Singhal, V. Arora, U. Chakravarty, R. A. Khan, P. D. Gupta, K. Nakajima, and T. Kameshima, Laser and Plasma Accelerators Workshop, Terceira Island, Azores, Portugal, Jul. 9-13, **2007**.


Sanyasi Rao Bobbili

DEDICATION

*I dedicate this thesis to my parents and
two sisters whose struggles and sacrifices helped
me chase and realize my dreams.*

ACKNOWLEDGEMENTS

The present thesis work would not have been possible without the active support, encouragement, and counsel of a number of people. It is my pleasure to acknowledge the help they provided to me from time to time for successfully carrying out this thesis work.

First and foremost, I owe deep sense of gratitude to my thesis guide *Prof. P. D. Gupta* for his constant guidance, support, and encouragement. I am greatly indebted to him for impressing upon me many nuances of scientific analysis and effective presentation of experimental data during my early years. I am extremely thankful to him for sparing time despite his busy schedule as the Director, RRCAT, to ensure smooth progress and timely completion of the research work and the finalization of the thesis. His endless energy, high standards of work, and parallel management of variety of complex tasks in time bound schedules are awe inspiring and highly motivating. He has compelling influence on me directly and indirectly in so many good ways.

I am extremely thankful and indebted to my thesis co-guide *Prof. P. A. Naik* for his continuous guidance and providing all the support needed in planning and execution of various experiments, discussing the results on daily basis during the experiments, and in publishing the results. I am highly obliged to him for spending his invaluable time and efforts at various stages of the research work, thesis preparation and finalization. His easily approachable demeanour and extraordinary skill to explain complex physical concepts in simplest possible way are exemplary and highly inspiring.

I would like to thank my Doctoral Committee's Chairman and the members for their excellent suggestions from time to time for improvement during the yearly reviews of my thesis work.

The experiments reported in the thesis would not have been successful without active support and involvement of *Dr. J.A. Chakera*. I sincerely thank him for his constant encouragement and providing ideas during experiments.

I am profoundly thankful to *Dr. A. Moorti* for his valuable support, encouragement, and contribution in planning, setting up of laser wakefield acceleration (LWFA) experiments, preparation of manuscripts, and spending his precious time in going through the initial version of the this thesis.

I sincerely thank *Prof. K. Nakajima*, KEK, Japan, one of the pioneers in the field of laser wakefield acceleration (LWFA), for his help and sharing his expertise during the initial collaborative experiments.


Mr. Vipul Arora has been a constant, reliable source of help to me, particularly on various technical and administrative matters through all these years. I had pleasant experience working with him in some of the experiments reported in the thesis. I cannot thank him enough for his constant support and friendly counsel through highs and lows on professional and personal fronts.

I thank *Dr. H. Singhal* and *Dr. U. Chakravarty* for their contribution in initial experiments on LWFA and enjoyable company they provided over the years. I thank and highly appreciate *Mr. Mukund Kumar* for his enthusiastic participation and active involvement in the experiment on pre-pulse effect on LWFA. I thank *Dr. Suman Bagchi*, *Ms. Ranjana Rathore*, and *Mr. Tirtha Mandal*, for their contribution in some of the experiments on LWFA. I also thank *Dr. M. P. Singh* for setting-up HELIOS simulation software and *Dr. Ajit Upadhyay* for running PIC simulations for one of our experiment on LWFA.

Thanks are due to *Mr. S. R. Kumbhare* for helping me in setting up the experiments. I have learnt many technical skills from him, which has made me self-reliant on many aspects of working in laboratory. My sincere thanks to *Mr. R. A. Khan* for providing the laser support and staying late to make it available after office hours and on holidays. His enthusiastic involvement and staying late nights during the experiments are praise worthy. I also thank *Mr. R. K. Bhat* for being very supportive during the experiments and *Mr. R. A. Joshi* for operation of the Ti:sapphire laser. My thanks also go to *Mr. Kushwaha*, *Mr. Sebastin*, and *Mr. K. Paramar* for actively providing constant mechanical support.

I am extremely thankful to my wife *Mrs. Sailaja* for her unconditional love, support, devotion, and the great pains she endured to take care of me and our beloved son *Hrisheek* during all these years. Without her contribution, this thesis completion would not have been possible.

Finally, I owe deep sense of gratitude to my parents and two sisters for their love and affection shown towards and their struggles and sacrifices without which I would not have reached to this stage in my life.



Sanyasi Rao Bobbili

CONTENTS

SYNOPSIS	I
LIST OF FIGURES	VII
LIST OF TABLES	XIII
CHAPTER 1: INTRODUCTION	1 - 43
1.1 Laser-driven plasma based acceleration: An overview	1
1.2 Scope of the present thesis work	4
1.3 Basics of electromagnetic waves	6
1.3.1 Gaussian laser beam	7
1.4 Basics of plasma	9
1.4.1 Plasma oscillations	9
1.4.2 Electromagnetic wave propagation in plasma	11
1.5 Ultra-high intense laser-matter interactions	12
1.5.1 Laser induced ionization of matter	13
1.5.2 Motion of a free electron in an electromagnetic field	15
1.5.3 Ponderomotive force	18
1.5.4 Self-focusing and self-guiding	20
1.5.5 Self-steepening and self-compression	23
1.6 Laser wakefield acceleration of electrons	23
1.6.1 Strength of laser wakefield	25
1.6.2 Self-injection	28
1.6.3 Limits for energy gain	29
1.6.4 Different regimes of laser wakefield acceleration	32
1.7 Fast electrons and bremsstrahlung x-ray generation	36
1.7.1 Resonance absorption	36
1.7.2 Vacuum heating	38
1.7.3 J×B heating	39
1.7.4 Direct laser acceleration	40
1.7.5 Bremsstrahlung x-ray generation	42
CHAPTER 2: EXPERIMENTAL SET-UP AND DIAGNOSTIC SYSTEMS	43 - 63
2.1 Ti:sapphire laser system	43
2.2 Characterization of laser parameters	47
2.2.1 Laser spectrum and pulse duration	47
2.2.2 Measurement of focal spot	50
2.2.3 Measurement of the pre-pulse contrast	53
2.3 Gas jet system	56

2.4 Electron beam diagnostics	58
2.4.1 Phosphor screen	59
2.4.2 Integrating current transformer	60
2.4.3 Electron spectrograph	61
CHAPTER 3: STUDY OF LASER WAKEFIELD ACCELERATION IN SELF-MODULATED REGIME	64 - 81
3.1 Experimental details	66
3.2 Electron beam profile measurement	67
3.3 Forward Raman scattering measurements	68
3.4 Laser channelling in plasma	69
3.5 Energy spectrum of accelerated electrons	70
3.6 Effect of chirp	72
3.6.1 On electron beam charge	73
3.6.2 On forward Raman Scattering	74
3.6.3 On quasi-mono-energetic electron beam	75
3.7 Discussion	76
CHAPTER 4: EFFECT OF INTERACTION PARAMETERS ON LASER WAKEFIELD ACCELERATION	82 -109
4.1 Effect of pre-pulse on laser guiding and electron acceleration	83
4.1.1 Experimental details	83
4.1.2 Effect of pre-pulse on laser propagation	86
4.1.3 Effect of pre-pulse on electron acceleration	92
4.1.4 Discussion	97
4.2 Effect of gas medium on laser wakefield acceleration	98
4.2.1 Experimental details	99
4.2.2 Comparison of electron beams from He, N ₂ , and Ar	100
4.2.3 Discussion	105
CHAPTER 5: LASER-DRIVEN ELECTRON ACCELERATION IN LASER PRODUCED PLASMA PLUME	110 - 122
5.1 Experimental details	111
5.2 Quasi-mono-energetic electron beam generation from laser produced plasma plume	113
5.3 Quasi-mono-energetic electron beam from laser - solid interaction at grazing incidence	116
5.4 Discussion	117

CHAPTER 6: STUDY OF BREMSSTRAHLUNG RADIATION AND FAST ELECTRON GENERATION FROM LASER - SOLID INTERACTION	122 - 138
6.1 Experimental details	123
6.2 Angular distribution of bremsstrahlung hard x-rays	126
6.3 Sources of x-rays and direction of fast electron emission	127
6.4 Angular distribution of fast electrons	130
6.5 Energy measurement and scaling of fast electrons	131
6.6 Discussion	134
CHAPTER 7: SUMMARY AND FUTURE OUTLOOK	139 -143
7.1 Summary of the important results	139
7.2 Future outlook.....	142
REFERENCES	144 -164

SYNOPSIS

The advancements in laser technology over the years have led to the generation of femto-second duration laser pulses of terawatt to petawatt power from table-top systems, which has opened up new research areas. The ultra-short, high power laser pulses can be easily focused to a spot size of the order of $10\text{ }\mu\text{m}$ resulting in intensity exceeding $\sim 1 \times 10^{18}\text{ W/cm}^2$. Matter subjected to such ultra-high intensities gets instantly ionized by the leading edge of the laser pulse due to the extremely strong electric field and turns into a plasma. The oscillatory velocity of the free electrons in such intense laser fields becomes relativistic. This relativistic regime of laser-plasma interactions has attracted great interest of the scientific community due to the potential of these interactions in generating high energy electrons, ions, and neutrons, as well as x-rays, with unique properties. The duration of the emission of both high energy particles and the short wavelength radiation is expected to be ultra-short. This has many applications in basic science, medicine, and technology. In addition, ultra-short laser pulses with a few fs duration allow experimentalists to study highly transient processes in a time resolved manner.

Electron acceleration by the large amplitude relativistic plasma waves driven by a high intensity, ultra-short laser pulse propagating in the plasma, created mostly from a gaseous medium, is interesting due to the extremely strong accelerating fields of $\sim 100\text{ GV/m}$ of the plasma wave. This method of acceleration, referred to as laser wakefield acceleration (LWFA), was proposed in the year 1979 by Tajima and Dawson. The strong accelerating field of the plasma wave enables generation of high energy electrons from a compact and low cost accelerator setup. Therefore, this method is being actively pursued as an alternative to the present day high energy accelerators, whose size and consequently the cost becomes huge, mainly due to the accelerating field in the conventional radio-frequency technology being

limited to less than 100 MV/m. Generation of hundreds of MeV electrons from laser driven acceleration in millimeter long plasmas was demonstrated several years ago. However, the electron beams were typically characterized by large divergence and exponentially decreasing energy distribution. With more controlled experiments and advancement in understanding of the processes involved, high quality electron bunches characterized by quasi-mono-energetic peak and low divergence (< 10 mrad) were produced under widely different laser pulse and plasma density parameters. While the generation of high quality electron beam is a big step forward towards the usability of the laser wakefield accelerator for applications, there are several key issues related to further improvement in quality, stability, and repetition rate of the electron beam. Currently active research is going on at major laboratories around the world including at Laser Plasma Division, RRCAT in India, to improve these parameters for realizing a practical laser wakefield accelerator which can be installed in a small scale setup for wide ranging applications. In parallel, demonstration experiments of electron beams produced from laser wakefield accelerators for applications in soft x-ray undulator, radiography, transmutation etc. have been performed and further applications in free-electron lasers are being explored.

While laser wakefield acceleration is of interest for generation of high energy electrons with several tens of MeV to GeV from a compact accelerator setup, multi-MeV energy electrons generation from intense laser - solid interactions through various mechanisms, such as resonance absorption, $v \times B$ acceleration, etc., are being investigated actively over the years to understand the interaction processes under wide ranging laser and target parameters and also due to their application in the fast ignition concept of inertial confinement fusion. The energetic electrons produced from interaction of laser with solid targets are generally referred to as “hot” or “fast” electrons. The fast electrons when retarded in the target material produce a bright source of hard x-rays, which can be useful for a variety

of research and technological applications. For instance, such sources have been used for activation of short-lived isotopes which can be used in radiological diagnostics for positron emission tomography, transmutation of elements by neutron capture to deactivate long-lived fission fragments, and for nuclear fission of actinides. Again, many of these applications require collimated energetic electrons in a well-defined direction. Therefore, careful control of the laser and plasma conditions is required to generate collimated electron beams from solid target.

In the present thesis work, several experimental studies have been carried out on laser wakefield acceleration using different laser interaction parameters and gas jet target media, with an objective to generate high energy and high quality electron beams and the optimum conditions for the same have been identified. Laser driven acceleration in solid plasma plume target was studied as an alternative to the conventional gas jet targets, due to its ability to be operated at high repetition rate. Quasi-mono-energetic electron beams were demonstrated from the solid plasma target through optimization of pre-pulse and target conditions. Generation and characterization of fast electrons from high intensity laser - solid interactions were also carried out under different laser irradiation conditions to understand the interaction process. Angular distribution of the bremsstrahlung x-ray emission produced by the fast electrons was studied. The chapter-wise summary of these studies is given below.

Chapter 1 gives theoretical foundations of various ultra-high intensity laser matter interaction processes relevant to the present thesis work. Starting with basics of electromagnetic waves and plasma, electromagnetic wave propagation in plasma, laser induced ionization of atoms, motion of a free electron in laser field, ponderomotive acceleration, self-focussing etc. are discussed. Laser wakefield acceleration and related concepts viz. electron self-injection, dephasing, pump depletion along with various regimes of

electron acceleration are presented. Finally, energetic electrons and bremsstrahlung x-ray generation in resonance absorption, vacuum heating, and $\mathbf{J} \times \mathbf{B}$ heating are described.

All the experiments presented in the thesis were carried out using a table-top 10 TW, 45 fs Ti:sapphire laser system at Laser Plasma Division, RRCAT. **Chapter 2** gives the overall description of the Ti:sapphire laser system. Next, measurements of various laser pulse parameters viz., laser pulse duration, spectrum, focal spot, and pre-pulse intensity contrast are described and the results are presented. Experiments on laser wakefield acceleration require relatively low density plasmas which are mostly generated from supersonic gas jet targets. The supersonic gas jet system used in the present thesis work is described. The detection and measurement of high energy electrons was done using various diagnostics. Magnetic spectrometer is an important diagnostic for measuring the energy of the high energy electrons. The magnetic spectrometer used in the experiments is described in detail.

Chapter 3 describes the experimental setup for electron acceleration. In achieving electron generation and acceleration, alignment of the setup and finding the right parameters is very crucial. Unless these are adjusted properly, no electrons are generated/ accelerated. This chapter also presents the results on generation of high quality electron beam from self-modulated laser wakefield acceleration. In this chapter, the dependence of electron beam parameters viz. charge, divergence, and the electron spectrum, on the plasma density is also discussed. The electron energy spectrum typically showed 100% spread at lower plasma density but at a relatively high density $\sim 8.5 \times 10^{19} \text{ cm}^{-3}$, high quality electron beam having divergence $< 10 \text{ mrad}$, and quasi-mono-energetic distribution with energy spread ($\Delta E/E < 10 \%$) was produced with a peak energy of $\sim 20 \text{ MeV}$. These results, along with simultaneous detection of Raman peak in the forward laser scattering measurements, are described in detail. The results suggest strong self-modulation of the laser pulse. The underlying physics of high

quality beam generation based on self-modulation is discussed. The effect of positively/negatively chirped laser pulses on self-modulation and electron acceleration was also investigated. Asymmetric dependence of laser self-modulation, electron beam charge and energy on the magnitude and sign of the chirp is presented.

The effect of various interaction parameters viz. laser pre-pulse and gas medium on laser wakefield acceleration has been investigated to find optimum laser pre-pulse parameters and target gas medium for generating higher energy and stable electron beam. **Chapter 4** presents the results of the study on the role of nanosecond duration pre-pulse pedestal in the propagation of 45 fs Ti:sapphire laser pulses and on the wakefield acceleration in a helium gas jet. Guiding of the fs laser pulses over few Rayleigh lengths in a pre-formed plasma channel, created by optimum pre-pulse level is described. Generation of electrons with higher energy (~ 50 MeV) due to laser guiding is discussed. The results of investigation on laser-driven electron acceleration in different gas jet targets viz. helium (He), nitrogen (N₂), and argon (Ar), with reduced pre-pulse pedestal intensity are presented. The parameters of the electron beam produced from all the 3 gas jets are compared in detail and explanation for the observed results is given.

Although the relativistic electron beams produced from laser wakefield acceleration in gas jet plasma targets have high peak current of \sim kA, the average current is limited mainly due to low repetition rate operation of pulsed gas jet targets. Laser driven acceleration in plasma produced from solid targets is investigated to find the possibility of quasi-mono-energetic electron beam generation at high repetition rate. **Chapter 5** describes the experimental set-up and the results of quasi-mono-energetic electron beam generation from laser produced plasma plume. The results of low divergence, quasi-mono-energetic electron beam generation from Nylon target plasma plume, along with the target and target surface

distance from the fs laser axis, are presented and the physics behind the electron acceleration is discussed. Relativistic electrons were also observed, without the use of separate laser pulse for plasma formation, when the femtosecond laser beam interacted with the solid target at grazing incidence. However, the beam quality was found to depend critically on the level of ASE pre-pulse and consequently on the scale length of the pre-plasma produced in front of the solid target surface. The optimization procedure for generating quasi-mono-energetic electron beam in this case will also be discussed.

Ultra-intense laser interaction with solid target at oblique incidence results in absorption of laser energy through various mechanisms and generates fast electrons. The angular and energy distribution of these electrons is critically dependent on various laser and target interaction parameters. **Chapter 6** presents the study of fast electrons generated from the interaction of the Ti:sapphire laser pulses with planar copper target at 45° incidence angle, under different irradiation conditions. The measurements on the angular spread and the energy spectrum of the fast electrons for both p- and s-polarized laser irradiation at intensities in the range 4×10^{16} - 4×10^{17} W/cm² (for a fixed pulse duration of 45 fs) and for pulse duration in the range 45 fs – 1.2 ps (for a fixed laser fluence of 1.8×10^4 J/cm²) is described and scaling laws for temperature of fast electrons with laser intensity and pulse duration are presented. Measurement of the angular distribution of the hard x-ray bremsstrahlung radiation (> 40 keV) generated due to the fast electrons produced from the solid copper target, is also presented. A physical explanation for fast electron generation and observed x-ray dose distribution is also given.

In **Chapter 7**, a summary and conclusions derived from the presented work are given. Finally, an outlook for extension of the present work in future is also outlined.

LIST OF FIGURES

Figure No.	Figure Caption	Page No.
1.1	<i>Schematic of a Gaussian laser beam showing beam waist, w_0, Rayleigh length, z_R, and divergence angle, θ.</i>	8
1.2	<i>Schematic of a slab of plasma in which a sheet of electrons (-) with thickness δx is displaced by an amount δx from the ions (+). A restoring force F acts on the electrons and sets up oscillations, called “plasma oscillations, about equilibrium position.</i>	10
1.3	<i>Illustration of the ionisation process by a laser field. For a weak laser electric field, the Coulomb potential, $V(x)$ of the atom is slightly perturbed as shown in a) and ionisation occurs through multi-photon absorption. The unperturbed potential of the atom is indicated in “grey” line, the potential of laser field is indicated with “green dashed line”, and the electron is illustrated by a wave-packet shown in “blue”. The binding potential, $-U_p$, is shown in “black dashed line”. b) and c) illustrate tunnelling and barrier suppression ionization due to potential barrier deformation in laser electric field, E_L, with increase in strength.</i>	13
1.4	<i>a) Trajectory of a free electron in a plane, linearly polarised electromagnetic wave as seen from lab frame. b) Figure of 8 trajectory in the drift frame.</i>	17
1.5	<i>a) Laser pulse intensity distribution is shown in 2D and the associated ponderomotive force direction and magnitude is indicated with arrows, b) shows Gaussian line intensity profile of the laser pulse (red) along the propagation axis and the associated ponderomotive force (blue). The peaks of the forward and backward ponderomotive force are separated by the pulse FWHM duration, $c\tau_0$.</i>	19
1.6	<i>Illustration of laser self-focussing and self-guiding in plasma.</i>	22
1.7	<i>Illustration of excitation of plasma oscillations by intense laser pulse and laser wakefield acceleration. Process is explained in the text.</i>	24
1.8	<i>One-dimensional laser wakefield for two different laser strength parameters, a) $a_0^2 = 0.2$ and b) $a_0^2 = 2$.</i>	27
1.9	<i>Schematic of pump laser pulse energy depletion during wakefield acceleration. Initially the laser pulse is intense and drives high amplitude plasma waves in its wake and electron gains energy from the plasma wave. The laser pulse energy depletes and very low amplitude plasma wave exists after a propagation length close to pump depletion length. Beyond this distance acceleration will not occur.</i>	30
1.10	<i>Schematic of electron dephasing in laser wakefield. Initially an electron injected at the peak of the accelerating region of the plasma wave. After a certain length called dephasing length, in the lab frame (in the plasma wave frame electron moves over half plasma wave length), the electron reaches the bottom of the plasma wave and thereafter it starts losing energy back to the plasma wave.</i>	31

1.11	<i>Schematic of self-modulated laser wakefield acceleration.</i>	33
1.12	<i>Schematic of laser wakefield acceleration in bubble regime.</i>	35
1.13	<i>Illustration of resonance absorption process. A p-polarized laser pulse obliquely incident in the pre-plasma profile at a target front. Reflection occurs at density n_R before the critical density, n_c. If the distance between the standing wave pattern at the turning point and the position of the critical density is short enough, the evanescent decaying electric field can excite plasma oscillations at this position down the plasma density gradient. Since this oscillation is excited resonantly, it can be driven so strongly that it breaks and produces hot electrons along the target normal direction in to vacuum. Subsequently, some escaping hot electrons are pulled back into the target by the space charge field developed by the electrons left initially.</i>	37
1.14	<i>Illustration of vacuum heating mechanism.</i>	39
2.1	<i>The principle of chirped pulse amplification.</i>	44
2.2	<i>Overall schematic layout of the Ti: sapphire laser system.</i>	45
2.3	<i>Photograph of the 10 TW Ti:sapphire laser system at Laser Plasma Division, RRCAT.</i>	46
2.4	<i>A typical spectrum of the Ti:sapphire laser pulse at full power of operation.</i>	48
2.5	<i>Schematic of a typical single shot second order intensity autocorrelator.</i>	49
2.6	<i>(a) Typical CCD camera image of autocorrelation trace corresponding to shortest pulse duration, and (b) its line profile taken along the width of the trace.</i>	49
2.7	<i>Variation of laser pulse duration with grating separation relative to the compressor zero.</i>	50
2.8	<i>a) Typical high power laser beam profile, and b) its intensity distribution in 3D.</i>	51
2.9	<i>a) A schematic diagram of the focal spot imaging setup, and b) an image of a graticule recorded by the setup for calibration purpose.</i>	52
2.10	<i>a) 2D image of the focal spot, b) line intensity profile along $Y=0$, and c) 3D plot of the intensity distribution of the focused laser beam.</i>	53
2.11	<i>a) Measured signals due to leakage replica pre-pulse, and b) ASE pre-pulses of different durations along with the main pulse.</i>	56
2.12	<i>a) Design of the supersonic nozzle, b) gas jet nozzle with inlet port on one side for gas entry from a high pressure cylinder through a connecting tube and fast solenoid valve at the bottom for regulating the gas jet duration and repetition rate, c) Control unit for fast solenoid valve driver, and d) magnified view of the nozzle showing the dimensions of the slit type orifice.</i>	57
2.13	<i>a) 3D plot of helium gas density profile normalized w.r.to the backing pressure and b) gas density variation with backing pressure.</i>	57
2.14	<i>Schematic diagram of the experimental setup for laser wakefield acceleration.</i>	58

2.15	<i>(a) A photograph of the ICT used in experiments and b) a typical ICT signal after high frequency filtering.</i>	60
2.16	<i>a) A photograph of the permanent dipole magnet with circular poles of 50 mm diameter and pole gap 9 mm. A slit at the entrance of the magnet can be seen in the picture. b) The measured and effective magnetic field in the mid plane of the two poles.</i>	61
2.17	<i>Geometry of the permanent magnet based electron spectrometer.</i>	62
2.18	<i>a) Dispersion curve for the spectrograph for phosphor screen kept at a distance of 35 mm from the geometric centre of the magnet. b) Trajectories of electrons with different energies.</i>	63
3.1	<i>A schematic diagram of the experimental set-up used for electron acceleration.</i>	66
3.2	<i>Images of electron beam profiles at plasma density a) $6.5 \pm 0.5 \times 10^{19} \text{ cm}^{-3}$, b) $7.5 \pm 0.5 \times 10^{19} \text{ cm}^{-3}$, and c) $8.5 \pm 0.5 \times 10^{19} \text{ cm}^{-3}$ with 30 μm aluminium foil in front of phosphor screen. d) A well collimated electron beam with broad background observed at plasma density $6.5 \pm 0.5 \times 10^{19} \text{ cm}^{-3}$ when a 5 mm thick aluminium plate was kept in front of the phosphor screen to cut off the low energy ($< 5 \text{ MeV}$) electrons.</i>	68
3.3	<i>Forward Raman spectra at different plasma densities.</i>	69
3.4	<i>Thomson scattering side image laser channelling in plasma showing bifurcation of the laser beam into two filaments as indicated by the arrows on the right. The vertical dotted line shows the location of top of the gas jet density ramp.</i>	70
3.5	<i>a) A typical image of continuous energy distribution of electron beam at plasma density $8.5 \pm 0.5 \times 10^{19} \text{ cm}^{-3}$. b) Energy spectra of the electron beam produced at different plasma densities.</i>	70
3.6	<i>Quasi-mono-energetic electron beams at plasma density $8.5 \pm 0.5 \times 10^{19} \text{ cm}^{-3}$. a) Raw images of energy dispersed quasi-mono-energetic electron beam, b) Processed image of a quasi-mono-energetic electron beam, and c) corresponding energy spectrum showing peak at 21 MeV.</i>	71
3.7	<i>Variation in the integrated electron beam charge at two different plasma densities (Solid squares: $8.5 \pm 0.5 \times 10^{19} \text{ cm}^{-3}$, and hollow squares : $6.5 \pm 0.5 \times 10^{19} \text{ cm}^{-3}$) with compressor grating pair separation (chirp) measured w.r.t. the “zero” setting (separation corresponding to minimum pulse duration). The total charge for “zero” setting of the compressor is 2 nC and 8 nC respectively for plasma density $6.5 \pm 0.5 \times 10^{19} \text{ cm}^{-3}$ and $8.5 \pm 0.5 \times 10^{19} \text{ cm}^{-3}$. The variation of the laser pulse width (circles) with grating separation is also shown.</i>	73
3.8	<i>The transmitted laser spectra at two different plasma densities : a) without interaction with plasma, b) to f) with interaction at : $n_e \approx 6.5 \pm 0.5 \times 10^{19} \text{ cm}^{-3}$, for grating separation of 0 (45 fs), -320 μm (70 fs), -600 μm (125 fs), -800 μm (170 fs), and +200 μm (52 fs) respectively, g) to i) at $n_e \approx 8.5 \pm 0.5 \times 10^{19} \text{ cm}^{-3}$ for grating separation of 0 (45 fs), -400 μm (85 fs), and +200 μm (52 fs) respectively. No distinct Raman peak could be resolved from the transmitted spectra due to large broadening of laser spectrum (as shown in (e)) for grating separation $\gtrsim -800 \mu\text{m}$, for a density of $6.5 \pm 0.5 \times 10^{19} \text{ cm}^{-3}$. Similar observation</i>	75

was made for $n_e \approx 6.5 \pm 0.5 \times 10^{19} \text{ cm}^{-3}$ at grating separation of $> -400 \text{ } \mu\text{m}$ (spectra not shown here). Raman peaks disappear for grating separation $\geq +200 \text{ } \mu\text{m}$ (-ve chirp).

3.9	<i>Images of quasi-mono-energetic electron spectra recorded at $n_e \approx 8.5 \pm 0.5 \times 10^{19} \text{ cm}^{-3}$, for different separations of the laser pulse compressor gratings : a) $0 \text{ } \mu\text{m}$ (45 fs), b) $-320 \text{ } \mu\text{m}$ (70 fs), and c) $-640 \text{ } \mu\text{m}$ (135 fs).</i>	76
4.1	<i>A schematic diagram of the experimental setup.</i>	83
4.2	<i>Pre-pulse due to amplified spontaneous emission (ASE) measured with a fast photo-diode with 0.8 ns rise time. The dash-dot (black, $\sim 1 \text{ ns}$) and the dashed (red, $\sim 3 \text{ ns}$) traces correspond to different switching times of the pulse cleaning Pockels cell.</i>	84
4.3	<i>Shadowgram of the pre-formed plasma channel produced by 1 ns long section of ASE pre-pulse of intensity $3 \times 10^{12} \text{ W/cm}^2$. The main laser beam was focused near the entrance edge of the gas jet, which is indicated by the vertical dotted line and the direction of laser propagation is indicated by a horizontal arrow on the left. The density of helium gas was $n_{\text{He}} \sim 3.2 \times 10^{19} \text{ cm}^{-3}$.</i>	87
4.4	<i>Guiding of 45 fs duration 4 TW laser pulse focused to intensity $3 \times 10^{18} \text{ W/cm}^2$. The images of guiding recorded by (a) top-view CCD, and (b) side-view CCD. The images were recorded at helium gas density $\sim 3.2 \times 10^{19} \text{ cm}^{-3}$ under the conditions of ASE pre-pulse duration $\sim 1 \text{ ns}$ and its intensity $\sim 3 \times 10^{12} \text{ W/cm}^2$. The double sided arrow represents the direction of laser polarization.</i>	89
4.5	<i>Side-view image of 45 fs laser pulse guiding in plasma with channel splitting (as indicated by two arrows) observed in some of the shots. The arrow and a vertical line on the left of the channel image represent direction of laser propagation and the front edge of the gas jet. The images were recorded at helium gas density $\sim 3.2 \times 10^{19} \text{ cm}^{-3}$ under the conditions of ASE pre-pulse duration $\sim 1 \text{ ns}$ and its intensity $\sim 3 \times 10^{12} \text{ W/cm}^2$.</i>	90
4.6	<i>The side-view image of plasma due to non-linear Thomson scattering of main 45 fs duration laser pulse at helium gas density of $3.2 \times 10^{19} \text{ cm}^{-3}$ and with ASE pre-pulse duration of $\sim 2 \text{ ns}$ and intensity $3 \times 10^{12} \text{ W/cm}^2$.</i>	91
4.7	<i>Results of the electron beam profile measurement. (a) Image of the low divergence electron beam observed when ASE pre-pulse duration was 1 ns. The concentric circles represent 5° and 10° full cone angles and the common centre of the circles represents the laser axis in vacuum and is shown with white coloured dot. (b) Low intensity and large divergence images of electrons observed occasionally when ASE pre-pulse duration was 2 ns.</i>	92
4.8	<i>Measurement of pointing variation of the electron beam produced in a series of laser shots. a) Images of the low divergence electron beam. The concentric circles in each image represent 5°, 10°, and 15° full cone angles and the common centre of the circles represents the laser axis in vacuum. b) Plot of pointing variation of well collimated electron beam. The dotted circle (red) represents laser divergence (in vacuum) cone angle with its centre at laser axis. The rectangle at the centre represents the acceptance angle of the electron energy spectrometer. The average pointing angle of the electron beam is shown with symbol '\otimes'</i>	94

4.9	<i>Result of energy measurement of the accelerated electron beam. a) Image of the energy dispersed electron beam showing low divergence and quasi-mono-energetic feature, and b) energy spectrum with quasi-mono-energetic distribution with peak at 50 MeV.</i>	95
4.10	<i>A schematic diagram of the experimental setup.</i>	99
4.11	<i>Electron beam profiles observed from 3 different gases He, N₂ and Ar at electron density of $5.8 \times 10^{19} \text{ cm}^{-3}$, $3.0 \times 10^{19} \text{ cm}^{-3}$, and $3.0 \times 10^{20} \text{ cm}^{-3}$ respectively.</i>	101
4.12	<i>Images of electron beam profiles observed from helium gas jet at plasma density around $5.8 \times 10^{19} \text{ cm}^{-3}$, $6.8 \times 10^{19} \text{ cm}^{-3}$, and $8.6 \times 10^{19} \text{ cm}^{-3}$ respectively.</i>	101
4.13	<i>Pointing variation of electron beams produced from He, N₂ and Ar at plasma density $5.8 \times 10^{19} \text{ cm}^{-3}$, $3.0 \times 10^{19} \text{ cm}^{-3}$, and $3.0 \times 10^{20} \text{ cm}^{-3}$ respectively.</i>	102
4.14	<i>Images of energy spectra of the electron beams produced from He and N₂ plasma density $5.8 \times 10^{19} \text{ cm}^{-3}$ and $3.0 \times 10^{19} \text{ cm}^{-3}$ respectively.</i>	103
4.15	<i>The line out profiles of energy spectra of the electron beams produced from He and N₂ at plasma density $5.8 \times 10^{19} \text{ cm}^{-3}$ and $3.0 \times 10^{19} \text{ cm}^{-3}$ respectively.</i>	104
5.1	<i>A schematic diagram of the experimental setup. [BPF – Band pass filter which transmits radiation within $400 \pm 20 \text{ nm}$, CCD – Charge coupled detector, and ICT – Integrating current transformer to measure the charge of the accelerated electron beam.]</i>	111
5.2	<i>a) Image of the Ti:sapphire laser beam guiding in plasma plume obtained from the non-linear Thomson scattered radiation at 400 nm (2ω of laser). The arrow represents the direction of the laser propagation, and b) the intensity profile of the guiding channel image along the laser axis.</i>	113
5.3	<i>Results of the electron beam profile measurement. Typical image of the electron beam produced from Nylon plasma plume at a target distance of a) 150 μm, and b) 50 μm; c) Pointing variation of the low divergence electron beam shown in a); d) Typical image of the electron beam produced at a target distance of $\sim 50 \mu\text{m}$ in the plasma plume produced from carbon target.</i>	115
5.4	<i>Results of the electron beam energy measurement. a) Image of the energy dispersed electron beam and b) quasi-mono-energetic spectrum of the electron beam. The spectrum is obtained by integrating the image (a) along the vertical direction over $\pm 10 \text{ mrad}$ about the beam central axis.</i>	115
5.5	<i>Images of electron beam produced from the ASE pre-pulse produced pre-plasma of solid target when the main laser pulse focused a) at grazing incidence and b) at normal incidence.</i>	116
5.6	<i>Energy spectrum of the electrons produced from the interaction of main laser pulse at grazing incidence.</i>	117
5.7	<i>Transmitted spectrum of the fs laser beam after its interaction with the Nylon plasma plume at a distance of 150 μm from the target surface.</i>	119

6.1	<i>A schematic diagram of the experimental setup used for the measurement of radiation dose due to x-rays passing through the glass windows of the plasma chamber.</i>	124
6.2	<i>A schematic diagram of the setup used for energy spectrum measurement of fast electrons emitted from laser-solid interaction.</i>	125
6.3	<i>The angular distribution of the hard x-ray dose rate ($h\nu > 40$ keV) outside the interaction chamber, at a distance of 500 mm from the copper target.</i>	127
6.4	<i>Hard x-ray dose rate variation with distance from the plasma chamber centre.</i>	128
6.5	<i>Hard x-ray dose rate variation with distance from the plasma chamber centre, with lead slab kept at a distance of 50mm from the target.</i>	129
6.6	<i>a) A typical image of the fast electrons produced from the interaction of 45 fs duration Ti:sapphire laser pulses focused to $4 \times 10^{16-17}$ W/cm², for both p- and s-polarization, on planar copper solid target at oblique incidence of 45° w.r.t. the target normal; b) The lineout gives the intensity profile of the fast electrons with an HWHM angular spread of 20°.</i>	130
6.7	<i>Energy spectra of the fast electrons produced from the interaction of 45 fs duration, p- or s- polarized Ti:sapphire laser pulses, focused to 4×10^{17} W/cm² on planar copper solid target at oblique incidence of 45° w.r.t. target normal.</i>	131
6.8	<i>The energy spectra of the fast electrons produced from the interaction of 45 fs duration, p-polarized Ti:sapphire laser pulses, focused to two different intensities.</i>	132
6.9	<i>Energy spectra of the fast electrons produced from the interaction of p-polarized laser pulses of different durations, keeping the laser fluence constant at 1.8×10^4 J/cm².</i>	133
6.10	<i>Variation of the temperature of the fast electrons a) with laser intensity at a fixed pulse duration of 45 fs and b) with pulse duration at a fixed laser fluence of 1.8×10^4 J/cm².</i>	134
6.11	<i>Plasma density profiles obtained from 1D hydrodynamics simulation (using HELIOS code) of the ASE pre-pulse of 1 ns duration irradiating a copper target at 45°.</i>	135

LIST OF TABLES

Table No.	Table Caption	Page No.
1.1	<i>Ionisation energy, E_i in eV and corresponding threshold intensity, I_{BSI} in W/cm^2 for some ions for barrier suppression ionization.</i>	15
1.2	<i>Parameters of the 10 TW Ti:sapphire laser system.</i>	47
4.1	<i>Summary of the electron beams produced from the three gases He, N_2 and Ar.</i>	103

Chapter 1: Introduction

1.1 Laser-driven plasma-based acceleration: An overview

High energy particle accelerators are the most important inventions of the twentieth century which have led to enormous advances in scientific understanding of the things around us. Despite their grand success, the present day high energy accelerators are hitting practical limits due to their large size and cost. This is because the accelerating gradients in conventional radio-frequency (RF) accelerators are currently limited to < 50 MV/m by the field breakdown of the accelerating structure. To address this major issue many advanced accelerator techniques have been proposed and some of them are being actively pursued. Most of the advanced techniques [1, 2] were inspired by the continuous progress in the laser technology over the past 30 years [3-8]. Especially table-top tera-watt power lasers with typical pulse duration of few 10 fs have contributed immensely to the advancements in acceleration techniques based on lasers. An ultra-short pulse high power laser beam when focussed to a spot size of the order of $10\text{ }\mu\text{m}$ results in ultra-high intensity in excess of 10^{18} W/cm^2 . The electric fields corresponding to such intensities are much higher ($\sim 3\text{ TV/m}$) than the Coulomb fields holding electrons in atoms. Therefore, matter subjected to such extreme intensities is immediately ionized at the pedestal intensity of such pulses and turns into plasma state. The electrons in the plasma being light respond almost instantaneously to the electromagnetic fields of the most intense portion of the laser pulse which results in a number of interesting physical processes, along with generation of high-energy electrons. The latter in turn generate energetic ions, neutrons, and x-rays through secondary processes [9]. Of the various laser driven electron acceleration techniques, laser wakefield acceleration (LWFA) offers at least 3 orders of magnitude large electric fields and is considered to be the most promising one for realizing compact high energy accelerators. LWFA was proposed more

than three decades ago by Tajima and Dawson in 1979 [10]. In the LWFA scheme, an intense laser pulse propagating in plasma drives a relativistic electrostatic plasma wave in its wake. The electric field associated with the plasma wave is known as wakefield. The strength of the wakefield can be extremely high of the order of 100 GV/m (for typical plasma density $n_e \sim 10^{19} \text{ cm}^{-3}$). Electrons injected into the accelerating phase of the wakefield can be accelerated to GeV energy over centimetre length. The wakefield can be driven efficiently when the laser pulse duration is short enough to be contained within one period of the wake, which for electron densities of $\sim 10^{19} \text{ cm}^{-3}$ corresponds to laser pulse lengths of $\sim 30 \text{ fs}$. However, when LWFA was first proposed, the available laser pulse lengths were more than 3 orders of magnitude longer. Beating of two co-propagating laser pulses with a frequency difference equal to plasma frequency (beat-wave LWFA, or BW-LWFA) provided a platform for early theoretical and experimental work [11]. The first demonstration of wakefield excitation with this technique was reported in 1985 [12], but it was not until 1993 that electrons were successfully injected into, trapped, and accelerated by the wakefield [13]. The beat-wave LWFA technique is more challenging because it requires a two-frequency laser system, and the frequency difference must be exactly matched to the plasma frequency in order to drive the wake and requires external injection of electrons into the wake.

Invention of chirped pulse amplification (CPA) technique in 1985 [5] made sub-ps laser pulses with several terawatts of power available. While the available pulse lengths were still too long to excite wakefields directly, the laser intensity was high enough to drive the forward Raman scattering instability [14], which in turn was able to produce the plasma waves desired for LWFA studies [15]. This is known as the self-modulated LWFA (SM-LWFA) regime, and it offered several advantages over the beat-wave scheme (most notably the ability to use a single frequency laser) and hence replaced BW-LWFA scheme. Electron spectra with Maxwellian energy distribution extending to nearly 100 MeV were produced for

the first time using this technique [16], and the electric field was deduced to be more than 100 GeV/m (compared with less than 10 GeV/m from BW-LWFA). Subsequently many groups demonstrated electron energies up to ~ 100 MeV from SM-LWFA [17-22]. However, the quality of the accelerated electron bunch was not suitable for many applications. With further advancement in laser technology, the situation dramatically changed in 2004 when three groups [23-25] demonstrated the production of electron bunches with small energy spread ($<10\%$) and low divergence (<10 mrad). A high quality electron bunch was possible due to the newly discovered regime of LWFA which is known as “bubble” or “blow-out” regime [26, 27]. Operation of LWFA in this regime requires the laser pulse spatial extent ($c\tau_0$) and the focal spot (w_0) to be of the order of the plasma wavelength and intensity $> 10^{19}$ W/cm². Although the above experiments did not meet this condition initially, non-linear self-evolution of the laser pulse through propagation in the plasma eventually led to acceleration in this regime under precisely controlled experimental conditions. Subsequently, using a plasma-channel-guided laser, high-quality electron bunches up to 1 GeV have been experimentally demonstrated in 2006 for the first time [28]. Recently, stable and controllable electron beams of high energy up to few 100 MeV have been demonstrated under different interaction conditions and injection schemes and efforts are still continuing for further improvements [29-45]. The rapid developments in this field along with unique features of the electron beams produced from LWFA (viz. few femtosecond duration, low emittance, and high peak current) are now becoming highly attractive for a variety of new applications [46]. In future, high quality GeV-class electron bunches will enable applications of LWFAs in front-end injectors for conventional accelerators and as drivers for compact, short-pulse radiation sources. These developments open the door to far more efficient and compact staged particle accelerators utilizing next generation petawatt power lasers to achieve TeV scale particle energies.

In addition to the laser wakefield acceleration, which is pursued as an alternative to the conventional accelerators, generation of fast electrons and their subsequent transport in high intensity laser-solid interaction has been intensely studied, both theoretically and experimentally over the years, mainly due to its importance in inertial confinement fusion (ICF) [47-60]. In addition, they also govern a number of secondary processes such as high-energy ion production, neutron generation, continuous energy hard x-ray emission and monochromatic K- α x-ray emission [61-66]. Various mechanisms such as resonance absorption, vacuum heating, and $\mathbf{J} \times \mathbf{B}$ acceleration produce fast electrons [47-52]. The exact mechanism of fast electrons generation and their angular distribution depends on laser and target interaction conditions [67-70]. The fast electrons going into the target material would slow down and produce a bright source of hard x-rays, which can be useful for a variety of research and technological applications. For instance, such sources have been used for activation of short-lived isotopes which can be used in radiological diagnostics for positron emission tomography, transmutation of elements by neutron capture to deactivate long-lived fission fragments, and for nuclear fission of actinides [71-74]. Many practical applications require collimated energetic electrons in a well-defined direction. Therefore, there is continuing research to obtain a well-collimated fast electron beam emitted in a particular direction, with a careful control of the laser and plasma conditions.

1.2 Scope of the present thesis work

This thesis work mainly focuses on generation of relativistic, quasi-mono-energetic, and low divergence electron beams from laser wakefield acceleration using multi-TW, 45 fs laser pulse interaction with sub-mm length plasma generated from gas jet targets and from solid targets. This work also deals with the generation of MeV energy fast electrons and

bremsstrahlung hard x-ray generation from intense laser-solid interactions and their characterization.

In the case of experiments on LWFA using under-dense gas jet targets, the electron beam generation has been studied under different laser and gas jet conditions to find optimum parameters to generate stable, high-quality, and high-energy electron beams. The effect of laser frequency chirp on laser pulse self-modulation and electron acceleration has also been studied. Control of the laser self-modulation, electron beam charge, and electron energy has been demonstrated by controlling the chirp. Next, the role of laser pre-pulse on the main laser propagation and on electron acceleration has been studied and optimum pre-pulse conditions have been found to form a plasma wave-guide that facilitates guiding of the main laser pulse, and to accelerate electrons to higher energies. Further, LWFA in different gases like helium, nitrogen, and argon has been investigated. It was observed that stable and high-quality electron beams can be produced from high density helium and nitrogen gas jets. Finally, laser wakefield acceleration has been demonstrated for the first time in laser produced solid plumes to produce high quality, low divergence, quasi-mono-energetic electron beams. This is an important step forward as it offers electron acceleration in various targets and most importantly allows electron acceleration in high rep-rate mode, in comparison to conventional gas jet targets.

In the case of experiments on laser interaction with solid targets, angular distribution of the bremsstrahlung hard x-rays has been studied and the fast electrons have been identified to be the source of the bremsstrahlung x-rays. This result is important from both application as well as radiation safety point of view. The angular and energy distribution of the fast electrons generated from the solid target have been characterized under various laser irradiation conditions and scaling laws have been obtained. These results are important to

control the fast electrons for various applications viz., ion acceleration, x-ray generation, and fast ignition in inertial confinement fusion.

In what follows, various concepts relevant to understand the work presented in this thesis will be explained.

1.3 Basics of electromagnetic waves

An electromagnetic wave is represented by electric $\mathbf{E}(z, t)$ and magnetic $\mathbf{B}(z, t)$ fields which vary in space, z and time, t . The propagation of an electromagnetic wave in a medium is described by Maxwell's equations:

$$\begin{aligned}\nabla \cdot \mathbf{E} &= \frac{\rho}{\epsilon_0}, & \nabla \times \mathbf{E} &= -\frac{\partial \mathbf{B}}{\partial t}, \\ \nabla \cdot \mathbf{B} &= 0, & \nabla \times \mathbf{B} &= \mu_0 \mathbf{j} + \frac{1}{c^2} \frac{\partial \mathbf{E}}{\partial t}\end{aligned}\tag{1.1}$$

where ρ , \mathbf{j} , ϵ_0 , and μ_0 are the charge density, current density, electric permittivity and magnetic permeability of vacuum respectively. The quantities ϵ_0 , and μ_0 are related to each other by the speed of light in vacuum, $c = 1/\sqrt{\epsilon_0 \mu_0}$. The fields of the electromagnetic wave are generally expressed by a vector potential \mathbf{A} and a scalar potential Φ [75]:

$$\mathbf{E} = -\frac{\partial \mathbf{A}}{\partial t} - \nabla \Phi, \quad \mathbf{B} = \nabla \times \mathbf{A}\tag{1.2}$$

In vacuum, the electric and magnetic field amplitudes are related to the vector potential amplitude by $E_0 = cB_0 = \omega A_0$. Also $\mathbf{E} \parallel \mathbf{A}$, $\mathbf{E} \perp \mathbf{B}$, and $\mathbf{B} \perp \mathbf{k}$. The dispersion relation for electromagnetic wave propagation in vacuum is given by:

$$\omega^2 = k^2 c^2\tag{1.3}$$

The electromagnetic waves transport energy with energy flux density given by the Poynting vector, \mathbf{S} which is given by:

$$\mathbf{S} = \epsilon_0 c^2 (\mathbf{E} \times \mathbf{B})\tag{1.4}$$

An expression for the corresponding intensity I can be found by making use of the fact that $\mathbf{E} \perp \mathbf{B}$ and $E = cB$ and time averaging over one oscillation period of the fields:

$$I = \langle S \rangle = \varepsilon_0 c \langle E^2 \rangle = (\varepsilon_0 c / 2) E_0^2 \quad \text{or}$$

$$E_0 \left(\frac{V}{cm} \right) \simeq 27.4 \sqrt{I \left(\frac{W}{cm^2} \right)} \quad (1.5)$$

1.3.1 Gaussian laser beam

The electric and magnetic fields, \mathbf{E} and \mathbf{B} , of a high power pulsed laser beam can be represented mathematically by a Gaussian function in space and time. For a linearly polarised laser beam in vacuum, the electric field of the laser pulse can be represented as follows:

$$\mathbf{E}(r, z, t) = \hat{\mathbf{x}} \frac{E_0}{2} \cdot f(t, z) \cdot \frac{w_0}{w(z)} \cdot \exp \left(-\frac{r^2}{w^2(z)} - i \frac{k_0 r^2}{2R(z)} + i\varphi(z) \right) + cc,$$

$$f(t, z) = \exp \left(-2 \ln 2 \left(\frac{t - z/c}{\tau_0} \right)^2 \right) \quad (1.6)$$

Here w_0 is called the beam waist which is defined as the radius of the beam at $1/e$ of the peak electric field or $1/e^2$ of the peak intensity at the focal plane, $z = 0$. The waist, w_0 and the full width at half maximum (FWHM) spot size, d_0 are connected by $d_0 = \sqrt{2 \ln 2} w_0$. τ_0 is the pulse duration at FWHM, and $k_0 = \omega_0/c$ is the wave number corresponding to a carrier frequency ω_0 . The functions $w(z)$ and $R(z)$ represent respectively the radius at $1/e$ of the electric field and the radius of curvature of the wave front and $\varphi(z)$ is the Gouy phase. These functions are defined as follows:

$$w(z) = w_0 \sqrt{1 + \frac{z^2}{z_R^2}},$$

$$R(z) = z \left(1 + \frac{z_R^2}{z^2} \right), \quad (1.7)$$

$$\varphi(z) = \tan^{-1} \left(\frac{z}{z_R} \right)$$

where $z_R = \pi w_0^2 / \lambda_0$ is the Rayleigh length. It is the distance, from focal plane, $z=0$, at which the laser intensity decreases by a factor of 2 relative to the intensity at the focal spot. The depth of focus of the beam, also called the “confocal parameter” is defined as twice the Rayleigh length. A schematic of Gaussian laser beam is shown in Fig. 1.1.

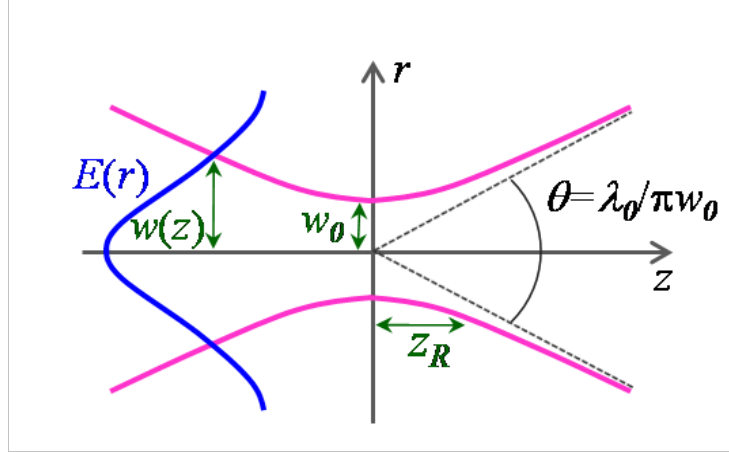


Figure 1.1: Schematic of a Gaussian laser beam showing beam waist, w_0 , Rayleigh length, z_R , and divergence angle, θ .

In the focal plane, the relation between the peak intensity, I_0 , the peak power, P_0 , and the total energy, \mathcal{E} , in the pulse are related as follows:

$$I_0 = \frac{2P_0}{\pi w_0^2} \quad \text{and} \quad P_0 = 2 \sqrt{\frac{\ln 2}{\pi}} \cdot \frac{\mathcal{E}}{\tau_0} \approx 0.94 \frac{\mathcal{E}}{\tau_0} \quad (1.8)$$

In practice, a high power laser beam is focused to achieve high intensities at the interaction point. The spatial profile remains Gaussian at focus if the laser beam before focusing has Gaussian profile. Therefore, the focal spot waist, w_0 can be estimated from the propagation equations of Gaussian laser beam. If a laser beam with initial radius, W is focused using a focusing optics of focal length, f , then the beam waist at the focus is given by:

$$w_0 = \frac{\lambda_0}{\pi W} \cdot f \quad (1.9)$$

However, the practical high power laser beam spatial profile deviates from the ideal Gaussian function. In such cases, the measured focal spot will be larger than that predicted by the above equation. The ratio of the measured beam waist to the predicted value is represented by M^2 which is called beam quality parameter. The Rayleigh length of an actual beam is given by $z_R = \pi w_m^2 / M^2 \lambda_0$.

1.4 Basics of plasma

Plasma is an overall neutral ensemble of charged particles (in the case of a fully ionized plasma, only of electrons and positively charged ions) which exhibit collective behaviour. Two conditions must be satisfied for a collection of charged particles to be called plasma [76]. One, the distance over which a charge inserted into the plasma is shielded out must be much smaller than the plasma size. This distance, called Debye length, is given by:

$$\lambda_D = \sqrt{\frac{\epsilon_0 k_B T_e}{n_0 e^2}} \quad (1.10)$$

where k_B is the Boltzmann constant, T_e is the electron temperature. This condition can also be regarded as quasi-neutrality condition, i.e. on a length scale λ_D the plasma appears to be electrically neutral. The second condition is that, the number of particles N_D in the Debye's sphere must be large i.e.

$$N_D = n_0 \cdot \frac{4\pi}{3} \cdot \lambda_D^3 \gg 1 \quad (1.11)$$

1.4.1 Plasma oscillations

When the quasi-neutrality of the plasma is disturbed by some external force, the plasma electrons being much lighter compared to ions, respond collectively to shield the external force. The collective behaviour results in local oscillation of plasma electrons. These oscillations are called “*plasma oscillations*”. The plasma oscillations also results in oscillating electrostatic field. Ions respond comparatively on much longer time scales and they are of no

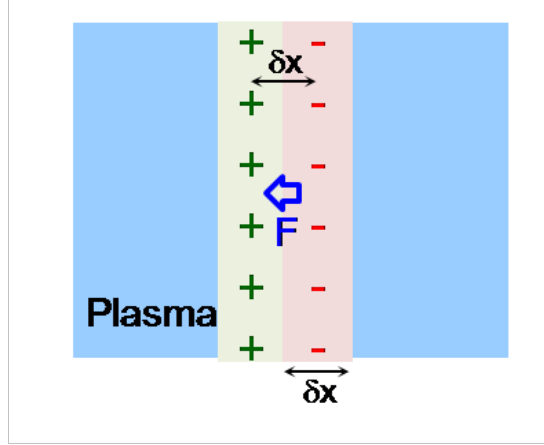


Figure 1.2: Schematic of a slab of plasma in which a sheet of electrons (-) with thickness δx is displaced by an amount δx from the ions (+). A restoring force F acts on the electrons and sets up oscillations, called “plasma oscillations, about equilibrium position.

interest to the present theses work which uses femto-second duration laser pulse. In order to understand the concept of plasma oscillations, let us consider displacement of a slab of plasma electrons with thickness L as illustrated in Fig. 1.2, while the ions remain fixed [76, 77]. The displacement of plasma electrons by a distance $\delta x \ll L$ produces positive charge on one side, and negative charge on the other side of the slab, with surface charge density $\sigma = \pm e \cdot n_0 \delta x$. The electric field of these charges, $E = \sigma / \epsilon_0$, where e is the electron charge magnitude and n_0 the electron density, exerts a restoring force. The motion of the electrons due to this restoring force is governed by the following equation:

$$\frac{d^2 \delta x}{dt^2} + \omega_p^2 \delta x = 0 \quad (1.12)$$

This is the equation of a harmonic oscillator with frequency $\omega_p = \sqrt{n_0 e^2 / m_0 \epsilon_0}$, where m_0 is the electron rest mass. The charge separation sets up the plasma density oscillation at a characteristic frequency ω_p , referred to as the electron plasma frequency and defines a time scale, $\tau_p = 2\pi / \omega_p$ on which collective electron effects in a plasma take place. The plasma frequency is also given by the expression:

$$\omega_p \simeq 5.64 \times 10^4 \sqrt{n_0(\text{cm}^{-3})} \text{ rad/s} \quad (1.13)$$

In a collisional plasma with mean inter-collision time τ_c , for the plasma to show collective behaviour, one should have the condition $\omega_p \gg 1/\tau_c$ or $\omega_p \tau_c \gg 1$. This condition is also referred to as the third condition for an ensemble of charged particles to qualify to be called plasma.

In a warm plasma with electron temperature T_e , the plasma oscillations excited by local disturbance can propagate by virtue of the electron thermal motion and these are known as “plasma waves” or “Langmuir waves”. The phase and group velocity of such waves is governed by “Bohm-Gross dispersion relation” [76]:

$$\omega^2 = \omega_p^2 + 3v_{th}^2 k^2 \quad (1.14)$$

where $v_{th} = \sqrt{k_B T_e / m_0}$ is the thermal velocity of the plasma electrons and k_B is the Boltzmann constant.

In a cold plasma with $T_e = 0$, the dispersion relation will be $\omega = \omega_p$. This implies that the plasma oscillations are localized and do not carry energy as their group velocity ($d\omega/dk$) is zero. Slower electrostatic modes, known as *ion acoustic waves*, can also exist in plasma. These fulfil the dispersion relation $\omega = k_i c_s$, where c_s is the ion sound velocity which is given in (cm/s) by:

$$c_s \simeq 1 \times 10^6 \sqrt{\left(Z + \frac{3T_i}{T_e}\right) \frac{m_0}{m_i} T_e (\text{eV})} \quad (1.15)$$

1.4.2 Electromagnetic wave propagation in plasma

The propagation of electromagnetic waves in plasma is governed by the dispersion relation:

$$\omega^2 = \omega_p^2 + k^2 c^2 \quad (1.16)$$

The phase velocity v_ϕ and group velocity v_g of the electromagnetic wave and the refractive index η of the plasma can be derived from the dispersion relation as:

$$\begin{aligned} v_\phi &= \frac{\omega}{k} = c / \sqrt{1 - \frac{\omega_p^2}{\omega^2}}, \\ v_g &= \frac{\partial \omega}{\partial k} = c \sqrt{1 - \frac{\omega_p^2}{\omega^2}}, \\ \text{and } \eta &= \frac{c}{v_\phi} = \sqrt{1 - \frac{\omega_p^2}{\omega^2}}. \end{aligned} \tag{1.17}$$

As can be seen from the above expressions, the group velocity and the phase velocity of an electromagnetic wave in plasma are simply related by the expression $v_\phi \times v_g = c^2$.

The refractive index η is real when the frequency of the electromagnetic wave is more than the plasma frequency and it is imaginary when the wave frequency is less than the plasma frequency. So an electromagnetic wave can propagate through the plasma only when its frequency is above the plasma frequency. The density at which the refractive index of the plasma as well as the group velocity of the electromagnetic wave become zero (i.e. at $\omega = \omega_p$) is known as the *critical density*, n_c , given by:

$$n_c = \frac{\omega^2 m_0 \epsilon_0}{e^2} = \frac{1.1 \times 10^{21}}{\lambda^2 (\mu m)} \text{ cm}^{-3}. \tag{1.18}$$

1.5 Ultra-high intense laser-matter interactions

In the case of ultra-high intensity ($>1 \times 10^{16} \text{ W/cm}^2$) femto-second duration laser pulses, the associated electric field will be larger than the Coulomb field binding the electrons to the nucleus. Matter subjected to such ultra-intense fields will be ionized instantly. Therefore, the description of laser-matter interaction reduces to laser-plasma interaction. The plasma electrons being lighter move almost instantaneously in the high frequency optical

fields of the laser pulse and they acquire relativistic velocities. The relativistic motion of the electrons manifests a variety of interesting processes. Some of the processes relevant to the thesis work will be explained in the following sections.

1.5.1 Laser induced ionization of matter

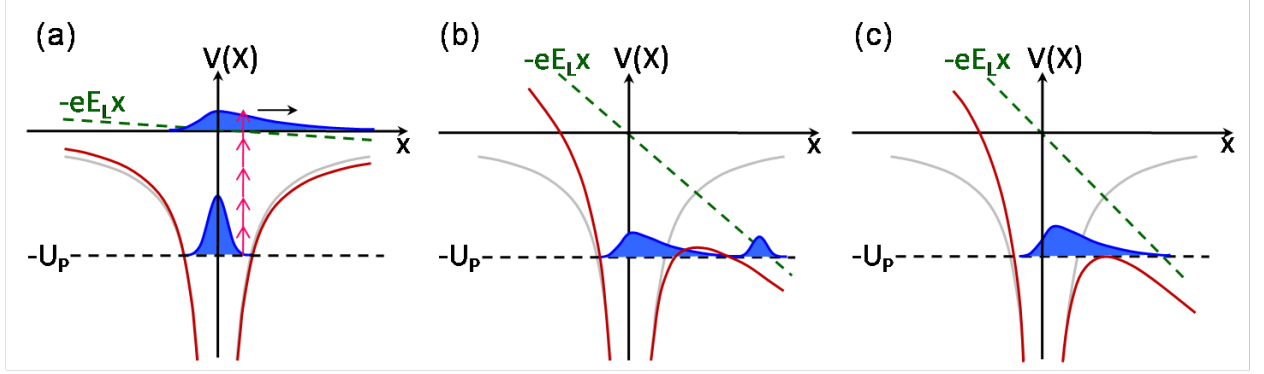


Figure 1.3: Illustration of the ionisation process by a laser field. For a weak laser electric field, the Coulomb potential, $V(x)$ of the atom is slightly perturbed as shown in a) and ionisation occurs through multi-photon absorption. The unperturbed potential of the atom is indicated in “grey” line, the potential of laser field is indicated with “green dashed line”, and the electron is illustrated by a wave-packet shown in “blue”. The binding potential, $-U_p$, is shown in “black dashed line”. b) and c) illustrate tunnelling and barrier suppression ionization due to potential barrier deformation in laser electric field, E_L , with increase in strength.

Depending on the intensity and wavelength of the laser, different models are used to explain the ionisation process. At relatively lower intensities, the laser field perturbs the Coulomb potential of the atom or ion slightly and the ionisation occurs by multi-photon absorption (see Fig. 1.3a). If the energy of one photon (e.g. photon energy $\hbar\omega_L = 1.5$ eV for Ti:sapphire laser with wavelength $\lambda_L = 800$ nm) is less than the ionization energy (ionization energy for hydrogen $E_i = 13.6$ eV), absorption of n_{ph} simultaneously incident photons with summed up energy $n_{ph}\hbar\omega_L > E_i > (n_{ph} - 1)\hbar\omega_L$ results in “multi-photon ionization (MPI)” of the atom or ion [78]. Here “simultaneously” means that the $i + 1^{st}$ photon should arrive within the lifetime of the i^{th} virtual excited state, which is usually in fs, and easily fulfilled with a finite probability for ultra-high intensity laser pulses with energy few 100 mJ ($n_{ph} \sim 1 \times 10^{18}$ at $\lambda_L = 800$ nm) and several 10 fs duration.

In the ultra-high intense laser field approaching the strength of the Coulomb potential of the atom, the potential will be significantly deformed, and consequently the potential barrier height and width will get reduced. The bound electrons now have a certain probability of tunnelling through the barrier and ionisation takes place as illustrated in Fig. 1.3b. This process of ionization is called “*tunnel ionization (TI)*”. When the laser intensity is further increased, the potential barrier will be so heavily suppressed that the electron is immediately set free as shown in Fig. 1.3c. This effect is called “*barrier suppression ionization (BSI)*” and this is also known as “*Over-the-barrier ionization (OBI)*”. Both TI and BSI regimes are quantitatively described in the theory by Ammosov, Delone and Krainov (ADK theory) [79]. A simple model was developed by Bethe and Salpeter [80] to explain the deformation of the atomic binding potential and ionization due to the laser field. The model predicts the threshold laser intensity required for BSI which holds remarkably well even for more complicated electron systems. The threshold intensity for BSI is given by:

$$I_{BSI} \left(\frac{W}{cm^2} \right) \simeq 4 \times 10^9 E_i^4 (eV) \cdot Z^{-2}, \quad (1.19)$$

where Z is the charge state of the atom or ion after the ionization and E_i is the energy required for ionization of the atom or ion. The threshold intensities for the BSI of some of the gaseous atoms and their ions are presented in Table 1.1. We see immediately that, for $I_0 > 1 \times 10^{18} W/cm^2$ and for the gases (H_2 , He, N_2 , and Ar) used in the experiments presented in the thesis, the leading edge of the focused pulse fully ionizes H_2 and He, and partially ionizes N_2 and Ar. The most intense part of the pulse therefore interacts with ionized state, plasma, of the gases.

<i>Ion</i>	<i>E_i(eV)</i>	<i>I_{BSI} (W/cm²)</i>
H+	13.6	1.4×10 ¹⁴
He+	24.6	1.4×10 ¹⁵
He2+	54.4	8.8×10 ¹⁵
N5+	97.9	1.5×10 ¹⁶
N6+	552.1	1.0×10 ¹⁹
N7+	667.1	1.6×10 ¹⁹
Ar8+	143.5	2.6×10 ¹⁶
Ar10+	478.7	2.1×10 ¹⁸

Table 1.1: Ionisation energy, E_i in eV and corresponding threshold intensity, I_{BSI} in W/cm^2 for some ions for barrier suppression ionization.

1.5.2 Motion of a free electron in an electromagnetic field

A free electron in electric field $E = E_0 \cos(\omega t - kz)$ of an electromagnetic wave with frequency ω oscillates along the electric field direction with a velocity, called the quiver velocity, whose amplitude is given by:

$$v_o = \frac{eE_0}{m_0\omega} \quad (1.20)$$

The average kinetic energy of the oscillating electron is known as the ponderomotive potential, U_p which is given by:

$$U_p = \frac{1}{4} \frac{e^2 E_0^2}{m_0 \omega^2}$$

$$\text{or } U_p(eV) \simeq 9.33 \times 10^{-14} \cdot I_0 \left(\frac{W}{cm^2} \right) \cdot \lambda^2(\mu m) \quad (1.21)$$

In an ultra-intense laser field, v_o becomes relativistic when the electron's oscillatory kinetic energy exceeds its rest mass energy $m_0 c^2$. To characterize the strength of the laser field, a dimensionless parameter a_0 called *normalized vector potential* or *laser strength parameter* is defined as:

$$a_0 = \frac{eA_0}{m_0c} = \frac{p_0}{m_0c} \quad (1.22)$$

where p_0 is the maximum oscillatory momentum of the electron. In practical units,

$$a_0 \simeq 0.85\sqrt{I_0(\times 10^{18} \text{ W/cm}^2) \cdot \lambda^2(\mu\text{m})}. \quad (1.23)$$

The a_0 related to relativistic factor γ (of the oscillating electron) by the following relation:

$$\gamma^2 = 1 + a_0^2 \quad (1.24)$$

The parameter a_0 represents “relativistic-ness” of the electron motion. Intensities yielding $a_0 \gtrsim 1$ are called “relativistic intensities” and the interaction regime is called “relativistic regime”. As an example, a Ti:sapphire laser pulse with wavelength $\lambda_0 = 800$ nm and intensity $I_0 = 2.14 \times 10^{18} \text{ W/cm}^2$ corresponds to $a_0 = 1$, which indicates relativistic effects will begin to play a significant role. In the relativistic regime, the electron motion is no longer determined by the electric field alone, but the magnetic field also becomes important. The equation of motion for a free electron should include Lorentz force due to both electric and magnetic fields of electromagnetic wave.

$$\frac{d\mathbf{p}}{dt} = -e(\mathbf{E}(\mathbf{r}, t) + \mathbf{v} \times \mathbf{B}(\mathbf{r}, t)) \quad (1.25)$$

where $\mathbf{p}(t) = \gamma m_0 \mathbf{v}(t)$ is the relativistic electron momentum, γ the relativistic Lorentz factory = $(1 - \mathbf{v}^2/c^2)^{-1/2} = [1 + p^2/(m_0c)^2]^{1/2}$, $\mathbf{E}(\mathbf{r}, t)$ and $\mathbf{B}(\mathbf{r}, t)$ are the electric field and magnetic field respectively at the electron's actual position $\mathbf{r}(t)$ and $\mathbf{v}(t)$ the electron velocity. The trajectory of a free electron in an infinite, plane electromagnetic wave $\mathbf{E}(\mathbf{r}, t) = \hat{x} E_0 \sin(kz - \omega t)$, linearly polarized along x-axis and propagating in z-direction can be obtained from solving the Eq. 1.25. By variable transformation, $\tau = t - z/c$, which describes the phase of the wave and is also the proper-time t/γ of the electron, the solution to the Eq. 1.25 is obtained as:

$$x(\tau) = \left(\frac{ca_0}{\omega}\right) \sin(\omega\tau)$$

$$y(\tau) = 0$$

$$z(\tau) = \left(\frac{ca_0^2}{4} \right) \left(\tau + \frac{1}{2\omega} \sin(2\omega\tau) \right) \quad (1.26)$$

It is clear from the above solutions that the electron oscillates with frequency ω parallel to the electric field vector E and at double frequency 2ω along the wave-propagation axis z . The electron also drifts along z -axis in the lab frame with velocity given by :

$$v_{drift} = c \frac{a_0^2}{a_0^2 + 4} \quad (1.27)$$

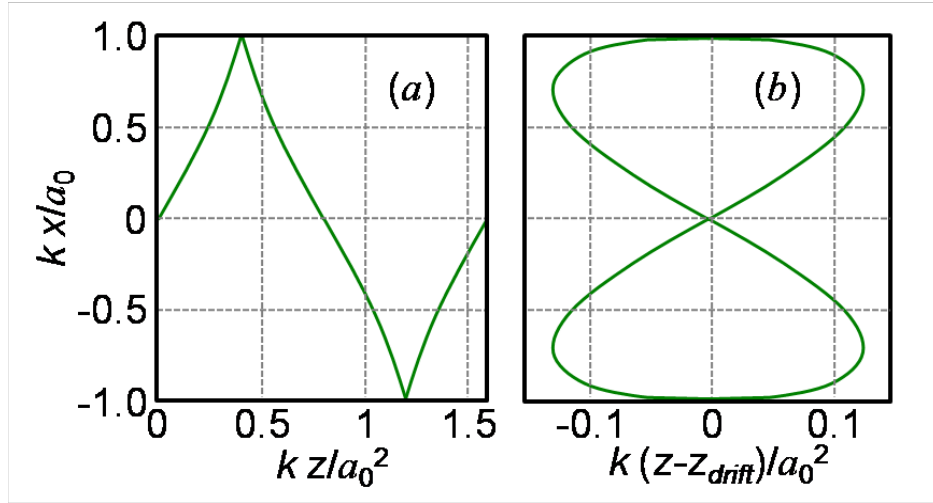


Figure 1.4: a) Trajectory of a free electron in a plane, linearly polarised electromagnetic wave as seen from lab frame. b) Figure of 8 trajectory in the drift frame.

Since the transverse force eE due to electric field is proportional to a_0 and the longitudinal force ($evB \propto eE^2$) due to magnetic field is proportional to a_0^2 , the motion is predominantly in the transverse direction when $a_0 \ll 1$, and it is predominantly longitudinal when $a_0 \gg 1$. The electron motion as observed from lab frame and a frame drifting with v_{drift} along z -axis are shown in Fig. 1.4. The electron motion in drift frame appears as “Figure of 8” trajectory. This motion in the laser field causes emission of harmonic radiation of laser which is called *non-linear Thomson scattering* [9]. Thomson-scattered light is emitted

from the plasma at regions of high intensity. Therefore this is mostly emitted from the region of laser self-focusing (discussed later) and guiding in the plasma. The region of self-focusing is called self-focussing channel. The scattered radiation at fundamental (linear Thomson scattering) and the second harmonic frequency (non-linear Thomson scattering) are used to observe the self-focusing channels in the laser wakefield acceleration experiments presented in this thesis.

The trajectory of electron has been derived in this section using the constants of the motion that arise from the symmetry of the simple case of an infinite plane wave. The motion of electrons in more realistic situations is generally more complex. However if the laser pulse amplitude varies slowly compared to the oscillatory phase of the field, then the constants of the motion vary adiabatically and can still be used. This fact is used in the concept of the ponderomotive force.

1.5.3 Ponderomotive force

In the case of a plane wave, the laser field pushes the electron in the direction of propagation of the wave. The net effect is therefore just a forward translation of the electron, and it will remain at rest once the laser pulse has passed resulting in zero net energy gain. Under the experimental conditions used in the present thesis work, the wave is far from a plane wave, as the laser beam is focused, creating strong radial intensity gradients which gives rise to a force known as “*ponderomotive force*”.

The ponderomotive force results from the oscillation of the electrons in a laser field with spatial intensity variation (i.e. a peak in intensity on the axis, as is typical of focused laser spots, or finite pulse duration). The derivation for ponderomotive force can be found from [81] and the final expression is:

$$\mathbf{F}_p = -\frac{e^2}{4m_0\omega^2} \nabla \langle \mathbf{E}^2(\mathbf{r}) \rangle \propto -\nabla I \quad (1.28)$$

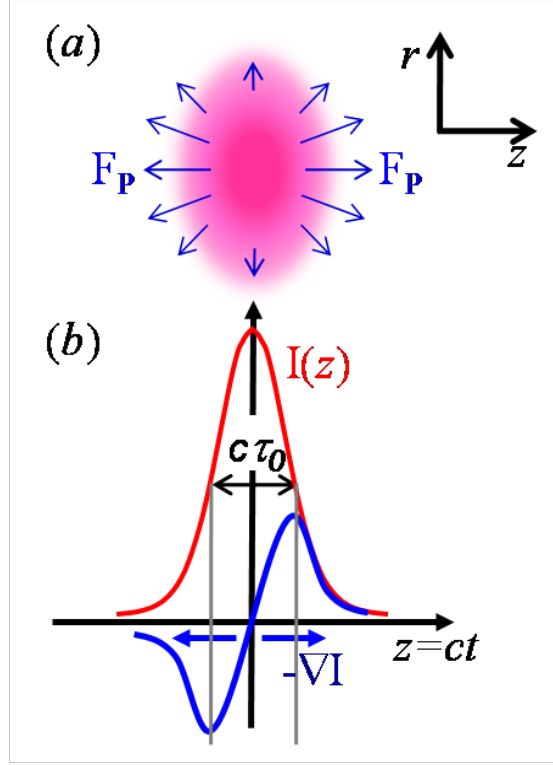


Figure 1.5: a) Laser pulse intensity distribution is shown in 2D and the associated ponderomotive force direction and magnitude is indicated with arrows, b) shows Gaussian line intensity profile of the laser pulse (red) along the propagation axis and the associated ponderomotive force (blue). The peaks of the forward and backward ponderomotive force are separated by the pulse FWHM duration, $c\tau_0$.

Note that due to the contribution of the magnetic field, there is an axial ponderomotive force as well as a radial one. The ponderomotive force expels electrons from regions of high laser intensity as shown in Fig. 1.5. The larger mass of ions results in very small amplitude ion oscillations in the laser field with the resulting displacement smaller by a factor $(m_0/m_i)^2 \approx 10^6$, where m_i is the ion mass. Hence, the ponderomotive force is much stronger for electrons than for ions. At ultra-high intensities of laser pulse, the relativistic effects of electron motion become important. Quesnel and Mora [82] have derived an expression for relativistic ponderomotive force, by including both the relativistic motion of the electron and electromagnetic fields that accurately describe a focused laser pulse and showed that:

$$F_{p,rel} = -\frac{1}{2}m_0c^2\nabla\langle a_0^2 \rangle = -m_0c^2\nabla\langle \gamma \rangle, \quad (1.29)$$

where $\langle \gamma \rangle = \sqrt{1 + a_0^2/2}$ is the cycle averaged relativistic factor for linearly polarized wave. The ponderomotive force is related to the ponderomotive potential by $F_p = -\nabla U_p$, and it is a conservative force.

1.5.4 Self-focusing and self-guiding

The index of refraction for a low intensity electromagnetic wave propagating in a plasma of uniform density n_0 is given by $\eta = (1 - \omega_p^2/\omega^2)^{1/2}$. For ultra-high intense waves, however, the electron oscillatory velocity becomes relativistic and the ponderomotive force is large. The relativistic effect increases the inertia ($m = \gamma m_0$) of the electrons under the laser field and the γ varies with the radial and axial intensity variation of the laser pulse. The ponderomotive force, on the other hand, expels the plasma electrons from the high intensity regions to the low intensity regions resulting in plasma density variation in the direction of radial and axial intensity gradients of the laser. The variation in the mass and density of the electrons under the laser field will modify the refractive index. Hence, the general expression for the index of refraction for a large amplitude electromagnetic wave in plasma can be written as [83]:

$$\eta(r, z) = \sqrt{1 - \frac{\omega_p^2}{\omega_0^2} \frac{\tilde{n}(r, z)}{\langle \gamma(r, z) \rangle}}, \quad (1.30)$$

where $\tilde{n} = n + \delta n(r, z)$ is the varying plasma density. The above expression can be expanded to get:

$$\begin{aligned} \eta(r, z) &\simeq 1 - \frac{1}{2} \frac{\omega_p^2}{\omega_0^2} \left(1 - \frac{a_0^2(r, z)}{2} + \frac{\delta n(r, z)}{n} + \frac{\delta n_{ch}(r, z)}{n} \right), \\ v_\phi(r, z) &= \frac{c}{\eta(r, z)} \simeq 1 + \frac{1}{2} \frac{\omega_p^2}{\omega_0^2} \left(1 - \frac{a_0^2}{2} + \frac{\delta n}{n} + \frac{\delta n_{ch}}{n} \right), \\ v_g(r, z) &= c\eta(r, z) \simeq 1 - \frac{1}{2} \frac{\omega_p^2}{\omega_0^2} \left(1 - \frac{a_0^2}{2} + \frac{\delta n}{n} + \frac{\delta n_{ch}}{n} \right). \end{aligned} \quad (1.31)$$

Here, the term containing a_0 causes the change of γ of the background electrons leading to relativistic self-focusing. δn is the density depletion due to the transverse ponderomotive force (which causes ponderomotive self-focusing), and δn_{ch} is the density depression due to preformed plasma channel for guiding the intense laser pulse. When an ultra-intense laser beam with a Gaussian intensity profile in the radial direction, propagates in the plasma, due to the relativistic mass dependence on intensity (or a_0), it would see higher refractive index on the axis in comparison to the edges. Since $v_\phi = c/\eta$, the phase velocity along the propagation axis will be less than it is towards the edges. This causes the laser phase fronts to curve inwards in the direction of propagation which causes radial focusing of the laser beam. This is called “relativistic self-focusing”. The self-focusing continues until it is balanced by the counteracting increased natural diffraction due to reduced spot size. This leads to self-guiding of the laser pulse over several Rayleigh lengths. The relativistic effect is the dominant cause for intense laser pulse self-focusing in plasmas. The relativistic self-focusing occurs for laser power, P exceeding certain critical power, P_c which is given by [84]:

$$P_c(GW) = 17.4 \frac{n_c}{n_0} \quad (1.32)$$

The radial ponderomotive force of the laser pushes the plasma electrons from high intensity region on the axis to the low intensity regions towards the edges. This will create radial density variation δn with lower electron density on axis and higher electron density towards the edges. This induces variation of the refractive index in radial direction, similar to one due to relativistic effect, and causes self-focusing which is known as “ponderomotive self-focusing”. The ponderomotive effect slightly reduces the critical power required for relativistic self-focusing [85]. The critical power due to both the effects then becomes:

$$P_c(GW) = 16.2 \frac{n_c}{n_0} \quad (1.33)$$

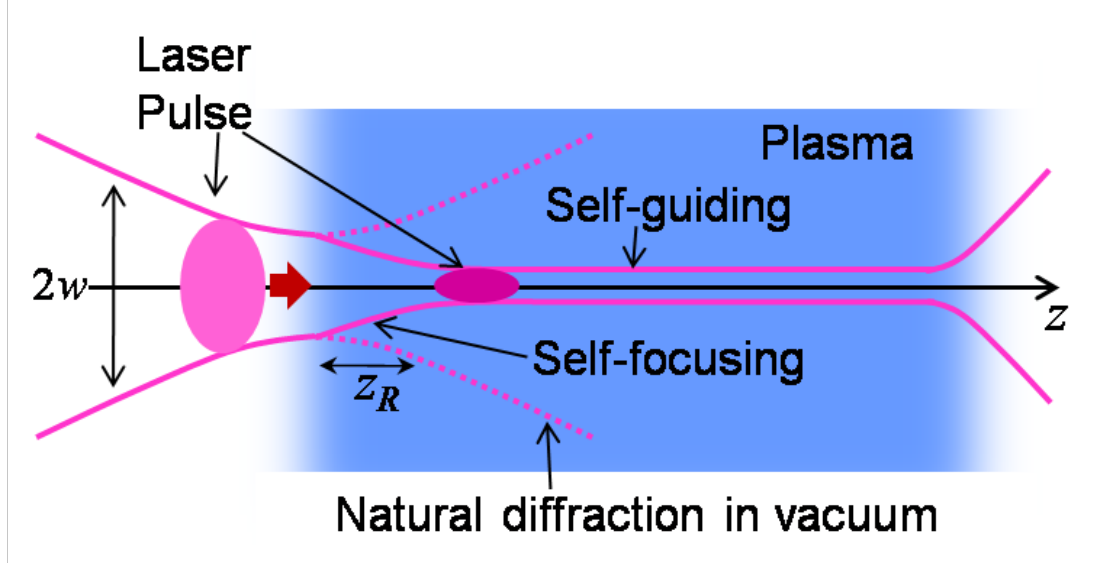


Figure 1.6: Illustration of laser self-focussing and self-guiding in plasma.

A schematic of laser self-focusing phenomena in plasma is shown in Fig. 1.6. The self-focusing helps to further increase the laser intensity obtained using focusing optics, and guide the intense beam over distances much longer than the Rayleigh length (the length limited by the natural diffraction). Both these effects are very useful for laser wakefield acceleration and also in the generation of fast electrons from solid target interactions, which is described later. Since $P_c \propto n_0^{-1}$, self-focusing and guiding in low density plasmas require higher laser power. Therefore pre-formed plasma channels (wave guides) with parabolic radial density variation of the form $n(r) = n_0 + \Delta n r^2 / w_0^2$, {where $\Delta n = n_e(r=w_0) - n_e(r=0)$ is the channel depth and w_0 is matched spot size} are used for guiding. Such plasma channels are generally created by using a ns duration laser pulse or electrical discharges to initially heat the plasma which causes hydrodynamic expansion of the plasma in the radially outward direction. This expansion causes formation of plasma channel suitable for guiding of intense laser beam. Pre-formed plasma channel reduces the threshold power for guiding. A Gaussian laser beam with power P will be guided in the plasma channel when:

$$P \geq P_{ch} = P_c(1 - \Delta n/\Delta n_{ch}), \quad (1.34)$$

where $\Delta n_{ch} [\text{cm}^{-3}] = 1.13 \times 10^{20}/w_0^2 [\mu\text{m}]$. When $P = P_{ch}$, the laser beam is smoothly guided with constant spot size. However, when $P > P_{ch}$ the laser is guided but the spot size oscillates along the length of the channel with a period $\lambda_{osc} = \pi z_R(\Delta n_{ch}/\Delta n)^{1/2}$ [84].

1.5.5 Self-steepening and self-compression

The variation in the plasma density and laser pulse intensity along the laser propagation direction (i.e. longitudinal direction) affects the refractive index variation along axis and modifies laser pulses. For longitudinally varying laser intensity profiles e.g. Gaussian, the relativistic correction in terms of a_0^2 leads to regions with different local group velocities along the length of the laser pulse. The group velocity will be higher at the peak of the laser pulse and it reduces on either side of the pulse. This will lead to “self-steepening” of the leading edge of the laser pulse [86]. The self-steepening of the laser pulse results in higher intensity gradient and consequently higher ponderomotive force at the front of the laser pulse. In addition, if the laser pulse is moving with a co-propagating plasma density profile having rising density along the propagation axis, the group velocity in the region of lower (higher) plasma density will be higher (lower) due to higher (lower) refractive index which leads to “self-compression” of the laser pulse. The “self-steepening” and “self-compression” lead to shortening of pulse duration and increase in peak intensity of the laser.

1.6 Laser wakefield acceleration of electrons

The laser wakefield acceleration was first discussed by T. Tajima and J. M. Dawson in 1979 [10]. The basic concept of laser wakefield acceleration is illustrated in Fig. 1.7.

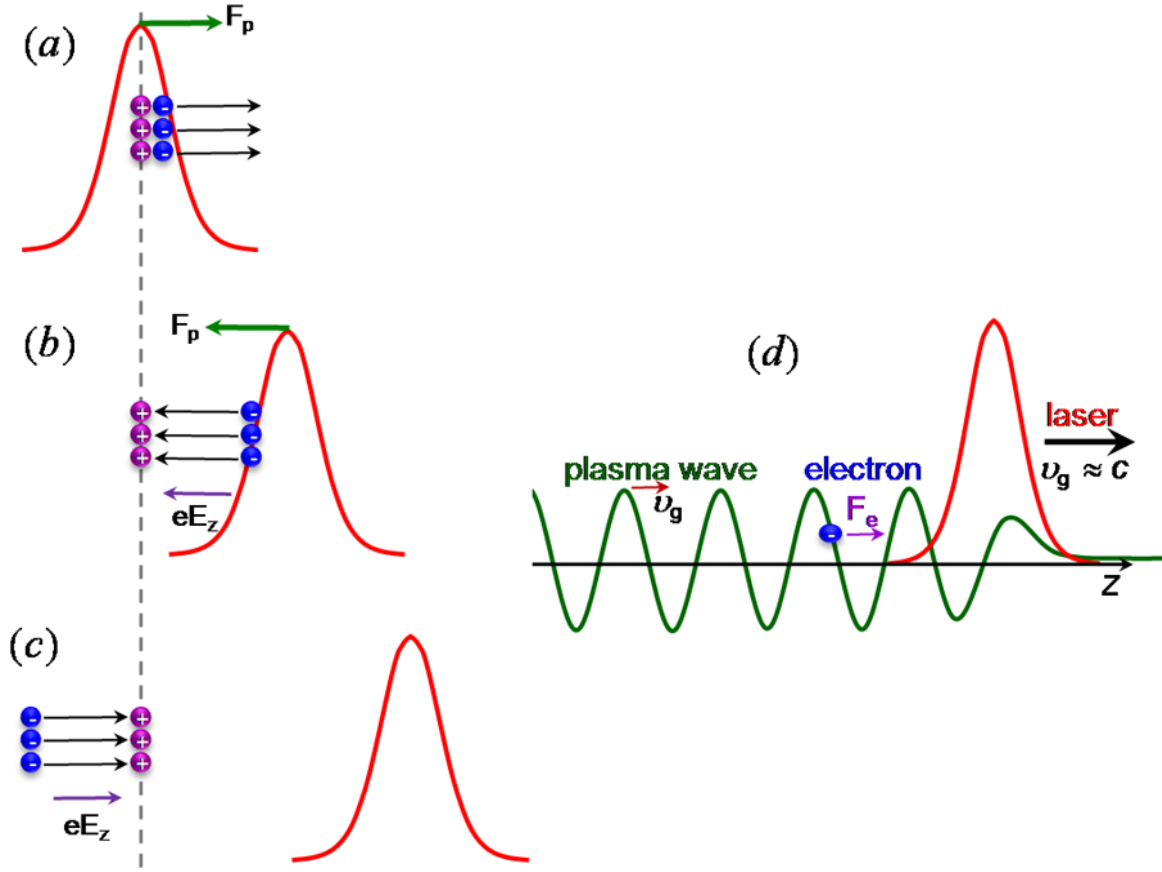


Figure 1.7: Illustration of excitation of plasma oscillations by intense laser pulse and laser wakefield acceleration. Process is explained in the text.

When an ultra-high intense laser pulse propagates in under-dense plasma, it pushes the plasma electrons in the forward direction (see Fig. 1.7a) from their equilibrium positions due to the axial ponderomotive force associated with the high intensity gradient of the laser pulse. Ions being much heavier do not respond to this force and they form positively charged background. This push changes the local electron density by an amount δn which depends mainly on the laser intensity gradient. A restoring force due to local space charge acts to pull the electrons back to their equilibrium position. Therefore, the electrons will be displaced up to a point where the forward ponderomotive force is balanced by the restoring force. As the laser pulse propagates ahead, the peak of the laser pulse overtakes the forward displaced electrons and the ponderomotive force due to trailing part edge of the pulse now pushes the

electrons backwards (see Fig. 1.7b). The electrons move towards their equilibrium position and they overshoot the equilibrium position due to inertia (see Fig. 1.7c) and set up plasma oscillations with frequency ω_p . This process happens in every next layer of plasma encountered by the laser pulse along its propagation direction. Furthermore, there is a definite phase relation between oscillations in each adjacent layer given by their individual time of excitation. Therefore, all the plasma oscillations together form a plasma wave behind the laser pulse (see Fig. 1.7d) like water waves behind a moving motor boat in water. The plasma waves are longitudinal and are associated with periodically varying intense static electric field. Since the field is excited behind the laser pulse like wake waves of a moving boat, it is called *laser wakefield*. It is easy to understand that the phase velocity of the plasma wave (wakefield) is equal to the group velocity of the laser pulse, which is close to c for $\omega_p/\omega \ll 1$. Therefore, these are referred to as *relativistic plasma waves*. If electrons are injected in to the right phase of the plasma wave, they can be accelerated and this method of laser driven plasma wave based acceleration is generally known as “*laser wakefield acceleration*”. The key advantage of using plasma waves is that they can be made to have a phase velocity very close to c , by choosing lower plasma density and therefore making it suitable for accelerating electrons to very high energies.

1.6.1 Strength of laser wakefields

The strength of the laser wakefield, E_{wf} associated with the relativistic plasma waves which can be obtained using the Gauss's law:

$$\nabla \cdot \mathbf{E}_{wf} = \frac{\rho}{\epsilon_0} \quad (1.35)$$

Let us consider a plane plasma wave with density variation of the form:

$$\tilde{n}(z, t) = n_0 + \delta n \cdot \exp [i(k_p z - \omega_p t)],$$

$$\rho = -e \cdot \delta n \cdot \exp [i(k_p z - \omega_p t)] \quad (1.36)$$

Using the ρ in the Eq. 1.35, one gets the solution:

$$\begin{aligned} \mathbf{E}_{wf} &= \mathbf{E}_z \cdot \exp [i(k_p z - \omega_p t + \pi/2)], \\ E_z &= |\mathbf{E}_z| = \epsilon(m_0 \omega_p c / e) \end{aligned} \quad (1.37)$$

where $\epsilon = \delta n / n_0$, and the fact that plasma wave phase velocity $v_\phi = \omega_p / k_p = v_g \simeq c$ (group velocity of the laser) is used to get final expression for E_z . This can be further reduced to:

$$E_z \left(\frac{V}{cm} \right) \simeq 0.96 \epsilon \sqrt{n_0 (cm^{-3})}, \quad (1.38)$$

e.g. for $n_0 \sim 10^{19} cm^{-3}$ (atmospheric gas density) and $\epsilon = 0.1$, $E_0 \sim 30$ GV/m, which is 1000 times higher compared to the maximum electric fields possible in conventional accelerators based on RF acceleration cavities.

From Fig. 1.5 it is clear that the time difference between the peaks of forward kick and the backward kick received by plasma electrons due to ponderomotive force of the laser pulse is equal to the FWHM duration τ_0 of the pulse. When τ_0 matches with the half the natural time period (τ_p) of plasma oscillations, the oscillations can be resonantly excited and high amplitude ($\epsilon \rightarrow 1$) plasma waves can be generated. The resonance condition in mathematical form is given by:

$$\tau_0 \simeq \frac{\tau_p}{2} \quad \text{or} \quad \text{Pulse length, } L = c\tau_0 \simeq \frac{\lambda_p}{2} \quad (1.39)$$

where λ_p is the plasma wavelength which can be obtained from $\omega_p / k_p = c$.

$$\lambda_p (\mu m) = 3.3 \times 10^{10} / \sqrt{n_e (cm^{-3})} \quad (1.40)$$

The amplitude of the plasma wave under resonance condition in the linear 1D regime ($a_0 \lesssim 1$) is given by $\epsilon = a_0^2$. For a simple case of sinusoidal wave form, the maximum amplitude of

the plasma wave is obtained when $\epsilon = 1$. The corresponding field is called cold non-relativistic wave-breaking field, E_{p0} .

$$E_{p0} = m_0 \omega_p c / e \quad (1.41)$$

At low intensities, the oscillatory motion of the electrons constituting the plasma wave is simple harmonic and the wakefield of sinusoidal wave form is generated as shown in Fig. 1.8a. However, at relativistic intensities, intense wakefields are generated in that the oscillatory velocity of the electrons constituting the plasma wave becomes relativistic. This modifies simple harmonic oscillation of the plasma wave to highly anharmonic as shown in Fig. 1.8b. By taking the relativistic effects in to account, the amplitude of the wakefield under resonant condition and in 1D limit is given by [84]:

$$E_{z,NL} = \frac{a_0^2/2}{\sqrt{1 + a_0^2/2}} E_{p0} \quad (1.42)$$

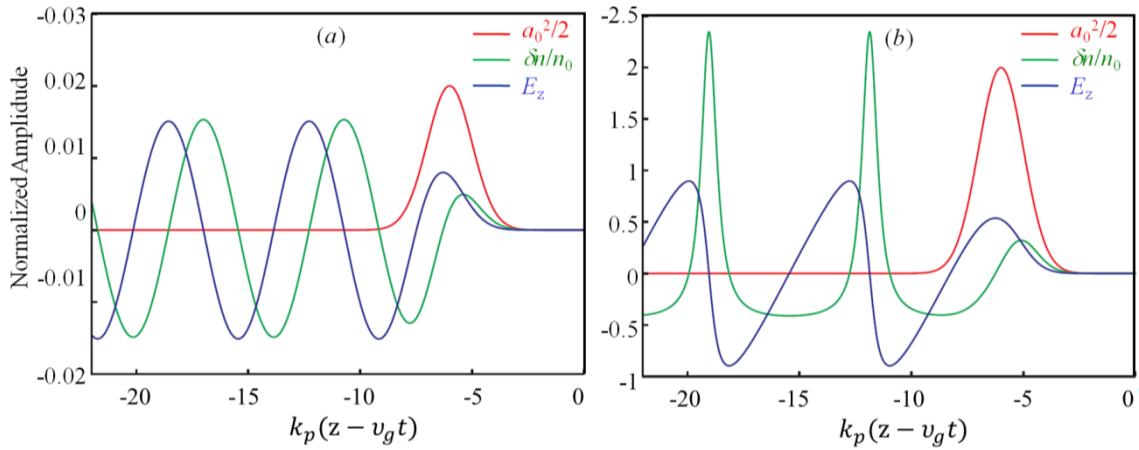


Figure 1.8: One-dimensional laser wakefield for two different laser strength parameters, a) $a_0^2 = 0.2$ and b) $a_0^2 = 2$.

It must be noted that the above description of the LWFA considers laser intensity and plasma density variations along the propagation direction only which corresponds to 1D limit. This simplified picture although useful in understanding the essential points, is a bit

unrealistic considering 3D nature of practical situations. In reality, the plasma wave amplitude varies with the radial distance due to the transverse intensity profile of the laser pulse which can affect the details of the wakefield dynamics and can play an important role in controlling the experiments. For example, the transverse ponderomotive force pushes the plasma electrons radially which sets up radial fields in plasma which act to focus or defocus the injected electrons depending on their location in the plasma wave.

1.6.2 Self- injection

Electrons should be injected in the accelerating phase of the electric field of the travelling relativistic plasma wave with significant forward velocity in order to be caught by the wave and subsequently to be accelerated by the field. A simple and mostly used method for injection is self-injection. In 1D, self-injection occurs through wave-breaking. Wave breaking takes place when the oscillatory velocity of the electrons constituting the plasma wave approaches the phase velocity of the wave. In low-amplitude plasma waves, electrons just swing back and forth about their equilibrium position. In large-amplitude waves, however, some of the oscillating electrons can slip out of the wave due to high oscillatory velocity, similar to white water caps at the ocean's surge. This process is called "wave-breaking". Wave-breaking happens at the right position of the wake (its maximum) where the electrons velocity is maximum and sufficient to catch the wave. For this reason, wave-breaking leads to *self-trapping* of the electrons. It must be noted that wave-breaking limits the maximum achievable amplitude of plasma wave or the wakefield inside the wave, similar to the breakdown limits the accelerating field in the RF accelerators. Furthermore, the injection of electrons reduces the strength of the longitudinal electric field and can therefore inhibit further electron injection. This effect is called *beam loading*, which leads to an inherent control of charge and energy of the accelerated electron beam. In a nonlinear 1D limit, wave-breaking field is given by [84]:

$$E_{wb} = \sqrt{2(\gamma_\phi - 1)}E_{p0} \quad (1.43)$$

where $\gamma_\phi = [1 - (v_\phi/c)^2]^{-1/2}$ is the relativistic factor associated with the phase velocity of the wakefield and which can be approximated to $\gamma_\phi \simeq \omega/\omega_p = \sqrt{n_c/n_0}$. In order to reach wave-breaking, $E_z \geq E_{wb}$, i.e.

$$\frac{a_0^2/2}{\sqrt{1 + a_0^2/2}} \geq \sqrt{2 \left(\sqrt{\frac{n_c}{n_e}} - 1 \right)} \quad (1.44)$$

For typical plasma densities used in LWFA experiments, the laser pulse intensity must be very high such that $a_0^2 \gg 1$. Although the laser pulse duration, focal spot, and intensities achieved by using most of the presently available high power laser systems do not meet the optimum conditions for self-injection immediately after the laser pulse entry in to the plasma, the laser pulse evolves non-linearly through self-focusing and self-compression during its interaction with the plasma which eventually leads to self-injection. If the electron density or the laser energy is too low, self-injection will not occur and no accelerated electron beam will be produced.

1.6.3 Limits for energy gain

The maximum attainable field in a laser-driven plasma wave has been discussed in the previous section. The final energy of the electron beam is determined by the strength of the accelerating electric field and the distance over which this field can be sustained and utilized to accelerate electrons. The relevant physical effects limiting the acceleration distance are discussed in the following.

Diffraction: The most obvious effect is the natural diffraction of the laser pulse. Excitation of large amplitude plasma waves requires high laser intensity. However, the high intensity of the laser at the focus decreases by 50% at a distance equal to Rayleigh length z_R and beyond

this point the laser spot grows quadratically, which reduces the intensity very rapidly. This limits the acceleration length typically to about $2z_R$, which in turn limits the maximum attainable energy in most of the LWFA experiments. In order to increase the acceleration distance, most of the experiments operate in the self-focusing regime which helps in guiding of the laser pulse with high intensity over several z_R . External plasma guiding channels are required for extending the interaction lengths beyond cm scale to generate > 1 GeV electron beams.

Pump depletion: The laser pulse loses energy continuously during the propagation through the plasma, mainly to drive and sustain the plasma wave in its wake. The plasma wave loses its energy to accelerate electrons. This process of losing laser energy to the plasma waves is called “*pump depletion*”. The depletion length, L_{dpl} is therefore defined as the length of the plasma wave behind the laser pulse at which the laser pulse energy is completely depleted (see Fig. 1.9).

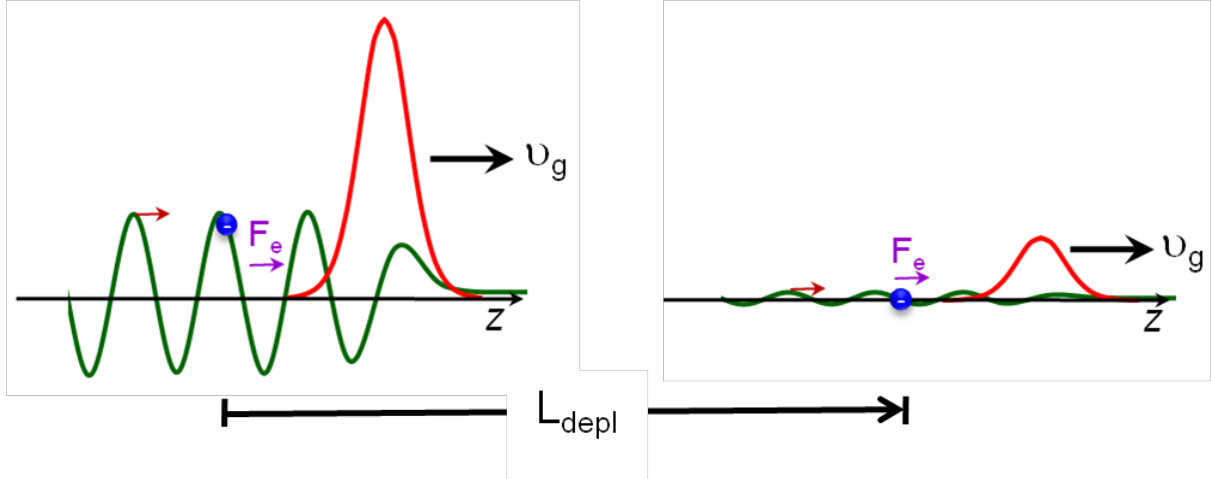


Figure 1.9: Schematic of pump laser pulse energy depletion during wakefield acceleration. Initially the laser pulse is intense and drives high amplitude plasma waves in its wake and electron gains energy from the plasma wave. The laser pulse energy depletes and very low amplitude plasma wave exists after a propagation length close to pump depletion length. Beyond this distance acceleration will not occur.

The energy density associated with the plasma wave is defined as $U = \epsilon_0 E_z^2 / 2$, and it is contained in a volume $V = \pi \omega_0^2 L_{dpl}$. In the 1D linear regime $E_z = a_0^2 E_{wb}$, the pump depletion length is estimated by comparing the laser pulse energy, $\mathcal{E} = \pi \omega_0^2 c \tau_0 \epsilon_0 E_0^2 / 2$ to

the energy left in the plasma wave. One gets the final expression for L_{dpl} by using $E_0 = a_0(m_0 c \omega / e)$ and $E_z = a_0^2 E_{p0} = a_0^2(m_0 c \omega_p / e)$:

$$L_{dpl}^L \simeq \frac{1}{a_0^2} \frac{n_c}{n_e} c \tau_0 \quad (1.45)$$

Dephasing: The electrons injected into the plasma wave can reach velocities that can approach the speed of light c during the acceleration. The plasma wave phase velocity, however, is equal to the group velocity, v_g of the laser, which is also close to the speed of light, but smaller roughly by $10^{-3}c$ for typical laser and plasma parameters. Thus, after some acceleration distance, the electrons become faster than the plasma wave and enter into the decelerating part of the plasma wave (see Fig.1.10). The dephasing length L_{dph}^L for nonrelativistic intensities can be calculated by estimating the distance it takes the electrons to advance $\lambda_p/2$ with respect to the plasma wave.

$$L_{dph}^L = \frac{\lambda_p}{2} \cdot \frac{c}{c - v_g} \simeq \frac{n_c}{n_e} \lambda_p \quad (1.46)$$

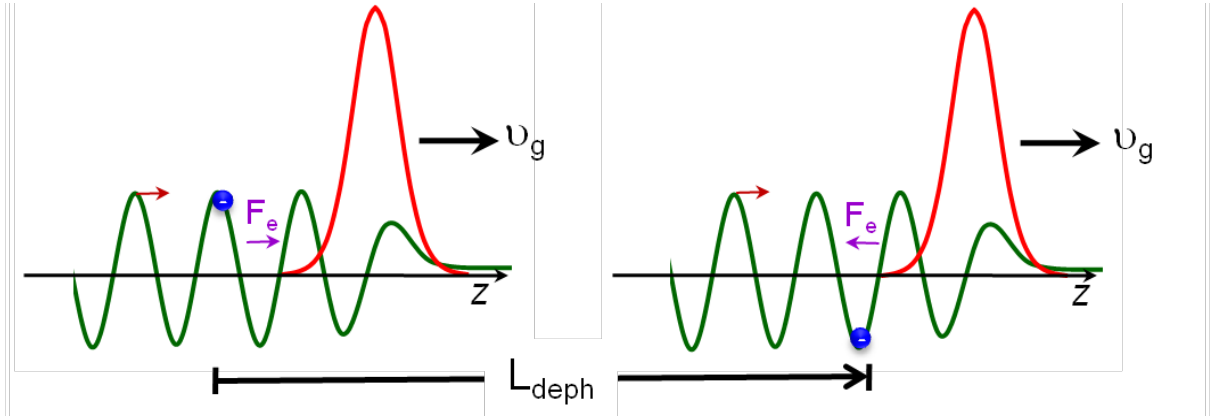


Figure 1.10: Schematic of electron dephasing in laser wakefield. Initially an electron injected at the peak of the accelerating region of the plasma wave. After a certain length called dephasing length, in the lab frame (in the plasma wave frame electron moves over half plasma wave length), the electron reaches the bottom of the plasma wave and thereafter it starts losing energy back to the plasma wave.

For highly nonlinear 1D regime, a more rigorous derivation for linearly polarized, square laser pulses of high intensities ($a_0 \gg 1$) can be found in [84].

$$L_{dph}^{NL} = L_{dph}^L \cdot \frac{\sqrt{2}a_0}{\pi N_p} \quad (1.47)$$

Here, N_p is the number of plasma periods behind the drive laser pulse (typically $N_p=1$).

We can see from equation 1.46 that the dephasing length is longer for a smaller plasma density. Thus, low densities are desirable to reach the higher electron energies. In principal, small amount of dephasing can reduce the energy spread of the accelerated electron bunch. It should also be mentioned that the Rayleigh range can be smaller than L_{deph} and L_{depl} for some experimental parameters. Especially when self-focusing in the plasma is involved, the distance over which the laser intensity is high enough for electron acceleration can be rather short. For typical experimental parameters $L_{deph} < L_{depl}$, therefore the energy gain is usually limited by the dephasing length. The maximum energy limited by the dephasing length is given by [84]:

$$W_{max} = 2m_0c^2 \cdot \frac{n_c}{n_0} \cdot \left(\frac{E_z}{E_{p0}} \right) \quad (1.48)$$

1.6.4 Different regimes of laser wakefield acceleration

Depending on the laser and plasma parameters, the laser wakefield acceleration has been characterized in to various regimes. Self-modulated laser wakefield acceleration and “bubble” or “blow-out” regime are two main regimes relevant to the work presented in the thesis. Therefore, these two regimes will be discussed here.

Self-modulated laser wakefield acceleration: When the laser pulse length $c\tau_L \gg \lambda_p$ and the laser peak power $P > P_C$, the laser pulse can undergo strong self-modulation leading to break up of long laser pulse into a train of short pulses each with FWHM width $\sim \lambda_p/2$, separated by the plasma wavelength λ_p . This process is referred to as self-modulation. Physically, self-modulation occurs from the plasma wave producing periodic regions of longitudinal focusing and defocusing. In the 1D limit, pulse modulation can occur via forward

Raman scattering (FRS). Although initial laser pulse is long, the laser pulse still excites a plasma wave by its ponderomotive force, but not as strong as in the resonant case of LWFA. The long pulse overlaps with the several wave periods of the excited wave. The laser interaction with the plasma wave produces forward scattered waves at Stokes and anti-Stokes frequencies at $\omega - \omega_p$, and $\omega + \omega_p$ respectively (ω is the frequency of the laser). The Stokes and the anti-Stokes waves beat with the pump laser wave to produce periodic modulation of the intensity envelope as shown in Fig. 1.11, with period $2\pi/\omega_p = \lambda_p$. The modulation increases the local ponderomotive force, which in turn increases the amplitude of the plasma wave. The increased plasma wave amplitude increases the FRS intensity, which will further increase the depth of modulation. This will go on in a positive feedback loop which eventually results in breakup of initially long laser pulse and excitation of intense plasma waves resulting in self-injection by wave-breaking.

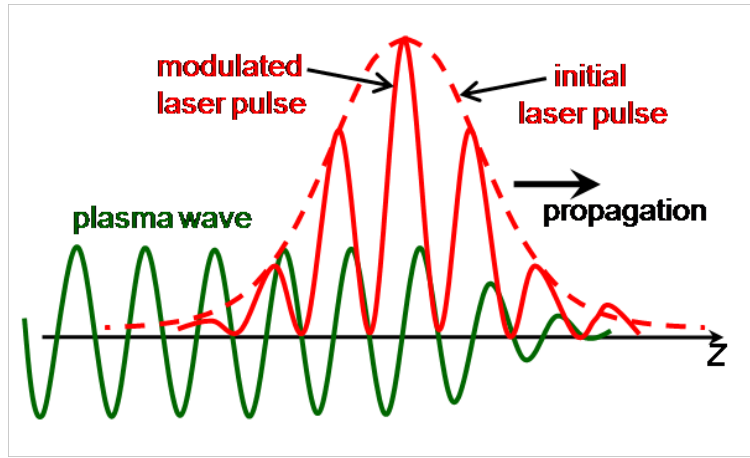


Figure 1.11: Schematic of self-modulated laser wakefield acceleration.

In addition to FRS, the periodic density variation of the plasma wave also helps in self-modulation. The part of the laser pulse at positions with reduced electron density propagates with higher group velocity than the parts at positions with increased density, as explained earlier in section 1.5.5. This leads to longitudinal bunching of the laser pulse and the laser pulse envelope becomes modulated with a periodicity of the plasma wavelength λ_p .

As this modulation leads to locally higher intensities, the generation of the plasma wave is enhanced. The density modulation grows, which in turn amplifies the laser pulse modulation and this will continue in a positive feedback loop. We see that thereby the SM-LWFA regime can be initiated at significantly less strict conditions on laser pulse duration and intensity. Since $\lambda_p \approx 2\pi c / \omega_p \propto 1/n_e^{1/2}$ and $P_C \propto 1/n_e$, for fixed laser parameters, the conditions $L \gg \lambda_p$ and $P > P_C$ can usually be satisfied by operating at a sufficiently high plasma density.

Bubble or Blow-out regime: The "bubble regime", which is also referred to as "blow-out regime", was discovered through computer simulations [26]. This regime is entered when the longitudinal and transverse size of the driving laser pulse/beam are smaller than the plasma wavelength and $a_0 \gg 1$. The simulations include 3D-effects of the plasma wave formation like a tightly focused laser pulse or large transverse oscillations of the electrons but also the mutual interaction between plasma and laser. The simulations show that ponderomotive force of the intense laser pulse blows out the electrons radially creating a bubble-like electron void region surrounding the laser pulse. Hence the name "bubble". This bubble exhibits strong electric fields pointing toward the bubble's centre. Electrons are injected at the rear side of the bubble and gather at a small region inside. This can lead to a partial compensation of the electric fields and stop further electron injection (due to beam loading). The resulting electron beam, due to this localization, will have ultra-short pulse duration, a narrowband energy spectrum, and is well-collimated. A phenomenological theory developed by Lu *et al* [27] gives matched conditions for bubble regime:

$$k_p w_0 \simeq k_p R \simeq 2\sqrt{a_0} \quad \text{and} \quad \tau_0 < \frac{R}{c} \quad (1.49)$$

where R is the bubble radius.

A schematic diagram of laser wakefield acceleration in the bubble regime is shown in Fig. 1.12. In the matched condition, the ponderomotive force of the laser and the restoring

force due to the charge separation of the ion cavity balance each other, thus defining the radius R of the bubble. Under these conditions, only a thin layer of electrons streams around the bubble, and the most ideal wake is produced. For sufficiently intense and ultra-short lasers with $a_0 > 4$, the bubble resembles a spherical cavity. For $2 < a_0 < 4$ electron blow-out still occurs, but the cavity deviates slightly from a spherical shape. It should be noted here that even when the initial laser spot and duration are larger than those required for bubble regime, the laser pulse evolution through self-focusing and self-modulation (compression) in high density plasmas can eventually lead to acceleration in the bubble regime.

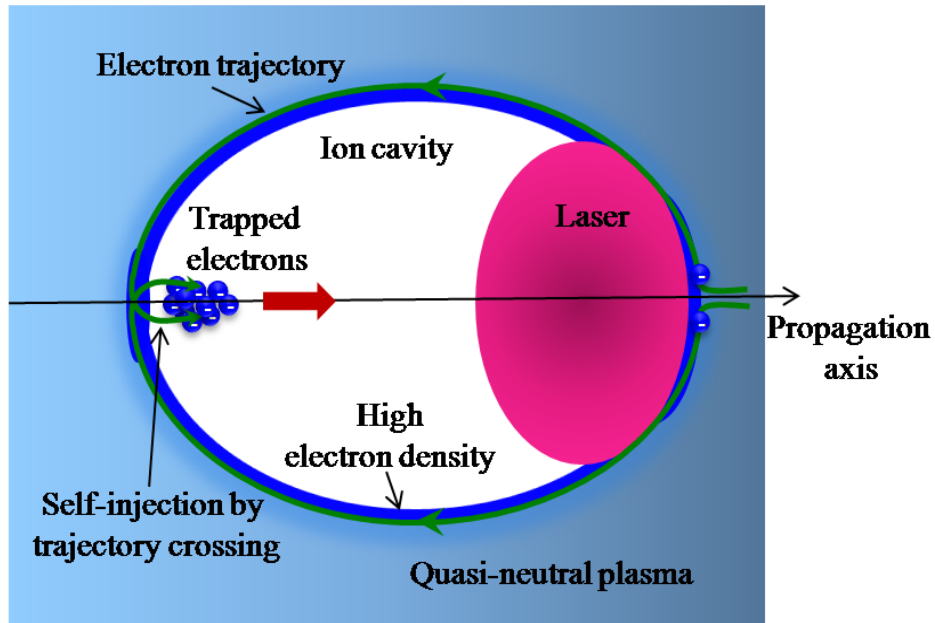


Figure 1.12: A schematic diagram of laser wakefield acceleration in bubble regime.

In the bubble regime, pump depletion occurs due to etching of the leading edge of the laser pulse [27] with a velocity given by:

$$v_{etch} \simeq c \frac{n_c}{n_e} \quad (1.50)$$

and the laser pulse will be fully eroded after the depletion length:

$$L_{dpl}^{NL} = \frac{c}{v_{etch}} c\tau_0 \simeq \frac{n_c}{n_e} c\tau_0 \quad (1.51)$$

The dephasing length in this 3D bubble regime is given by:

$$L_{dph}^{3D,NL} = L_{dph}^L \cdot \frac{2}{3\pi} \sqrt{a_0} \quad (1.52)$$

Next, the maximum energy gain limited by the dephasing length is:

$$E_{mono} = m_0 c^2 \left(\frac{P}{P_{rel}} \right)^{1/3} \left(\frac{n_c}{n_e} \right)^{2/3} \quad (1.53)$$

and charge of the electron beam is:

$$Q[\text{nC}] = 0.4 \frac{\lambda_L(\mu\text{m})}{0.6} \sqrt{\frac{P(\text{TW})}{100}} \quad (1.54)$$

1.7 Fast electrons and bremsstrahlung x-ray generation

The term “fast electrons” generally refers to (a large number of) electrons with more kinetic energy than would be expected through simple Maxwellian distribution. They are observed as long tails in the electron energy distribution with higher effective temperature than for the “bulk” plasma electrons. The electrons are accelerated in intense laser-solid interactions through various mechanisms and appear as fast electrons [87]. The fast electrons can carry a significant fraction of the incident laser energy. When these fast electrons are retarded inside the solid target, they generate intense bremsstrahlung high energy x-rays. Understanding the role of various acceleration mechanisms is essential for development of practical applications of fast electrons, as well as x-rays produced by them in the solid target. It is also important to understand the mechanisms and their dependency on various laser and plasma parameters. In the following sections some important laser absorption and fast electron generation mechanisms in laser - solid interactions are discussed.

1.7.1 Resonance absorption

A p-polarized laser beam obliquely incident onto a steeply rising plasma density profile can undergo resonance absorption. The resonance absorption mechanism is illustrated in Fig. 1.13. If the laser wave is incident at an angle θ with respect to the direction of the density grad

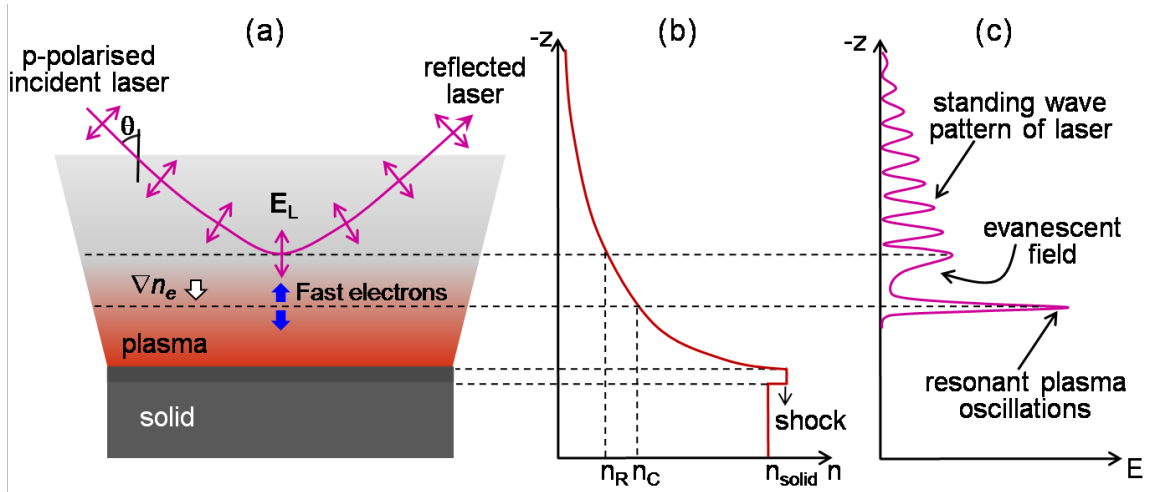


Figure 1.13: Illustration of resonance absorption process. A *p*-polarized laser pulse obliquely incident in the pre-plasma profile at a target front. Reflection occurs at a density n_R before the critical density, n_c . If the distance between the standing wave at the turning point and the position of the critical density is short enough, the evanescent decaying electric field can excite plasma oscillations at this position. Since this oscillation is excited resonantly, it can be driven so strongly that it breaks and produces hot electrons along the target normal direction into vacuum. Subsequently, some escaping hot electrons are pulled back into the target by the space charge field developed by the electrons left initially.

-ient ∇n_e , then the wave is reflected at a density $n_R = n_c \cos^2 \theta < n_c$. However, the laser field in the form of an evanescent wave can tunnel through the plasma beyond the turning point at n_R . The evanescent wave drives plasma waves resonantly at the critical density n_c where $\omega_p = \omega_L$. This driving field is responsible for the high laser light absorption, even when the electron-ion collision frequency is small. When the amplitude of plasma wave is large so that the oscillatory amplitude of plasma electrons exceeds the plasma wave length, a large number of electrons will be trapped in the plasma wave and get accelerated along the target normal direction, down the plasma density gradient [47,48]. This acceleration produces emission of fast electrons into vacuum along the target normal direction. However, the electric field produced in this region, due to the space charge effects, draws back some of these fast electrons into the solid target core, where they lose their energy and produce bremsstrahlung and characteristic x-rays of the solid target material. For s-polarized laser light, there is no electric field component along the density gradient and therefore resonance absorption does

not take place. The resonance absorption is sensitive to both the incidence angle and the steepness of the density profile. If the angle is close to normal incidence, the driver field parallel to the density gradient vanishes. If the angle is too large, the distance for tunnelling of the electric field to the critical density is also large. At high laser irradiance, a steepening of the density profile near the critical density can make resonance absorption less sensitive to the incidence angle due to shortening of the tunnelling distance. Moreover, since in contrast to the inverse bremsstrahlung that leads to heating of all electrons, in resonance absorption, the laser energy is transferred to only a small fraction of electrons which therefore can be accelerated to high kinetic energies beyond the thermal distribution. Typically, a bi-Maxwellian electron temperature is observed in which the “fast electron” component can significantly exceed the characteristic plasma thermal electron temperature, T_e .

1.7.2 Vacuum heating

Ultra-short laser pulses with high contrast ratio, when focused on a solid target, form plasma with a steep density gradient. The energy of the obliquely incident, high intensity p-polarized laser pulse can be efficiently coupled to such plasma through *vacuum heating* which is also called *Brunel heating* [49]. According to Brunel, when the quiver amplitude of an electron (v_{osc}/ω) in a strong laser field is greater than plasma scale length, $L \left(= \left(\frac{\partial \ln n}{\partial z} \right)^{-1} \right)$, the plasma electrons from the under-dense plasma are pulled into vacuum, well beyond the Debye length in the first half of laser cycle, and are sent back to the over-dense region in next half of cycle with a velocity $v \simeq v_{osc}$. The energetic electron moves unhindered into the over-dense plasma and also into the solid target as the laser field penetrates only up to a skin depth $\sim c/\omega_p$, and therefore cannot control these electrons. Thus, a population of “fast” electrons is produced in every cycle. The Brunel type of absorption is schematically illustrated in Fig. 1.14. The mechanism tends to be more efficient with

increasing strength of the driving field and also at greater incidence angles. Note that the geometry of the model is similar to that in the classical resonance absorption, but the mechanism is different. In particular, it requires a steep density gradient and is complementary to the classical resonance absorption that breaks down in the case of very steep density gradients.

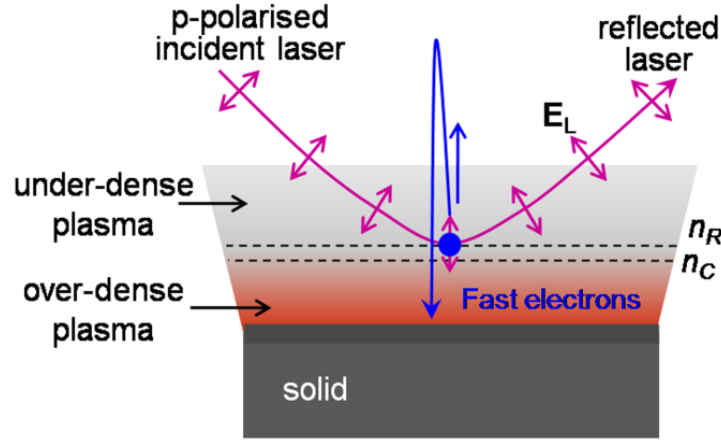


Figure 1.14: *Illustration of vacuum heating mechanism.*

1.7.3 $\mathbf{J} \times \mathbf{B}$ heating

The $\mathbf{J} \times \mathbf{B}$ heating mechanism [50, 51] becomes important for relativistic laser intensities ($a_0 \gtrsim 1$) where the effect of the laser magnetic field can no longer be ignored. In this mechanism, the plasma electrons are accelerated by the Lorentz force induced by the magnetic field component of the laser. The electrons execute "figure of 8" motion in the plane of laser polarization and hence possess longitudinal component of acceleration, irrespective of orientation of the laser polarization axis. In the presence of a steep density gradient, however, electrons which are pushed into the over-dense plasma region beyond the skin depth cannot be controlled by the laser field as in the case of vacuum heating. The energetic electrons thus form a fast electron tail in the spectrum. The characteristics of $\mathbf{J} \times \mathbf{B}$ heating mechanism is that

it works with arbitrary polarization direction and will accelerate the electrons in laser propagation direction twice every full laser cycle in comparison to once per laser cycle for resonance absorption and vacuum heating. The energy gain of the electrons is of the order of the ponderomotive potential, U_p of the laser field. As shown in simulations by Pukhov [88, 89], the mechanism will also work in the context of extended density ramps, i.e. relaxed requirements on the steepness of the profile. Here the laser pulse drives electrons in a snow-plough manner prior to when it reaches the critical surface. The electrons which are pushed beyond the critical surface retain their kinetic energy.

1.7.4 Direct laser acceleration

At relativistic laser intensities, other electron acceleration mechanisms can also be important. The rapid motion of a large numbers of particles can generate strong quasi-static fields that can affect particle trajectories so that they experience large acceleration in the fields. An example is the B-loop mechanism [89] where the electrons may undergo several ponderomotive acceleration phases by spinning around in azimuthal magnetic field generated by the large electron current. If the plasma scale length is much larger than the laser wavelength, the same mechanisms acting in under-dense plasma accelerators may become important, e.g. in laser wakefield acceleration [84] and direct laser acceleration [90, 91].

The direct laser acceleration (DLA) mechanism has been described in ref. 90. The electrons can be accelerated in the direct laser field of the laser when the laser pulse length $L > \lambda_p$, and $P > Pc$. In this mechanism, the electrons propagating in a plasma channel can interact resonantly with the laser pulse travelling in the same direction. The ponderomotive force of the laser pulse expels the electrons from the channel and creates a radial electrostatic

field. The laser pulse propagating in the channel also accelerates some plasma electrons in forward direction through $\mathbf{v} \times \mathbf{B}$ force as explained earlier, producing a current, which generates the azimuthal magnetic field.

If we roughly approximate laser plasma channel as a cylinder with uniform electron density $n_e = f n_0$ ($0 \leq f \leq 1$) we can write the radial electric field:

$$eE_r = (1 - f) \frac{m_0 \omega_p^2}{2} r \quad (1.55)$$

The current $-efn_0c$ produces the azimuthal magnetic field:

$$eB_\phi = f \frac{m_0 \omega_p^2}{2} r \quad (1.56)$$

The equation of radial motion for electron in such idealized channel will be reduced to :

$$\frac{d^2 r}{dt^2} + \frac{\omega_p^2}{2\gamma} r = 0 \quad (1.57)$$

As a result, the electron executes radial oscillation with betatron frequency $\omega_\beta = \omega_p/2\sqrt{\gamma}$.

In this model, the \mathbf{E} and \mathbf{B} fields cooperate in such a way, that the electrons move mainly in the direction of the channel axis, and in the radial direction the channel works as a potential well. As the electrons move along the channel axis with velocity close to c , they observe a strongly downshifted optical frequency $\omega' = \omega (1 + a_0^2/2)/(2\gamma^2)$ of the laser. When the betatron oscillation frequency ω_β is equal to the laser frequency in the frame of the accelerated electrons, energy can be efficiently exchanged between the electrons and the transverse laser field over many laser periods. It is the magnetic field of laser which turns the transverse motion into longitudinal motion through $\mathbf{v} \times \mathbf{B}$ force resulting in resonant acceleration of electrons by the laser field.

1.7.5 Bremsstrahlung x-ray generation

The ultra-short and high intensity laser - solid interaction produces directional fast electrons of several 100 keV - MeV energy through various mechanisms as explained in the previous sections. These electrons produce bremsstrahlung x-rays when they penetrate the solid target material behind the plasma. The spectrum of such x-rays can extend up to the maximum energy of the electrons. This produces a bright, micron sized source of x-rays. Although the duration of the hot electron bunch will be of the order of laser pulse duration, the duration of the x-rays is governed by the time the electrons take to slow down. For generating x-rays with high conversion efficiency, it is necessary to use high-Z targets which will increase the x-ray yield as well as reduce the bremsstrahlung x-ray pulse duration. The direction of the x-ray emission is dependent on the energy of the hot electrons produced.

Chapter 2: Experimental setup and diagnostic systems

In this chapter, we describe laser system and various important diagnostics used for carrying out the experimental studies on laser wakefield electron acceleration (LWFA) and laser-driven hot electron / bremsstrahlung radiation generation. All the experimental studies presented in the thesis have been carried out using the chirped pulse amplification (CPA) based table-top 10 TW, 45 fs Ti:sapphire laser system at Laser Plasma Division, Raja Ramanna Centre for Advanced Technology (RRCAT), Indore, India. First, overall description of the Ti:sapphire laser system is given. Next, measurements of various laser pulse parameters viz., laser spectrum and pulse duration, focal spot, and pre-pulse intensity contrast are described. Experiments on laser wakefield electron acceleration require relatively low density ($<1 \times 10^{20} \text{ cm}^{-3}$) plasmas which are mostly generated from supersonic gas jet targets. The supersonic gas jet system used in the present thesis work for LWFA is described. The detection and measurement of high energy electrons was done using various diagnostics. Magnetic spectrometer is an important diagnostic for measuring the energy of the high energy electrons. The magnetic spectrometer used in the experiments is described in detail.

2.1 Ti:sapphire laser system

The Ti:sapphire laser system used in the experimental study is a commercial system (M/s Thales, France) which is based on chirped pulse amplification (CPA) technique [5]. The principle of CPA technique is shown in Fig. 2.1. In this technique, short pulses are stretched in time by a factor of 10^4 in order to reduce its peak power and intensity. Then the pulse is safely amplified in various stages of amplification. It is finally compressed back to duration as close as possible to its initial value.

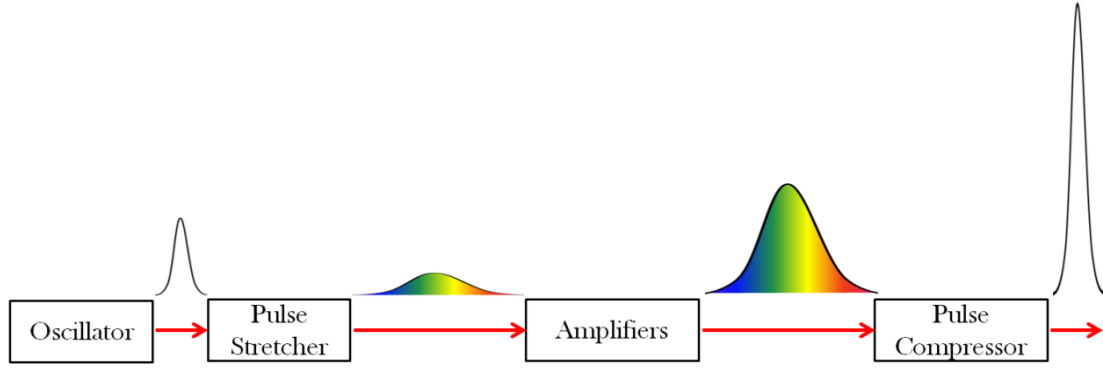


Figure 2.1: *The principle of chirped pulse amplification.*

The Ti:sapphire laser system used in the present thesis work delivers ultra-short pulses of ≥ 45 fs duration, at a wavelength of 800 nm, with maximum 10 Hz repetition rate and maximum energy 450 mJ. The overall layout of the Ti:sapphire laser system is shown in Fig. 2.2. At the front end, it has a Ti:sapphire laser oscillator (pumped by second harmonic of an Nd:YVO₄ laser) which generates ultra-short laser pulses of about 20 fs duration and few nJ energy at 76 MHz repetition rate. The femtosecond duration pulses are generated by Kerr-lens mode-locking (KLM) technique [7]. The femtosecond laser pulses are then stretched to about 200 – 300 ps duration using an Öffner type stretcher [92]. The stretching is achieved by separating different wavelengths (frequencies) in time (chirping). The stretcher introduces positive chirp in that the longer wavelengths (red) travel ahead of shorter wavelengths (blue) (see Fig. 2.1). The stretched pulses are then amplified first in a regenerative amplifier which is pumped by second harmonic of an Nd:YAG laser (COMPACT). The regenerative amplifier in a CPA based laser system is an important component which decides the spatial and temporal quality of the laser pulses finally generated. The regenerative amplifier (RGA) uses a TEM₀₀ laser resonator and delivers diffraction-limited beams. From the 76 MHz train of stretched pulses after the stretcher, a pulse selector switch selects laser pulses at 100 ms intervals (at 10 Hz repetition rate) which are amplified in the regenerative amplifier. The pulse selection is achieved by polarization

switching in a Pockels cell (KDP crystal based). The laser axis is on the C- axis of the crystal. The RGA works in small signal gain regime and gives total gain about 10^5 in 15 round trips in the cavity. The gain is limited so that this amplifier remains insensitive to thermal effect that may arise at high energy extraction rates. The amplified laser pulse is ejected out of the RGA cavity by switching the polarization. After the pulse ejection, a pulse cleaner based on a fast polarization switching (about 1 ns rise time) is used to suppress the unwanted pre-pulses in the amplified main laser pulse. The repetition rate of the laser pulses can be varied by changing the injection and ejection frequency of the pulses.

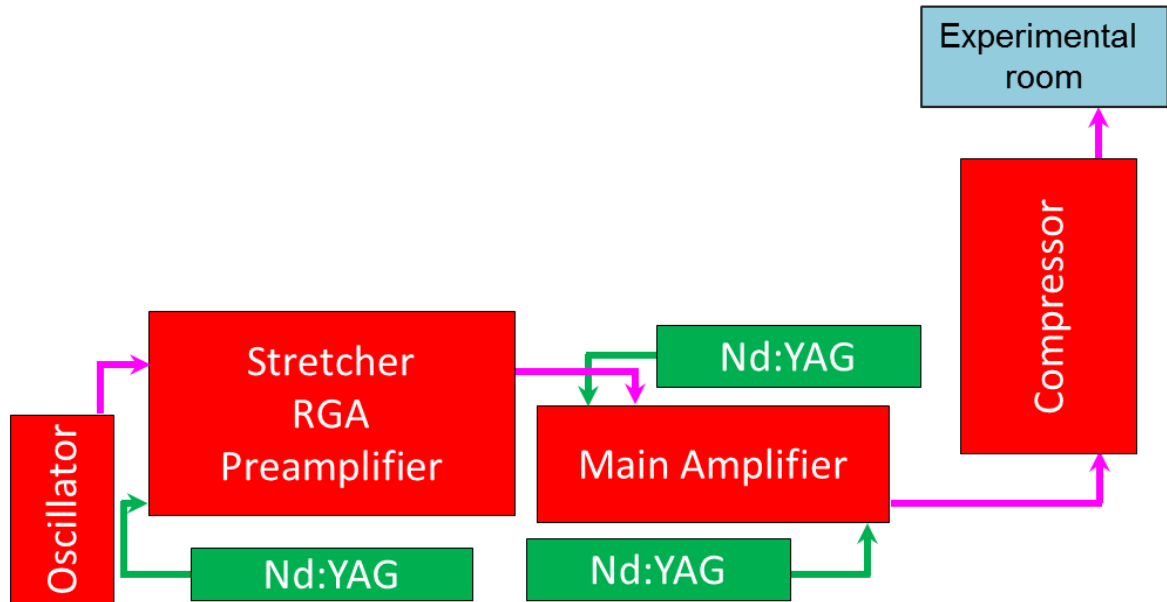


Figure 2.2: Overall schematic layout of the Ti: sapphire laser system.

The laser pulses, after the pulse cleaning stage, enter a multi-pass preamplifier pumped by the same Nd:YAG laser that pumps the RGA, and then into another multi-pass amplifier pumped by the second harmonic of two Nd:YAG lasers (SAGA). The regenerative amplifier, preamplifier and the multi-pass amplifiers use Ti:sapphire crystals of different sizes as gain medium. The overall gain of the amplifier system is about 10^9 . The amplified pulses are finally compressed in a pulse compressor [93] which consists of a pair of parallel gratings

separated by an optimum distance to compensate for positive chirp introduced purposefully by the stretcher and unavoidably added by amplifier crystals and other optics during amplification. For an unchirped laser pulse, the pair of grating introduces negative chirp whose magnitude depends on the separation between the two gratings. As the separation is increased, the negative chirp is increased and at optimum value of the grating separation, the positive chirp of the stretched ps laser pulse will be compensated to get back a compressed fs pulse. The compressor gratings have a groove density of 1500/mm and are separated by an optimal distance (365 mm) in vacuum to achieve shortest pulse duration. Incident angle of the laser pulse on grating is 45° . Increasing or decreasing the grating separation from the optimum value results in negatively or positively chirped pulses respectively. Due to the reduction of the laser spectral width through gain narrowing during the amplification [94], the final laser pulse duration achieved is limited to 45 fs, which is larger than the initial oscillator pulse duration. A photograph of the Ti:sapphire laser systems is shown Fig. 2.3 and the parameters of the laser are summarized in Table 2.1.

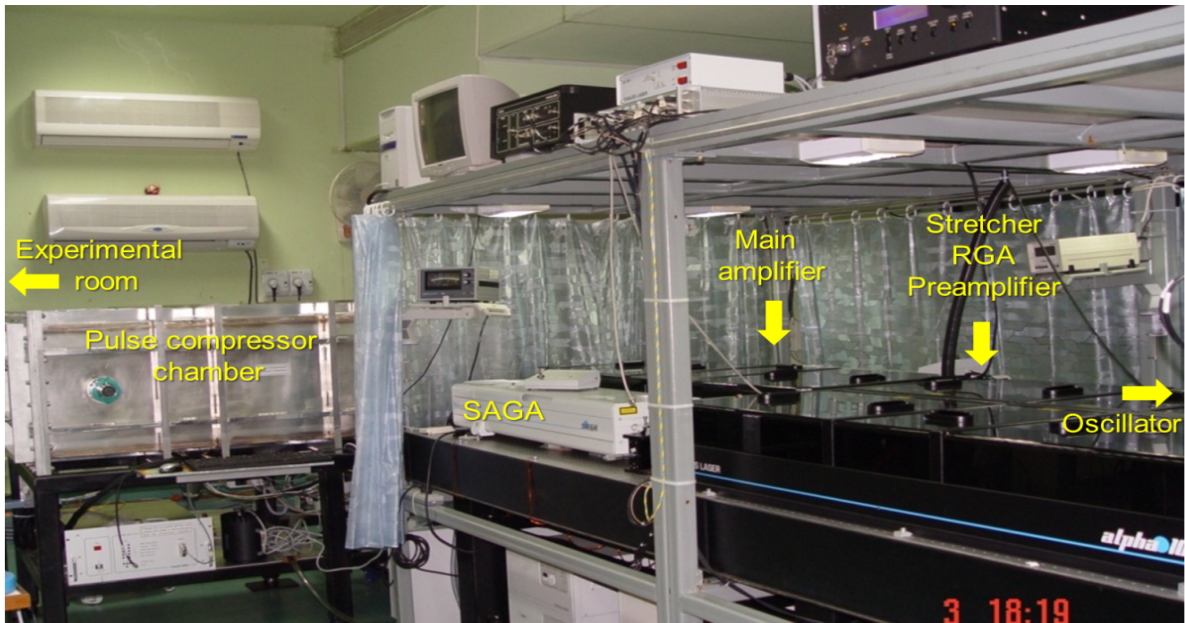


Figure 2.3: Photograph of the 10 TW Ti:sapphire laser system at Laser Plasma Division, RRCAT.

Parameter	Value
Pulse duration, τ_0	≥ 45 fs
Central wavelength, λ_0	800 nm
Spectral width, $\Delta\lambda$	20 nm
Pulse energy, \mathcal{E}	≤ 450 mJ
Pulse power, P	≤ 10 TW
Repetition rate	≤ 10 Hz
Pre-pulse contrast (ns level)	1×10^6

Table 2.1 *Parameters of the 10 TW Ti:sapphire laser system.*

2.2 Characterization of laser parameters

Before carrying out any experiment with the laser, it is essential to measure and characterize various parameters of the laser pulse, as they strongly influence the interaction process. In the following sections, the measurement of important laser parameters is discussed and the results are presented.

2.2.1 Laser spectrum and pulse duration

The spectral width of femtosecond laser pulses is an important parameter as it governs the shortest achievable pulse duration. Any unwanted reduction of spectral width before the pulse compressor would increase the pulse duration. We have measured spectral width using an optical spectrograph (Make: Avantes) prior to and during experiments. A typical spectrum of the laser pulse at full power operation is shown in Fig. 2.4. The measured laser spectrum has a peak wavelength at 800 nm and bandwidth (FWHM: full width at half maximum) of about 20 nm ($\Delta\lambda$). The transform limited pulse duration for the measured spectral width is 34 fs. However, practically the pulse duration is larger due to the nonlinear phase shifts (higher order dispersion) introduced in the laser pulse during amplification and propagation of the laser pulse through the gain medium, which cannot be fully compensated by the pulse compressor.

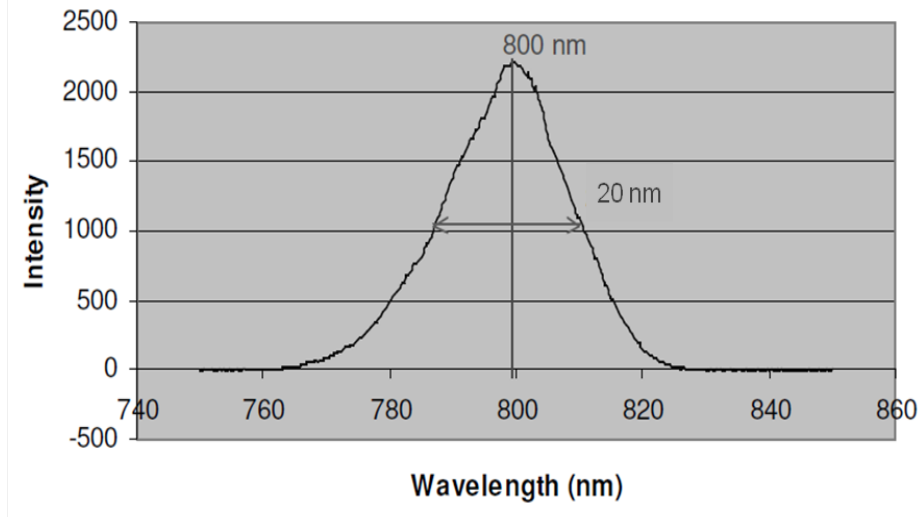


Figure 2.4: A typical spectrum of the Ti:sapphire laser pulse at full power of operation.

The laser pulse duration is a critical parameter in ultra-short laser-matter interactions. Single shot second order intensity autocorrelation technique [95] is used to measure the laser pulse duration. A schematic of the technique is shown in Fig. 2.5. A beam splitter splits the incoming laser beam into two, which are then overlapped both in space and time inside a non-linear crystal. A second harmonic beam (blue arrow in Fig. 2.5) is generated from the overlapped region in the direction mid-way between the two beams. The temporal overlap of the two beams is achieved by the adjustment of the delay line of one arm of the autocorrelator. The angle between two beams determines the spatial width of the autocorrelation trace which is related to the laser pulse duration. The FWHM width of the autocorrelation trace, Δx is related to the FWHM width τ_0 of the laser pulse by the following relation:

$$\tau_0 = 2 \frac{\Delta x \cdot \sin(\theta/2)}{Kc} \quad (2.1)$$

where θ is the cross-over angle between the two overlapping laser beams shown in Fig. 2.5, and K is a constant which depends on the exact temporal shape of the laser pulse.

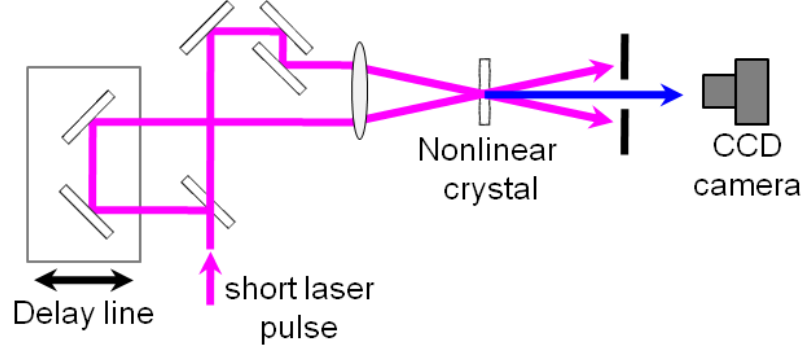


Figure 2.5: Schematic of a typical single shot second order intensity autocorrelator.

We have set up a single shot second order autocorrelator using a 0.5 μm thick BBO crystal and a 12-bit CCD camera (Make: PCO Pixelfly) for the pulse duration measurement. For experiments, the laser beam is normally transported from the compressor to the plasma chamber through an evacuated ($< 10^{-4}$ mbar) beam transport line. In order to measure the pulse duration, the laser beam was reflected out of the beam transport line through a glass window and was sent to the autocorrelator which was set up in air at a distance of 1 m from the glass window for the pulse duration measurement. The grating separation was scanned to obtain minimum laser pulse duration. The grating separation corresponding to the minimum pulse duration is referred to as “compressor zero”. A typical autocorrelation signal and its line out profile corresponding to minimum pulse duration condition are shown in Fig. 2.6. The full width at half maximum (FWHM) of the laser pulse is deduced from the second harmonic profile by assuming a sech^2 profile (convolution factor of 1.55).

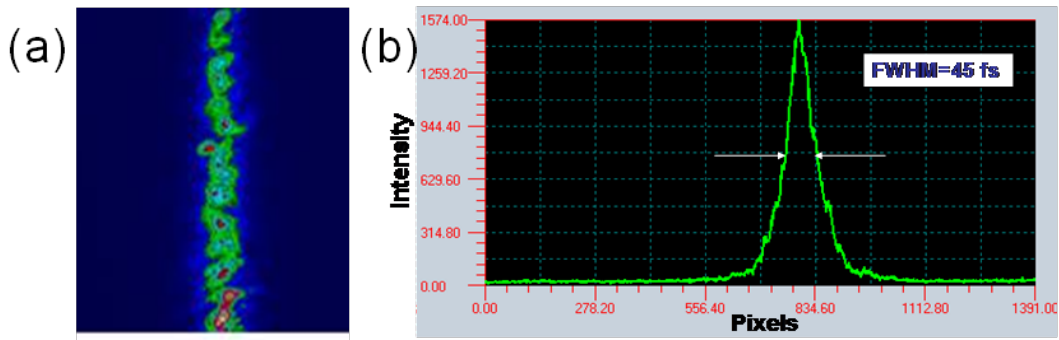


Figure 2.6: a) Typical CCD camera image of autocorrelation trace corresponding to shortest pulse duration, and b) its line profile taken along the width of the trace.

The variation of laser pulse duration was also measured for increasing or reducing grating separation from the “compressor zero”. Figure 2.7 shows dependence of pulse duration on the grating separation. This data is important for compensation of additional positive chirp introduced into the laser pulse due to any transmission optics (lenses/mirrors etc.) in the beam path. During the experiments, the laser beam propagates completely in vacuum. Therefore, in order to obtain shortest pulse at laser target interaction point in vacuum, the positive chirp introduced in the laser pulse by the group velocity dispersion in the glass window (the contribution of air being negligibly small) during pulse duration measurement is compensated by reducing the grating separation to add same amount of positive chirp. This position of the gratings was taken as the “compressor zero” for the experiments. In order to intentionally increase the laser pulse duration by adding either positive or negative chirp during the experiments, the grating separation was varied by known amount.

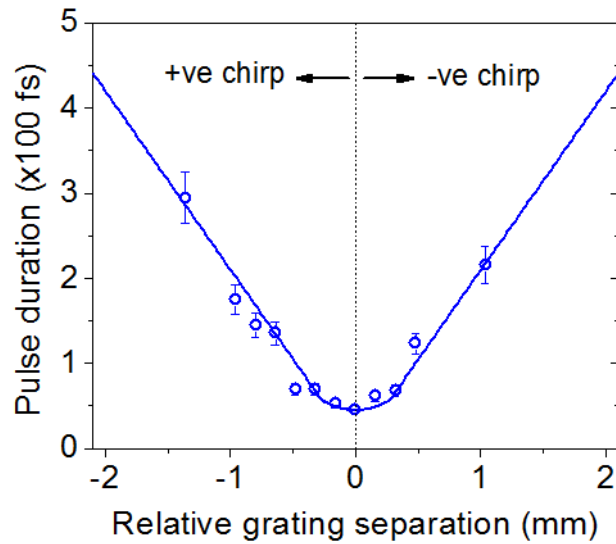


Figure 2.7: Variation of laser pulse duration with grating separation relative to the compressor zero.

2.2.2 Measurement of focal spot

The quality of laser focal spot and the peak intensity of the focussed laser beam on the target is an important parameter that governs the laser matter interaction processes. Since the

intensity is inversely proportional to square of the radius of the focal spot, a small improvement in focal spot size can mean significant enhancement in the intensity at the focus. Therefore, it is necessary to choose good quality focusing optics (reflective or refractive) and take utmost care in the alignment of the optics, especially parabolic mirrors, to eliminate aberrations which will be detrimental for achieving good quality spot and desired high intensity. In addition, the spatial profile of a high power laser beam normally differs from perfect Gaussian or flat-top and has complex spatial profile as seen in Fig. 2.8. Therefore, predicting the focal spot of a high power laser beam for given parameters of focusing optics is not straight forward. It is well known that a laser beam with near-field Gaussian profile maintains Gaussian profile in its far-field (at focus). However, the laser energy in the focal region may be spread over larger area for practical beams, thereby reducing the intensity either due to larger area or concentration of energy in multiple spots, in addition to a principal spot. Therefore, it is necessary to measure the spatial profile in the far-field (focal region) to find the spot size and energy content to estimate the peak intensity and to interpret the experimental results properly.

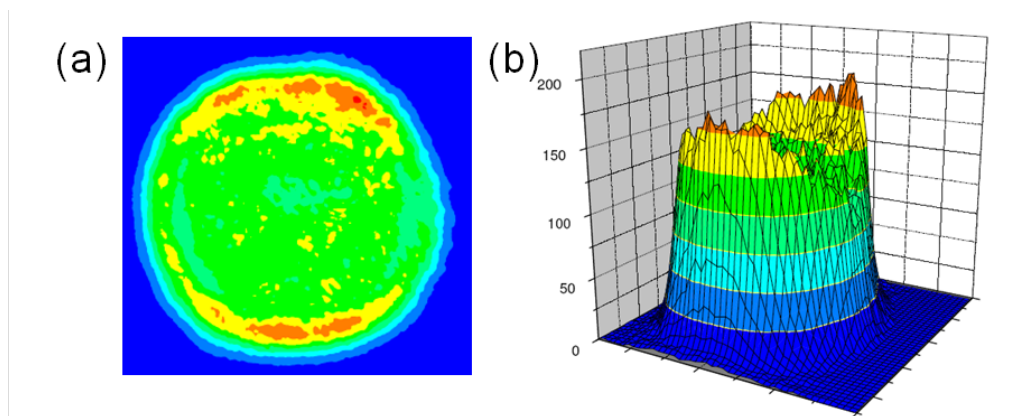


Figure 2.8: *a) Typical high power laser beam profile, and b) its intensity distribution in 3D.*

An imaging setup consisting of a 12-bit CCD camera (Model: PCO Pixelfly) coupled with a 40X microscope objective lens, as shown in Fig. 2.9, was used for measuring the focal

spot. The magnification of the imaging setup was measured from the image of a graticule with 100 μm known line spacing (see Fig. 2.9b). To avoid saturation and damage of the CCD sensor, the laser beam intensity was attenuated by using reflections from optical quality glass surfaces. The imaging setup was mounted on a translation stage for scanning along the laser propagation axis to find the beam waist and to measure the Rayleigh range. The same setup was also used for accurate alignment of focusing optics by on-line monitoring the quality of the spot near the focus.

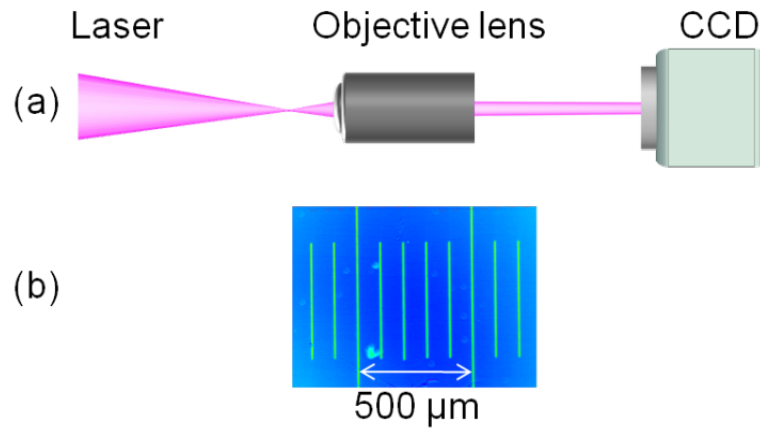


Figure 2.9: a) A schematic diagram of the focal spot imaging setup, and b) an image of a graticule recorded by the setup for calibration purpose.

An image of the focal spot measured using the above setup, when the laser beam focused with an $f/6$ off-axis parabolic mirror, is shown in the Fig. 2.10a. The intensity profile of the focal spot along a line at $Y=0$ is shown Fig. 2.10b and a 3D plot of the intensity distribution is also shown in Fig. 2.10c. The focal spot $1/e^2$ radius, $w_0 = 9 \mu\text{m}$ was determined from the the recorded images of the focal spot. For the laser and focusing optics used, the diffraction-limited spot size was estimated to be about 4 μm . The larger measured spot size may be attributed to the distortions in the beam profile accumulated during the amplification process. The energy content in $1/e^2$ focal spot was estimated from the ratio of the integrated

pixel counts under the focal spot of diameter $2w_0$ and the overall image area of the focus. It was estimated that 55% of total energy is contained in the $1/e^2$ focal spot. This is smaller in comparison to a perfect gaussian beam which would have about 87% of total energy within $1/e^2$ focal spot.

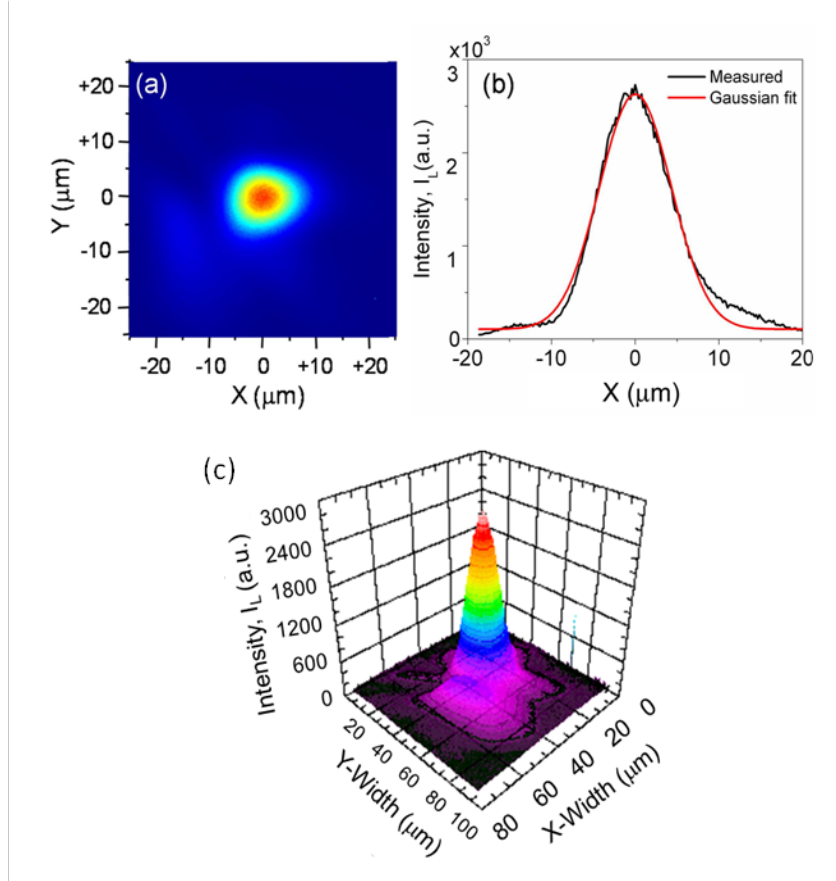


Figure 2.10: a) 2D image of the focal spot, b) line intensity profile along $Y=0$, and c) 3D plot of the intensity distribution of the focused laser beam.

2.2.3 Measurement of the pre-pulse contrast

The temporal profile of the femtosecond pulse delivered by a CPA based Ti:sapphire laser invariably consists of pre-pulse(s) accompanying the ultra-short high intensity pulse despite pulse cleaning system after the regenerative amplifier. The temporal purity of the main pulse is defined by its intensity contrast ratio w.r.t. the pre-pulses. The contrast ratio is defined as the intensity ratio of the main pulse to the intensity of undesired pulses occurring

before the main pulse. There are mainly two types of pre-pulses occur on ns time scale. A pre-pulse which is replica of main pulse (ultra-short duration) but with low intensity appears ~ 8 ns (the round trip time inside the RGA) before main pulse due to non-ideal pulse ejection and pulse cleaning switches. This contrast is referred to as the "replica contrast". A pre-pulse as a pedestal due to the amplified spontaneous emission (ASE) exists whose duration and rise time are governed by the time of switching of the pulse cleaner w.r.t. the main pulse and the rise time of the switching. This contrast is referred to as the "ASE contrast". The pre-pulses on ns time scales have to be controlled as they can alter the target conditions by the time the laser pulse arrives at the target. Pre-pulses on ps time scales also appear due to temporal phase distortions introduced during amplification stages.

The contrast ratio due to pre-pulses on ps time scale is 10^3 and 10^4 at 1 ps and 5 ps respectively for our laser system and these are measured using 3rd order autocorrelator (Sequoia). Although ps pre-pulse will be able to form plasma, it is not expected to modify the interaction conditions significantly as the hydrodynamic evolution of the plasma is negligible on few ps time scale. The ASE and replica contrast ratios were measured using a fast photodiode with 0.8 ns rise time on a 500 MHz digital oscilloscope (Tektronix TDS 3054B). It may be mentioned here that the photodiode signal on oscilloscope shows a pulse with about 1 ns FWHM duration although incident light is of 45 fs duration. In the case of replica pre-pulse due to leakage from the RGA and the pulse cleaner, the intensity contrast is estimated from the ratio of the measured signal height due to the main pulse and the replica pulse as the heights of the two pulses will be proportional to their corresponding intensities. The signal due to replica pre-pulse and the saturated main laser pulse is shown in Fig. 2.11a. The signal height due to main pulse was measured separately by attenuating its intensity by a known factor. The contrast ratio of about 1×10^6 was measured from the measured signal heights. This correspond to replica pre-pulse intensity $\sim 1 \times 10^{12}$ W/cm² and energy ~ 100 nJ for main pulse intensity of $\sim 1 \times 10^{18}$ W/cm² and energy ~ 100 mJ. Although intensity of this pre-pulse is not

enough to create plasma on target [79], proper care must be taken at the RGA stage to suppress these pulses by proper switching of the pulse ejection and cleaning switches.

In the case of ns duration ASE pre-pulse, the signal on oscilloscope retains the temporal information of the ASE pre-pulse. Although the temporal information is lost when shorter laser pulses are measured, the energy content of the laser pulse is still retained in the form of area under the pulse seen on oscilloscope. This can be exploited to estimate the contrast ratio due to the ASE pre-pulse. In order to get the contrast ratio due to ASE pre-pulse, the ratio of signal height due to main pulse and the ASE pre-pulse must be multiplied with the ratio of apparent main pulse duration (~ 1 ns) measured on oscilloscope and the actual duration (45 fs). The measured signals due to ASE with different pedestal durations and main pulse are shown in Fig. 2.11b. The switching-on time of the 5 ns wide high voltage pulse on the Pockels cell of the pulse cleaner (located after the RGA) was varied to change the pedestal duration. The green trace in the Fig. 2.11b is due to the 45 fs duration main laser pulse, while the different coloured traces are due to ASE pre-pulses of varying duration. A satellite fs pulse due to mismatch between round trip times of the oscillator and the RGA is also indicated. The ASE pre-pulse duration could not be reduced below ~ 1 ns due to the limit set by the rise time (~ 1 ns) of the Pockels cell switching. Attempt to further reduce the ASE pre-pulse duration was found to lower the main laser pulse energy. It also leads to large shot-to-shot fluctuation in the laser energy due to the jitter in switching time of the Pockels cell. The intensity contrast due to the ASE pre-pulse was estimated from the measured signals was about 1×10^6 . Although the nanosecond duration ASE pre-pulse has relatively low intensity, it has energy of few mJ, and can form plasma by cascade ionization and collisional heating mechanism [96,97]. This is because the threshold intensity for plasma production for a nanosecond duration pulse is much lower than that for a femtosecond duration pulse. The contrast ratio due to ASE critically depends on the alignment of the pump and the seed beams in the RGA. Therefore care must be taken in order to get high contrast pulses.

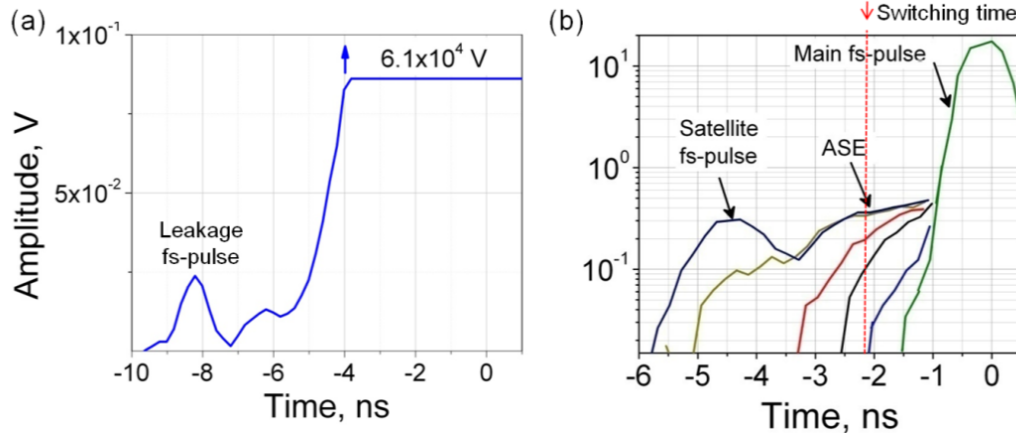


Figure 2.11: a) Measured signals due to leakage replica pre-pulse, and b) ASE pre-pulses of different durations along with the main pulse.

2.3 Gas jet system

The gas jet system used for the laser wakefield acceleration experiments is a shock-wave free supersonic gas jet system (Smartshell) which has three major components viz. a supersonic slit nozzle, high-speed solenoid valve, and fast pulsed valve driver. The system uses a Laval type slit nozzle (Fig.12) with dimensions of $10 \text{ mm} \times 1.2 \text{ mm}$ to produce highly localized high density gas jet with uniform gas density. The solenoid valve ejects high pressure gas (up to 100 bar) through an orifice with large diameter. Accordingly, this can allow using the slit nozzle with larger throat size and higher Mach number. The high pressure gas passes through a $120 \text{ }\mu\text{m}$ thick throat before coming out of the rectangular orifice. The valve can be operated with high speed opening and closing ($100\text{-}200 \text{ }\mu\text{s}$) by proper driving of the control pulse. The valve can open fully and provide a stable ejection pressure even under the condition of regulation pressure of 100 bar. Using the current output monitor signal from the fast pulsed driver, the gas jet operation can be precisely synchronized with laser pulses or signals from other devices.

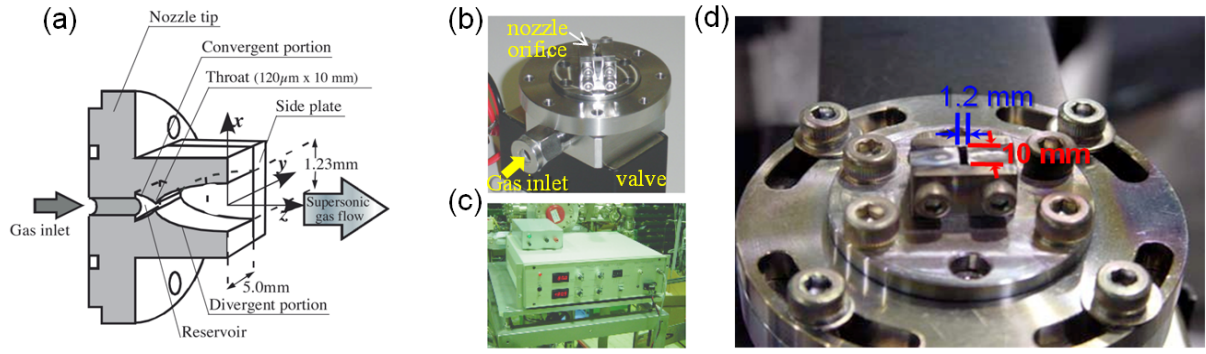


Figure 2.12: a) Design of the supersonic nozzle, b) gas jet nozzle with inlet port on one side for gas entry from a high pressure cylinder through a connecting tube and fast solenoid valve at the bottom for regulating the gas jet duration and repetition rate, c) Control unit for fast solenoid valve driver, and d) magnified view of the nozzle showing the dimensions of the slit type orifice.

The duration of the gas jet during the experiment was 2 ms and the repetition rate of the gas jet was limited to once in 20 s due to vacuum issues. A digital pressure sensor was used to monitor the backing gas pressure of the gas jet. The backing pressure of the gas jet was varied to change the density of the gas jet. The gas jet was well characterized [98] using interferometry and the results are shown in Fig. 2.13. Figure 2.13a shows the density profile of helium gas jet measured at the exit of the nozzle. The profile shows uniform density distribution with sharp entrance and exit boundaries. Fig. 2.13b shows the variation of the density of helium and nitrogen gases with input pressure. The density data was further confirmed from the forward Raman scattering measurements [34].

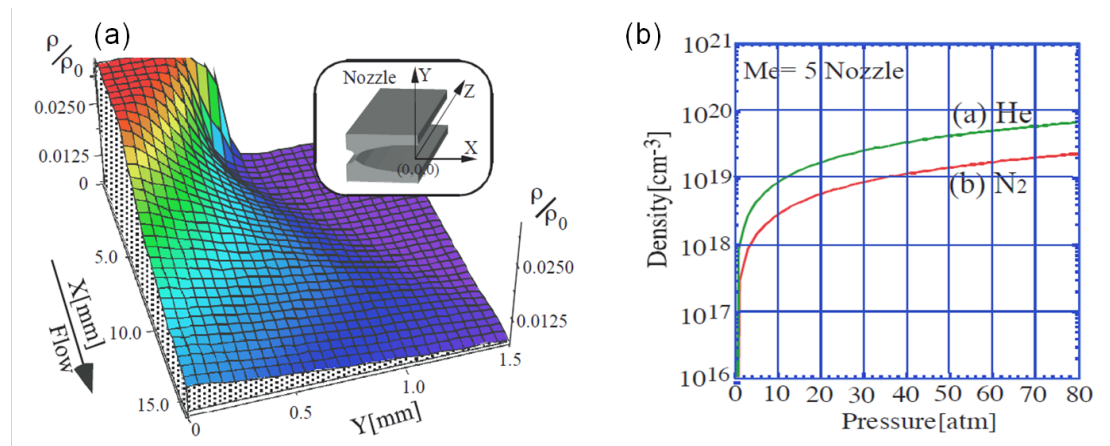


Figure 2.13: a) 3D plot of helium gas density profile normalized w.r.to the backing pressure and b) gas density variation with backing pressure.

2.4 Electron beam diagnostics

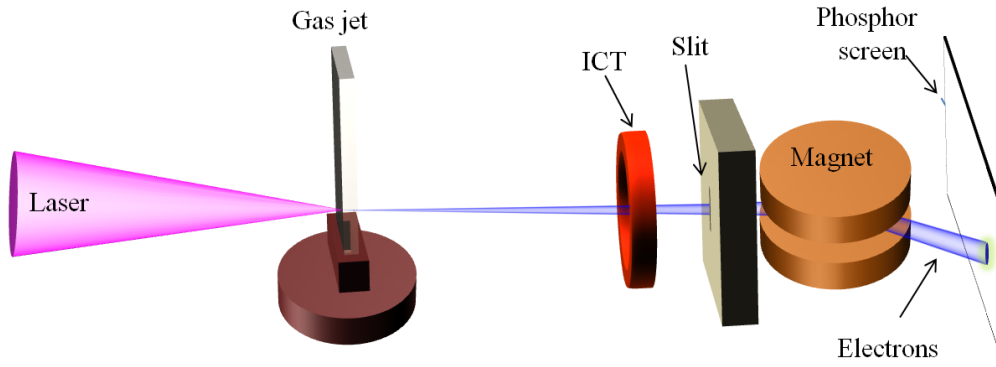


Figure 2.14: Schematic diagram of the experimental setup for laser wakefield acceleration.

A schematic diagram of the experimental setup for laser wakefield acceleration with various important diagnostics for electron beam characterization used is shown in Fig. 2.14. In a typical experiment, we focus the Ti:sapphire laser beam at the front edge of the supersonic gas jet at about 1 mm from the nozzle exit orifice. The high intensity laser beam while passing through the gas jet initially ionizes the gas atoms at its pedestal intensity and the main intense portion of the laser pulse essentially propagates in this plasma to excite intense plasma waves in its wake causing self-injection of electrons into the wakefields after few 100 μm propagation length. The self-injected electrons are accelerated and at the end of the interaction (typically after 500 μm interaction length) exit into vacuum from the plasma as shown in the Fig. 2.14. Measurement of the various parameters of the accelerated electron beam so generated is important to characterize the beam and to understand the acceleration process. Detection methods developed for state-of-the-art radio frequency linear accelerators (LINACs) have been partially adopted for relativistic electrons generated by this new acceleration scheme. However, the beam parameters of laser-plasma based accelerators are currently quite different from LINACs that can produce electron bunches in the MeV to GeV

range with a very narrow energy distribution and charge on the order of tens of pC to nC at repetition rates up to the megahertz range. Single-shot detection methods are crucial for laser accelerated electrons because of strong fluctuations in the electron bunch parameters in consecutive pulses. In the following sections, various diagnostics used for electron beam characterization are described.

2.4.1 Phosphor screen

A phosphor screen (DRZ-High) [99] was used to image the electron beam profiles and to measure the energy dispersion of the electron beam when used with electron spectrograph setup described later. The phosphor screen consists of a 310 μm thick coating of phosphor material ($\text{Gd}_2\text{O}_2\text{S:Tb}$) over a 188 μm thick plastic layer. It has a 9 μm thick plastic layer coated on the phosphor material as a protective layer. The phosphor material emits green light with wavelength around 550 nm, with a decay time of 2ms. The sensitivity of the phosphor screen is almost constant for high energy (≥ 1 MeV) electrons *i.e.*, the emission intensity is proportional to electron flux and independent of their energy [100]. Since there is a thick plastic base on one side of the screen, and a thin protecting layer on the other, the thickness of the plastic base causes high absorption of emitted green light of the phosphor screen as compared to the thin protecting layer. Hence, the screen is placed such that the thick layer faces the electron beam. The electron beam deposits a fraction of its energy in the phosphor layer and causes emission of green light from the phosphor. The phosphor screen surface was imaged using a 16 bit CCD camera (SBIG) to collect the emitted light and record electron beam images. A 100 μm thick layer of aluminium was placed in front of the screen facing the electron beam to protect the phosphor screen from the laser light. The sensitivity data [100] of the phosphor screen was used to estimate the spectrally dispersed beam charge and to generate electron energy spectrum.

2.4.2 Integrating current transformer

We have used an integrating current transformer (Bergoz Model: ICT-082-070-5:1) for measurement of the energy integrated total beam charge of the electrons in our experiments. The integrating transformer is a toroid shaped passive device designed to measure the charge in a very fast pulsed charged particle beam with high accuracy [101]. The ICT is a capacitively shorted transformer coupled to a fast readout transformer in a common magnetic circuit. It is capable of integrating a current pulse with very short rise-time with no significant losses. When an electron bunch passes through the ICT, the electron beam charge gets stored in the capacitors of the ICT through electromagnetic induction. This stored charge gets discharged subsequently through an inductive circuit which gives rise to output pulse of about 70 ns duration (at the base) irrespective of the electron bunch duration (less than its response time of few 10 ns). Fig. 2.15a shows a picture of the ICT used in our experiments and a typical ICT signal measured using 500 MHz oscilloscope with 50 ohm termination is shown in Fig. 2.15b. The area under the ICT output pulse gives the total charge of electron bunch. The charge of the electron beam is determined from the ICT sensitivity of 5.0 Vs/C. In practice, during laser plasma interactions, high level of electromagnetic noise is generated which masks the actual ICT pulse. Therefore, high frequency filtering is used to get the actual signal of the ICT.

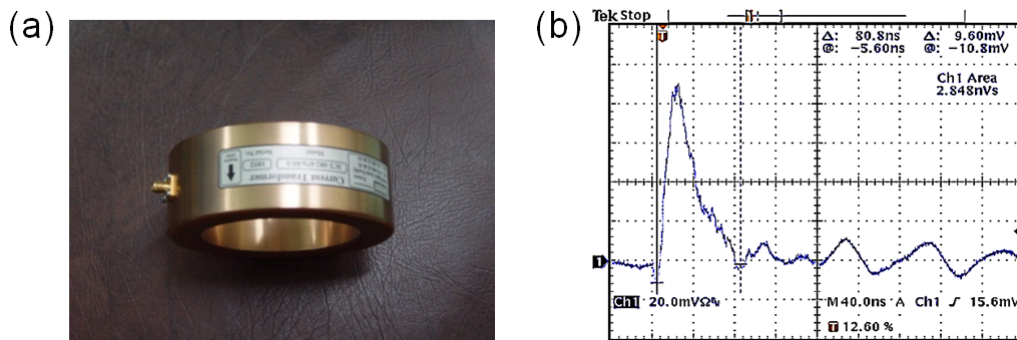


Figure 2.15: a) A photograph of the ICT used in experiments and b) a typical ICT signal after high frequency filtering.

2.4.3 Electron spectrograph

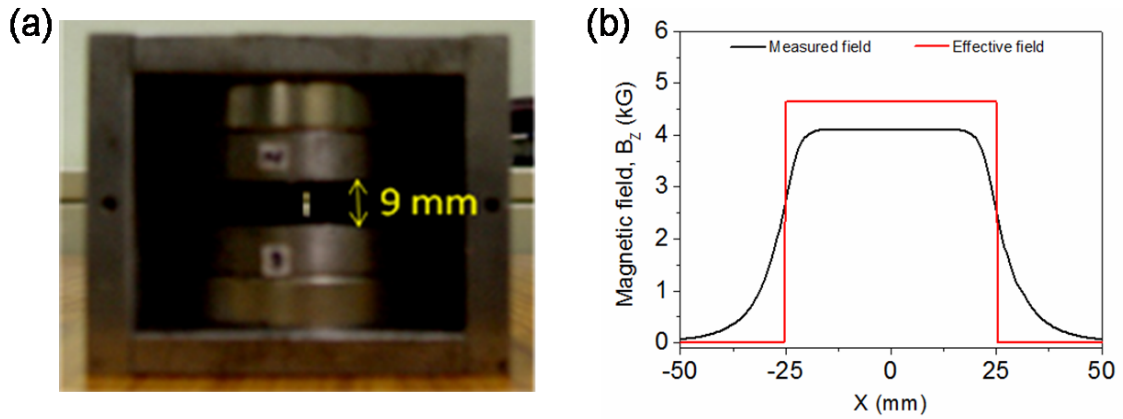


Figure 2.16: a) picture of the permanent dipole magnet with circular poles of 50 mm diameter and pole gap 9 mm. A slit at the entrance of the magnet can be seen in the picture. b) The measured and effective magnetic field in the mid plane of the two poles.

The electron spectrometer used in the laser wakefield acceleration experiments consists of two NdFeB circular magnets of 50 mm diameter separated by 9 mm pole gap, as shown in Fig. 2.16a. The magnetic field was measured using a Hall probe. The measured field, B_z in the horizontal plane at the middle of pole gap is shown in Fig. 2.16b. The measured field can be approximated with a uniform effective magnetic field, B_{eff} and it is estimated from the following expression:

$$B_{eff} = \frac{1}{L} \int_{-\infty}^{+\infty} B_z(x) dx \quad (2.2)$$

Here ‘L’ is the diameter of the poles. Fig. 2.16b shows the effective field of the magnet estimated from the Eq. 2.2. The geometry of the electron spectrograph used in the experiment is illustrated in Fig. 2.17. The magnet deflects the electron beam in the plane perpendicular to magnetic field. The deflected beam strikes the phosphor screen causing emission of light from the phosphor. The surface of the phosphor was imaged using a CCD camera (SBIG) with a large dynamic range. The light emitted from the phosphor screen was recorded to measure the electron spectrum in the dispersion plane and the divergence along the plane perpendicular to

it. A vertical slit is placed before the magnets to collimate highly divergent electron beam and to define a reference axis (a line joining the electron source and the slit). The slit is made of combination of an aluminium plate followed by a lead plate.

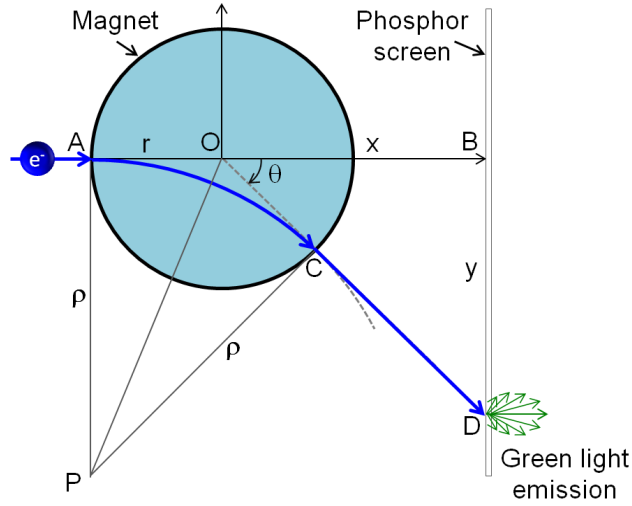


Figure 2.17: Geometry of the permanent magnet based electron spectrometer.

The trajectory of an electron from the time it enters the magnetic field to finally striking the phosphor screen is shown in blue colour in Fig. 2.17. The electron beam enters the field of the circular magnet with radius 'r' at point A along x-axis and then it moves on an arc along AC with radius 'ρ' in the field. The electron exits the field at C and then strikes the phosphor screen at point D after moving along the straight line CD. The deflection angle 'θ' or distance 'y' (on phosphor screen) of the electron from its initial direction along x-axis varies according to electron energy, E. The radius 'ρ' is related to the momentum and to the energy of the electron by the following equations:

$$p = Be\rho, \quad \text{and} \quad E = \sqrt{(pc)^2 + (m_0c^2)^2} \quad (2.3)$$

From the geometry shown in Fig. 2.17, $\angle AOP = \angle POC = \beta$, $\angle APO = \angle CPO = \alpha$, and the deflection angle 'θ' is given by:

$$\tan \theta = \frac{y}{x} \quad (2.4)$$

$$\theta = 2\alpha \quad \text{since} \quad 2\beta + \theta = \pi, \quad \text{and} \quad \alpha + \beta = \frac{\pi}{2} \quad (2.5)$$

Using the relation $\tan \alpha = r/\rho$, we get:

$$\tan \theta = \frac{2r\rho}{\rho^2 - r^2} \quad (2.6)$$

$$\text{and } y = x \cdot \tan \theta \quad (2.7)$$

The parameters ‘r’ and ‘x’ are known from the experimental setup. By measuring ‘y’, ρ is calculated and from that the energy E of the electron is determined from the Eq. 2.3.

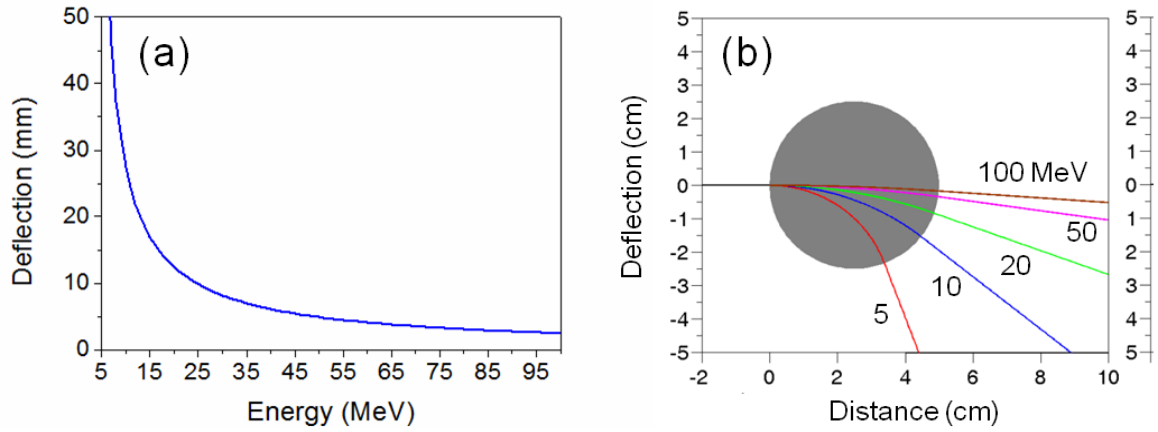


Figure 2.18: a) Dispersion curve for the spectrograph for phosphor screen kept at a distance of 35 mm from the geometric centre of the magnet. b) Trajectories of electrons with different energies.

The dispersion curve for the spectrograph with typical phosphor distance of 35 mm from the geometric centre to the magnet is shown in Fig. 2.18a. Actual phosphor distance in each experiment presented in the thesis changed depending on the resolution required in a particular experiment. Fig. 2.18b shows the computed trajectories of electrons with different energy for the circular magnet of $B_{eff} = 4.6$ kG. We have used rectangular magnets with smaller magnetic field for spectrograph setups for characterizing the relatively low energy electrons. The description of these magnets and the corresponding resolutions are given at appropriate places in the thesis.

Chapter 3: Study of laser wakefield acceleration in self-modulated regime

In order to induce self-injection of electrons for their acceleration in the laser wakefield, the wakefield amplitude should reach the wave-breaking limit. This could be more efficiently achieved when the wakefield is excited resonantly *i.e.* when the laser pulse length ($c\tau_0$, where τ_0 is the FWHM duration) is equal to half-wave period ($\lambda_p/2$) of the plasma wave, as described in Chapter 1. However, for laser pulse duration ~ 50 fs or more, produced from typical 10 TW kind of laser systems like one we have used for our investigations, the resonance condition requires that the plasma density n_e to be $< 10^{19} \text{ cm}^{-3}$ and the corresponding laser intensity required to drive the wakefield till wave-breaking takes place, is very large ($a_0 \gg 1$). Such a high intensity is not possible to achieve using 10 TW class lasers. As discussed in Chapter 1, relativistic self-focusing can increase the laser intensity inside the plasma, if the laser power is above the critical power for a given plasma density, *i.e.* $P > P_c$ [85]. However, due to a small fraction of power (usually $\sim 50\%$) in the focal spot and other competing processes in the plasma, self-focusing and guiding are observed for $P \gg P_c$ in typical experimental conditions. Therefore, practically laser pulse power much larger than 10 TW is required for observing self-focusing when the plasma density is $< 10^{19} \text{ cm}^{-3}$. However, since $P_c \propto n_e^{-1}$, the condition $P > P_c$ can be easily met at higher plasma densities for the moderate power lasers with $a_0 \sim 1$ at the focus. In addition, the laser pulse duration becomes much longer than the plasma wave length (*i.e.* $c\tau_0 \gg \lambda_p$) at higher plasma densities, which facilitates self-modulation of the laser pulse. Self-focusing and self-modulation of the laser pulse at higher plasma densities together lead to the laser wakefield acceleration in the self-modulated regime. In this regime, a single long laser pulse with duration $c\tau \gg \lambda_p$ breaks up

into multiple short pulses through forward Raman scattering (FRS) instability [14], each of which has a width of about half the plasma wavelength ($\lambda_p/2$) and separation between the pulse-lets equal to λ_p . Coherent (in phase) addition of the wakefields of these equi-spaced laser pulses results in a very large amplitude wakefield leading to its wave break-up, due to which the electrons from the background plasma get self-injected and are accelerated to high energies. However, the electron beams produced from SM-LWFA experimental studies in the past were reported to have large divergence and nearly 100% energy spread [84].

In this chapter, an experimental study on laser wakefield acceleration in the self-modulated regime is presented [34]. The dependence of electron beam parameters viz. charge, divergence, and the electron spectrum, on the plasma density, is discussed. Although the electron energy spectrum typically showed 100% spread at lower plasma density, at a relatively high density of $\sim 8.5 \times 10^{19} \text{ cm}^{-3}$, a high quality electron beam was produced with a divergence $< 10 \text{ mrad}$, and quasi-mono-energetic distribution with a peak energy $\sim 20 \text{ MeV}$, with small energy spread ($\Delta E/E < 10 \%$). These results, along with simultaneous detection of Raman peak in the forward laser scattering measurements, are described in detail in this chapter. The results suggest strong self-modulation of the laser pulse. Forward Raman scattering (FRS) is an inherent and important physical process occurring in the self-modulated laser wakefield acceleration. Therefore, controlling the FRS and thereby the wakefields is essential for controlling the charge, energy, and quality of the electron beam, in this regime. The effect of positively/negatively chirped laser pulses on the self-modulation induced by FRS and on electron acceleration, has been investigated [102]. The observed dependence of laser self-modulation, electron beam charge and energy on the magnitude and sign of the chirp is presented. The underlying physics of high quality beam generation based on strong self-modulation and pulse shape effects is discussed.

3.1 Experimental details

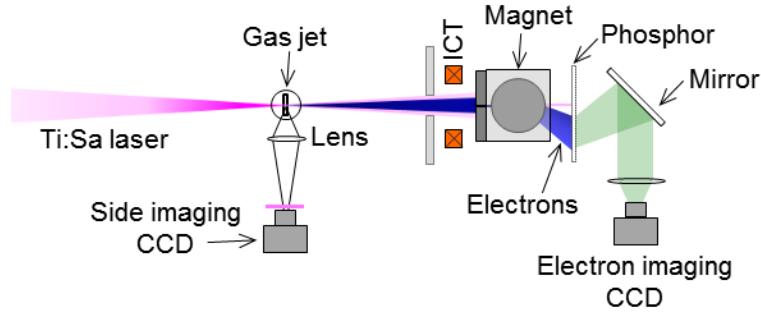


Figure 3.1: A schematic diagram of the experimental set-up used for electron acceleration.

A schematic of the setup used for the experiment is shown in Fig. 3.1. The Ti:sapphire laser pulses of 45 fs (FWHM) duration, with maximum 400 mJ of energy after the compressor chamber, were used for the experiment. The laser beam was focused 1 mm above and at the front edge of the gas jet nozzle orifice using an f/10 gold-coated off-axis parabolic mirror to a spot of FWHM diameter $d_0 = 18 \mu\text{m}$. The Rayleigh length of the focused laser beam was $z_R = \pi d_0^2 / (2M^2 \lambda \ln 2) \approx 300 \mu\text{m}$ and the peak intensity at the waist was $I_L = 4P_0 \ln 2 / \pi d_0^2 \approx 1.2 \times 10^{18} \text{W/cm}^2$, considering about 50% of the total power contained in the focal spot. Helium gas was used for the experiment and gas backing pressure was varied from about 10 bar to 70 bar, to vary the neutral gas density in the range of $1\text{-}5 \times 10^{19} \text{cm}^{-3}$. An integrating current transformer (ICT), with a 4 mm thick annular aluminium disc in front, was kept after the gas jet to measure the electron beam charge. The aluminium disc had a hole of 50 mm diameter to allow electrons emitted within a full cone angle of approximately 20° to pass through the ICT. A DRZ phosphor screen (covered with $30 \mu\text{m}$ thick aluminium foil on the front side to stop the laser light interaction with the phosphor screen) coupled with a 12-bit CCD camera (Make: SamBa) was used to detect the high energy electrons. The energy spectrum of the electrons was measured using an electron spectrograph (described in Chapter

2). The slit in front of the magnet had angular dimensions 33 mrad and 60 mrad in the plane containing energy dispersion direction and perpendicular to it, respectively. The laser-plasma interaction was observed through side imaging of the linear Thomson side-scattering of the laser radiation, with 5X magnification. A narrow band-pass filter was placed in front of the side imaging 12-bit CCD camera to allow only the scattered radiation from the plasma within the wavelength range of 800 ± 20 nm to pass through. To detect and measure the wavelength shifts in the transmitted spectrum due to forward Raman scattering, a part of the transmitted laser light from the interaction region at an angle of 6° w.r.to laser axis was attenuated, reflected using a glass wedge, collected by a lens, and focused onto the entrance slit of an optical spectrograph covering a spectral range of 550 – 1100 nm. A long pass filter (RG 850), in combination with an appropriate number of neutral density filters, was placed in front of the spectrograph to cut off the transmitted laser spectrum below 850 nm. This improved the sensitivity of detection of the less intense red-shifted signal expected due to stimulated FRS.

3.2 Electron beam profile measurement

After scanning the backing pressure of the gas jet and optimization of laser focus position in the gas jet, accelerated electron beam was observed for plasma electron densities above $5 \times 10^{19} \text{ cm}^{-3}$ in every laser shot, with energy integrated total charge in excess of 2 nC. As the ICT collected the electrons within a cone angle of 20° , therefore the total charge includes large divergence, low energy electrons also. When the density was below $\sim 5 \times 10^{19} \text{ cm}^{-3}$, no high energy electrons were observed, as in this case, the amplitude of the plasma wave was not high enough for self-injection of the electrons for acceleration. The images of the electron beam produced at different plasma densities are as shown in Fig. 3.2. As seen in this figure, the electron beam, in general, shows an increase in divergence with increase in

plasma density. Moreover, the images showed saturation at higher plasma density due to higher charge, as a result of which the finer features of the beam profile were lost. In order to overcome this saturation, a 5 mm thick aluminium plate was kept in front of the phosphor screen to cut off lower energy (<5 MeV) electrons reaching the phosphor screen. In this case, at a plasma density of around $8.5 \pm 0.5 \times 10^{19} \text{ cm}^{-3}$, a highly collimated (divergence < 10 mrad) electron beam was observed along with a background of broadly diffused electrons with larger divergence, as seen in Fig. 3.2(d). The pointing angle of the collimated beam varied from shot-to-shot within about ± 25 mrad.

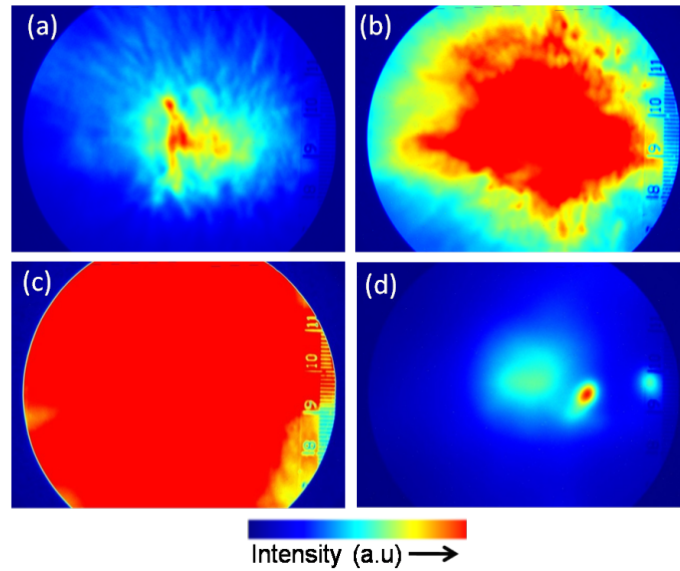


Figure 3.2: Images of electron beam profiles at plasma density a) $6.5 \pm 0.5 \times 10^{19} \text{ cm}^{-3}$, b) $7.5 \pm 0.5 \times 10^{19} \text{ cm}^{-3}$, and c) $8.5 \pm 0.5 \times 10^{19} \text{ cm}^{-3}$ with $30 \mu\text{m}$ aluminium foil in front of phosphor screen. d) A well collimated electron beam with broad background observed at plasma density $6.5 \pm 0.5 \times 10^{19} \text{ cm}^{-3}$ when a 5 mm thick aluminium plate was kept in front of the phosphor screen to cut off the low energy (< 5 MeV) electrons.

3.3 Forward Raman scattering measurements

For the plasma electron density in the range of $5 \times 10^{19} - 1 \times 10^{20} \text{ cm}^{-3}$, wherein the electron beams were observed, the plasma wavelength (λ_p) varies from $4.7 - 3.3 \mu\text{m}$. This implies that the laser pulse length ($c\tau_L = 13.5 \mu\text{m}$) is about 3 to 4 times λ_p . Also, for the above density range, the laser power in the focal spot was much larger than the critical power P_c

required for relativistic self-focusing (RSF). Therefore, the laser pulse can undergo strong self-modulation through forward Raman scattering instability. The occurrence of self-modulation was confirmed from the observation of the Stokes satellite in the forward Raman scattering spectrum. Fig. 3.3 shows the observed Stokes satellites due to forward Raman scattering and the variation of the Raman shift with the plasma density. The amplitude of Raman satellites increased with the plasma density, which shows that the self-modulation of the laser pulse becomes stronger at higher plasma density.

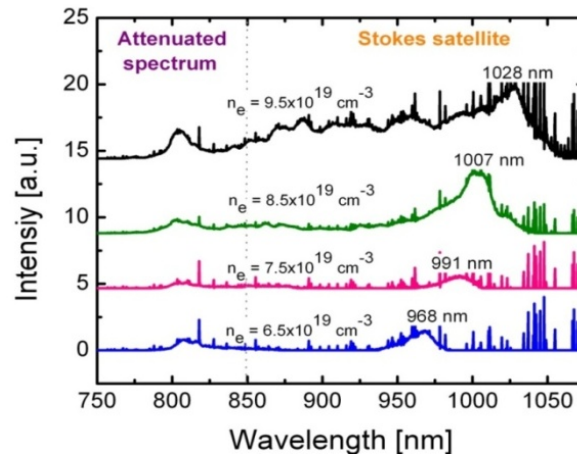


Figure 3.3: Forward Raman spectra at different plasma densities.

3.4 Laser channelling in plasma

As $P_L \gg P_C$ for the experimental conditions, a single, long interaction channel / filament extending to several z_R through RSF is expected. However, as seen in Fig. 3.4, a double filament-like structure was observed. Each of these filaments had diameter around 9 μm and length around 400 μm . The latter was about 1.3 times the z_R . The filaments appear at the beginning of the flat-topped portion of the gas jet profile as indicated in Fig. 3.4. They were observed in almost all the laser shots, within the density range of the experiment. In some shots at higher densities, multiple (scattered) filaments were observed. We did not observe any significant change in the length or the position of the filaments by varying the plasma density. However, there was shot-to-shot variation in the observed intensity and length of the filaments (from about 400 – 500 μm), which may be attributed to shot-to-shot

variations in laser-plasma interaction parameters. Next, there was increase in the Thomson scattering intensity with increase in the plasma density. This is expected as the scattering intensity is proportional to the plasma electron density. The separation between the filaments remained constant within the resolution of our measurement.

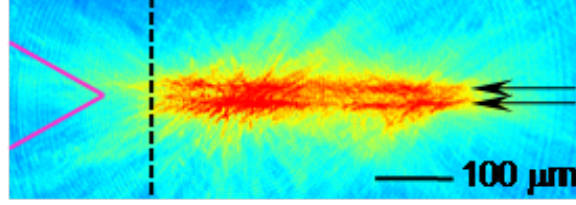


Figure 3.4: Thomson scattering side image laser channelling in plasma showing bifurcation of the laser beam into two filaments as indicated by the arrows on the right. The vertical dotted line shows the location of top of the gas jet density ramp.

3.5 Energy spectrum of accelerated electrons

The energy spectrum of the electron beam was measured at various plasma densities ranging from about $5 \times 10^{19} \text{ cm}^{-3}$ to $1 \times 10^{20} \text{ cm}^{-3}$. The representative electron energy spectra at different plasma densities are shown in Fig. 3.5. The typical spectra were continuous with energy distribution of the form $\sim \exp(-E/kT_{\text{eff}})$. The effective temperature (T_{eff}) of the electron beam is given by the slope of the semi-log plot of the spectra shown in the Fig. 3.5b. It can be seen that the temperature increased when the plasma density was increased from $6.5 \pm 0.5 \times 10^{19} \text{ cm}^{-3}$ to $8.5 \pm 0.5 \times 10^{19} \text{ cm}^{-3}$. Further increase in the plasma density to $9.5 \times 10^{19} \text{ cm}^{-3}$ reduced the temperature, which is close to the effective temperature at $7.5 \pm 0.5 \times 10^{19} \text{ cm}^{-3}$.

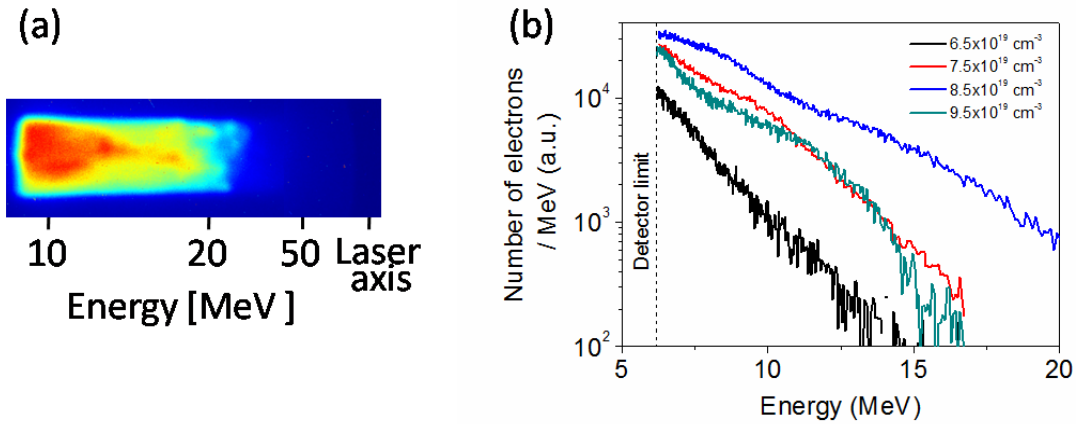


Figure 3.5: a) A typical image of continuous energy distribution of electron beam at plasma density $8.5 \pm 0.5 \times 10^{19} \text{ cm}^{-3}$. b) Energy spectra of the electron beam produced at different plasma densities.

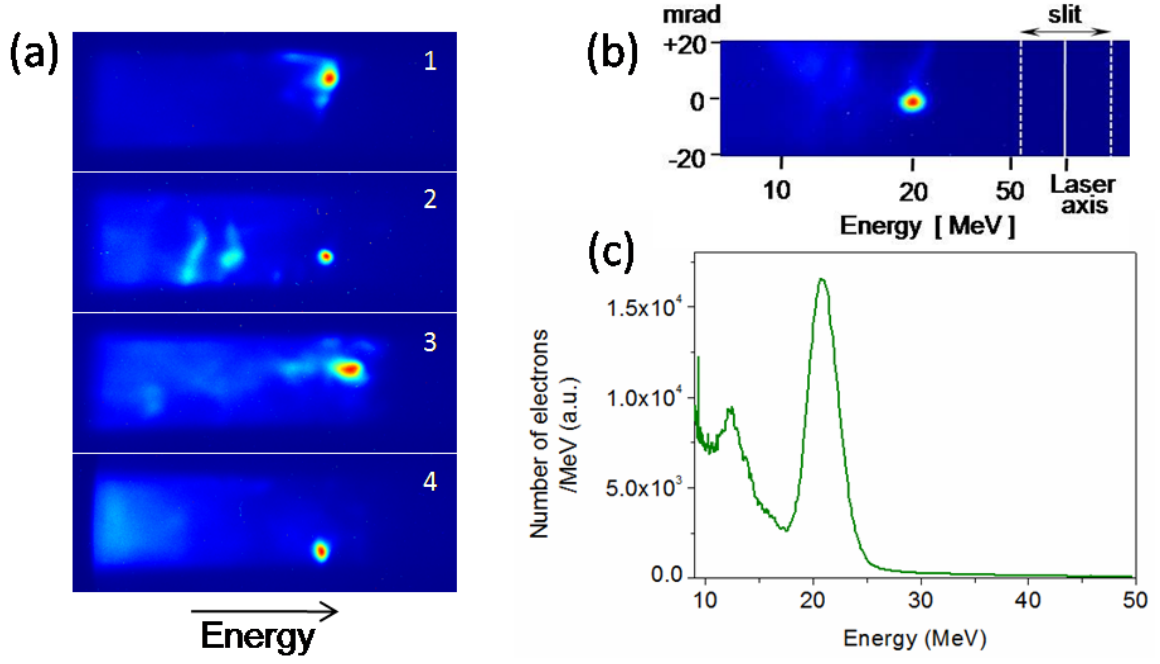


Figure 3.6: *Quasi-mono-energetic electron beams at plasma density $8.5 \pm 0.5 \times 10^{19} \text{ cm}^{-3}$. a) Raw images of energy dispersed quasi-mono-energetic electron beam, b) Processed image of a quasi-mono-energetic electron beam, and c) corresponding energy spectrum showing peak at 21 MeV.*

At electron density around $8.5 \times 10^{19} \text{ cm}^{-3}$, in about 20% of the laser shots, highly collimated and mono-energetic electron beam with few tens of pico-coulombs of charge was observed during the electron energy measurements. Since the pointing variation is larger than the half width of the slit (16.6 mrad) of the magnet spectrograph, the collimated electron beam might have missed the slit in some of the shots. Images of energy dispersed electron beams with low divergence and quasi-mono-energetic feature are shown Fig. 3.6. Quasi-mono-energetic electron beams with energy in the range of 10 – 21 MeV were observed in a series of shots during the experiment. It may be noted that the quasi-mono-energetic electron beam is usually accompanied by large divergence and continuous energy background, as shown in Fig. 3.6a. Once in a while, electron beams with less low energy background were also observed. The energy spectrum of a quasi-mono-energetic electron beam with relatively less low energy background and its corresponding energy spectrum with peak at 21 MeV, are shown in Fig. 3.6 b and c. The vertical dimension of the quasi-mono-energetic electron beams

in the Fig. 3.6a and b represents the divergence of the electron beam, as the beam size in this direction was not restricted by the slit height (60 mrad) of magnet spectrograph. The quasi-mono-energetic electron beam had divergence angle (2θ) in the range of 4 – 7 mrad (less than the slit width of 33 mrad), and energy spread ($\Delta E/E$) of $\pm 4 - 8 \%$. The resolution ($\Delta E/E$) of the spectrograph at 21 MeV is about 1% and the value becomes smaller at lower energies (e.g. 0.5% at 10 MeV). Therefore, the estimated energy spread was the upper limit which arises due to the finite size of the electron beam in the direction of energy dispersion on the DRZ-phosphor screen. Therefore, the actual energy spread may be smaller than the above stated value. The charge of the mono-energetic electron beam was estimated from the calibration of ICT signal against the intensity of electron beam image, as recorded using the DRZ-phosphor screen and the CCD camera. Although the total beam charge (energy integrated) was few nC, the mono-energetic electron beam had a maximum charge of about 60 pC, carrying about 0.5% of the laser energy. Transverse geometric emittance (ϵ_x) of the mono-energetic beam was as low as 0.01π mm.mrad. This was estimated by assuming the upper limit on the electron beam transverse size to be equal to the diameter of each filament and the measured divergence.

3.6 Effect of chirp

In order to study the effect of the laser chirp, the laser pulse duration (and consequently the chirp characteristics) was varied by scanning the compressor grating pair separation from its optimal separation. For a chirped laser pulse, one can define the instantaneous frequency ω as $\omega = \omega_0 + bt$, where t is the time in the pulse reference frame, b is the chirp parameter given by $b = 2 \ln 2 / \tau^2 [(\tau/\tau_0)^2 - 1]^{1/2}$ where τ and τ_0 are the FWHM duration of the chirped and unchirped pulse, respectively. Hence, for a negative chirp ($b > 0$), the “blue” frequencies are located at the front of the pulse and for a positive chirp ($b < 0$), the “red”

frequencies are located at the front of the pulse. Positively/negatively chirped pulses, with duration ranging from 45 fs to ± 450 fs (corresponding intensities varied from 1.2×10^{18} W/cm² down to 1.2×10^{17} W/cm²), were generated by translating one of the two gratings of the pulse compressor by 0 to ± 2 mm from their optimal separation for minimum pulse duration. Hereafter, “plus” or “minus” signs will be used (except for 45 fs) together with the pulse duration to indicate positively or negatively chirped laser pulses.

3.6.1 On electron beam charge

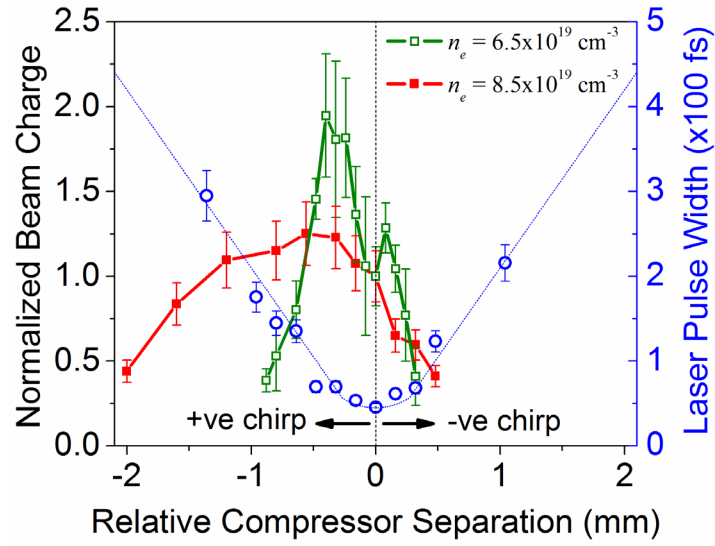


Figure 3.7: Variation in the integrated electron beam charge at two different plasma densities (Solid squares: $8.5 \pm 0.5 \times 10^{19} \text{ cm}^{-3}$, and hollow squares : $6.5 \pm 0.5 \times 10^{19} \text{ cm}^{-3}$) with compressor grating pair separation (chirp) measured w.r.t. the “zero” setting (separation corresponding to minimum pulse duration). The total charge for “zero” setting of the compressor is 2 nC and 8 nC respectively for plasma density $6.5 \pm 0.5 \times 10^{19} \text{ cm}^{-3}$ and $8.5 \pm 0.5 \times 10^{19} \text{ cm}^{-3}$. The variation of the laser pulse width (circles) with grating separation is also shown.

The effect of chirp on self-modulation and electron acceleration for two different plasma densities : $n_e \simeq 6.5 \pm 0.5 \times 10^{19} \text{ cm}^{-3}$ (Case 1) and $n_e \simeq 8.5 \pm 0.5 \times 10^{19} \text{ cm}^{-3}$ (Case 2) was studied. Figure 3.7 shows the variation of normalized charge of the electrons with relative separation of compressor gratings, for case 1 and case 2. For easy reference, the figure also shows the variation of the laser pulse duration with the grating separation. In both the cases, normalization of the charge was done w.r.t. the total charge observed with the

unchirped pulse (45 fs) interaction. The total charge for “compressor zero” setting was 2 nC and 8 nC for plasma density $6.5 \times 10^{19} \text{ cm}^{-3}$ and $8.5 \times 10^{19} \text{ cm}^{-3}$, respectively. An asymmetry in the electron beam charge w.r.t. the laser pulse chirp was observed for both the plasma densities. The maximum charge was observed for longer laser pulses with a small amount of positive chirp. The charge increased by nearly 100% and 25% for $n_e \approx 6.5 \pm 0.5 \times 10^{19} \text{ cm}^{-3}$ and $8.5 \pm 0.5 \times 10^{19} \text{ cm}^{-3}$ respectively, when positively chirped pulses of about +80 to +85 fs duration were used.

The minimum laser power at which electrons were observed was about 1.1 TW, corresponding to positively chirped laser pulse of +185 fs duration for $n_e \approx 6.5 \pm 0.5 \times 10^{19} \text{ cm}^{-3}$, and 0.45 TW corresponding to +420 fs for $8.5 \pm 0.5 \times 10^{19} \text{ cm}^{-3}$. This power is higher than the critical power $P_c \approx 0.43 \text{ TW}$ and 0.33 TW required for relativistic self-focusing at the two densities respectively. Along with the accelerated electrons, laser self-focusing channels of length 400–500 μm over this entire range were also observed in the Thomson scattering side images.

3.6.2 On forward Raman Scattering

Figure 3.8 shows the measured spectra of transmitted laser light w.r.t. the laser chirp / grating separation for $n_e \approx 6.5 \pm 0.5 \times 10^{19} \text{ cm}^{-3}$ and $8.5 \pm 0.5 \times 10^{19} \text{ cm}^{-3}$. The side bands at longer wavelengths due to stimulated FRS can be clearly seen. The wavelength shift of the side band with change in plasma density is consistent with FRS. The variation in the amplitude of the FRS signal with laser pulse chirp for a fixed density was consistent with the observed asymmetry in the electron beam charge with chirp. This clearly suggests that the laser pulse was undergoing strong self-modulation through stimulated FRS and resulting in excitation of large amplitude wakefields which could self-trap and accelerate background plasma electrons to high energy. The transmitted spectra also show red shifting of the laser light, which is

probably due to laser photon deceleration in the wakefield [103]. Since a high pass filter (RG-850), which strongly attenuates the spectrum below 850 nm, was used to attenuate the transmitted laser light, the blue shifted anti-Stokes satellite band due to FRS and blue shift due to photon acceleration [103] could not be seen in Fig. 3.8.

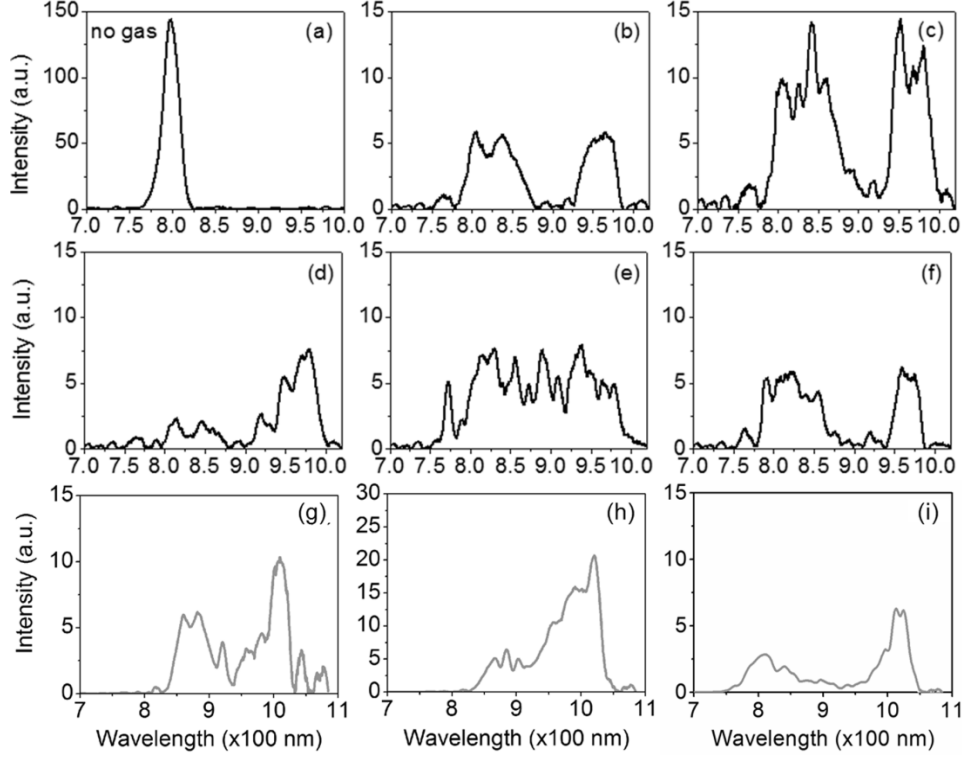


Figure 3.8: The transmitted laser spectra at two different plasma densities : a) without interaction with plasma, b) to f) with interaction at : $n_e \approx 6.5 \pm 0.5 \times 10^{19} \text{ cm}^{-3}$, for grating separation of 0 (45 fs), $-320 \mu\text{m}$ (70 fs), $-600 \mu\text{m}$ (125 fs), $-800 \mu\text{m}$ (170 fs), and $+200 \mu\text{m}$ (52 fs) respectively, g) to i) at $n_e \approx 8.5 \pm 0.5 \times 10^{19} \text{ cm}^{-3}$ for grating separation of 0 (45 fs), $-400 \mu\text{m}$ (85 fs), and $+200 \mu\text{m}$ (52 fs) respectively. No distinct Raman peak could be resolved from the transmitted spectra due to large broadening of laser spectrum (as shown in (e)) for grating separation $\gtrsim -800 \mu\text{m}$, for a density of $6.5 \pm 0.5 \times 10^{19} \text{ cm}^{-3}$. Similar observation was made for $n_e \approx 6.5 \pm 0.5 \times 10^{19} \text{ cm}^{-3}$ at grating separation of $> -400 \mu\text{m}$ (spectra not shown here). Raman peaks disappear for grating separation $\gtrsim +200 \mu\text{m}$ (-ve chirp).

3.6.3 On quasi-mono-energetic electron beam

The low divergence electron beam observed for the 45 fs duration laser pulse at plasma density of $n_e \approx 8.5 \pm 0.5 \times 10^{19} \text{ cm}^{-3}$, was present even when a positive chirp was introduced up to about +250 fs, while it vanished on introducing a small amount of negative

chirp (≥ -60 fs). In the case of $n_e \approx 6.5 \pm 0.5 \times 10^{19} \text{ cm}^{-3}$, once in a while, a low divergence electron beam was observed when positive chirp around 85 fs was introduced. The energy spectrum of the electron beam was measured at a plasma density of $n_e \approx 8.5 \pm 0.5 \times 10^{19} \text{ cm}^{-3}$ for different positive chirp values leading to variation in the laser pulse duration from 45 fs to 135 fs. Typical recorded spectra are shown in Fig. 3.9. Generation of collimated, quasi-mono-energetic electron beams was observed for the above range of positive chirped laser pulse duration, with maximum electron beam energy of 28 MeV observed for a positive chirped laser pulse of 70 fs duration. The reproducibility of the quasi-mono-energetic electron beam in the present experiment at a plasma density of $\approx 8.5 \pm 0.5 \times 10^{19} \text{ cm}^{-3}$ was $\sim 20\%$. No significant improvement in the reproducibility of the quasi-mono-energetic electron beam with the positive chirp was observed.

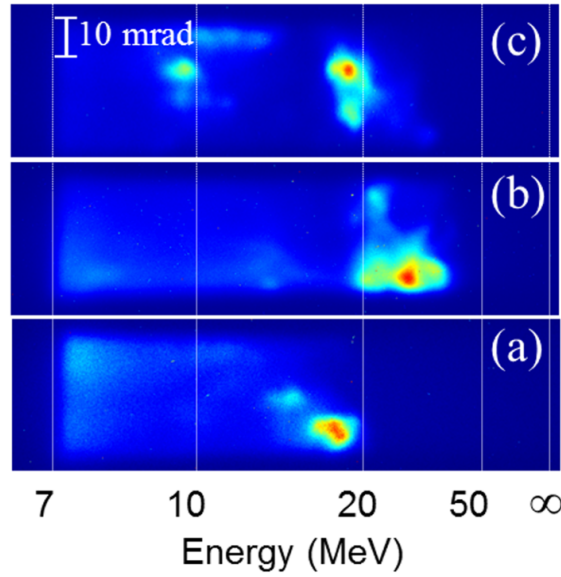


Figure 3.9: Images of quasi-mono-energetic electron spectra recorded at $n_e \approx 8.5 \pm 0.5 \times 10^{19} \text{ cm}^{-3}$, for different separations of the laser pulse compressor gratings : a) $0 \mu\text{m}$ (45 fs), b) $-320 \mu\text{m}$ (70 fs), and c) $-640 \mu\text{m}$ (135 fs).

3.7 Discussion

First of all we consider laser channelling in under-dense plasma. We observed formation of two channels in our experiment, as shown in Fig. 3.4. Two channels formation

due to bifurcation of a single channel after some length of interaction has been reported by few other groups. For example, Chen *et al* [104] inferred that such bifurcation of laser channel can result from presence of a pre-pulse. Ionization by pre-pulse splits the laser propagation channel by creating a sharp localized region of lower index of refraction. Andreev *et al* [105] have observed that short pulses ($c\tau_L < \lambda_p$) can undergo filamentation instability seeded by hot spots in the laser beam. Due to non-ideal, near-field radial profile (neither Gaussian nor circular flat top) of practical high power laser beams with $M^2 > 1$, the far-field profile of the laser beam may consist of one principal spot with one or more hot spots in its periphery. Since the value of a_0 required for the growth of these hot spots is quite small, it is quite possible that one of the intense hot spots grows on the rising edge of the laser pulse over 100 μm of the gas density ramp and forms second intense filament, along with the filament caused by the principal spot, by the time the laser reaches the top of the density ramp, as shown in Fig. 3.4. More recently, simulation and experimental results of Thomas *et al* [106] have shown that appropriate choice of focusing optics ($w_0 > \lambda_p$) would lead to smooth self-guiding of laser over a dephasing length and produce mono-energetic electrons in bubble regime ($c\tau_0 < \lambda_p$). They also report that for the case $w_0 < \lambda_p/2$, multiple filaments of size λ_p are formed and interaction length becomes much shorter. This laser filamentation was found to produce electron beams with large divergence and continuous energy spectrum. However, we observe low divergence and quasi-mono-energetic electron beam from double filamented propagation of laser at much higher plasma densities compared to Thomas *et al* [106].

Next, the occurrence of self-modulated wakefield excitation and the resulting electron acceleration can be understood as follows. The self-modulation process causes the laser pulse ($c\tau_0 = 13.5 \mu\text{m}$) to modulate itself into multiple pulse-lets of spatial length (FWHM) of approximately $\lambda_p/2$, separated by λ_p [33]. The fact that length of the filaments remains $\sim 400 - 500 \mu\text{m}$, but did not last for whole 1.2 mm length of the gas jet, suggests occurrence of strong

modulation, within the first 100 -300 μm of the interaction of the laser pulse both in the axial and transverse directions, leading to formation of pulse-lets of FWHM length $\lambda_p/2$. Both, numerical simulations [107] and laboratory experiments [108], showed that the relativistic self-guiding is greatly weakened for pulses shorter than λ_p , even if the laser power exceeds the critical power for relativistic self-focusing. Therefore, the pulse-lets may not be self-guided beyond 500 μm . Self-guiding may further be inhibited as the self-modulation results in significant laser energy depletion leading to reduction in laser power below critical power (P_C) for self-focusing. The side images of the plasma showed that the interaction length did not change much with variation of the electron density. This suggests that the laser pulse may be getting considerably modulated even at lower electron density. Although the laser modulation is detrimental for achieving long interaction lengths, it drives a large amplitude relativistic plasma wave that traps the background hot electrons produced by the stimulated side Raman scattering process. The trapped electrons can be accelerated by the relativistic plasma wave, excited by FRS, up to the dephasing length, L_{deph} , which is in the range of 160 – 60 μm for $n_e = 5 \times 10^{19} - 1 \times 10^{20} \text{ cm}^{-3}$. Therefore, it appears that the acceleration length (and hence the maximum energy of accelerated electrons) was not limited by the interaction length. Over the initial portion (about 100s μm) of channel length, the laser pulse evolves through self-modulation before it could drive strong plasma wave. The plasma wave then traps a significant number (\sim few nC) of background electrons and accelerate them. If the electrons exit the plasma after acceleration distance close to dephasing length, L_{deph} , the electrons gain maximum energy from the wakefield, as explained in Chapter 1.

An electron beam produced from self-modulated laser wakefield acceleration normally has high charge (typically few nano-coloumbs), large divergence (\sim 100 mrad or above), and continuous energy distribution (typically 100% energy spread) [22]. Also, at higher plasma electron densities (as in the present experiment), the relativistic electrons generated initially

from wakefield can gain further higher energy by direct laser acceleration (DLA) and have large divergence [91]. This may be the reason for the diffused background electrons seen in Fig. 3.2d. The same may also account for the observation of continuous energy spectrum as shown in Fig. 3.5 and 3.6. If the electrons are accelerated by only SM-LWFA, the maximum energy of the electrons is expected to decrease with electron density as the energy gain is inversely proportional to plasma density. This is due to the reduced dephasing length at higher densities. However, we have observed that the maximum energy of the electrons as well as the T_{eff} increased as the plasma electron density increased from 6.5×10^{19} to $8.5 \times 10^{19} \text{ cm}^{-3}$. This could occur if the electron acceleration took place due to cascade of SM-LWFA and DLA. As the laser modulation rate increases with increase in plasma density, trapping of electrons by the relativistic plasma wave would occur earlier for higher electron density. Subsequently, the electrons will be accelerated under the direct laser field for longer length resulting in increase in maximum energy or temperature of the accelerated electrons with increase in plasma electron density. Such an increase in maximum energy and T_{eff} , with electron density, has also been reported earlier [91, 109]. At electron density of around $8.5 \times 10^{19} \text{ cm}^{-3}$, the laser pulse may be significantly modulated over the first 200 - 300 μm of interaction length, leaving one or more pulse-lets of length $\sim \lambda_p/2$ which can drive wakefields in the “bubble” or “blow-out” regime. Simulations have shown that this regime is very well suited for producing high quality electron beams [26]. However, the location of electron injection into the bubble is sensitive to the history of pulse modulation, which significantly changes with slight variation in the initial laser and plasma parameters. In the case of electron exiting the plasma after L_{deph} , the electron beam exhibits continuous energy spectrum [24] as seen in Fig. 3.5. For plasma density beyond $8.5 \times 10^{19} \text{ cm}^{-3}$, the growth rate of modulation may become so large that the laser pulse gets self-modulated very early during the interaction. The pulse-lets drive wakefield in the bubble regime and produce accelerated electron beam. Since

the injection of electrons into bubble occurs much earlier in the interaction and the dephasing length is shorter at high plasma densities, the maximum energy of the beam is reduced and the quality becomes poor [24].

The effect of laser chirp on FRS and on electron acceleration can be understood as follows. In the standard description of FRS, the growth of laser intensity modulations is caused by local enhancement of axial energy transport (group velocity dispersion) due to plasma wave density perturbations [110]. A linear chirp will be affected by the group velocity dispersion (GVD) in the plasma, which can elongate (for negative chirp) or compress (for positive chirp) the laser pulse, leading to rapid growth, higher accelerating fields, and a more rapid onset of particle trapping. The change in group velocity (v_g) due to the frequency chirp in practical parameters is $\Delta v_g \simeq -c (n_e/n_c)(\Delta\lambda/\lambda)$ [111]. The propagation distance L_{GVD} required for the laser pulse to modulate at the plasma wavelength (which will drive or suppress the FRS growth) due to a linear chirp over a plasma wavelength is $L_{GVD} \simeq c\lambda_p/\Delta v_g$. For a plasma density $n_e \simeq 6.5 \times 10^{19} \text{ cm}^{-3}$ and laser parameters $\lambda = 800 \text{ nm}$ and $\Delta\lambda/\lambda = 2.5\%$, the propagation distance for GVD to enhance or suppress the FRS growth is 4.3 mm (2.8 mm at $8.5 \times 10^{19} \text{ cm}^{-3}$), which is much greater than the growth length for the FRS instability, given by $k_p L_{GVD} \gg w_p/\gamma_{\text{FRS}} = [8(n_c/n_e)]^{1/2}/a_0$, where γ_{FRS} is the growth rate of FRS. This indicates that although the chirp affects the GVD throughout the pulse, the enhanced modulation due to GVD has an insignificant effect on the FRS process.

Both, analytical and PIC simulations have shown that a few percent chirp (as in the present experiment) leads to a change in growth of FRS on the order of a few percent only [111]. However, in addition to the laser pulse duration, the variation in compressor grating separation also affects the pulse shape. Leemans and his co-workers [20, 112] have studied the effect of compressor grating separation on the laser pulse shape. They have shown that an incomplete compensation (by the pulse compressor) of the positively biased non-linear

spectral phases, which arise due to laser pulse propagation in material medium (e.g. the Ti:sapphire crystal), gives rise to pulse shape asymmetry, resulting in fast/slow rising edge when slight positive/negative chirp is introduced. This was further confirmed in a recent experiment by Hafz *et al* [113] using SPIDER setup. The temporal intensity profiles of such pulses can be well fitted to a skewed Gaussian of the form: $I(t) = I_0 \{ [-t^2/(2\tau^2)] [1 + st/(\tau^2 + t^2)^{1/2}]^{-1} \}$, where $|s| < 1$ is the skew parameter which is positive (negative) for fast (slow) rise time and τ is the pulse duration, and I_0 is the peak intensity. The simulations in the self-modulated LWFA regime [20] indicate that a larger wakefield is excited for positive skewed laser pulses, compared to the negative skewed laser pulses. FRS is seeded by the density perturbations which contain frequency components at the plasma frequency. It was observed in the above simulations that the maximum amplitude of the seed decreases with increasing density or pulse duration. This explains less enhancement in charge (25%) at $n_e \simeq 8.5 \pm 0.5 \times 10^{19} \text{ cm}^{-3}$ compared to that (100%) in the case of smaller $n_e \simeq 6.5 \pm 0.5 \times 10^{19} \text{ cm}^{-3}$ observed in our experiment. For slow rise times in the case of negatively chirped laser pulse, the response is weaker and lower amplitude plasma waves ensue. The previous study by Leemans *et al* [20] in the self-modulated LWFA regime has reported enhancement of electron yield by using laser pulse of intensity $> 10^{19} \text{ W/cm}^2$ interacting with plasma density $n_e \simeq 3 \times 10^{19} \text{ cm}^{-3}$. They found that the effect of envelope asymmetry on enhancement of FRS and self-modulation to be more important than that of linear chirp in pulses with symmetric temporal envelopes. The asymmetric dependence of the total electron beam charge on the grating separation observed in the present experiment agrees qualitatively well with that observed by Leemans *et al* [20, 112], although the two experiments differ in laser intensity and plasma density. This similarity indicates qualitatively similar laser pulse shape variation with grating separation in the two experiments.

Chapter 4: Effect of interaction parameters on laser wakefield acceleration

As described in Chapter 3, we have observed generation of very low divergence (< 10 mrad) and quasi-mono-energetic electron beams with energy up to ~ 20 MeV even from laser wakefield acceleration (LWFA) in self-modulated regime, in contrast to earlier observations by others [84]. In addition, it was also shown that introducing small amount of positive chirp could increase the electron beam energy to ~ 30 MeV. In order to further increase the quasi-mono-energetic electron beam energy, it is required to produce the beam at lower plasma density which will provide longer acceleration length (i.e. longer dephasing length). However, self-injection at lower plasma density requires higher initial laser intensity and self-guiding over longer interaction lengths. It is difficult to achieve self-focusing and self-guiding at lower plasma densities. Therefore, pre-formed plasma channels are required to reinforce self-focusing. In addition, the stability could be affected by various laser and target interaction conditions. With an aim to improve the energy and stability of the quasi-mono-energetic electron beam, the effect of various interaction parameters viz. laser pre-pulse and gas medium on laser wakefield acceleration has been investigated to find the optimum laser pre-pulse parameters and target gas medium. In the first half of this Chapter, we present the results of the study on the role of nanosecond duration pre-pulse pedestal in the propagation of 45 fs Ti:sapphire laser pulse and on the laser wakefield acceleration in a helium gas jet. In the second half, we present our studies on laser wakefield acceleration in different gas jet targets viz. helium (He), nitrogen (N_2), and argon (Ar), compare the electron beams produced from above gas jets, and discuss the results.

4.1 Effect of pre-pulse on laser guiding and electron acceleration

The ASE pre-pulse forms a few nanoseconds long, low intensity pedestal to the ultra-high intense main 45 fs laser pulse. Depending on its duration, it may have a significant fraction of the laser pulse energy (unlike the short replica pre-pulse), and can create pre-plasma, as discussed in Chapter 2. A study on the role of ASE pre-pulse on laser propagation and wakefield acceleration in helium gas jet is presented in the following sub-section.

4.1.1 Experimental details

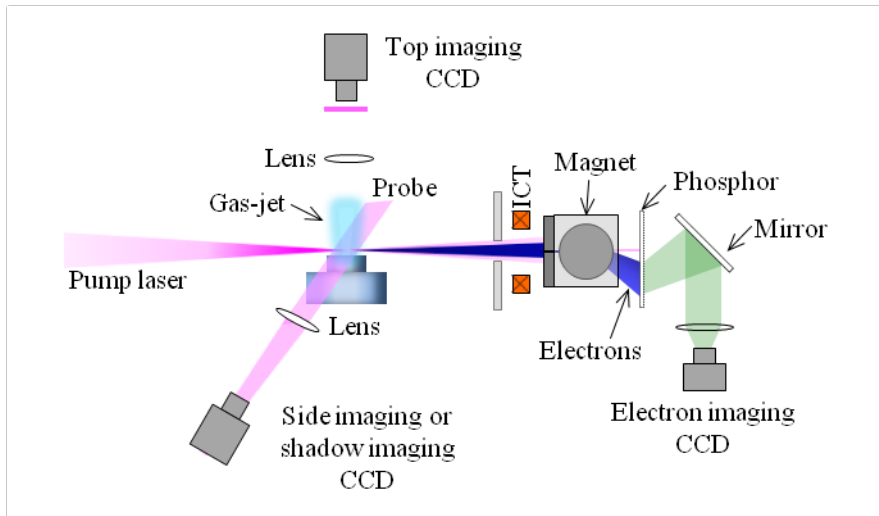


Figure 4.1: A schematic diagram of the experimental setup

The experimental setup used is shown schematically in Fig. 4.1. The 45 fs Ti:sapphire laser pulses were used. The laser beam with energy 320 mJ (after accounting for the losses in beam transport) was focused with a gold coated f/6 off-axis parabolic mirror to a focal spot size $w_0 = 9 \mu\text{m}$. The focal spot contained about 55% of total laser energy, providing a peak power of $\sim 4 \text{ TW}$ and peak intensity $I_0 = 3 \times 10^{18} \text{ W/cm}^2$ on the target. This intensity corresponds to a normalized vector potential $a_0 = 1.2$. While the reduced focal spot increased the peak laser intensity, it reduced the Rayleigh length to about $100 \mu\text{m}$, which is one-third of the Rayleigh length used for the experiment described in Chapter 3. The 45 fs duration main laser pulse was focused at a height of 1 mm above the entrance edge of the 1.2 mm wide

supersonic helium (He) gas jet. The backing pressure of the solenoid valve was varied to change the helium gas atom density (n_{He}) in the gas jet.

The duration of the ASE pre-pulse pedestal was controlled by changing the switching-on time of the 5 ns wide high voltage pulse on the Pockels cell of the pulse cleaner (located after the regenerative amplifier). The typical ASE pre-pulse pedestals for two different switching times of the Pockels cell are shown in Fig. 4.2. The solid trace in the figure is due to the 45 fs duration main laser pulse, while the dashed and dash-dot traces are due to the ASE pre-pulse starting about 3 ns and 1 ns prior to the main pulse, respectively. The ASE pre-pulse duration could not be reduced below ~ 1 ns before the main pulse due to the limit set by the rise time (~ 1 ns) of the high voltage pulse on the Pockels cell. Attempt to further reduce the ASE pre-pulse duration was found to lower the main laser pulse energy. It also leads to large shot-to-shot fluctuation in the laser energy due to the jitter in switching time of Pockels cell. The intensity of the ASE pre-pulse was estimated from the signals shown in Fig. 4.2 to be around $3 \times 10^{12} \text{ W/cm}^2$.

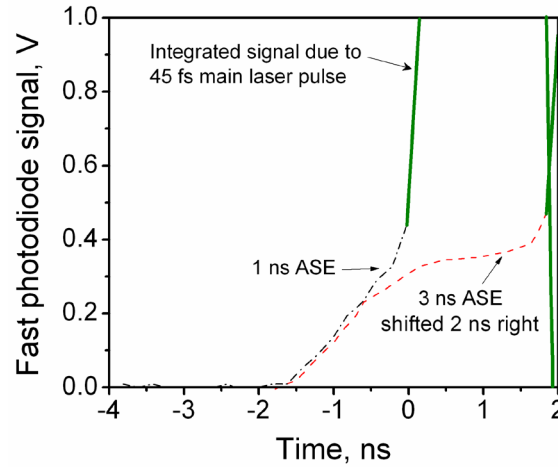


Figure 4.2: Pre-pulse due to amplified spontaneous emission (ASE) measured with a fast photo-diode with 0.8 ns rise time. The dash-dot (black, ~ 1 ns) and the dashed (red, ~ 3 ns) traces correspond to different switching times of the pulse cleaning Pockels cell.

For diagnostics of the interaction region, a part of the main 45 fs duration laser pulse was used as a probe beam (back lighter). The probe beam for shadowgram imaging was

obtained from the leakage of main laser beam through a dielectric coated folding mirror just before the off-axis parabola. The probe beam ($\lambda=800$ nm) was sent through the gas jet in the direction perpendicular to both the propagation of the main laser beam and the gas jet flow, as shown in Fig. 4.1. The probe pulse reaches the gas jet at a fixed negative delay of 2 ns (before) w.r.t. the peak of the main 45 fs duration laser pulse. The shadowgram of pre-plasma formation due to ASE pre-pulse pedestal of the main laser pulse was imaged using the probe beam and a 12-bit CCD camera with a band pass filter for 800 ± 20 nm kept in front of it. Guiding of the main laser beam in the plasma was diagnosed using the Thomson self-scattering of the laser during its propagation in the plasma. Thomson scattering radiation by the plasma, at wavelength 800 nm, in the direction perpendicular to the laser polarization was imaged from the top (top-view imaging) using a 12-bit CCD camera with a band pass filter for 800 ± 20 nm kept in front of it. The non-linear Thomson scattering radiation by the plasma, at second harmonic wavelength (400 nm), in the direction of the laser polarization, was imaged from the side (side-view imaging) using the same 12-bit CCD camera which was used for shadowgram imaging, but with a band pass filter for 400 ± 20 nm kept in front of it in place of band pass filter for 800 ± 20 nm. It should be noted here that the shadowgram images formed by probe beam at $\lambda=800$ nm and laser guiding images due to non-linear Thomson scattering at $\lambda=400$ nm, were recorded in different series of laser shots but under similar experimental conditions. Finally, the electron beam was detected using a DRZ-phosphor screen, and characterized using the integrating current transformer, and the permanent magnet based electron spectrograph. The fluorescent green light from the phosphor screen was collected using a lens which imaged the phosphor screen output on a 16-bit CCD (SBIG make) camera. A vertical rectangular slit made in a combination of thick aluminium and lead plates was mounted in front of the magnet to provide an angular acceptance of 22 mrad and 32 mrad in horizontal and vertical direction respectively. The slit was used to define a

reference axis from which the deflection of the electron beam in the magnetic field was measured. The electrons entering the magnet through the slit were dispersed by the magnet in the horizontal plane (in Fig. 4.1 it is shown vertically, for convenience). The spectral resolution of the electron spectrograph was limited by the divergence of the electron beam and it was typically 6 % at 50 MeV.

4.1.2 Effect of pre-pulse on laser propagation

The nanosecond duration ASE pre-pulse with relatively low intensity but having energy of few mJ, as in the present experiment, can form plasma by cascade ionization and collisional heating mechanism [96, 97]. This is because the threshold intensity for plasma production for a nanosecond duration pulse is much lower than that for a femtosecond duration pulse. For the helium gas density around $3.2 \times 10^{19} \text{ cm}^{-3}$, for which low divergence ($<10 \text{ mrad}$) electron beam was observed during the present experiment, the threshold intensity for cascade ionization by 1 ns duration pulse will be less than the ASE pre-pulse intensity of $\sim 3 \times 10^{12} \text{ W/cm}^2$ [114, 115]. Therefore, the ASE pre-pulse is expected to form pre-plasma before the arrival of main femtosecond laser pulse. Since the probe pulse reaches the gas jet at a fixed time of 2 ns prior to the arrival of main pulse (due to the geometry of our experimental setup), the ASE pre-pulse pedestal duration was increased to $\sim 3 \text{ ns}$ (dashed line in Fig. 4.2) to experimentally verify the formation of pre-plasma by the initial 1 ns long section of this ASE pre-pulse. In this condition, the probe pulse, reaching the target 1 ns after the onset of 3 ns long ASE pre-pulse, probes the plasma produced by the initial 1 ns long section of the ASE pre-pulse of 3 ns full duration. Therefore, the shadowgram image of pre-plasma produced by the probe pulse would be similar to that produced in the case of actual 1 ns duration ASE pre-pulse (dash-dot line in Fig. 4.2). As mentioned in the section 4.1.1, a band pass filter ($800 \pm 20 \text{ nm}$) was kept in front of the side viewing CCD camera for shadowgram imaging using the

probe beam at $\lambda=800$ nm. Since the laser is horizontally polarized, there was no Thomson scattered radiation at wavelength 800 nm along the direction of the probe beam. In addition, the emission at 400 nm (second harmonic) due to non-linear Thomson scattering was blocked by the band pass filter (800 ± 20 nm). This filter also blocks any continuum light emission from the plasma. Under these conditions, we have observed formation of pre-plasma due to the initial 1 ns section of ASE pre-pulse pedestal of ~ 3 ns full duration. The typical shadowgram image of the pre-plasma is shown in Fig. 4.3. When the shadowgram was recorded with the ASE pre-pulse duration of ~ 1 ns (black colour dash-dot trace in Fig. 4.2), it did not show any pre-plasma, confirming that the 45 fs replica pre-pulse present ~ 8 ns ahead of the main laser pulse could not create plasma, as its intensity was much less than the threshold intensity required for plasma formation.

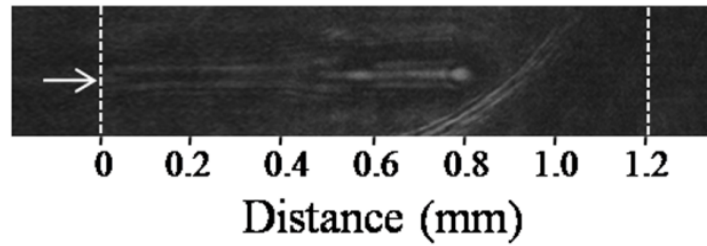


Figure 4.3: Shadowgram of the pre-formed plasma channel produced by 1 ns long section of ASE pre-pulse of intensity 3×10^{12} W/cm². The main laser beam was focused near the entrance edge of the gas jet, which is indicated by the vertical dotted line and the direction of laser propagation is indicated by a horizontal arrow on the left. The density of helium gas was $n_{\text{He}} \sim 3.2 \times 10^{19}$ cm⁻³.

The total length of the pre-plasma formed due to the 1 ns long section of ASE pre-pulse was about 800 μm (see Fig. 4.3). It may also be noticed from the Fig. 4.3 that the initial ~ 500 μm length of the plasma has bright features on either side of the laser axis with a separation ~ 20 μm , which is approximately equal to the diameter of the laser focal spot. These features represent the regions of sharp radial density transitions characteristic of edges of plasma channel. The channel-like structure is produced due to hydrodynamic expansion of the pre-formed plasma in the radial direction from the laser axis [116]. Plasma channel formed by

ASE pre-pulse have been observed (or inferred) in previous experiments under different experimental conditions [114, 115, 117].

To understand the formation of the plasma channel in our experiment, we analyze the plasma channel formation dynamics as follows. Since the origin of ASE pre-pulse is different from that of the main fs duration laser beam, the ASE pre-pulse beam may have different divergence. Giulietti *et al* [115] have measured that the focus of the ASE pre-pulse was 400 μm away from the focus of the main laser pulse. This observation suggests that the ASE beam has a larger divergence compared to the main fs laser beam. Since the laser used in the present experiment is similar to that used by Giulietti *et al*, it is estimated that the focus of the ASE beam should lie about 500 μm away from the entrance edge of the gas jet nozzle (or main laser focus) with our f/6 focusing geometry. In this condition, as described by Ostrovskaya *et al* [97], initially the nanosecond duration pulse (ASE pre-pulse in our experiment) produces plasma at its focus which is about 500 μm away from the entrance edge of the gas jet in the present experiment. Subsequently the layer of gas outside the plasma, although it is transparent to the laser beam, is heated by the plasma radiation. This outside gas close to the plasma lying towards the focusing optics will in turn be ionized to such an extent that it will absorb the laser light. This layer will then be further heated very rapidly and the temperature increases. By this time a new layer of plasma near the laser will have become strongly absorbing, so the boundary of the plasma will move towards the focusing optics (off-axis parabolic mirror in this experiment). The hot plasma thus formed on the laser axis will expand radially, leading to a lower plasma density on the axis and higher density on the periphery. It is well known that hydrodynamic expansion of the pre-formed plasma leads to the formation of plasma density channels of the form, $n_e = n_0 + \Delta n r^2 / w_0^2$, where $\Delta n = n_e(r=w_0) - n_e(r=0)$ is

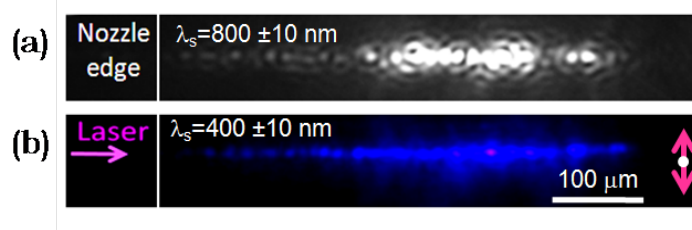


Figure 4.4: Guiding of 45 fs duration 4 TW laser pulse focused to intensity 3×10^{18} W/cm². The images of guiding recorded by (a) top-view CCD, and (b) side-view CCD. The images were recorded at helium gas density $\sim 3.2 \times 10^{19}$ cm⁻³ under the conditions of ASE pre-pulse duration ~ 1 ns and its intensity $\sim 3 \times 10^{12}$ W/cm². The double sided arrow represents the direction of laser polarization.

the channel depth and w_0 is matched spot size. Plasma channel of this parabolic form would reinforce the relativistic self-focusing and reduce the power required for self-focusing [84, 108, 117]. A Gaussian laser beam will be guided in the plasma channel when $\Delta n > \Delta n_c$, where Δn_c (cm⁻³) = $1.13 \times 10^{20} / w_0^2$ (μm). In fact we have observed the guiding of the main laser beam (45 fs) for distance about five times the z_R , as shown in the top-view and side-view images of interaction region (see Fig. 4.4). One can clearly see periodic focusing and defocusing of the laser beam, with period approximately 20 μm, in both the side and top-view images of laser-plasma interaction. This periodic nature of focusing further indicates to the laser beam guiding supported by pre-formed plasma channel. The oscillation period of spot size in pre-formed plasma channel is given by $\lambda_{osc} = \pi z_R (\Delta n_c / \Delta n)^{1/2}$ [84]. The measured oscillation period indicates that the channel depth Δn in our experiment should be around 10^{20} cm⁻³. Due to the channel formation by hydrodynamic expansion of the plasma, the electron density on the axis, $n(0)$ will be lower than 6.4×10^{19} cm⁻³, the value expected due to full ionization of helium gas of density 3.2×10^{19} cm⁻³. Therefore, the plasma density at the edge of the channel ($n_e(r=w_0) = \Delta n + n_e(r=0) \sim \Delta n$) will also be of the order of 10^{20} cm⁻³. It was observed in the experiment by Durfee *et al* [116] that the plasma density on the axis of the channel is typically about 1/5th of density at the edges. Therefore, the on-axis density in the present experiment would be around 2×10^{19} cm⁻³. It should be noted that although the above

estimate provides some insight into the channel structure, more accurate values of the plasma density and the density profile of the plasma channel can be obtained using interferometry.

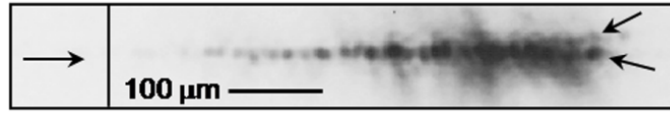


Figure 4.5: Side-view image of 45 fs laser pulse guiding in plasma with channel splitting (as indicated by two arrows) observed in some of the shots. The arrow and a vertical line on the left of the channel image represent direction of laser propagation and the front edge of the gas jet. The images were recorded at helium gas density $\sim 3.2 \times 10^{19} \text{ cm}^{-3}$ under the conditions of ASE pre-pulse duration $\sim 1 \text{ ns}$ and its intensity $\sim 3 \times 10^{12} \text{ W/cm}^2$.

Although typical side-view images of laser guiding (with 1 ns ASE) due to non-linear Thomson scattering are as shown in Fig. 4.4, in some of the laser shots, the images showed splitting of guiding channel into two filaments towards the end of the channel image, as shown in Fig. 4.5. The two channels after splitting are indicated in the figure with arrows. It is interesting to note that the splitting was seen in the side-view images and not in the top-view images. When the polarization of laser beam rotated from horizontal to vertical plane to examine the role of polarization on the channel splitting, it was observed that the plane of channel splitting remains vertical. The splitting in the laser guiding images can be understood on closer examination of the pre-plasma channel structure shown in Fig. 4.3. It can be clearly noticed from this figure that the plasma channel structure splits in to two channels after about $500 \mu\text{m}$ from the entrance edge of the gas jet. Monot *et al* [118] have observed that the location of the channel splitting shifts along the laser axis due to shot-to-shot fluctuation in the energy of the ASE pre-pulse. Therefore, while in most of the shots the main laser beam guiding ends near the location of channel splitting, in some shots, the laser guiding might have extended beyond the region of splitting and resulted in laser propagation in two separate channels. As observed in earlier experiments [104,118], the sharp transverse plasma density

gradient at the focus of the ASE pre-pulse due to the rapid ionization by its initial portion leads to refraction of the remaining portion of the pre-pulse resulting in splitting of the main plasma channel.

When the duration of the ASE pre-pulse was increased to 2 ns, the side-view image of the interaction region occasionally showed diffused images as shown in Fig. 4.6. The image has a feature near the front edge of the gas jet with length 100 μm which is equal to the Rayleigh length of about 100 μm . To compensate the decrease in density on the axis due to larger time of heating and expansion by ASE pre-pulse of 2 ns duration, the gas jet density was increased but this did not have any favourable influence on the guiding. This might be due to efficient absorption of laser light at higher density, resulting in a much hotter plasma. The hotter plasma expands faster and forms broader plasma channel not suitable for stable guiding. The pre-pulse duration could not be reduced below 1 ns without reducing the main laser pulse energy. Nevertheless, when we tried to record the side images, they showed features similar to those observed in the case of ASE of 2 ns duration. These observations suggest that the ASE pre-pulse of 1 ns duration is able to produce plasma channel suitable for guiding.

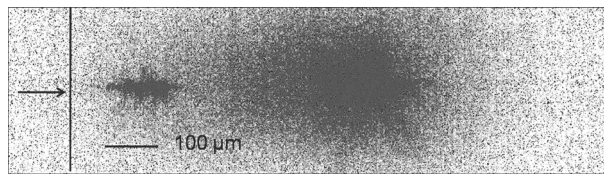


Figure 4.6: The side-view image of plasma due to non-linear Thomson scattering of main 45 fs duration laser pulse at helium gas density of $3.2 \times 10^{19} \text{ cm}^{-3}$ and with ASE pre-pulse duration of $\sim 2 \text{ ns}$ and intensity $3 \times 10^{12} \text{ W/cm}^2$.

Plasma channel formation by the ASE pre-pulse has been investigated earlier by Hosokai *et al* [29]. However, these investigations were carried out at helium gas density of $4 \times 10^{19} \text{ cm}^{-3}$ with tight focused laser beam of intensity $\sim 10^{19} \text{ W/cm}^2$ and ASE pre-pulse intensity $\sim 10^{13} \text{ W/cm}^2$. The main laser pulse intensity and the ASE pre-pulse intensity used in

our experiment were much lower. The observations of our present experiment indicate to different mechanism of plasma channel formation compared to that by Hosokai *et al.* This is mainly due to relatively large f-number focusing and Rayleigh length used here. In a recent experiment, Hosokai *et al* [119] have shown that the plasma channel length can be extended to many times the z_R by applying an external axial magnetic field and controlling the pre-pulse on picoseconds time scale. In these experiments, the picosecond pre-pulse pedestal was controlled by rotating one of the gratings of laser pulse compressor. It will be interesting to investigate the effect of external magnetic field and picoseconds pre-pulses to extend the plasma channel length under our experimental conditions.

4.1.3 Effect of pre-pulse on electron acceleration

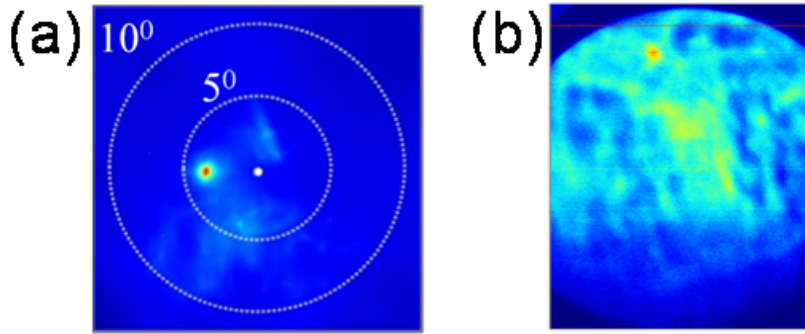


Figure 4.7: Results of the electron beam profile measurement. (a) Image of the low divergence electron beam observed when ASE pre-pulse duration was 1 ns. The concentric circles represent 5° and 10° full cone angles and the common centre of the circles represents the laser axis in vacuum and is shown with white coloured dot. (b) Low intensity and large divergence images of electrons observed occasionally when ASE pre-pulse duration was 2 ns.

Figure 4.7 shows a typical image of well collimated electron beam generated by LWFA in the plasma channel formed by the ASE pre-pulse of duration of ~ 1 ns and helium gas density $n_{He} \sim 3.2 \times 10^{19} \text{ cm}^{-3}$. The dot (white colour) at the centre of the Fig. 4.7a indicates the location of the laser axis in vacuum, and the two concentric circles represent full cone angles of 5° and 10° . As seen from Fig. 4.7a, the electron beam was produced off-axis from the laser in most of the shots and its location varied from shot-to-shot unlike the observations reported

earlier [120]. It may also be noticed from the Fig. 4.7a that there is a less intense background halo, in comparison to the electron beams shown in Chapter 3, in the form of spatially dispersed low energy electrons, which is a characteristic feature of low divergence electron beam produced from low density plasma. The divergence of the electron beam was observed to be within 3 – 6 mrad (FWHM) opening angle. The charge contained in the accelerated electron beam was typically few tens of pC and in some shots, charge of about 100 pC was measured. When the ASE pre-pulse duration was increased to 2 ns, the electron beam formation became unstable and occasionally, a low intensity image of electrons, as shown in Fig. 4.7b, was observed on the DRZ-phosphor screen. The contrast of the image in Fig 4.7b has been increased for visual clarity. An image of this nature was observed only when the side image as shown in Fig. 4.6 was observed. No image was observed on the DRZ phosphor screen for ASE pre-pulse duration of 3 ns. The radiation dose produced as a result of the electron beam striking the interaction chamber walls was measured using an ionization chamber based radiation survey meter. The measurement showed high dose only in the case ASE pre-pulse of 1 ns duration for which a collimated electron beam was produced, indicating that the electron beam is of high energy. The generation of low divergence electron beam was found to have strong correlation with the laser guiding seen in the side-view and top-view images. A well collimated beam was observed even with the laser channel splitting seen in the side-view images as shown in Fig. 4.5. The pointing of the electron beam was observed to vary from shot-to-shot. The images of electron beam recorded in a typical series of laser shots are shown in Fig. 4.8a. A plot showing the pointing variation of the electron beam is shown in Fig. 4.8b. The average pointing of the electron beam is shown with symbol ‘ \otimes ’ in Fig. 4.8b. The standard deviation of electron beam pointing was estimated to be ± 25 mrad and ± 38 mrad in horizontal and vertical direction respectively. The pointing

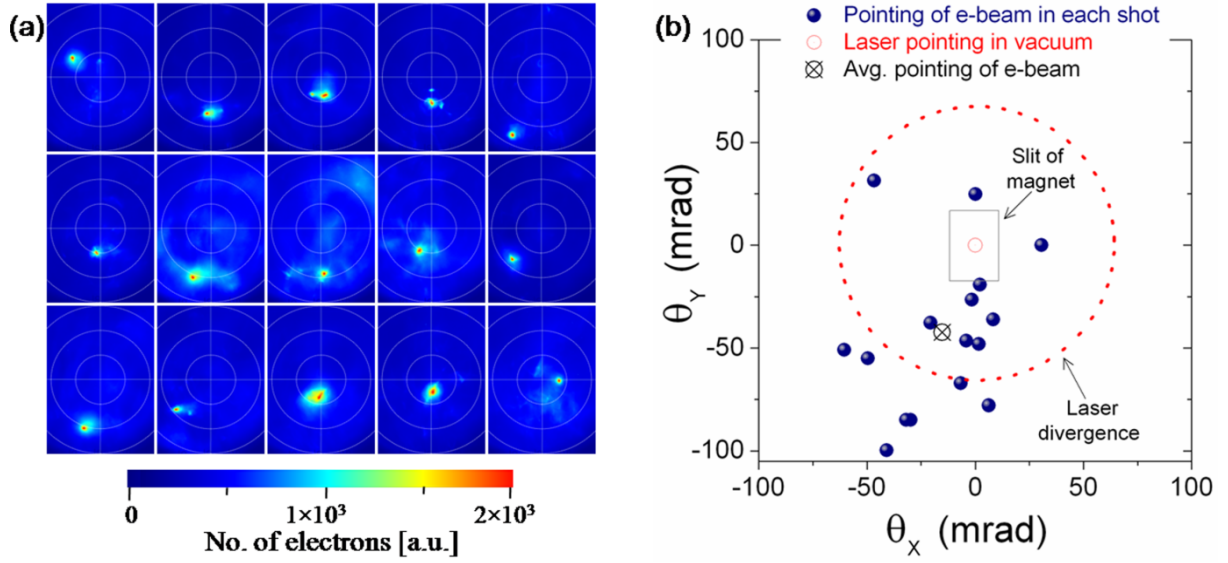


Figure 4.8: Measurement of pointing variation of the electron beam produced in a series of laser shots. a) Images of the low divergence electron beam. The concentric circles in each image represent 5° , 10° , and 15° full cone angles and the common centre of the circles represents the laser axis in vacuum. b) Plot of pointing variation of well collimated electron beam. The dotted circle (red) represents laser divergence (in vacuum) cone angle with its centre at laser axis. The rectangle at the centre represents the acceptance angle of the electron energy spectrometer. The average pointing angle of the electron beam is shown with symbol ‘ \otimes ’

variation was much larger than the pointing variation of the laser beam in vacuum (i.e. without gas jet). However, most of the laser shots were found to produce electron beam within the cone angle of the laser beam in vacuum as shown in Fig. 4.8b. The pointing fluctuations of the electron beam may be due to the betatron oscillations of the electron beam in the plasma channel [90]. The oscillation phase at the exit of the plasma channel perhaps determines the pointing of the electron beam. The change in phase at the exit will be determined by the pre-plasma and it changes from shot-to-shot due to the variation in the ASE pre-pulse parameters, as observed in this experiment. However, the use of ASE pre-pulse with controlled intensity and duration or applying static axial magnetic field may result in improvement in the pointing stability [119, 120].

In the case of ASE pre-pulse of 1 ns duration, the energy measurement of the electron beam showed quasi-mono-energetic distribution with peak energy in excess of 20 MeV and

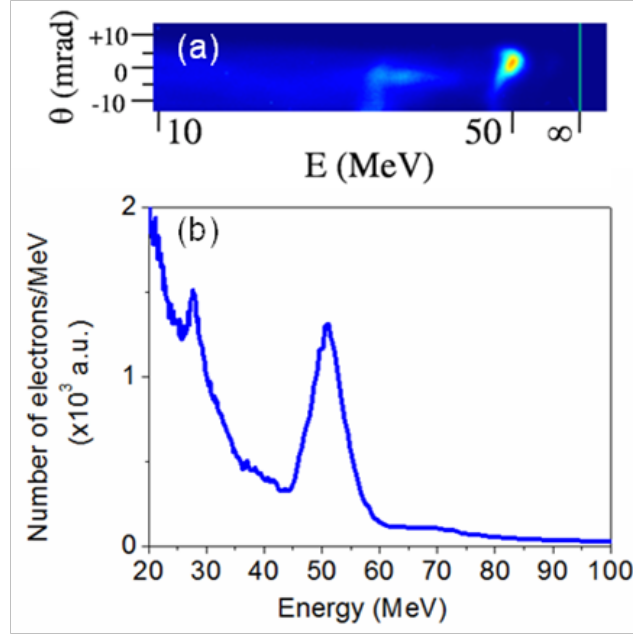


Figure 4.9: Result of energy measurement of the accelerated electron beam. a) Image of the energy dispersed electron beam showing low divergence and quasi-mono-energetic feature, and b) energy spectrum with quasi-mono-energetic distribution with peak at 50 MeV.

maximum up to 50 MeV. The observed variation of the electron energy may also be caused partly by the uncertainty in the energy measurement due to the finite width of the slit. We have estimated the energy with the assumption that the electron beam enters the magnetic field along the slit edge on the lower energy side of energy dispersion. Therefore the quoted energy figures are the lower limits and actual energy could be larger than these values. The angular dimensions of the slit are indicated in Fig. 4.8b with a rectangle (grey colour) centred on the laser axis. An image of the energy dispersed high energy electron beam is shown in Fig. 4.9a, and the corresponding electron energy spectrum is shown in Fig. 4.9b. In the case of ASE pre-pulse duration of 2 ns or more, the energy spectrum measurement did not show any features on DRZ-phosphor screen. This indicates that the large divergence electron beam shown in Fig. 4.8b contains electrons with energy less than the lower detection limit (10 MeV) of the electron spectrometer. The plasma channel formation by the 1 ns duration ASE pre-pulse explains the production of high energy electron beam. It was shown in earlier studies that the matching of laser-plasma interaction length with the dephasing length ($L_D \approx$

$\lambda_p \gamma_\phi^2$, where λ_p is plasma wavelength) is important for production of quasi-mono-energetic electron beam from laser-driven electron acceleration [23, 24]. Therefore, assuming that the dephasing length in our experiment is approximately equal to the laser-plasma interaction length, which is 500 μm in our case, the plasma density in the channel is expected to be around $2.5 \times 10^{19} \text{ cm}^{-3}$, which is close to the value predicted from laser spot-size oscillation period. The maximum energy ($W_{\text{max}} \approx 2\gamma_\phi^2 m_o c^2$, where $\gamma_\phi^2 = n_o/n_e$) corresponding to the density $2.5 \times 10^{19} \text{ cm}^{-3}$ is about 70 MeV. The maximum energy measured in the experiment is close to this value. It is however common to have energies either above or below this simple estimate due to competing effects. For example, nonlinear increase in the plasma wavelength, the accelerating field, and the dephasing length can increase the acceleration length while laser diffraction or depletion can reduce the acceleration length. Nevertheless, this simple estimate suggests that the plasma channel formation by the 1 ns duration ASE pre-pulse provides favourable conditions for both guiding of the main laser beam and for generation of quasi-mono-energetic electron beam of high energy. When we increased the laser pulse duration slightly, either by introducing positive or negative chirp, the electron beam disappeared. This indicates that the electron acceleration is very sensitive to the pulse duration in this regime. In the experimental results at higher plasma density (with the condition $c\tau_L \gg \lambda_p$) presented in Chapter 3, enhancement in the accelerated electron charge was observed when the pulse duration was increased by introducing positive chirp, which is one of the indications for electron acceleration in the self-modulated regime [111]. With the above simple estimate of upper limit on the electron density $\sim 2.5 \times 10^{19} \text{ cm}^{-3}$ in the pre-formed plasma channel in the present experiment, the laser pulse length $c\tau_L \leq 2\lambda_p$ and therefore electron acceleration in the self-modulation regime is unlikely. Under this condition, however, electron acceleration in bubble regime is possible [121].

4.1.4 Discussion

Giulietti *et al* [115] have observed pre-plasma channel formation in helium gas jet at a density around 10^{19} cm^{-3} due to 1 ns duration ASE pre-pulse of intensity $2 \times 10^{12} \text{ W/cm}^2$. They have also shown that the pre-plasma channel helps to guide the 60 fs laser pulse of intensity $3 \times 10^{18} \text{ W/cm}^2$. In the present experiment, in addition to the guiding of 45 fs laser beam at intensity $3 \times 10^{18} \text{ W/cm}^2$ in the pre-formed plasma channel generated by 1 ns duration ASE pre-pulse, we have also shown generation of collimated high energy electrons with quasi-mono-energetic distribution at optimal helium gas density of $3.2 \times 10^{19} \text{ cm}^{-3}$. The earlier study by Hosokai *et al* [29] had also shown guiding of the laser pulse ($I_L \sim 1 \times 10^{19} \text{ W/cm}^2$) in the plasma cavity generated by the ASE pre-pulse pedestal of intensity 10^{13} W/cm^2 . Generation of quasi-mono-energetic electron beam of $\sim 10 \text{ MeV}$ was also observed at plasma density of $8 \times 10^{19} \text{ cm}^{-3}$ in these experiments when the fs laser pulse traversed the plasma density transition, produced in the path of laser beam by hydrodynamic shock formation by the ASE pre-pulse. They have also observed strong plasma emission in the side-view images at the point of density transition. In the present experiment, however, sharp density gradient along the laser axis within the $500 \mu\text{m}$ long guiding channel or strong localized emission in the side-view image of laser guiding was not observed. Therefore, it is clear that the injection of electrons in our conditions is not induced by density transition. The electrons could be accelerated to much higher energy in our case perhaps due to lower plasma density in the channel compared to Ref. 34. A more recent work by Hosokai *et al* [119] showed generation of $\sim 100 \text{ MeV}$ quasi-mono-energetic electron beams using moderate power (7 TW) tightly focused laser beam in helium gas jet with the static magnetic field. They attributed the energy boosting to the long narrow plasma channel produced by combination of pre-pulses on nanosecond and picosecond time scales. In light of this, it will be encouraging to study the combined effect of external magnetic field and picoseconds pedestal on the stability and

maximum energy of the accelerated electron beam in our experimental conditions. Mangles *et al* [120] have shown strong dependence of the stability of the laser-driven acceleration on ASE pre-pulse. However, these experiments were done at a lower plasma density compared to our experiment reported here. They showed that a laser with a low level of ASE pre-pulse produces more stable beams. They also inferred that a high level of the ASE pre-pulse reduces the stability. However, they did not observe any pre-formed plasma even for high level of ASE pre-pulse and attributed the poor stability at lower ASE contrast to the ionization instability. In a recent experiment, Mori *et al* [114] observed that with the same parameters of laser, the interaction length in case of high-Z argon gas jet was larger than that in helium gas. They have inferred that the ASE pre-pulse was able to form pre-plasma channel in the case of argon gas and it led to stable laser guiding over longer interaction length and production of electron beam with lower energy of about 9 MeV but with higher stability in energy and beam pointing. The low energy of the electrons was attributed to the higher density plasma produced in the case of argon gas jet. Since the ASE pre-pulse in our case was able to produce pre-plasma channel of apparently lower density in helium gas, we could achieve high energy. However, large pointing variation of electron beam in our case may partly be attributed to the shot-to-shot variation in the ASE pre-pulse level due to significant jitter (\sim few 100 ps) in the Pockels cell switching, which in the case of Mori *et al* [114] was about 14 ps. Therefore, stable ASE pre-pulse is expected to stabilize the performance of the laser guiding and production of high energy electron beam.

4.2 Effect of gas medium on laser wakefield acceleration

Mostly, low-Z gas like helium has been used for laser wakefield acceleration experiments. The laser pulses with intensity $> 10^{18}$ W/cm² employed for these experiments ionize the helium completely at its pedestal intensity of about 10^{16} W/cm² through over-the-barrier ionization (OBI). Therefore the intense portion of the laser pulse essentially interacts

with the helium plasma and excites plasma waves, and the interaction process becomes simpler. However, use of high-Z gases makes the process little complex and interesting in terms of theoretical understanding and experimental optimizations. The higher-Z gases continue to ionize till the peak of the laser pulse and the ionization dynamics can affect the smooth laser self-focussing and electron acceleration in these gas jet plasmas. In the following sub-sections, we present a comparative study of three gases viz. helium (He), nitrogen (N₂), and argon (Ar) on self-guiding and laser wakefield acceleration.

4.2.1 Experimental details

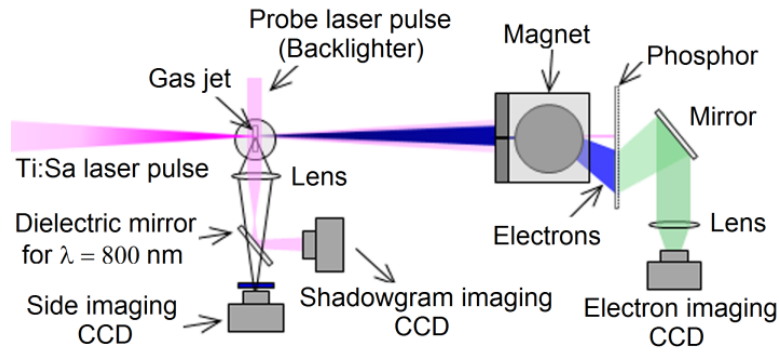


Figure 4.10: A schematic diagram of the experimental setup.

A schematic diagram of the experimental setup is shown in Fig. 4.10. During this experiment, the Ti:sapphire laser beam was focused using an f/5 off-axis parabola. The full width at $1/e^2$ maximum size of the focal spot was $27 \mu\text{m} \times 15 \mu\text{m}$, and was approximated with an equivalent area circular spot of $1/e^2$ width, $2w_0 = 20 \mu\text{m}$ to estimate the peak intensity. The peak power of the laser pulse on the target was $P_L = 3$ TW considering $E_L = 145$ mJ contained in the focal spot and assuming a Gaussian temporal profile (which is close to the sech^2 pulse shape of an ultra-short pulse). The peak intensity in the focal spot was estimated to be $I_L = 2 \times 10^{18} \text{ W/cm}^2$ ($a_0 \approx 1$). Three different gases viz. helium (He), nitrogen (N₂), and argon (Ar) were investigated in the experiment. Backing pressure of the gas jet was varied to take care of the different atomic number densities of He and Ar and molecular density of N₂ gas. From the

known density data of He, N₂, and estimated density of Ar, the corresponding plasma densities were determined by considering OBI of the three gases to He²⁺, N⁵⁺, and Ar¹⁰⁺ for the laser intensity used. Further ionization to N⁶⁺, and Ar¹¹⁺ requires laser intensity 1×10^{19} W/cm² and 2.8×10^{18} W/cm² respectively which is less than the initial laser intensity used. For measuring the electron energy spectrum, the same electron spectrograph described earlier in section 4.1.1 was used. A small fraction of the drive laser beam, with variable delay relative to the main laser beam, was used as a probe beam (back-lighter) to record the shadowgram images of the interaction region with 2 ps time resolution. A multilayered dielectric mirror, with high reflectivity at 800 nm radiation, was placed in front of the side imaging CCD camera to reflect the probe beam onto a separate 12-bit CCD camera, while allowing the 400 nm radiation to reach the side imaging CCD camera for side imaging from non-linear Thomson scattered radiation at 2ω , as shown in Fig.4.10. A narrow band-pass filter that allows the wavelengths within 800 ± 20 nm was kept in front of the shadowgram imaging CCD camera.

4.2.2 Comparison of electron beams from He, N₂, and Ar

After scanning the gas jet backing pressure and fine tuning the laser focus position w.r.to the front edge of the gas jet, accelerated electrons with less charge and large divergence having diffused profile were observed for plasma densities $n_e \geq 3.6 \times 10^{19}$ cm⁻³ in He, $\geq 2 \times 10^{19}$ cm⁻³ in N₂, and $\geq 1.3 \times 10^{20}$ cm⁻³ in Ar. When the plasma density increased from the corresponding threshold densities, highly stable and well collimated electron beams with divergence of the order of 10 mrad were observed at plasma density $n_e \approx 5.8 \times 10^{19}$ cm⁻³ in He and $\approx 3.0 \times 10^{19}$ cm⁻³ in N₂. In comparison, the acceleration was highly unstable in Ar gas jet and a well-defined electron beam with relatively higher divergence (~ 40 mrad) was observed occasionally at an estimated plasma density 3.0×10^{20} cm⁻³. The images of typical good quality

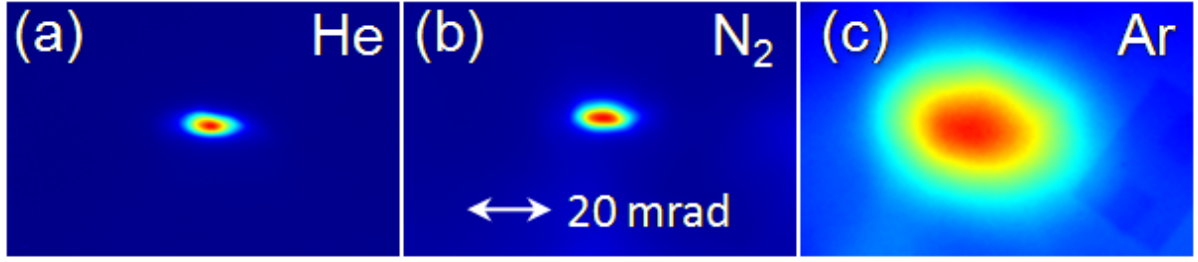


Figure 4.11: *Electron beam profiles observed from 3 different gases He, N₂ and Ar at electron density of $5.8 \times 10^{19} \text{ cm}^{-3}$, $3.0 \times 10^{19} \text{ cm}^{-3}$, and $3.0 \times 10^{20} \text{ cm}^{-3}$ respectively.*

electron beams observed in three gas targets are shown in Fig. 4.11. It should be noted from Fig. 4.11 that the electron beams produced from helium have virtually no background halo, in contrast to the well collimated electron beams presented earlier in this thesis, and also in most of the earlier experiments by other groups, particularly at high plasma density ($> 2 \times 10^{19} \text{ cm}^{-3}$) [84]. There is a very feeble halo of back ground electrons in the case of N₂ and significant background halo in the case of Ar. When the plasma density was increased beyond $5.8 \times 10^{19} \text{ cm}^{-3}$ in He, collimated electron beam with high spatial contrast was still present, but the divergence increased with density, as shown in Fig. 4.12. Similar behaviour in divergence was also observed in N₂ when the plasma density was increased beyond $3 \times 10^{19} \text{ cm}^{-3}$. However, when the density was increased in the case of Ar, the collimated beam shown in Fig. 4.11 disappears and highly divergent electrons with no distinct collimated feature in the profile were observed.

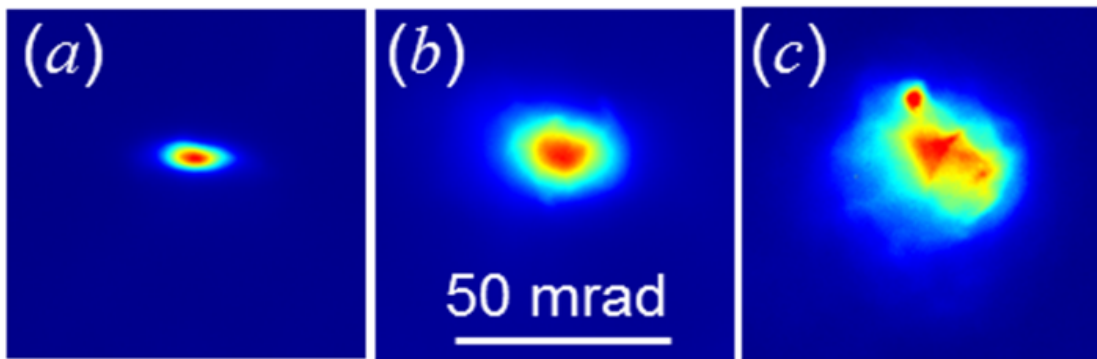


Figure 4.12: *Images of electron beam profiles observed from helium gas jet at plasma density around $5.8 \times 10^{19} \text{ cm}^{-3}$, $6.8 \times 10^{19} \text{ cm}^{-3}$, and $8.6 \times 10^{19} \text{ cm}^{-3}$ respectively.*

The low divergence electron beams from He and N₂ gases, shown in Fig. 4.11, were highly reproducible with > 90 % probability, in a series of about 10 – 20 shots during most of the experimental runs. As seen in Fig. 4.11, the transverse profiles of the electron beams were elliptical in shape with major axis along the horizontal direction, which was the direction of laser polarization. The mean ellipticity (defined here as the ratio of the length of major axis to minor axis) of the electron beam was estimated to be $\varepsilon = 1.9$ in the case of He and N₂ while it was 1.2 in the case of Ar. The mean FWHM divergence of the electron beams produced from He, N₂, and Ar was $\Delta\theta_x = 13.1$ mrad, 14.5 mrad, and 40.6 mrad, respectively. The pointing variation of the best quality electron beams from the three gases is shown in Fig. 4.13. The reproducibility and pointing variation of the electron beam were observed to degrade with increasing plasma density. The images of the energy spectra of the well collimated electron beams observed from He and N₂ gas at $n_e \simeq 5.8 \times 10^{19} \text{ cm}^{-3}$ and $3.0 \times 10^{19} \text{ cm}^{-3}$ respectively in a series of shots during one of the experimental runs is shown in Fig. 4.14. We observed a spectral feature showing electrons with little higher than 10 MeV energy only once in few series of 10 – 20 shots during our investigation in Ar gas jet at plasma density of $3.0 \times 10^{20} \text{ cm}^{-3}$. This could be due to low energy < 10 MeV (low energy cut-off of the spectrograph) of accelerated electrons produced in most of the shots.

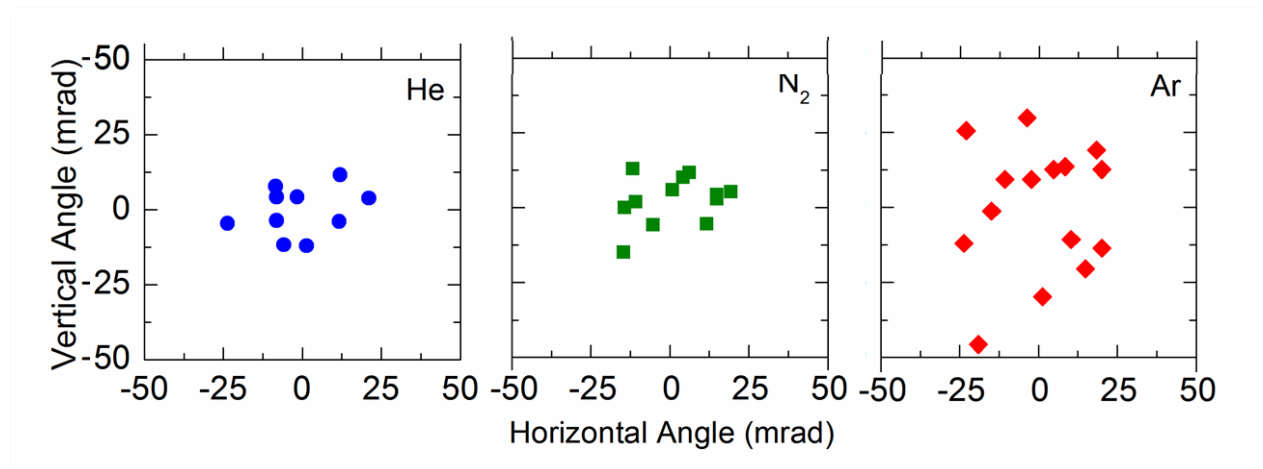


Figure 4.13: Pointing variation of electron beams produced from He, N₂ and Ar at plasma density $5.8 \times 10^{19} \text{ cm}^{-3}$, $3.0 \times 10^{19} \text{ cm}^{-3}$, and $3.0 \times 10^{20} \text{ cm}^{-3}$ respectively.

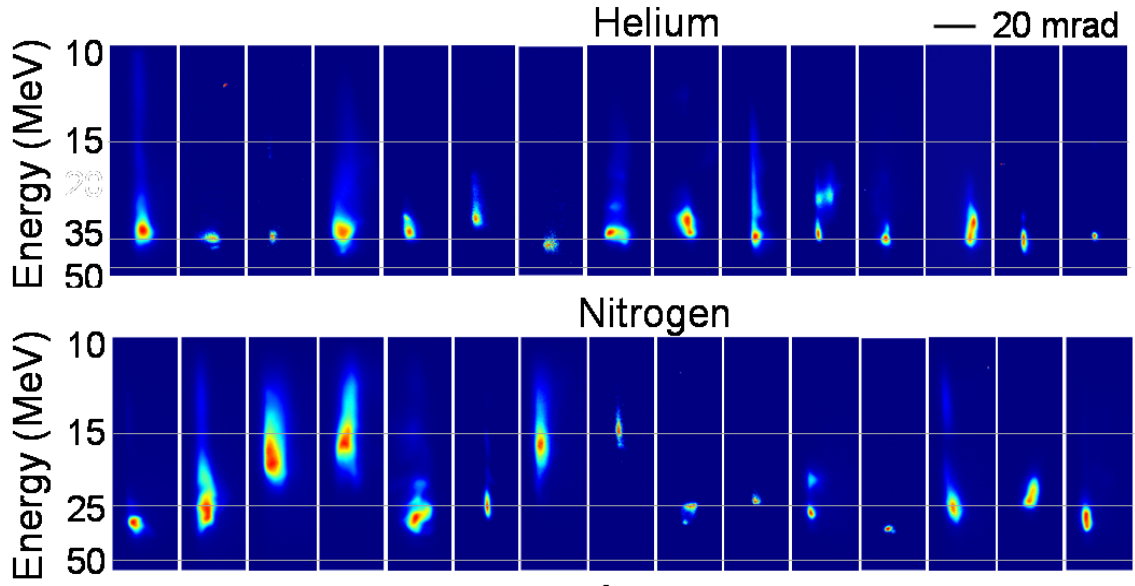


Figure 4.14: Images of energy spectra of the electron beams produced from He and N₂ plasma density $5.8 \times 10^{19} \text{ cm}^{-3}$ and $3.0 \times 10^{19} \text{ cm}^{-3}$ respectively.

Gas	Plasma density ($\times 10^{19} \text{ cm}^{-3}$)	<Divergence> (mrad) $\theta_H \times \theta_V$	<Pointing> (mrad) $\Delta\theta_H \times \Delta\theta_V$	<Energy> (MeV) E_{peak}	<Energy Spread > (%) $\Delta E/E_{\text{peak}}$	<Charge> (pC) Q
He	5.8	$13.1^{+4.6}_{-2.0} \times 7.2^{+2.8}_{-0.7}$	12.3×7.6	$35.6^{+3.9}_{-2.5}$	$29.02^{+9.6}_{-11.2}$	$3.8^{+2.8}_{-1.2}$
N ₂	3	$14.5^{+5.3}_{-4.1} \times 8.0^{+2.0}_{-2.3}$	11.9×8.1	$25.5^{+5.3}_{-7.9}$	$28.3^{+13.7}_{-13.4}$	$27.9^{+38.0}_{-7.6}$
Ar	30	$40.6^{+10.1}_{-8.8} \times 34.1^{+8.4}_{-5.1}$	15.0×20.7	< 10 MeV	--	$41.8^{+39.3}_{-22.8}$

Table 4.1: Summary of the electron beams produced from the three gases He, N₂ and Ar.

The Table 4.1 summarises the parameters of the best quality electron beams observed from He, N₂ and Ar. The errors shown are the root-mean-square (RMS) deviations from the mean value. To account for the asymmetric distributions, the RMS value was independently calculated for the occurrences with higher-than-average and lower-than-average values. Good shot-to-shot stability was observed in the central energy (energy at the peak charge density) of the electron bunch produced from He and N₂. In fact, the stability in the beam parameters was

better in He compared to N₂. While the peak energy (E_{peak}) of the quasi-mono-energetic beam was slightly higher in the case of He compared to N₂, the beam charge was about a factor of 10 less in the case of He. Majority of the spectra showed virtually background-free, quasi-mono-energetic peak for both He and N₂. A typical line-out of the electron spectrum is shown in Fig. 4.15. There will be some uncertainty due to the pointing variation of the electron beam in the dispersion plane. Since the acceptance angle (8 mrad) of the slit in front of the spectrograph was smaller than the pointing variation of the beam in the dispersion plane, actual value of the uncertainty is decided by the acceptance angle of the spectrograph. In addition, the maximum angular dimension of the beam on the phosphor screen in the case of mono-energetic electrons would be ~ 8 mrad. This finite size of the beam in the dispersion plane causes an apparent energy spread of 26.7 % about the mean peak energy in the case of He and 20.3% in the case of N₂. This energy spread due to finite size of the beam on phosphor is very close to the measured mean energy spread in the case of He while it is smaller in the case of N₂. This suggests that the energy spread in the case of He is limited by the resolution of the spectrograph and it is not so in the case of N₂.

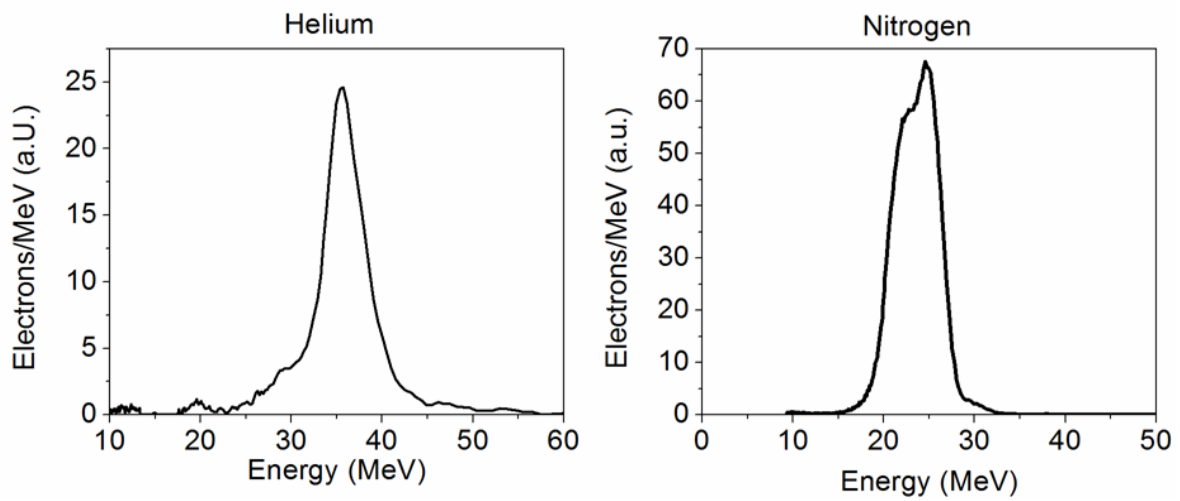


Figure 4.15: The line out profiles of energy spectra of the electron beams produced from He and N₂ at plasma density $5.8 \times 10^{19} \text{ cm}^{-3}$ and $3.0 \times 10^{19} \text{ cm}^{-3}$ respectively.

The shadowgram images recorded at about 2 ps before the arrival of the driver laser pulse showed no pre-plasma in the case of He and N₂ gas jet. This indicates that the intensity of the pre-pulse pedestal due to amplified spontaneous emission (ASE) in front of the femtosecond laser pulse was below the ionization threshold for He and N₂. Simultaneous measurement of nonlinear Thomson side-scattering images showed smooth and stable self-guiding channels with length about 490 μm and 440 μm in He and N₂, respectively. The ASE created pre-plasma channel was observed in the case of Ar which assisted laser guiding over longer interaction lengths of 600 – 700 μm observed in the side images.

4.2.3 Discussion

The high quality electron beam observed from He and N₂ in the present experiment strongly suggests laser wakefield acceleration in the blowout regime. In what follows, we explain the physics of electron acceleration in He gas target. In the bubble regime, transverse self-injection of electrons into the 3D wakefield occurs for $a_0 \gtrsim 3$, and these electrons get accelerated and achieve an energy gain $\{W_{gain} = (2/3) (n_c/n_e) a_0 m_o c^2\}$ limited by the dephasing length [27]. For the plasma density $n_e \gtrsim 3.6 \times 10^{19} \text{ cm}^{-3}$ in the case of He (where self-injected electrons with large divergence electrons, less charge, and diffused profile were observed) relativistic self-focusing was observed, as expected, since $P_L/P_c \gtrsim 3.7$, where $P_c(\text{GW}) \simeq 17(n_c/n_e)$ is the critical power for self-focusing [85]. For the above density range, the plasma wavelength $\lambda_p(\mu\text{m}) \simeq 10.5 \times n_e^{-0.5} (\times 10^{19} \text{ cm}^{-3}) \lesssim 5.5 \mu\text{m}$ is smaller than the laser pulse length ($c\tau_L = 13.5 \mu\text{m}$) and the focal spot ($w_0 = 10 \mu\text{m}$) by a factor $\gtrsim 2.5$ and $\gtrsim 1.8$ respectively. Although the initial laser pulse parameters do not satisfy the conditions for matched spot ($w_0 \simeq \lambda_p$ and $c\tau_L \simeq \lambda_p/2$) and self-injection ($a_0 \gtrsim 3$) immediately upon entry in to the plasma, all the above parameters evolve nonlinearly over some initial interaction length in the plasma through self-focusing and self-compression of the laser pulse due to refractive

index gradients of the plasma wave, eventually leading to the self-injection of electrons [23, 122]. The self-evolution of the laser pulse in the present condition is expected to be different from the self-modulation phenomenon explained in the Chapter 3, as the ratio of the initial laser focal spot to the pulse length is 50% lower and the intensity is higher in the current experimental regime. Therefore, three dimensional effects are more possible in the present case. If one assumes that the compressed beam waist tends towards λ_p , and the compressed pulse length towards $\lambda_p/2$, an expression $a_{0,eff} = 6.55 \times 10^{-6} \cdot \sqrt{\frac{n_e}{n_c} \cdot \frac{E_L(J)}{\tau_L(s)}}$ for effective a_o can be obtained from the relation $\frac{P_L}{P_C} \simeq \frac{\pi^2}{8} a_0^2 \frac{w_0^2}{\lambda_p^2}$. For $n_e \sim 3.6 \times 10^{19} \text{ cm}^{-3}$, $\tau_0 = \lambda_p/2c$ and $E_L = 145 \text{ mJ}$, one gets $a_{0,eff} \simeq 3.8$, which agrees well with the findings of self-injection threshold in earlier experiments, theory, and 3D PIC simulations [23, 27, 122]. The low charge just near the threshold density could be due to relatively slow evolution at lower density, which results in the matched conditions being reached close to the end of the interaction length. This would result in onset of self-injection close to the end of the interaction length, leading to production of low energy and low charge electrons due to the small acceleration length available. However, at a higher density of $5.8 \times 10^{19} \text{ cm}^{-3}$, the pulse evolution could be sufficiently fast so that the self-injection occurs well before the end of the interaction length, providing sufficient length for generation of high energy quasi-mono-energetic electron beam. The energy expected according to the expression for W_{gain} at $5.8 \times 10^{19} \text{ cm}^{-3}$ is 54 MeV, considering matched $a_{0,eff} \simeq 5.4$ estimated for this density. The measured energy $35.6_{-2.5}^{+3.9} \text{ MeV}$ is reasonably close to the expected value, considering that the energy expression is based on simple assumptions. The predicted value might be on the higher side due to a slightly higher value of $a_{0,eff}$ estimated based on the assumption that all of the energy is trapped and compressed, which is less likely at high plasma density and also due to reduced coupling of

the laser energy to the bubble due to non-ideal focal spot [123]. The difference may also arise when the length of acceleration from the point of self-injection is shorter than the dephasing length. Generation of quasi-mono-energetic electron beams with virtually no low energy background may be attributed to the self-injection just above the threshold condition, which ensures termination of the self-injection process very quickly. The near-threshold condition was confirmed from the observation that the decrease in plasma density by about 10% from $5.8 \times 10^{19} \text{ cm}^{-3}$ resulted in reduction of the electron beam charge and reproducibility significantly. Although the near-threshold operation of the accelerator limits the beam charge to a relatively lower value, it significantly improves the electron beam quality due to negligible beam loading effect [123]. The measured charge of few pC is much smaller compared to the charge $\sim 100 \text{ pC}$ predicted by the scaling laws of blowout regime, based on the beam loading effect [27]. This further supports the idea that the self-injection is limited by near-threshold injection process but not by the beam loading effect. The observed ellipticity of the electron beam may be attributed to the interaction of injected electrons with the transverse laser electric field, resulting in momentum gain along the horizontal / polarization direction [124]. The stronger transverse focusing force of the bubble at higher plasma densities could make the defocusing force due to the laser field less significant at higher plasma density, which would perhaps explain the ellipticity of the electron beam observed in the present experiment.

The results from the N_2 gas can also be understood from the above arguments with the inclusion of the effect of ionization induced injection. The lower threshold density for electron self-injection in the case of N_2 is due to OBI of N^{5+} . Although the initial laser intensity is not sufficient, the laser pulse evolution through self-focusing and self-compression over the initial interaction length in the plasma may enhance the laser intensity to $> 1 \times 10^{19} \text{ W/cm}^2$ ($a_0 > 2.2$) required for OBI of N^{5+} . This could happen before the laser pulse intensity

(or a_0) reaches the threshold for transverse self-injection by trajectory crossing at vertex of the “bubble”. The lesser mean peak energy of 25.5 MeV could be due to the beam loading effect caused by higher beam charge observed in the case of N_2 . The larger relative energy spread could also be due to injection by OBI which happens for longer duration. In the case of Ar, the ionization up to Ar^{10+} takes place continuously up to the peak of the laser pulse as it enters the gas jet. More importantly, large gradients in refractive index occur due to radial intensity variation of the laser which causes ionization defocusing. The ionization defocusing plays a critical role in the laser beam propagation. Although $P_L > P_c$, it may not be sufficient to overcome the defocusing effect due to ionization induced defocusing. Therefore, the ASE pre-pulse formed plasma channels are required to guide the laser pulse in Ar gas jet target as observed in the experiment. Appropriate pre-formed channels are formed at estimated gas density of $\sim 3 \times 10^{19} \text{ cm}^{-3}$ (plasma density of $\sim 3 \times 10^{20} \text{ cm}^{-3}$) for 1 ns duration ASE pre-pulse and well-defined electron beam with larger divergence was observed occasionally. The unstable behavior of the electron beam could be due to instabilities associated with the interaction at high plasma density. Formation of clusters can also be an important factor in Ar gas jet which needs to be further investigated. While the long channels in Ar gas jet are interesting for further studies, it is evident that the argon gas jet is not suitable for laser wakefield acceleration for the parameter regime of our experiment.

Self-injection based stable quasi-mono-energetic electron beam generation was earlier reported at $n_e = 5 \times 10^{19} \text{ cm}^{-3}$ using He in the regime $c\tau_L \simeq 2\lambda_p$ at 10 times higher power [125] compared to that in the present experiment. However, the beam was reported to have background halo, in contrast to the observation in the present experiment. A background-free, quasi-mono-energetic electron beam with peak energy $\lesssim 25 \text{ MeV}$ was reported in a previous experiment at $n_e = 2 \times 10^{19} \text{ cm}^{-3}$ in the regime $c\tau_L < \lambda_p/2$ using 8 fs laser pulses of $\sim 5 \text{ TW}$ power [126]. However, the stability of the beam was not discussed. One important aspect of

this experiment was that the interaction length was only about 100 μm , as the pulse did not require much evolution before triggering self-injection. In the present experiment, however, few hundred micron interaction length, combined with the high density, perhaps facilitated sufficient pulse evolution, eventually leading to the self-injection and acceleration in the bubble regime. Quasi-mono-energetic beams at lower energy ~ 20 MeV (presented in Chapter 3) were observed at relatively higher plasma density of $8.5 \times 10^{19} \text{ cm}^{-3}$ using the lower intensity but with almost double the focal spot size. In that experiment, the wakefield excitation and the electron acceleration occurred as a result of strong self-modulation seeded by the forward Raman scattering instability [127], which is inherently susceptible to shot-to-shot fluctuations. It was noted from the study of pre-pulse effect that the ASE pre-pulse with sufficient intensity and duration can form pre-plasma which helps to guide the main laser beam in the low density plasma and accelerate the electrons to higher energies [128]. However, the inherent shot-to-shot variation of the pre-pulse parameters can cause fluctuation in electron beam parameters. Although the electron energy is relatively less, a low level of pre-pulse below plasma formation threshold in the present study has led to a large improvement in the stability of the electron beam parameters compared to those observed in earlier studies.

Chapter 5: Laser-driven electron acceleration in laser produced plasma plume

Supersonic fast pulsed gas-jet is the most commonly used target medium for laser wakefield acceleration (LWFA) of electrons up to few 100 MeV energy [84]. However, operation of the gas-jet at high repetition rate is limited by the requirement of high vacuum before each gas-jet pulse. Although the relativistic electron beams produced from laser wakefield acceleration in gas jet plasma targets have high peak current \sim kA, the average current is limited typically due to low repetition rate operation of pulsed gas jet targets. High repetition rate operation of the laser-wakefield accelerators would be one of the key factors determining their suitability for various applications. Future advancement in the laser technology is expected to increase the repetition rate of the high power laser systems used for laser wakefield acceleration. Therefore, it is important to investigate new targets for LWFA which could be operated at relatively high repetition rate. In this context, using laser produced plasma plume from a solid target could be one such option. The advantage of plasma produced from laser ablation of the solid target is that negligible amount of material is released into the highly evacuated interaction chamber in comparison to a gas-jet, and therefore allows high repetition rate \sim 1 kHz or more.

In this chapter, we present and discuss the results of laser driven laser wakefield acceleration in plasma plume produced by a nano-second laser pulse ablation of solid targets. Various experimental parameters are optimised to produce self-guiding of femto-second laser pulse and generation of quasi-mono-energetic electron beam with energy \sim 12 MeV [44]. We also present and discuss the observation of multi-MeV quasi-mono-energetic electrons from the grazing incidence interaction of femtosecond laser beam with the solid target through

optimization of level of inherent ASE pre-pulse in the femtosecond laser pulse and consequently the scale length of the pre-plasma produced in front of the solid target surface.

5.1 Experimental details

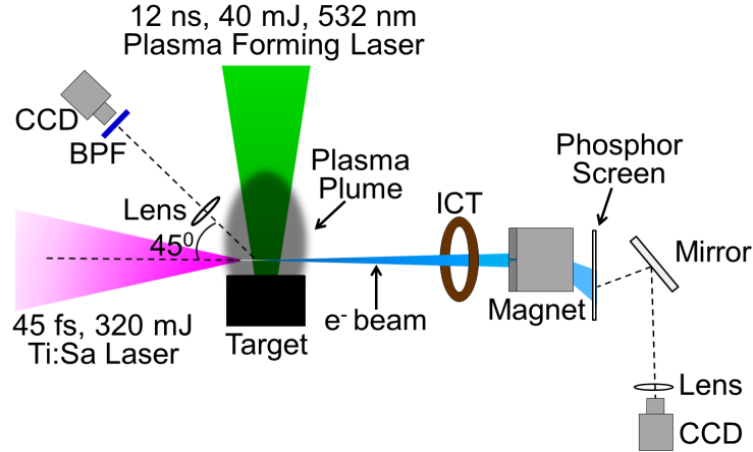


Figure 5.1: A schematic diagram of the experimental setup. [BPF – Band pass filter which transmits radiation within 400 ± 20 nm, CCD – Charge coupled detector, and ICT – Integrating current transformer to measure the charge of the accelerated electron beam.]

A schematic diagram of the experimental setup used is shown in Fig. 5.1. The experiment was set up inside an orthogonal shaped interaction chamber evacuated to $\sim 10^{-5}$ mbar. A part of the second harmonic converted Nd:YAG laser ($\lambda = 532$ nm), which pumps the final amplifier of the Ti:sapphire laser system, was used for producing plasma plume from a solid target. This laser pulse had 40 mJ energy and 12 ns duration (FWHM) and it was focused at normal incidence onto a solid Nylon target $(C_{12}H_{22}N_2O_2)_n$ of 5 mm thickness and $3 \text{ mm} \times 10 \text{ mm}$ surface area, using an $f/12.5$ lens to a spot diameter of $\sim 200 \mu\text{m}$ (FWHM) with an intensity of $\sim 10^{10} \text{ W/cm}^2$. For a comparative study, other target materials like solid carbon, Teflon, and aluminium were also investigated. The main Ti:sapphire laser pulse of 45 fs duration, interacted with the plasma plume orthogonal to the plasma expansion direction, as shown in Fig 5.1. The Ti:sapphire laser pulse arrives on the target at a fixed delay of ~ 90 ns w.r.to the Nd:YAG laser pulse, and the synchronization jitter between the two laser pulses

was ~ 1 ns, which is short compared to the evolution time of the plasma plume. The 45 fs laser pulse with energy of 320 mJ (7 TW) was focused using $f / 3.5$ gold coated off-axis parabolic mirror to $1/e^2$ spot radius (w_0) $\sim 7 \mu\text{m}$ on the front edge of the plasma plume, at a distance of $\sim 50 - 300 \mu\text{m}$ away from the Nylon target surface. The focal spot contained about 50 % of the laser energy (3.5 TW power) resulting into a peak intensity of $\simeq 5 \times 10^{18} \text{ W}\cdot\text{cm}^{-2}$. The Rayleigh length of the focused laser beam was measured to be $\simeq 60 \mu\text{m}$. The pre-pulse intensity contrast was measured to be $\sim 2 \times 10^6$ due to amplified spontaneous emission (ASE) pedestal.

The Ti:sapphire laser pulse propagation in the plasma plume was imaged with 4X magnification by collecting and focusing the non-linear Thomson scattered radiation at 400 nm (2w of Ti:sapphire laser) using a lens onto a 12-bit CCD camera kept at an angle of 45° relative to the incident Ti:sapphire laser axis and the laser polarization direction, as shown in Fig 5.1. A narrow band pass filter (BPF) was placed in front of the CCD camera to allow radiation within $400 \pm 20 \text{ nm}$ to enter the CCD sensor. A part of the transmitted Ti:sapphire laser beam was collected by an $f / 20$ concave mirror kept at an angle of 6° w.r.to the Ti:sapphire laser axis, and focused at the entrance of an optical spectrograph (AvaSpec-3648-USB2) to measure the spectrum. A highly reflecting dielectric mirror, coated for $800 \pm 50 \text{ nm}$, was placed in between the concave mirror and the spectrograph to attenuate the transmitted light and avoid any spectral modification induced by the glass window of the interaction chamber.

The accelerated electron beam was recorded using a DRZ-phosphor screen coupled to a 16-bit CCD camera with imaging lens. The electron beam charge was measured using an integrating current transformer (Bergoz: ICT-082-070-5:1), and the energy spectrum was measured using a permanent magnet based electron spectrograph (magnetic field: 0.14 T, size: 50x80 mm, pole separation: 10 mm). A slit (angular acceptance: $22 \text{ mrad} \times 35 \text{ mrad}$)

made in a combination of thick aluminium and lead plates was mounted in front of the magnet to define a reference axis from which the deflection of the electron beam in the magnetic field was measured. The spectral resolution of the electron spectrograph was about 4 % at 10 MeV. The electron beam charge was estimated using the absolute calibration data of the DRZ phosphor screen [100].

5.2 Quasi-mono-energetic electron beam generation from laser produced plasma plume

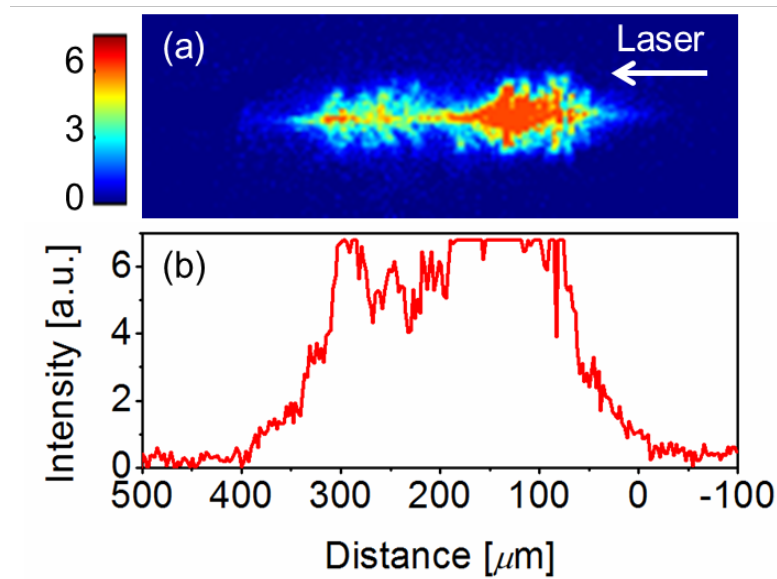


Figure 5.2: a) Image of the Ti:sapphire laser beam guiding in plasma plume obtained from the non-linear Thomson scattered radiation at 400 nm (2ω of laser). The arrow represents the direction of the laser propagation, and b) the intensity profile of the guiding channel image along the laser axis.

First of all, the spatial profile of the high energy electron beam generated along with the self-guided channel formed by 45 fs Ti:sapphire laser pulse interaction with the plasma plume was studied. The plasma density was varied *in situ* by changing the distance between the 45 fs laser beam axis and the Nylon target surface. Fig.5.2a shows the image of the laser beam propagation in the Nylon plasma plume, for a distance of 150 μm from the target surface, and Fig.5.2b shows the line intensity profile of the image along the laser propagation direction. It can be seen that the laser beam is self-guided over a length of 400 μm (start to

end) which is about seven times the Rayleigh length ($\approx 60 \mu\text{m}$) of the laser beam in vacuum. In addition to the laser guiding, a highly collimated electron beam was also produced in the forward direction. A typical image of the electron beam is shown in Fig. 5.3a. The divergence and the charge of the electron beam was estimated to be $\sim 10 \text{ mrad}$ and $\sim 50 \text{ pC}$, respectively. With the decrease in the distance between the Ti:sapphire laser axis and the target surface, the charge of the electron beam increased. A typical electron beam profile observed for a distance of $50 \mu\text{m}$ from the Nylon target surface is shown in Fig. 5.3b. The electron beam profile typically has multiple features with a dominant feature having a larger divergence of $\sim 50 \text{ mrad}$. Generation of collimated electron beam (as shown in Fig. 5.3a) was observed for multiple shots fired on the same location on the Nylon target surface and refreshing the target surface (by raster scanning) in each shot was not required. Fig. 5.3c shows pointing stability of such a low divergence electron beam. The electron beam was produced within a half cone angle of 25 mrad around its average pointing direction in about 85% of the shots. It may be mentioned here that when the plasma plume was produced from carbon (C), and Teflon (CF_2) targets, generation of electron beam was observed only when Ti:sapphire laser axis was very close to the target surface i.e. within $50 \mu\text{m}$ distance. In this case, the divergence of the electron beam was large (mostly $> 50 \text{ mrad}$) and the reproducibility was also very poor. A typical image of the electron beam produced from carbon plasma plume, with lowest observed divergence, is shown in Fig. 5.3d. The energy spectrum measurement of the electron beam produced from the Nylon plasma plume at a distance of $150 \mu\text{m}$ (as shown in Fig. 5.3a) showed quasi-mono-energetic feature. A typical electron beam spectrum recorded is shown in Fig. 5.4. The electron beam has peak energy at $\sim 12 \text{ MeV}$ with energy spread of $\Delta E/E \approx \pm 20 \%$, which is limited by the finite size of electron beam on the phosphor screen.

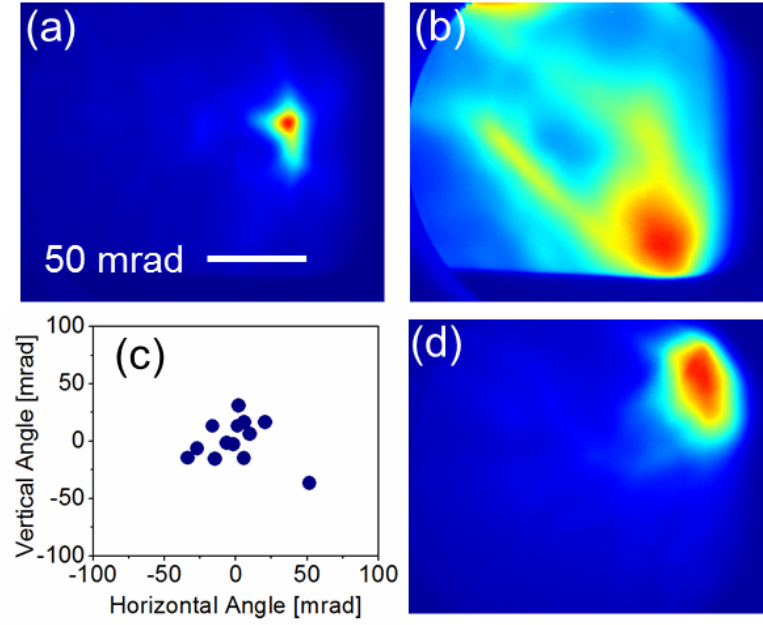


Figure 5.3: Results of the electron beam profile measurement. Typical image of the electron beam produced from Nylon plasma plume at a target distance of a) 150 μm , and b) 50 μm ; c) Pointing variation of the low divergence electron beam shown in a); d) Typical image of the electron beam produced at a target distance of $\sim 50 \mu\text{m}$ in the plasma plume produced from carbon target.

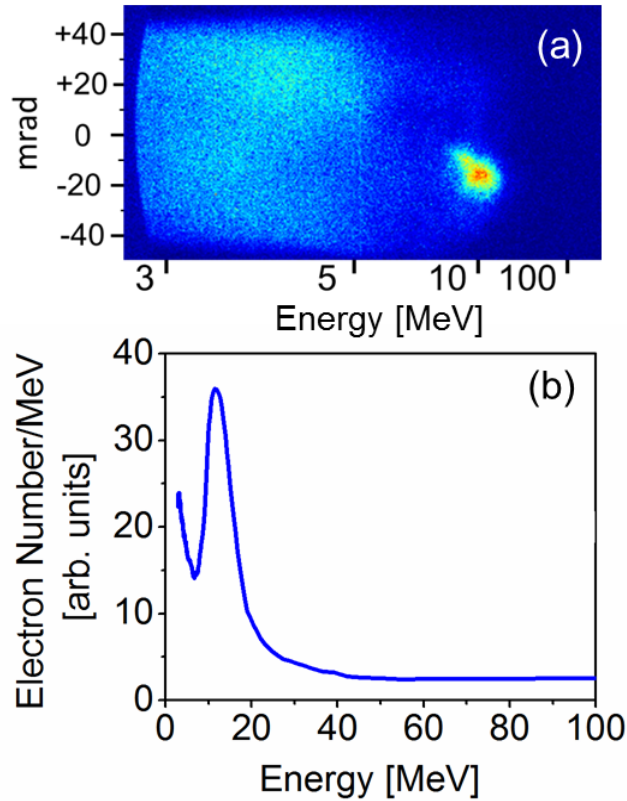


Figure 5.4: Results of the electron beam energy measurement. a) Image of the energy dispersed electron beam and b) quasi-mono-energetic spectrum of the electron beam. The spectrum is obtained by integrating the image a) along the vertical direction over ± 10 mrad about the beam central axis.

5.3 Quasi-mono-energetic electron beam from laser - solid interaction at grazing incidence

We have also investigated the high-energy electrons generation from femtosecond laser pulse interaction with solid carbon target surface at grazing incidence (rather than using a separate laser pulse for plasma plume formation as done in the above mentioned study). In this case also, we have observed generation of multi-MeV electron beam with a low divergence ($\sim 3^\circ$) when the ASE pre-pulse duration was ~ 1 ns duration. A typical image of the well collimated electron beam generated by interaction of the 45 fs laser pulse with ASE pre-pulse level of about 1 ns with carbon solid target surface at grazing incidence is shown in Fig.5.5a. For laser interaction at normal incidence with the 1mm thick carbon target, electron beams with large divergence were produced along the laser axis. A typical image of the electrons emitted from the target rear surface is shown in Fig.5.5b. The measurement of electrons energy for grazing incidence showed quasi-mono-energetic feature as shown in Fig. 5.6, with peak energy about 3 MeV.

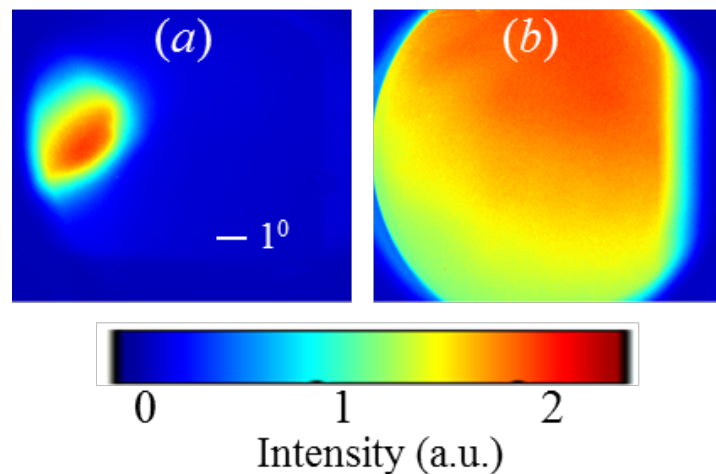


Figure 5.5: Images of electron beam produced from the ASE pre-pulse produced pre-plasma of solid target when the main laser pulse focused a) at grazing incidence and b) at normal incidence.

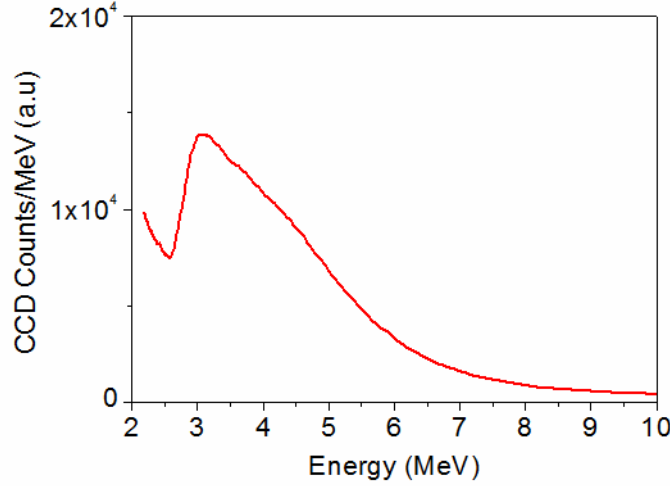


Figure 5.6: *Energy spectrum of the electrons produced from the interaction of main laser pulse at grazing incidence.*

In order to understand the role of ASE pre-pulse on electron generation in the case of grazing incidence, the laser ASE duration was changed by changing the Pockels' cell switching time in the laser system. As the pre-pulse duration was increased beyond 2 ns or reduced below 1 ns, the highly collimated electron beam disappeared, although large divergence and low intensity electrons were observed along the target surface. The energy spectrum exhibited a Maxwellian distribution with electrons energy < 2 MeV. The energy spectrum of the electrons produced from the rear-side of the target for normal incidence was typically Maxwellian-like, with no peaked structure.

5.4 Discussion

First we consider high energy electron generation in laser produced plasma plume. The experimental observations suggest that a laser produced plasma plume could be effectively used for the production of high quality, quasi-mono-energetic electron beam of energy > 10 MeV. For intensity level of $\sim 10^{10}$ W/cm² on Nylon target, a high density plasma (critical density of plasma for 532 nm is $\sim 4 \times 10^{21}$ cm⁻³) of several eV temperature is produced on the target [128]. The plasma produced starts expanding into the vacuum. During the laser pulse, plasma continuously absorbs laser energy and expands isothermally, and after

the end of the laser pulse, the thermal energy of the plasma is converted into kinetic energy and it expands adiabatically [129, 130]. At a given distance from the target surface, the plasma plume arrives after a delay. The density at that point first increases with time and later on, the density drops with time (t) as t^{-3} as there is no further ablation from the target after the end of the laser pulse [129-131]. We have estimated the density profile of the plasma plume for CH target using a 1-D hydrodynamic simulation (HELIOS) under the present experimental conditions. The simulation showed that after a delay of ~ 90 ns of the plasma production (time after which 45 fs Ti:sapphire laser pulse interacts with the plasma plume) the electron density is in the range of $\sim 2 - 3 \times 10^{19} \text{ cm}^{-3}$ within a distance of $\sim 50\text{-}300 \text{ }\mu\text{m}$ from the target surface, and density increases sharply close to the target surface. The plasma plume contains neutrals, free electrons, and ions of the constituent atoms of the target. In the case of Nylon ($\text{C}_{12}\text{H}_{22}\text{N}_2\text{O}_2$) target used in the present experiment, hydrogen constitutes about 58% of the total atoms, and therefore the plasma plume pre-dominantly consists of hydrogen, a significant fraction of which is ionized. This is further supported by the fact that the time delay of arrival of a particular ion at a given location is proportional to the square root of its mass [130]. Therefore, at a given distance from the target surface, the hydrogen ions reach earlier compared to the other heavier constituents of the target. However, a small fraction of other high-Z constituents in Nylon (singly and doubly ionized C, N and O) is also expected to be present due to momentum exchange process during the initial stages of plasma expansion [130]. The interaction of the 45 fs duration Ti:sapphire laser pulse with the Nylon plasma plume leads to relativistic self-focusing and guiding of the laser beam (Fig.5.2).

The measurement of spectrum of the transmitted laser from plasma plume showed a broad, blue-shifted spectrum with multiple periodic peaks, as shown in Fig.5.7. While the blue shift may arise due to the laser induced ionization, anti-Stokes Raman scattering with contribution of its higher orders [132], and / or photon acceleration [133], the presence of

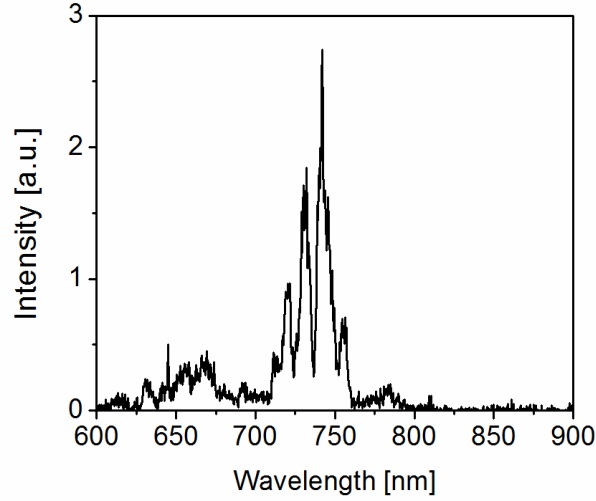


Figure 5.7: *Transmitted spectrum of the fs laser beam after its interaction with the Nylon plasma plume at a distance of 150 μm from the target surface.*

multiple peaks indicates a strong modulation of the laser pulse due to the laser wakefield. The ionization blue shift can be due to the neutral atoms of hydrogen and / or partially ionized atoms of high-Z constituent atoms of the target material in the plasma plume [131]. By changing the distance of the laser axis from the target surface, different density regions were explored and generation of highly-collimated electron beam (Fig.5.3a) was observed when the laser pulse interacted with the plasma plume at a distance of $\sim 150 \mu\text{m}$ from the target surface. With decrease in the distance, the beam divergence and the charge increased (Fig.5.3b). This is similar to the observation made with gas jet targets where an optimum value of electron density has been found for generation of highly collimated quasi-mono-energetic electron beam in gas jet targets (presented in earlier chapters). The generation of collimated quasi-mono-energetic electron beam arises due to transverse wave-breaking of laser wakefield excited in bubble regime [26, 27]. However, optical field ionization of high-Z ions inside the bubble, present as a small fraction in the plasma plume, may also contribute to the electron injection and further acceleration [39,134].

With the carbon and Teflon (CF_2) targets, generation of electron beam was not observed at similar distances from the target surface, although the electron density is expected to be in

the same range, because the ionization induced defocusing [118] of the laser beam could be dominant in these relatively high-Z targets. Only close to the target surface where electron density is higher, and consequently ratio of laser power to the critical power for self-focusing [85] is also higher, generation of electron beam is observed, but with poor quality (Fig. 5.3d). Matsuoka *et al* [131] have also reported electron acceleration in Teflon plasma plume with density in the range of $\sim 3 \times 10^{19} \text{ cm}^{-3}$, but using a higher laser power (30 TW) and quality of electron beam generated was also not as good as observed with the Nylon plasma plume in the present experiment. This difference could be because of the higher abundance of hydrogen in the Nylon target, which perhaps minimizes the effect of ionization induced defocusing and instabilities.

The demonstration of high quality electron beam is a big step forward in the effort to find suitable targets with high repetition rate capability, along with easy and low cost target setup, and broad choice of target composition. Further, deriving the laser pulses for plasma plume formation and laser wakefield acceleration from a single laser system (as done in the present experiment) allows perfect synchronization and makes the setup even more simple and of lower cost. With these advantages, plasma plume targets opens up a wide range of possibilities for future investigations to further optimize several parameters in this scheme to generate higher energy electron beams with more stability and control.

Now we examine the case of grazing incidence laser beam (without plasma plume generation by a separate Nd:YAG laser). Intense quasi-static electric and magnetic fields can be generated during the interaction of 45 fs laser pulse with the pre-plasma produced on the target surface by the ASE pre-pulse [69]. Energetic electrons are generated and guided by the combined fields and move along the target surface with betatron oscillation, as shown in simulations by Mao *et al* [135]. At grazing incidence, as in the present experiment, enhanced self-generated electro-magnetic fields are generated due to the electron current generated

along the target surface [136]. The generation of quasi-mono-energetic peak could be explained by the betatron oscillation process in the under-dense pre-plasmas [90, 137]. When the frequency of the transverse electron oscillation in the self-generated electromagnetic field is resonantly coupled with the laser frequency, the surface electrons would gain energy efficiently from the laser wave and get accelerated. However, particle-in-cell simulations by Mao *et al* [135] show that the electrons are accelerated in the initial phase. Later in time, they experience deceleration when the laser begins to defocus and the betatron oscillation frequency goes out of resonance with the laser frequency. Time dependent modeling shows a peaked electron spectrum, as observed in the present experiment. The peaked structure of electron beam with energy ~ 1 MeV was also seen in an earlier experiment [138, 139]. The high peak energy of 3 MeV in the present experiment can be attributed to efficient acceleration of electrons in the intense quasi-static fields generated due to much lower grazing incidence angle ($< 1^\circ$) of interaction compared to the other reported experiments [139]. Further study shows that the target surface electron guiding process and acceleration critically depend on the laser pulse contrast. In our experiment, the laser with ASE pre-pulse heats the target and generates pre-plasma of appropriate scale length. This pre-plasma provides an under-dense plasma environment to generate the quasi-static electro-magnetic fields that effectively trap the electron beam and guide it along the target surface [138]. Such an electron beam, in principle, can be produced at high repetition rate using 1 kHz, few TW lasers presently available, which could be as an injection beam for high energy accelerators or as igniter in fast ignition concept of inertial confinement fusion.

Chapter 6: Study of bremsstrahlung radiation and fast electron generation from laser - solid interaction

Generation of fast electrons in high intensity laser-solid interaction and their subsequent transport has been extensively studied; both theoretically and experimentally, over the years [47 - 59] mainly due to its relevance to fast ignition based inertial confinement fusion (ICF) scheme [60]. The fast electrons penetrating into the target material slow down and produce a bright source of bremsstrahlung hard x-rays with multi-keV to MeV x-rays, which is useful for various applications. For instance, such sources have been used for activation of short-lived isotopes which can be used in radiological diagnostics for positron emission tomography [140], transmutation of elements by neutron capture to deactivate long-lived fission fragments [141, 142], and for nuclear fission of actinides [143]. Therefore, understanding the mechanisms of fast electron generation and the knowledge of their angular and energy distribution under different laser irradiation conditions is critical for controlling them for various applications including ICF. Also, measurement of the bremsstrahlung x-rays and their angular distribution are necessary for optimum utilization of these sources for applications. On the other hand, this x-ray radiation with significant dose levels may be harmful to the experimentalists. The fast electrons leaving the target may result in production of x-ray sources other than at the target itself, when they are slowed down in the surrounding materials. From the safety point of view, it is desirable to identify and characterize all sources of such radiation to take necessary precautionary measures like using low-Z materials to stop the fast electrons or/and by providing appropriate shield for the hard x-rays. In addition, angular distribution measurements can also provide information on the preferential direction of emission of electrons.

In this Chapter, we present a study of the bremsstrahlung hard x-ray emission and the fast electrons generated from the interaction of Ti:sapphire laser pulses with planar copper

target at 45° incidence angle, under different irradiation conditions. Measurements of the angular distribution of the hard x-ray bremsstrahlung radiation generated due to the fast electrons produced from the interaction region and identification of secondary source of x-rays and fast electron emission direction are presented. The measurements on the angular spread and the energy spectrum of the fast electrons for both p- and s-polarized laser irradiation at intensities in the range 4×10^{16} - 4×10^{17} W/cm² (for a fixed pulse duration of 45 fs) and for pulse duration in the range 45 fs – 1.2 ps (for a fixed laser fluence of 1.8×10^4 J/cm²) is described and scaling laws for temperature of fast electrons with laser intensity and pulse duration are presented. The results of the x-ray and fast electrons measurements are discussed.

6.1 Experimental details

Figure 6.1 shows a schematic diagram of the experimental setup used. The experiment was performed with the Ti:sapphire laser system delivering horizontally polarized (p-polarized) 45 fs duration pulses with energy ~150 mJ per pulse on the target. The laser beam was focused at 45° incidence angle on a polished copper slab target (10 mm thickness) to a FWHM focal spot of ~18 μ m. The peak intensity of the laser on target was $> 10^{17}$ W/cm² considering oblique incidence of the laser on the target. The target was positioned at the centre of an octagonal plasma chamber evacuated to $\sim 10^{-5}$ mbar pressure. It was mounted on a stepper motor controlled raster scanning system to have fresh target surface for each laser pulse. The plasma chamber had 20 mm thick aluminium walls fixed on all eight sides of a stainless steel frame with octagonal shaped base and top. In the plane containing the target normal and the incident laser beam, 10 mm thick BK-7 glass windows were fixed to aluminium walls on all sides, except in the direction of laser incidence. In this direction, a

focusing lens was fixed to the aluminium wall, to focus the laser beam on the target. The glass windows were located at a distance of 430 mm from the copper target / chamber centre.

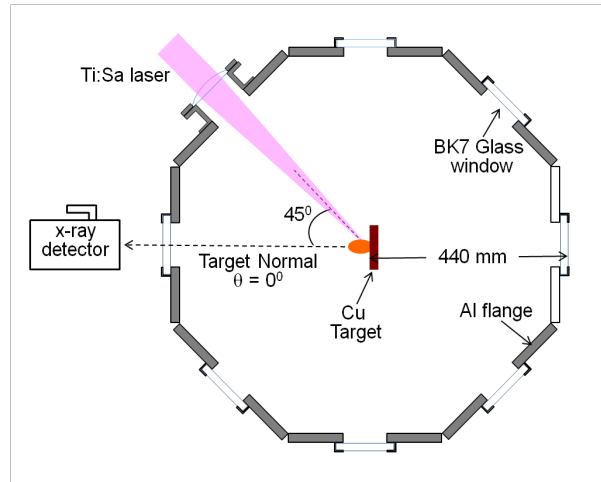


Figure 6.1: A schematic diagram of the experimental setup used for the measurement of radiation dose due to x-rays passing through the glass windows of the plasma chamber.

A pressurized ion chamber based radiation detector (Victoreen, 450 P) was used for radiation dose rate measurement. The detector was kept at a distance of ~ 50 mm from the glass window for the dose measurements. The sensitive area of the detector which was collecting the x-rays was $\sim 30 \text{ cm}^2$. This detector can detect photons of energy more than 25 keV and electrons of energy more than 1 MeV. The instrument was calibrated with a Cs^{137} (0.662 MeV γ -rays) radiation source and it can measure radiation dose rate as small as 0.01 $\mu\text{Sv/h}$ up to 50 mSv/h, with accuracy better than 10%. Natural background radiation dose rate was measured to be less than 0.2 $\mu\text{Sv/h}$. The radiation dose rate due to hard x-rays passing through the 10 mm glass windows of the plasma chamber was measured as a function of the angle w.r.t. the target normal. Time averaged and spectrally integrated hard x-ray dose rate measurements were carried out outside the plasma chamber at a distance of about 50 cm from the plasma chamber centre. To keep the x-ray dose rate low, the laser was operated at 2 Hz for all our measurements except once, when it was operated at 10 Hz rep-rate to compare

the dose with that produced at 2 Hz rep-rate. As expected, the measured dose rate at 10 Hz rep-rate was higher by a factor of 5.

The angular spread of the fast electrons generated from laser-target interaction was measured using a radio-chromic film (RCF) kept at a distance of 80 mm from the target front surface, along the direction of its normal. The RCF was covered with an aluminium foil to protect it from the debris and to stop the background of low energy (<50 keV) electrons.

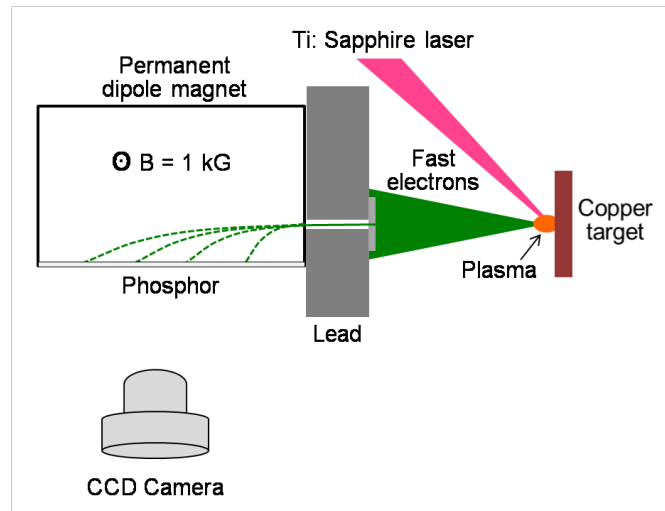


Figure 6.2: A schematic diagram of the setup used for energy spectrum measurement of fast electrons emitted from laser-solid interaction.

After identifying the direction of the fast electron emission (from the angular and radial distribution measurements of the x-ray dose) to be along the target normal, the characterization of fast electrons emitted from the solid target was done by setting up an electron diagnostics system inside the interaction chamber, as shown in Fig. 6.2. A permanent dipole magnet consisting of two rectangular pole pieces of size 50 mm \times 80 mm was used to energy disperse the fast electrons produced from the laser - target interaction. The magnetic field profile of the dipole magnet was measured prior to the experiment and an effective magnetic field of 1 kG was obtained inside the pole gap of 30 mm. The magnet was placed on a retractable mount to facilitate movement of the magnet in and out of the path of the incoming electrons. To increase the resolution of the energy measurement, a stainless steel slit

of 0.8 mm width and 1.6 mm height was put in front of a 35 mm thick lead collimator with a 3 mm diameter hole. The collection solid angle of the slit was 4×10^{-5} sr. The resolution of the spectrograph was estimated to be about 10% for 200 keV and 5% for 5 MeV electrons. The DRZ-phosphor screen was used to detect the energy dispersed electrons. A thick aluminium foil was placed on top of the DRZ screen to cut off the electrons with energy < 150 keV and to avoid its exposure to the low energy x-rays. In addition, 35 mm thick interlocking lead bricks were also used to shield the phosphor screen from direct exposure to the electrons and x-rays. A 12-bit CCD camera (SamBa) was used to image the phosphor screen. The CCD counts of the electron image were converted to electron number using the absolute calibration data available for the DRZ-phosphor screen [100].

6.2 Angular distribution of bremsstrahlung hard x-rays

The measurements of radiation dose rate as a function of the angle (w. r. t. the target normal direction) were carried out. The angular distribution of the radiation dose rate was strongly peaked along the target normal direction with a dose rate as high as $40 \mu\text{Sv/h}$, as shown in Fig. 6.3. This is more than 200 times the background radiation dose rate of $\sim 0.2 \mu\text{R/h}$. The x-ray $1/e$ cut-off energy of 10 mm thick glass window was calculated from standard mass-attenuation coefficients to be ~ 40 keV [144]. It is important to note here that the measured dose rate is only due to x-rays and not due to electrons. This is because the electrons with energy up to few MeV will be stopped completely within the thickness of the glass window. Since the dose rate is measured outside the experimental plasma chamber, close to the glass window, the observed dose rate is due to the hard x-rays with energy more than ~ 40 keV. The measured hard x-rays (exceeding several tens of keV to MeV energy) are emitted due to the generation of fast electrons in the ultra-intense laser-solid interaction and their subsequent slowing down in the solid target or in surrounding materials.

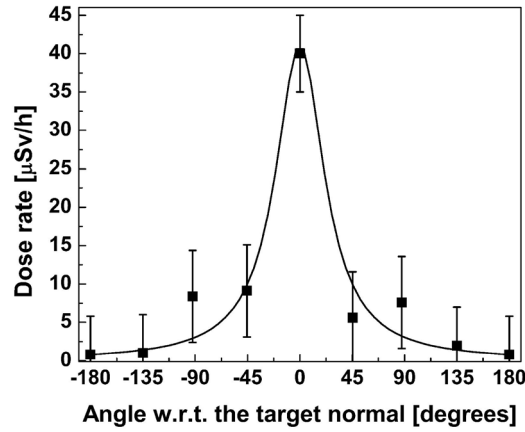


Figure 6.3: The angular distribution of the hard x-ray dose rate ($h\nu > 40$ keV) outside the interaction chamber, at a distance of 500 mm from the copper target.

For fast electrons of few 100 keV temperature (or average kinetic energies) generally observed for the laser intensity used in the experiment, the angular distribution of the bremsstrahlung x-ray continuum is expected to be isotropic [62]. However, as seen from Fig. 6.3, the x-ray dose rate shows a minimum in the direction opposite to the target normal ($\theta = 180^\circ$). As we have used a 10 mm thick copper target, it is possible that the x-rays undergo strong attenuation in the target which may result in the observed minimum dose rate behind the target ($\theta = 180^\circ$). In order to check whether this is true, a much thinner copper foil-target of 150 μm thickness was used in place of the 10 mm thick copper-slab target. It was found that the angular distribution remains unaffected; indicating that the minimum of x-ray dose observed on the backside of the target is not due to attenuation while traversing the target thickness.

6.3 Sources of x-rays and direction of fast electron emission

In order to investigate the cause for the observed peak dose in the direction of the target normal, we have measured the dependence of the x-ray dose rate as a function of distance, in the same direction (i. e. θ unchanged). Figure 6.4 shows the variation of the dose

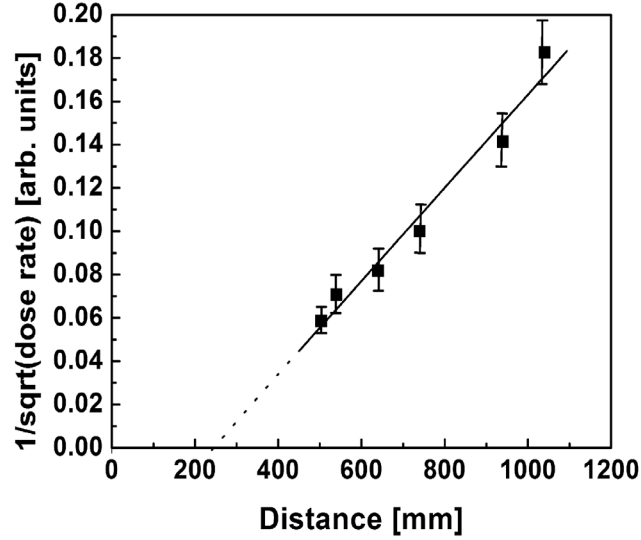


Figure 6.4: *Hard x-ray dose rate variation with distance from the plasma chamber centre.*

rate measured outside the plasma chamber with distance measured from the plasma chamber centre (in mm), along the direction of the target normal. The data points are fitted to inverse square dependence of the form: dose rate $\propto (r - 220)^{-2}$. The functional form of the above distance dependence indicates as if a hard x-ray point source is located at a distance of ~ 220 mm from the target surface. The reason for this virtual shift is due to generation of another source of x-rays at the glass window located at a distance of ~ 430 mm from the target, along the target normal direction ($\theta = 0^\circ$) in addition to the one located at the target. A combination of these two sources, one at the laser irradiated target surface and the other at the glass window at the chamber wall, can give rise to the experimentally observed distance dependence. This was verified by placing a 6 mm thick, $50 \times 50 \text{ mm}^2$ lead slab in front of the target, at a distance of 50 mm, and measuring the x-ray dose rate as a function of the distance from the target (outside the plasma chamber). This variation is shown in Fig.6.5. The fitted curve in this case showed that the effective source is at a distance of only ~ 20 mm away from the target. The second source is produced by high energy electrons streaming in the direction of target normal [141, 68] which are stopped either by the glass window (in the first case) or by the lead slab (in the second case). The angular dependence was not measured with the lead

piece inserted in the plasma chamber, as in this case, varying thickness of the lead slab (high-Z material having large x-ray absorption cross-section) seen in different directions would itself be the major factor distorting the angular distribution.

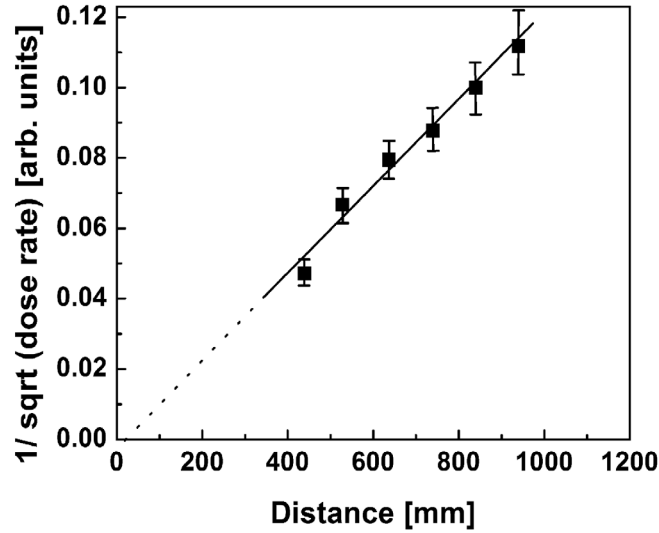


Figure 6.5: Hard x-ray dose rate variation with distance from the plasma chamber centre, with lead slab kept at a distance of 50mm from the target.

The observed angular distribution in Fig. 6.3 can be understood to arise from the combination of the two sources, one at the laser irradiated target surface and the other at the glass window on the chamber wall facing the target. The x-rays generated from both the sources should be isotropic in nature. In general, any angular distribution due to two sources located at different points can be anisotropic due to change in distance as well as direction for different angles of observation. In our experiment, the maximum dose rate variation is observed between the forward ($\theta = 0^\circ$) and backward ($\theta = 180^\circ$) directions, for which case, only the distances (and not the angles) of the detector w.r.t. the second source are different. While for $\theta = 0^\circ$, the distance of the detector from the two sources is 480 mm and 50 mm respectively, the corresponding distances for $\theta = 180^\circ$ are 480 mm and 910 mm. From this, we infer that different distance of the second source for various angles is mainly affecting the angular distribution.

6.4 Angular distribution of fast electrons

The angular and energy distributions of the fast electron were characterized under different laser irradiation conditions. The image of the fast electrons emitted along the target normal direction is shown in Fig. 6.6a and a lineout of the intensity profile of the fast electrons is shown in Fig. 6.6b. The image on the RCF was due to its accumulated exposure to the fast electrons produced in 500 shots when the laser irradiated the target in the intensity range of 4×10^{16} - 4×10^{17} W/cm². This was done for both, p- and s-polarized laser light. The figure clearly shows that the fast electrons were indeed produced along the target normal direction in the form of a collimated jet within a half cone angle of about 20° around the target normal direction, which is comparable to the observations in earlier studies [141]. To confirm that the image on the RCF was mainly due to the fast electrons, a permanent dipole magnet was kept between the target and the RCF, along the target normal direction. The magnet deflected the fast electrons away from the target normal direction, while the x-rays emitted from the target surface could still reach the RCF. The RCF, in presence of the magnet, did not show any distinct image even after it was exposed for longer duration than in the case of no magnet. This could be either due to the x-ray dose being lesser compared to the electrons, and/or lesser sensitivity of the RCF to the x-rays. However, this clearly confirms that the image shown in Fig. 6.6 is due to the fast electrons only.

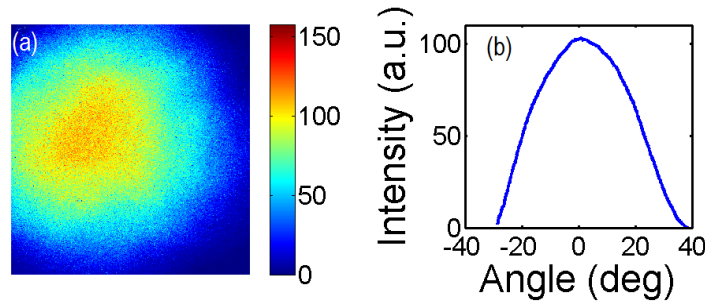


Figure 6.6: a) A typical image of the fast electrons produced from the interaction of 45 fs duration Ti:sapphire laser pulses focused to $4 \times 10^{16-17}$ W/cm², for both p- and s-polarization, on planar copper solid target at oblique incidence of 45° w.r.t. the target normal; b) The lineout gives the intensity profile of the fast electrons with an HWHM angular spread of 20°.

6.5 Energy measurement and scaling of fast electrons

During the energy measurement, the DRZ-phosphor screen image was initially recorded with and without the magnet in the path of fast electrons and it was found that the x-ray contribution was less than 5% of the signal measured due to both, electrons and x-rays. This confirmed that the electron energy dispersion images from DRZ-phosphor screen were mainly due to the electrons, and x-rays only give rise to a low intensity, uniform background. Subsequently, the measurement of the fast electrons energy spectrum was made under various laser-target interaction conditions. The image of the electron energy spectrum was recorded by integrating over 10 seconds (100 shots) for each interaction condition, and the averaged spectral profile was plotted per shot. Fig.6.7 shows the energy spectra of the electrons produced when 45 fs laser pulses focused to an intensity of $4 \times 10^{17} \text{ W/cm}^2$, under two different (p and s) polarization conditions. In both the conditions, the electron spectra resembled Maxwell–Boltzmann distribution in energy $\{dN(E)/dE \sim E^{1/2} \cdot \exp(-E/kTe)\}$, characterized typically by two temperatures. The temperature corresponding to the fast

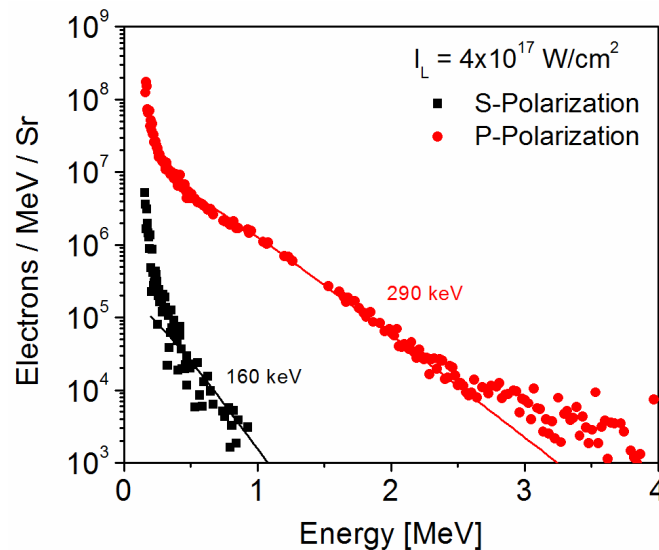


Figure 6.7: Energy spectra of the fast electrons produced from the interaction of 45 fs duration, p- or s- polarized Ti:sapphire laser pulses, focused to $4 \times 10^{17} \text{ W/cm}^2$ on planar copper solid target at oblique incidence of 45° w.r.t. target normal.

electrons was obtained by fitting the high energy component of the spectrum to the above distribution. In the case of p-polarization, the temperature of fast electrons was ~ 290 keV, while in the case of s-polarization, it was ~ 160 keV. It is important to note that the fast electrons were produced along the target normal direction even for s-polarization, although the temperature of the fast electrons was less compared to that in the case of p-polarization. These observations are consistent with the reduced hard x-ray dose measured along the target normal direction.

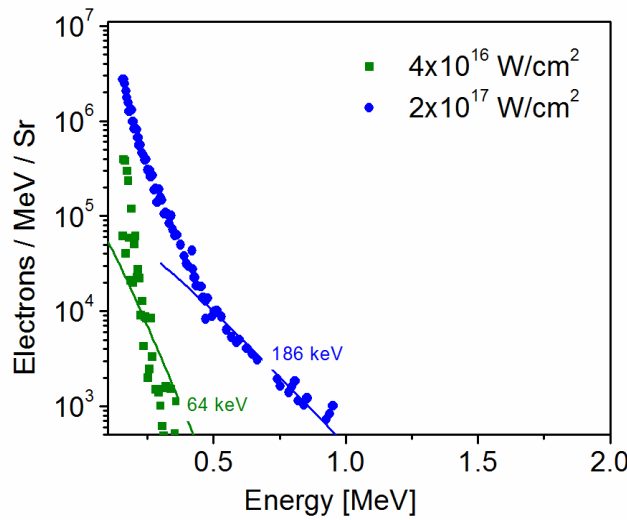


Figure 6.8: The energy spectra of the fast electrons produced from the interaction of 45 fs duration, p-polarized Ti:sapphire laser pulses, focused to two different intensities.

The energy spectrum of the fast electrons was measured at different laser intensities in the range of 4×10^{16} to 4×10^{17} W/cm², with p-polarization and 45 fs pulse duration. The intensity of the laser beam was reduced from its maximum value of 4×10^{17} W/cm² by using appropriate neutral density filters. Figure 6.8 shows the energy spectra of the electrons at two different intensities: 4×10^{16} W/cm² and 2×10^{17} W/cm². The figure shows that the temperature of the fast electrons as well as their number decrease with decreasing the laser intensity. The temperature of fast electrons decreased from 290 keV at 4×10^{17} W/cm² (Fig.6.7) to 64 keV at 4×10^{16} W/cm² (Fig.6.8). Since the angular spread of the fast electrons was measured from the

accumulated RCF image (shown in Fig.6.5) due to the electrons emitted over the intensity range of 4×10^{16} - 4×10^{17} W/cm², the quoted angular spread of 20° obtained from Fig.6.6 is the upper limit. Wang *et al* [59] have reported that the divergence angle of the fast electrons along the target normal direction decreases with decreasing intensity. This suggests that the fast electrons produced at lower intensities in the present experiment may have divergence < 20°.

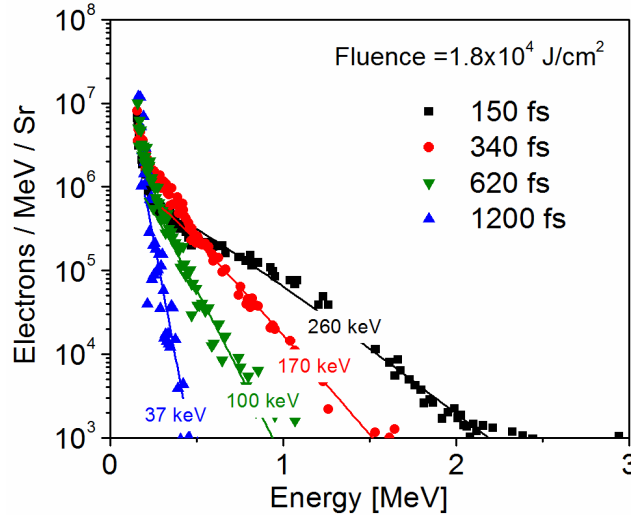


Figure 6.9: Energy spectra of the fast electrons produced from the interaction of p-polarized laser pulses of different durations, keeping the laser fluence constant at 1.8×10^4 J/cm².

The electron energy spectrum was also measured at different pulse durations of the Ti:sapphire laser, keeping the laser fluence constant. The pulse duration was increased from the shortest possible value of 45 fs to a maximum of 1.2 ps by changing the distance between the pair of parallel gratings in laser pulse compression system. The electron energy spectrum taken at 45 fs duration is already displayed in Fig. 6.7 (corresponding to laser intensity $\sim 4 \times 10^{17}$ W/cm²) and the spectra taken at pulse durations of 150 fs, 340 fs, 620 fs, and 1200 fs at a constant fluence of 1.8×10^4 J/cm² are shown in Fig.6.9. It can be seen that the temperature as well as the number of the fast electrons reduced with increasing the pulse duration. It must be noted that when the laser pulse duration is increased, the laser intensity reduces from 4×10^{17} W/cm² at 45 fs to 1.5×10^{16} W/cm² at 1200 fs or 1.2 ps. The temperature

of fast electrons was plotted against the laser intensity and the laser pulse duration and it is shown in Fig.6.10. A power law best fit to the temperature variation with laser intensity $\{kT_e [\text{keV}] \approx 120 [I (\text{W}/\text{cm}^2)/10^{17}]^{2/3}\}$ showed an intensity scaling of 2/3 (Fig.6.10a). Similar intensity dependence was also observed in a recent study using thick Al planar targets in the same intensity regime [145]. An exponential decay of the form $kT_e [\text{keV}] \approx 320 \exp[-\tau (\text{fs}) / 540]$ fits well for the temperature variation with the pulse duration (Fig.6.10b).

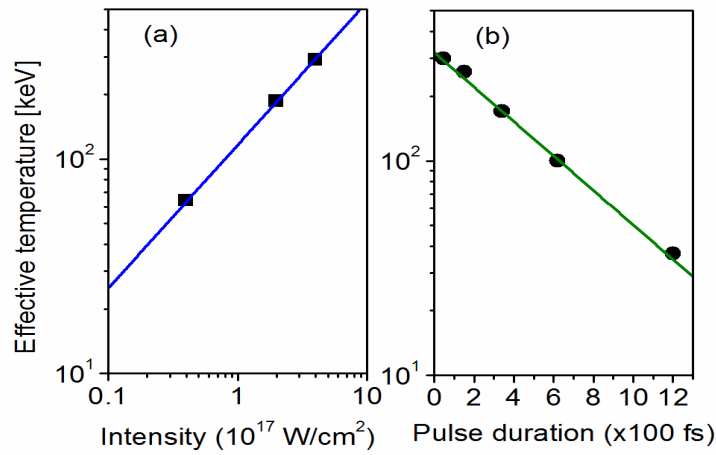


Figure 6.10: Variation of the temperature of the fast electrons a) with laser intensity at a fixed pulse duration of 45 fs and b) with pulse duration at a fixed laser fluence of $1.8 \times 10^4 \text{ J}/\text{cm}^2$.

6.6 Discussion

Dosimetric measurements of hard x-rays and their angular distribution at intensities $\geq 10^{19} \text{ W}/\text{cm}^2$ in laser-solid interactions have been carried out by few groups earlier for radiation shielding point of view [146, 147]. However, such measurements for laser intensities of $\sim 10^{17} - 10^{18} \text{ W}/\text{cm}^2$ are not available although the latter laser intensities are routinely used at many laboratories equipped with 10 TW Ti:sapphire lasers. Since the angular dose rate distribution shows a strong peak in the forward direction, with a peak dose rate value $\sim 40 \mu\text{Sv}/\text{h}$ at a distance of 500 mm for a laser rep-rate of 2 Hz, operation of the same laser at 10 Hz repetition rate would result in a peak dose rate of $\sim 200 \mu\text{Sv}/\text{h}$ at the same distance from the target. Therefore, an exposure to such radiation fields for longer than 100

hours in a year would result in a radiation dose of 20 mSv, which is the annual permissible limit on dose [148]. These results are important in devising suitable radiation shielding as well as for some useful applications of hard x-rays. Moreover, as the location of the second source can be changed, it provides more flexibility in using this radiation. In addition, the radiation dose measurement of hard x-rays produced from intense laser-solid interactions can be an easy method to identify the x-ray sources and direction of fast electron emission, as demonstrated in the present study.

The fast electrons can be produced in the target normal direction by vacuum heating or resonance absorption mechanism, when p-polarized laser obliquely irradiates a solid target [149]. However, for vacuum heating to take place, the plasma electron excursion length, $x_{osc} = eE_0/m\omega^2$ in the laser field must be longer than the plasma density scale length $L = [(1/n_e)(dn_e/dx)]^{-1}$, i.e. $x_{osc} > L$. The plasma density scale length is normally determined by the laser pulse duration in the case of longer pulses. However, in the experiments using femtosecond ultra-high intensity ($I > 10^{17} \text{ W/cm}^2$) lasers, it strongly depends on the intensity contrast of the ASE pre-pulse. Therefore, even for the maximum intensity of $4 \times 10^{17} \text{ W/cm}^2$ used in the present experiment, considering the high pre-pulse intensity ($4 \times 10^{11} \text{ W/cm}^2$ for contrast ratio of 10^6), the condition $x_{osc} > L$ cannot be met. The ASE pre-pulse creates long scale length pre-plasma before the arrival of the peak of the ultra-short laser pulse, thereby substantially altering the target condition by the time ultra-short pulse arrives on the target, thus influencing the nature of the interaction [55]. Using HELIOS 1-D hydrodynamic code [150], we have simulated density profile of the pre-plasma at the end of the 1 ns duration ASE pre-pulse interaction with copper target. The simulations showed that the ASE pre-pulse indeed produces plasma on the target surface under the interaction conditions of our experiment. The density profiles of pre-plasma electron density (normalized to critical

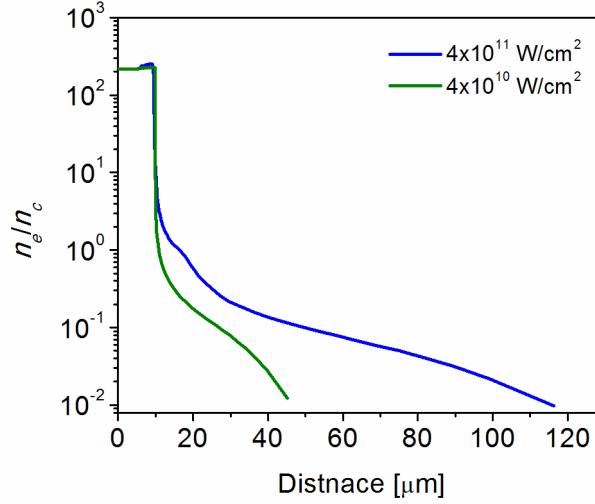


Figure 6.11: Plasma density profiles obtained from 1D hydrodynamics simulation (using HELIOS code) of the ASE pre-pulse of 1 ns duration irradiating a copper target at 45°.

density) at pre-pulse intensities of $4 \times 10^{10} \text{ W/cm}^2$ and $4 \times 10^{11} \text{ W/cm}^2$, corresponding to main pulse intensity of $4 \times 10^{16} \text{ W/cm}^2$ and $4 \times 10^{17} \text{ W/cm}^2$ respectively are shown in Fig. 6.11. It can be easily noticed from the figure that the density profiles cannot be approximated by a single exponent. The pre-plasma has a very short scale length in the vicinity of critical density followed by long scale-length under-dense region in front of the target. The presence of long scale length under-dense plasma supports growth of laser driven plasma instabilities [143]. We have observed $3\omega/2$ radiation emission arising due to two-plasmon decay instability which provided additional confirmation to the presence of long scale length plasma [151]. The presence of such long scale length plasma does not support fast electron generation through vacuum heating. The alternate mechanism which can produce energetic electrons along the target normal direction is resonance absorption. Although the plasma density scale length in the vicinity of the critical density appears (see Fig. 6.11) to be larger than the optimal scale length ($L \sim \lambda$) for resonance absorption [152], radiation pressure due to intense picosecond pedestals ($\sim 10^{13-14} \text{ W/cm}^2$) can reduce the scale length which can be close to optimum value. In the resonance absorption mechanism, the incident p-polarized laser electric field resonantly excites a plasma wave at the critical density surface. Fast electrons are

produced along the target normal direction, down the density gradient by Landau damping or plasma wave-breaking mechanism [152]. However, the electric fields produced in this region, due to the space charge effects, draw back a portion of these fast electrons into the solid target core, where they lose their energy and produce bremsstrahlung x-rays from the solid target [153]. Therefore, the observed peak in the angular distribution of hard x-ray dose rate along the target normal can thus be attributed to the bremsstrahlung radiation produced by the jet of fast electrons produced along the target normal through resonance absorption. These electrons will be stopped over a depth of sub-mm in the glass window, opposite to the target normal.

In similar experimental conditions as ours, observation of a fast electron jet has been reported along the target normal direction due to resonance absorption [141]. The variation of the temperature of fast electrons with laser intensity in the range of 10^{17-19} W/cm² has been observed by Beg *et al* [53] to scale as kT_e (keV) = $100 [I_L(\text{W/cm}^2) \lambda^2(\mu\text{m}) / 10^{17}]^{1/3}$, in the regime of resonant absorption. The temperature predicted by this scaling for 4×10^{17} W/cm² is about 140 keV, while the measured value from the Fig.6.7 is about 290 keV. As mentioned earlier, the temperature of the fast electrons also showed a higher scaling of $I^{2/3}$ in the present experiment. This could be due to the laser intensity enhancement by self-focusing in the long scale length under-dense plasma in front of the target [68]. As the main laser pulse intensity increases, the scale length of the under-dense plasma in front of the target also increases (Fig. 6.11) due to increase in the ASE pre-pulse intensity. Therefore, self-focusing is expected to increase non-linearly with the increase in laser intensity, resulting in a higher intensity scaling. The appearance of fast electrons along the target normal direction for s-polarization can be due to the non-zero component of p-polarization at the focus of the laser beam (due to microscopic target non-uniformity) and also due to the modification of the critical density surface [152]. The variation of the electron energy with the laser pulse duration may be due to

the fact that the longer pulse duration would be able to heat the pre-plasma and modify its characteristics such that the laser energy is absorbed more efficiently through resonance absorption, compared to the 45 fs duration laser pulse. Detailed understanding of the dependence of resonance absorption under laser irradiation with different pulse durations, in the presence of ASE pre-pulse, would require further investigation using simulations and experiments.

A recent experimental study by Wang *et al* [59] has reported fast electron angular distribution at different laser intensities in the range of $2.6 \times 10^{16-18}$ W/cm², and under different polarization and pre-pulse conditions. The fast electrons jet observed in the present experiment for both p- and s-polarization, with the pre-pulse present, is consistent with that reported in Ref. 10. Cai *et al* [141] have characterized the angular and energy distribution of the fast electrons along the target normal direction under ASE pre-pulse condition similar to ours, but at a fixed intensity of $\sim 10^{17}$ W/cm². The measured angular spread and temperature of the fast electron jet in our experiment is similar to that observed by Cai *et al* at similar intensity.

Chapter 7: Summary and Future outlook

In this thesis work, experimental investigations on laser wakefield acceleration of self-injected electrons were carried out under wide ranging laser pulse and target conditions using a table-top 45 fs, 10 TW laser system. The investigations showed that precise control of interaction parameters is crucial for producing stable relativistic electron beams with low divergence and small energy spread. Studies on fast electrons and x-rays generation from laser solid interaction at oblique incidence were also carried out. The summary of these studies and outline of future work that can be carried out in this field, are discussed in this chapter.

7.1 Summary of the important results

The study on laser wakefield acceleration of electrons in the self-modulation regime using helium gas jet showed generation of low divergence (< 10 mrad), and quasi-mono-energetic ($\Delta E/E < 10\%$) electron beam, with energy up to about 20 MeV, at a high plasma density of $8.5 \times 10^{19} \text{ cm}^{-3}$, in contrast to the poor quality beams reported in many earlier experiments in this regime. Simultaneous observation of forward Raman scattering (FRS) confirms strong modulation of the laser pulse and excitation of large amplitude plasma wave. The results clearly suggest that even if the initial laser pulse length $c\tau_0$ is much longer than the plasma wavelength λ_p , strong self-modulation of the laser pulse supported by a high plasma density produces intense pulse-lets of longitudinal size of $\sim \lambda_p/2$ and transverse size and inter-pulse separation $\sim \lambda_p$, which eventually leads to acceleration in “bubble” like wakefield and generates quasi-mono-energetic electron beam. We have shown that the self-modulation and consequently the accelerated electron charge and energy could be controlled by introducing frequency chirp in the laser pulse. We have also shown that an optimum value of positive

chirp generates a laser pulse with faster rise time which produces intense seed for stronger modulation of the laser pulse and consequently a stronger wakefield excitation, leading to higher electron beam charge and energy. Although SM-LWFA relies on FRS instability, the plasma wave amplitude could be controlled by controlling the seed. Since the ponderomotively excited wake dominates over other noise sources in this parameter regime, pulse shaping through laser chirp provides a handle to control the seed for the instability. This offers a method for minimizing shot-to-shot output fluctuations in the beam properties in the SM-LWFA.

The effect of interaction parameters viz., pre-pulse and gas media has also been studied. We have shown that the ASE pre-pulse pedestal associated with the CPA based high power laser pulses can be used advantageously to form pre-plasma in helium gas jet suitable for intense laser pulse guiding. Guiding of intense fs laser pulses over few times Rayleigh length in the ASE pre-pulse formed plasma channel was observed under optimum conditions. It has been shown that the laser beam guiding could facilitate generation of high energy electrons due to the longer interaction length and lower plasma density on the axis. It was further demonstrated that accelerated electron beam with low divergence and quasi-mono-energetic distribution with peak energy more than 50 MeV could be produced. However, the stability of the electron beam produced from these pre-plasma channels is affected by the shot-to-shot fluctuations of the ASE pre-pulse. We have shown that with reduction in pre-pulse intensity below the ionization threshold, the stability and the quality of the quasi-mono-energetic electron beam could be improved significantly, although the peak energy is limited to a smaller value ~ 35 MeV. The results agree with the scaling laws of the “blowout” regime, clearly suggesting that this regime could be accessed even at higher density to produce high quality electron beams. Investigation of LWFA in nitrogen (N_2) gas jet under same experimental conditions showed comparable stability and quality of the accelerated

electron beam. However, the mean electron energy (25 MeV) is less than that observed from He gas jet target. Electron acceleration in Ar gas jet was unstable and collimated electron beams of 40 – 50 mrad were observed once in a while at plasma density $> 10^{20} \text{ cm}^{-3}$. Highly stable, quasi-mono-energetic electron beams from He and N₂ are extremely attractive for application of the accelerator in future, especially due to the wide spread availability of ≤ 10 TW class lasers with a number of laser plasma laboratories around the world.

A study on the novel technique of laser-driven electron acceleration in solid plasma plumes showed fs laser pulse self-guiding and quasi-mono-energetic electron beam (~ 10 MeV) generation from wakefield acceleration in solid Nylon plasma plume target. The nanosecond laser pulse for plasma plume formation and the fs laser pulse for wakefield acceleration of electrons, were derived from the same Ti:sapphire laser system. This scheme is simple, low cost, and has the capability for high repetition rate operation. This scheme is therefore highly attractive for future investigations.

Collimated relativistic electron beams were also observed when the fs laser pulse interacted at grazing incidence with a pre-formed under-dense plasma on the solid target generated by the inherent ASE pre-pulse. The level of ns laser pre-pulse is found to be critical for the generation of the electron beam along the target surface. By optimal choice of pre-pulse, highly collimated electron beam with angular divergence $\sim 3^\circ$ and quasi-mono-energetic peak at 3 MeV was achieved. The electron beam produced from this technique is a potential candidate for applications which require high repetition rate. This can also be used as an injector for high energy conventional accelerators or laser-plasma wakefield accelerators and also for many other possible applications.

Further, measurement of the angular distribution of the hard x-ray bremsstrahlung radiation ($> 40 \text{ keV}$) generated due to the fast electrons produced from the solid copper target from the interaction of the Ti:sapphire laser pulses with planar copper target at 45° incidence

angle was carried out. The secondary sources of x-rays and the direction of fast electrons emission were identified from the angular and distance dependence of x-ray dose distribution measurements. Next, the fast electrons were characterized under different laser irradiation conditions. The measurements on the angular spread showed that the fast electron jet along the target normal direction with a half cone angle $< 20^\circ$. The energy spectrum of the fast electrons for both p- and s-polarized laser irradiation at intensities in the range 4×10^{16} - 4×10^{17} W/cm² (for a fixed pulse duration of 45 fs) and for pulse duration in the range 45 fs – 1.2 ps (for a fixed laser fluence of 1.8×10^4 J/cm²) were investigated. The fast electron temperature showed a power law scaling with laser intensity of the form $I^{2/3}$ and exponential scaling of the form $\exp(-\tau / 540 \text{ fs})$ with the pulse duration. The results clearly suggested that the fast electrons were generated from the resonance absorption mechanism.

7.2 Future outlook

Demonstration of stable electron beams from laser wakefield accelerator is an important outcome of the present thesis work. However, controlling the electron beam parameters (e.g. energy and charge) is another important requirement for any practical accelerator. In this context, other controlled injection schemes e.g. those using density transitions [154-158] or colliding pulses [159-162] could also be investigated. Laser produced solid plasma plumes can be further investigated for different target and laser interaction condition, for producing controlled and stable electron beams. The effect of controlled pre-pulse in presence of external magnetic field can be explored for extended laser guiding and enhanced energy gain of electrons in the wakefield [110]. There is also a need to further increase the electron energy to near-GeV and above, which invariably requires use of higher power lasers. It would be interesting to perform similar investigations on laser wakefield acceleration using the 150 TW laser which has recently been installed in our laboratory, for

beyond 100 MeV to near-GeV acceleration in different gas jets and plasma plumes. The use of capillary plasma wave-guides can also be investigated for longer interaction lengths and further high energies.

Investigation of collimated quasi-mono-energetic electron beam generation from solid surface pre-plasma by laser grazing incidence can be extended to study the role of target material, angle of incidence, and laser parameters (e.g. intensity, polarization and chirp/pulse duration) for higher energy and higher quality electron beams, which will be interesting for number of applications including the fast ignition concept of inertial confinement fusion. Further, the study of fast electron generation from laser-solid interaction at oblique incidence can be extended to study in detail the role of angle of incidence on the efficiency of fast electron generation, their angular distribution and energy spectrum. The fast electrons can be used to generate hard x-ray bremsstrahlung which can be explored for applications like transmutation of nuclear isotopes through (γ , n) reactions.

REFERENCES

1. C. Joshi, “The development of laser- and beam-driven plasma accelerators as an experimental field,” *Phys. Plasmas* **14**, 055501 (2007).
2. P. A. Naik, B. S. Rao, and P. D. Gupta, “Advanced acceleration schemes,” *Proceedings of IPAC2011*, San Sebastián, Spain, **A13**, 1945 (2011).
3. R. W. Hellwarth, “*Advances in Quantum Electronics*,” Columbia University Press, New York, 1961.
4. H.W. Mocker and R. J. Collins, “Mode competition and self-locking effects in a Q-switched ruby laser,” *Appl. Phys. Lett.* **7**, 270 (1965).
5. D. Strickland and G. Mourou, “Compression of amplified chirped optical pulses,” *Opt. Commun.* **56**, 219 (1985).
6. P. Maine, D. Strickland, P. Bado, M. Pessot, and G. Mourou, “Generation of ultrahigh peak power pulses by chirped pulse amplification,” *IEEE J. Quant. Elect.* **24**, 389 (1988).
7. D. E. Spence, P. N. Kean, and W. Sibbett, “60-fsec pulse generation from a self-mode-locked Ti:sapphire lasers,” *Opt. Lett.* **60**, 42 (1990).
8. G. A. Mourou, T. Tajima, and S. V. Bulanov, “Optics in the relativistic regime,” *Rev. Mod. Phys.* **78**, 309 (2006).
9. P. Gibbon, “*Short pulse laser interactions with matter*”, Imperial College Press, London, 2005.
10. T. Tajima and J. M. Dawson, “Laser electron accelerator,” *Phys. Rev. Lett.* **43**, 267 (1979).
11. C. Joshi, W. B. Mori, T. Katsouleas, J. M. Dawson, J. M. Kindel, and D. W. Forslund, “Ultrahigh gradient particle-acceleration by intense laser-driven plasma-density waves,” *Nature* **311**, 525 (1984).

12. C. E. Clayton, C. Joshi, C. Darrow, and D. Umstadter, "Relativistic plasma-wave excitation by collinear optical mixing," *Phys. Rev. Lett.* **54**, 2343 (1985).
13. C. E. Clayton, K. A. Marsh, A. Dyson, M. Everett, A. Lal, W. P. Leemans, R. Williams, and C. Joshi, "Ultrahigh-gradient acceleration of injected electrons by laser-excited relativistic electron-plasma waves," *Phys. Rev. Lett.* **70**, 37 (1993).
14. T. M. Antonsen Jr and P. Mora, "Self-focusing and Raman scattering of laser pulses in tenuous plasma," *Phys. Fluids B* **5**, 1440 (1993).
15. J. Krall, A. Ting, E. Esarey, and P. Sprangle, "Enhanced acceleration a self-modulated-laser wakefield accelerator," *Phys. Rev. E* **48**, 2157 (1993).
16. A. Modena, Z. Najmudin, A. E. Dangor, C. E. Clayton, K. A. Marsh, C. Joshi, V. Malka, C. B. Darrow, C. Danson, D. Neely, and F. N. Walsh, "Electron acceleration from the breaking of relativistic plasma-waves," *Nature* **377**, 606 (1995).
17. K. Nakajima, D. Fisher, T. Kawakubo, H. Nakanishi, A. Ogata¹, Y. Kato, Y. Kitagawa, R. Kodama, K. Mima, H. Shiraga, K. Suzuki, K. Yamakawa, T. Zhang, Y. Sakawa, T. Shoji, Y. Nishida, N. Yugami, M. Downer, and T. Tajima, "Observation of ultrahigh gradient electron acceleration by a self-modulated intense short laser pulse," *Phys. Rev. Lett.* **74**, 4428 (1995).
18. D. Umstadter, S.-Y. Chen, A. Maksimchuk, G. Mourou, and R. Warner, "Nonlinear optics in relativistic plasmas and laser wakefield acceleration of electrons," *Science* **273**, 472 (1996).
19. A. Ting, C. I. Moore, K. Krushelnick, C. Manka, E. Esarey, P. Sprangle, R. Hubbard, H. R. Burris, R. Fischer, and M. Baine, "Plasma wakefield generation and electron acceleration in a self-modulated laser wakefield accelerator experiment," *Phys. Plasmas* **4**, 1889 (1997).

20. W. P. Leemans, P. Catravas, E. Esarey, C. G. R. Geddes, C. Toth, R. Trines, C. B. Schroeder, B. A. Shadwick, J. van Tilborg, and J. Faure, “Electron-yield enhancement in a laser wakefield accelerator driven by asymmetric laser pulses,” *Phys. Rev. Lett.* **89**, 174802 (2002).
21. V. Malka, S. Fritzler, E. Lefebvre, M.-M. Aeonard, F. Burgy, J.-P. Chambaret, J.-F. Chemin, K. Krushelnick, G. Malka, S. P. D. Mangles, Z. Najmudin, M. Pittman, J.-P. Rousseau, J.-N. Scheurer, B. Walton, and A. E. Dangor, “Electron acceleration by a wake field forced by an intense ultra-short laser pulse,” *Science* **298**, 1596 (2002).
22. Z. Najmudin, K. Krushelnick, E. L. Clark, S. P. D. Mangles, B. Walton, A. E. Dangor, S. Fritzler, V. Malka, E. Lefebvre, D. Gordon, F. S. Tsung, and C. Joshi, “Self-modulated wakefield and forced laser wakefield acceleration of electrons,” *Phys. Plasmas* **10**, 2071 (2003).
23. S. P. D. Mangles, C. D. Murphy, Z. Najmudin, A. G. R. Thomas, J. L. Collier, A. E. Dangor, E. J. Divall, P. S. Foster, J. G. Gallacher, C. J. Hooker, D. A. Jaroszynski, A. J. Langley, W. B. Mori, P. A. Norreys, F. S. Tsung, R. Viskup, B. R. Walton, and K. Krushelnick, “Mono-energetic beams of relativistic electrons from intense laser–plasma interactions,” *Nature* **431**, 535 (2004).
24. C. G. R. Geddes, Cs. Tóth, J. van Tilborg, E. Esarey, C. B. Schroeder, D. Bruhwiler, C. Nieter, J. Cary, and W. P. Leemans, “High-quality electron beams from a laser wakefield accelerator using plasma-channel guiding,” *Nature* **431**, 538 (2004).
25. J. Faure, Y. Glinec, A. Pukhov, S. Kiselev, S. Gordienko, E. Lefebvre, J. –P. Rousseau, F. Burgy, and V. Malka, “A laser–plasma accelerator producing mono-energetic electron beams,” *Nature* **431**, 541 (2004).
26. A. Pukhov, and J. Meyer-ter-Vehn, “Laser wake field acceleration: the highly non-linear broken-wave regime,” *Appl. Phys. B* **74**, 355 (2002).

27. W. Lu, M. Tzoufras, C. Joshi, F. S. Tsung, W. B. Mori, J. Vieira, R. A. Fonseca, and L. O. Silva. “Generating multi-GeV electron bunches using single stage laser wakefield acceleration in a 3D nonlinear regime,” *Phys. Rev. ST Accel. Beams* **10**, 061301 (2007).
28. W. P. Leemans, B. Nagler, A. J. Gonsalves, C. Toth, K. Nakamura, C. G. R. Geddes, E. Esarey, C. B. Schroeder, and S. M. Hooker, “GeV electron beams from a centimetre-scale accelerator,” *Nature Phys.* **2**, 696 (2006).
29. T. Hosokai, K. Kinoshita, T. Ohkubo, A. Maekawa, M. Uesaka, A. Zhidkov, A. Yamazaki, H. Kotaki, M. Kando, K. Nakajima, S. V. Bulanov, P. Tomassini, A. Giulietti, and D. Giulietti, “Observation of strong correlation between quasi-mono-energetic electron beam generation by laser wakefield and laser guiding inside a pre-plasma cavity,” *Phys. Rev. E* **73**, 036407 (2006).
30. E. Miura, K. Koyama, S. Kato, N. Saito, M. Adachi, Y. Kawada, T. Nakamura, and M. Tanimoto, “Demonstration of quasi-mono-energetic electron-beam generation in laser-driven plasma acceleration,” *Appl. Phys. Lett.* **86**, 251501 (2005).
31. T.-Y. Chien, C.-L. Chang, C.-H. Lee, J.-Y. Lin, J. Wang, and S.-Y. Chen, “Spatially localized self-injection of electrons in a self-modulated laser wakefield accelerator by using a laser-induced transient density ramp,” *Phys. Rev. Lett.* **94**, 115003 (2005).
32. T. Hosokai, K. Kinoshita, A. Zhidkov, A. Maekawa, A. Yamazaki, and M. Uesaka, “Effect of external static magnetic field on the emittance and total charge of electron beams generated by laser wakefield acceleration,” *Phys. Rev. Lett.* **97**, 075004 (2006).
33. B. Hidding, K.-U. Amthor, B. Liesfeld, H. Schwöerer, S. Karsch, M. Geissler, L. Veisz, K. Schmid, J. G. Gallacher, S. P. Jamison, D. Jaroszynski, G. Pretzler, and R. Sauerbrey, “Generation of Quasi-mono-energetic Electron Bunches with 80-fs Laser Pulses,” *Phys. Rev. Lett.* **96**, 105004 (2006).

34. B. S. Rao, A. Moorti, P. A. Naik, and P. D. Gupta, “Generation of highly collimated, mono-energetic electron beam from laser-driven plasma-based acceleration,” *New J. Phys.* **12**, 045011 (2010).
35. N. Hafz, T. M. Jeong, I. W. Choi, S. K. Lee, K. H. Pae, V. V. Kulagin, J. H. Sung, T. J. Yu, K.-H. Hong, T. Hosokai, J. R. Cary, D.-K. Ko, and J. Lee, “Stable generation of GeV-class electron beams from self-guided laser–plasma channels,” *Nat. Photonics* **2**, 571 (2008).
36. S. Kneip, S. R. Nagel, S. F. Martins, S. P. D. Mangles, C. Bellei, O. Chekhlov, R. J. Clarke, N. Delerue, E. J. Divall, G. Doucas, K. Ertel, F. Fiuza, R. Fonseca, P. Foster, S. J. Hawkes, C. J. Hooker, K. Krushelnick, W. B. Mori, C. A. J. Palmer, K. Ta Phuoc, P. P. Rajeev, J. Schreiber, M. J.V. Streeter, D. Urner, J. Vieira, L. O. Silva, and Z. Najmudin, “Near-GeV Acceleration of Electrons by a Nonlinear Plasma Wave Driven by a Self-Guided Laser Pulse,” *Phys. Rev. Lett.* **103**, 035002 (2009).
37. D. H. Froula, C. E. Clayton, T. Do͞ppner, K. A. Marsh, C. P. J. Barty, L. Divol, R. A. Fonseca, S. H. Glenzer, C. Joshi, W. Lu, S. F. Martins, P. Michel, W. B. Mori, J. P. Palastro, B. B. Pollock, A. Pak, J. E. Ralph, J. S. Ross, C.W. Siders, L. O. Silva, and T. Wang, “Measurements of the critical power for self-injection of electrons in a laser wakefield accelerator,” *Phys. Rev. Lett.* **103**, 215006 (2009).
38. J. Faure, C. Rechatin, A. Norlin, A. Lifschitz, Y. Glinec, and V. Malka, “Controlled injection and acceleration of electrons in plasma wakefields by colliding laser pulses,” *Nature* **444**, 737 (2006).
39. C. McGuffey, A.G.R. Thomas, W. Schumaker, T. Matsuoka, V. Chvykov, F. J. Dollar, G. Kalintchenko, V. Yanovsky, A. Maksimchuk, and K. Krushelnick, “Ionization induced trapping in a laser wakefield accelerator,” *Phys. Rev. Lett.* **104**, 025004 (2010).

40. A. J. Gonsalves, K. Nakamura, C. Lin, D. Panasencko, S. Shiraishi, T. Sokollik, C. Benedetti, C. B. Schroeder, C. G. R. Geddes, J. Van Tilborg, J. Osterhoff, E. Esarey, C. Toth, and W. P. Leemans, “Tunable laser plasma accelerator based on longitudinal density tailoring,” *Nat. Phys.* **7**, 862 (2011).
41. M. Z. Mo, A. Ali, S. Fourmaux, P. Lassonde, J. C. Kieffer, and R. Fedosejevs, “Quasi-mono-energetic electron beams from laser wakefield acceleration in pure nitrogen,” *Appl. Phys. Lett.* **100**, 074101 (2012).
42. S. Banerjee, S.Y. Kalmykov, N. D. Powers, G. Golovin, V. Ramanathan, N. J. Cunningham, K. J. Brown, S. Chen, I. Ghebregziabher, B.A. Shadwick, and D. P. Umstadter, “Stable, tunable, quasi-mono-energetic electron beams produced in a laser wakefield near the threshold for self-injection,” *Phys. Rev. ST Accel. Beams* **16**, 031302 (2013).
43. A. Buck, J. Wenz, J. Xu, K. Khrennikov, K. Schmid, M. Heigoldt, J. M. Mikhailova, M. Geissler, B. Shen, F. Krausz, S. Karsch, and L. Veisz, “Shock-front injector for high-quality laser-plasma acceleration,” *Phys. Rev. Lett.* **110**, 185006 (2013).
44. B. S. Rao, A. Moorti, R. Rathore, J. A. Chakera, P. A. Naik, and P. D. Gupta, High quality electron beam from laser wakefield acceleration in a solid plasma plume target, *Appl. Phys. Lett.* **102**, 231108 (2013).
45. B. S. Rao, A. Moorti, R. Rathore, J. A. Chakera, P. A. Naik, and P. D. Gupta, “High-quality stable electron beams from laser wakefield acceleration in high density plasma,” *Phys. Rev. Spec. Topics-Accel. Beams* (To be published).
46. V. Malka, J. Faure, Y. A. Gauduel, E. Lefebvre, A. Rousse, and K. T. Phuoc, “Principles and applications of compact laser–plasma accelerators,” *Nature Phys.* **4**, 447 (2008).

47. D. W. Forslund, J. M. Kindel, K. Lee, E. L. Lindman, and R. L. Morse, “Theory and simulation of resonant absorption in a hot plasma,” *Phys. Rev. A* **11**, 679 (1975).
48. J. P. Freidberg, R. W. Mitchell, R. L. Morse, and L. I. Rudsinski, “Resonant absorption of laser light by plasma targets,” *Phys. Rev. Lett.* **28**, 795 (1971).
49. F. Brunel, “Not-so-resonant, resonant absorption,” *Phys. Rev. Lett.* **59**, 52 (1987).
50. W. L. Kruer and K. Estabrook, “J×B heating by very intense laser light,” *Phys. Fluids* **28**, 430 (1985).
51. S. C. Wilks, W. L. Kruer, M. Tabak, and A. B. Langdon, “Absorption of ultra-intense laser pulses,” *Phys. Rev. Lett.* **69**, 1383 (1992).
52. P. Gibbon, “Efficient production of fast electrons from femtosecond laser interaction with solid targets,” *Phys. Rev. Lett.* **73**, 664 (1994).
53. F. N. Beg, A. Bell, A. Dangor, C. Danson, A. Fewes, M. Glinsky, B. Hammel, P. Lee, P. Norreys, and M. Tatarakis, “A study of picosecond laser–solid interactions up to 10^{19} W.cm⁻²,” *Phys. Plasmas* **4**, 447 (1997).
54. G. Malka, J. Fuchs, F. Amiranoff, S. D. Baton, R. Gaillard, J. L. Miquel, H. Pépin, C. Rousseaux, G. Bonnaud, M. Busquet, and L. Lours, “Suprathermal electron generation and channel formation by an ultrarelativistic laser pulse in an underdense preformed plasma,” *Phys. Rev. Lett.* **79**, 2053 (1997).
55. M. I. K. Santala, M. Zepf, I. Watts, F. N. Beg, E. Clark, M. Tatarakis, K. Krushelnick, A. E. Dangor, T. McCanny, I. Spencer, R. P. Singhal, K. W. D. Ledingham, S. C. Wilks, A. C. Machacek, J. S. Wark, R. Allott, R. J. Clarke, and P. A. Norreys, “Effect of the plasma density scale length on the direction of fast electrons in relativistic laser-solid interactions,” *Phys. Rev. Lett.* **84**, 1459 (2000).

56. L. M. Chen, J. Zhang,¹ Y. T. Li, H. Teng, T. J. Liang, Z. M. Sheng, Q. L. Dong, L. Z. Zhao, Z.Y. Wei, and X.W. Tang, “Effects of laser polarization on jet emission of fast electrons in femtosecond-laser plasmas,” *Phys. Rev. Lett.* **87**, 225001 (2001).
57. Z. L. Chen, J. Zhang, T. J. Liang, H.Teng, Q. L. Dong, Y. T. Li, J. Zhang, Z. M. Sheng, L. Z. Zhao, and X.W. Tang, “Z-dependence of hot electron generation in femtosecond laser interaction with solid targets ,” *J. Phys. B* **37**, 539 (2004).
58. J. Zhang, J. Zhang, Z. M. Sheng, Y. T. Li, Y. Qiu, Z. Jin, and H. Teng, “Emission direction of fast electrons in laser-solid interactions at intensities from the nonrelativistic to the relativistic,” *Phys. Rev. E* **69**, 046408 (2004).
59. W. Wang, J. Liu, Y.Cai, C. Wang, L. Liu, C. Xia, A. Deng, Y.Xu, Y.Leng, R. Li, and Z.Xub, “Angular and energy distribution of fast electrons emitted from a solid surface irradiated by femtosecond laser pulses in various conditions,” *Phys. Plasmas* **17**, 023108 (2010).
60. M. Tabak, J. Hammer, M. E. Glinsky, W. L. Kruer, S. C. Wilks, J. Woodworth, E. M. Campbell, M. D. Perry, and R. J. Mason, “Ignition and high gain with ultra-powerful lasers,” *Phys. Plasmas* **1**, 1626 (1994).
61. S. P. Hatchett, C. G. Brown, T. E. Cowan, E. A. Henry, J. S. Johnson, M. H. Key, J. A. Koch, A. B. Langdon, B. F. Lasinski, R. W. Lee, A. J. Mackinnon, D. M. Pennington, M. D. Perry, T. W. Phillips, M. Roth, T. C. Sangster, M. S. Singh, R. A. Snavely, M. A. Stoyer, S. C. Wilks, and K.Yasuike, “Electron, photon, and ion beams from the relativistic interaction of petawatt laser pulses with solid targets,” *Phys. Plasmas* **7**, 2076 (2000).
62. H. Schwoerer, P. Gibbon, S. Düsterer, R. Behrens, C. Ziener, C. Reich, and R. Sauerbrey, “MeV x-rays and photo-neutrons from femtosecond laser-produced plasmas,” *Phys. Rev. Lett.* **86**, 2317 (2001).

63. K. W. D. Ledingham, P. McKenna, and R. P. Singhal, "Applications for nuclear phenomena generated by ultra-intense lasers," *Science* **300**, 1107 (2003).
64. B. S. Rao, P. A. Naik, V. Arora, R. A. Khan, and P. D. Gupta, "Angular distribution and dose measurements of hard x-ray emission from intense laser-plasma interaction," *J. Appl. Phys.* **102**, 063307 (2007).
65. A. B. Sefkow, G. R. Bennett, M. Geissel, M. Schollmeier, B. C. Franke, and B. W. Atherton, "Efficiency enhancement for K_α X-Ray yields from laser-driven relativistic electrons in solids," *Phys. Rev. Lett.* **106**, 235002 (2011).
66. V. Arora, H. Singhal, P. A. Naik, and P. D. Gupta, "Enhancement of K-alpha emission through efficient hot electron generation in carbon nanotubes on intense laser pulse irradiation," *J. Appl. Phys.* **110**, 083305 (2011).
67. S. Bastiani, A. Rousse, J. P. Geindre, P. Audebert, C. Quiox, G. Hamoniaux, A. Antonetti, and J.-C. Gauthier, "Experimental study of the interaction of sub-picosecond laser pulses with solid targets of varying initial scale lengths," *Phys. Rev. E* **56**, 7179 (1997).
68. Y. Sentoku, H. Ruhl, K. Mima, R. Kodama, K. A. Tanaka, and Y. Kishimoto, "Plasma jet formation and magnetic-field generation in the intense laser plasma under oblique incidence," *Phys. Plasmas* **6**, 2855 (1999).
69. Y. T. Li, X. H. Yuan, M. H. Xu, Z. Y. Zheng, Z. M. Sheng, M. Chen, Y. Y. Ma, W. X. Liang, Q. Z. Yu, Y. Zhang, F. Liu, Z. H. Wang, Z. Y. Wei, W. Zhao, Z. Jin, and J. Zhang, "Observation of a fast electron beam emitted along the surface of a target irradiated by intense femtosecond laser pulses," *Phys. Rev. Lett.* **96**, 165003 (2006).
70. B. S. Rao, V. Arora, P. A. Naik, and P. D. Gupta, "Study of fast electron jet produced from interaction of intense laser beam with solid target at oblique incidence," *Phys. Plasmas* **19**, 113118 (2011).

71. K. W. D. Ledingham, J. Magill, P. McKenna, J. Yang, J. Galy, R. Schenkel, J. Rebizant, T. McCanny, S. Shimizu, L. Robson, R. P. Singhal, M. S. Wei, S. P. D. Mangles, P. Nilson, K. Krushelnick, R. J. Clarke, and P. A. Norreys., “Laser-driven photo-transmutation of ^{129}I —a long-lived nuclear waste product,” *J. Phys. D* **36**, L79 (2003).
72. F. Ewald, H. Schwoerer, S. Düsterer, R. Sauerbrey, J. Magill, J. Galy, R. Schenkel, S. Karsch, D. Habs, and K. Witte, “Application of relativistic laser plasmas for the study of nuclear reactions,” *Plasma Phys. Controlled Fusion* **45**, A83 (2003).
73. J. Magill, H. Schwoerer, F. Ewald, J. Galy, R. Schenkel, and R. Sauerbrey, “Plasma jet formation and magnetic-field generation in the intense laser plasma under oblique incidence,” *Appl. Phys. B: Lasers Opt.* **77**, 387 (2003).
74. H. Schwoerer, F. Ewald, R. Sauerbrey, J. Galy, J. Magill, V. Rondinella, R. Schenkel, and T. Butz, “Fission of actinides using a tabletop laser,” *Europhys. Lett.* **61**, 47 (2003).
75. J. D. Jackson, “*Classical electrodynamics*,” John Wiley & Sons, New York, 2nd edition 1975.
76. J. A. Bittencourt, “*Fundamentals of Plasma Physics*,” Springer-Verlag, New York, 2004.
77. D. R. Nicholson, “*Introduction to plasma theory*,” John Wiley and Sons, New York, 1983.
78. G. Mainfray and G. Manus, “Multi-photon ionization of atoms,” *Reports on Progress in Phys.* **54**, 1333 (1991).
79. M. V. Ammosov, N. B. Delone, and V. P. Krainov, “Tunnel ionization of complex atoms and of atomic ions in an alternating electromagnetic field,” *Soviet Physics, J. Experimental and Theoretical Phys.* **64**, 1191 (1986); N. B. Delone and V. P. Krainov, “*Multiphoton processes in atoms*,” Springer Verlag, Heidelberg, 2nd edition, 1994.

80. H. A. Bethe and E. E. Salpeter, “*Quantum mechanics of one- and two electron atoms*,” Plenum, New York, 1977.
81. F. F. Chen, “*Introduction to Plasma Physics and Controlled Fusion*,” Plenum Press, New York, 1984.
82. B. Quesnel and P. Mora, “Theory and simulation of the interaction of ultra-intense laser pulses with electrons in vacuum,” *Phys. Rev. E* **58**, 3719 (1998).
83. P. Sprangle, E. Esarey, J. Krall, and G. Joyce, “Propagation and guiding of intense laser pulses in plasmas,” *Phys. Rev. Lett.* **69**, 2200 (1992).
84. E. Esarey, C. B. Schroeder, and W. P. Leemans, “Physics of laser-driven plasma based electron accelerators,” *Rev. Modern Phys.* **81**, 1229 (2009).
85. G. Z. Sun, E. Ott, Y. C. Lee, and P. Guzdar, “Self-focusing of short intense pulses in plasmas,” *Phys. Fluids* **30**, 526 (1987).
86. C. D. Decker, W. B. Mori, and T. Katsouleas, “Particle-in-cell simulations of Raman forward scattering from short-pulse high-intensity lasers,” *Phys. Rev. E* **50**, R3338 (1994).
87. S. C. Wilks and W. L. Kruer, “Absorption of ultra-short, ultra-intense laser light by solids and over-dense plasmas,” *IEEE Journal of Quantum Electronics*, 33, 1954 (1997).
88. A. Pukhov and J. Meyer-ter-Vehn, “Laser hole boring into over-dense plasma and relativistic electron currents for fast ignition of ICF targets,” *Phys. Rev. Lett.* **79**, 2686 (1997).
89. A. Pukhov and J. Meyer-ter-Vehn, “Relativistic laser-plasma interaction by multi-dimensional particle-in-cell simulations,” *Phys. Plasmas* **5**, 1880 (1998).
90. A. Pukhov, Z.-M. Sheng, and J. Meyer-ter-Vehn, “Particle acceleration in relativistic laser channels,” *Phys. Plasmas* **6**, 2847 (1999).

91. C. Gahn, G. D. Tsakiris, A. Pukhov, J. Meyer-ter-Vehn, G. Pretzler, P. Thirolf, D. Habs, and K. J. Witte, "Multi-meV electron beam generation by direct laser acceleration in high-density plasma channels," *Phys. Rev. Lett.* **83**, 4772 (1999).
92. G. Cheriaux, P. Rousseau, F. Salin, and J. P. Chambaret, "Aberration-free stretcher design for ultra-short pulse amplification," *Opt. Lett.* **21**, 414 (1996).
93. E. Treacy, "Optical pulse compression with diffraction gratings," *IEEE J. Quant. Electr.* **5**, 454 (1969).
94. A. E. Siegman, "*Lasers*," University Science books, USA, p 359 (1986).
95. A. Brun, P. Georges, G. Le Saux, and F. Sain, "Single-shot characterization of ultra-short light pulses," *J. Phys. D: Appl. Phys.* **24**, 1225 (1991).
96. Y. P. Raizer, "Breakdown and heating of gases under the influence of a laser beam," *Sov. Phys. Usp.* **8**, 650 (1965).
97. G. V. Ostrovskaya and A. N. Zaidel, "Laser spark in gases," *Sov. Phys. Usp.* **16**, 834 (1974).
98. T. Hosokai, K. Kinoshita, T. Watanabe, K. Yoshii, T. Ueda, A. Zhidkov, and M. Uesaka, "Supersonic gas jet target for generation of relativistic electrons with 12 TW-50fs laser pulse", *Proc. 8th European Particle Accelerator Conf. (EPS)*, p. 981 (2002).
99. <http://www.mcio.com/Products/drz-screens.aspx>
100. Y. C. Wu, B. Zhu, K. G. Dong, Y. H. Yan, and Y. Q. Gu, "Note: Absolute calibration of two DRZ phosphor screens using ultra-short electron bunch," *Rev. Sci. Instrum.* **83**, 026101 (2012).
101. http://www.bergoz.com/index.php?option=com_content&view=article&id=56&Itemid=471

102. B. S. Rao, A. Moorti, P. A. Naik, and P. D. Gupta, “Effect of chirp on self-modulation and laser wakefield electron acceleration in the regime of quasi-mono-energetic electron beam generation,” *Phys. Rev. Spec. Topics-Accel. Beams* (To be published).
103. C. D. Murphy, R. Trines, J. Vieira, A. J. W. Reitsma, R. Bingham, J. L. Collier, E. J. Divall, P. S. Foster, C. J. Hooker, A. J. Langley, P. A. Norreys, R. A. Fonseca, F. Fiuza, L. O. Silva, J. T. Mendonça, W. B. Mori, J. G. Gallacher, R. Viskup, D. A. Jaroszynski, S. P. D. Mangles, A. G. R. Thomas, K. Krushelnick, and Z. Najmudin, “Evidence of photon acceleration by laser wake fields,” *Phys. Plasmas* **13**, 033108 (2006).
104. T.-Y. Chen, W. -T. Chen, Y. H. Chen, C. -H. Lee, J. Y. Lin, J. Wang, and S. -Y. Chen, “Prepulse controlled splitting of relativistically self-guided channel and suppression of Raman forward scattering instability,” *Phys. Plasmas* **11**, 1173 (2004).
105. N. E. Andreev, L. M. Gorbunov, P. Mora, and R. R. Ramazashvili, “Filamentation of ultra-short laser pulses propagating in tenuous plasmas,” *Phys. Plasmas* **14**, 083104 (2007).
106. A. G. R. Thomas, S. P. D. Mangles, C. D. Murphy, A. E. Dangor, P. S. Foster, J. G. Gallacher, D. A. Jaroszynski, C. Kamperidis, K. Krushelnick, K. L. Lancaster, P. A. Norreys, R. Viskup, and Z. Najmudin, “Ultra-short pulse filamentation and mono-energetic electron beam production in LWFAs,” *Plasma Phys. Control. Fusion* **51**, 024010 (2009).
107. L. M. Gorbunov, S. Kalmykov, and P. Mora, “Laser wakefield acceleration by petawatt ultra-short laser pulses,” *Phys. Plasmas* **12**, 033101 (2005).
108. J. Faure, V. Malka, J. R. Marques, P. G. David, F. Amiranoff, K. TaPhuoc, and A. Rousse, “Effects of pulse duration on self-focusing of ultra-short lasers in under-dense plasmas,” *Phys. Plasmas* **9**, 756 (2002).

109. M. Adachi, E. Miura, Kato, K. Koyama, S. Masuda, T. Watanabe, H. Okamoto, A. Ogata, and M. Tanimoto, “Cascade Acceleration of Electrons by Laser Wakefield and Direct Laser Field,” *Jap. J. Appl. Phys.* **45**, 4214 (2006).
110. W. B. Mori, “The physics of the nonlinear optics of plasmas at relativistic intensities for short-pulse lasers,” *IEEE J. Quantum Electron.* **33**, 1942 (1997).
111. C.B. Schroeder, E. Esarey, C.G.R. Geddes, Cs. Toth, B.A. Shadwick, J. van Tilborg, J. Faure, and W. P. Leemans, “Frequency chirp and pulse shape effects in self-modulated laser wakefield accelerators,” *Phys. Plasmas* **10**, 2039 (2003).
112. Cs. Tóth, J. Faure, J. van Tilborg, C. G. R. Geddes, C. B. Schroeder, E. Esarey, and W. P. Leemans, “Tuning of laser pulse shapes in grating-based compressors for optimal electron acceleration in plasmas,” *Opt. Lett.* **28**, 1823 (2003).
113. N. A. M. Hafz, T. J. Yu, S. K. Lee, T. M. Jeong, J. H. Sung, and J. Lee, “Controlling the pointing angle of a relativistic electron beam in a weakly-nonlinear laser wakefield accelerator,” *Appl. Phys. Express* **3**, 076401 (2010).
114. M. Mori, K. Kondo, Y. Mizuta, M. Kando, H. Kotaki, M. Nishiuchi, M. Kado, A. S. Pirozhkov, K. Ogura, H. Sugiyama, S.V. Bulanov, K. A. Tanaka, H. Nishimura, and H. Daido, “Generation of stable and low-divergence 10-MeV quasi-mono-energetic electron bunch using argon gas jet,” *Phys. Rev. ST Accel. Beams* **12**, 082801 (2009).
115. A. Giulietti, P. Tomassini, M. Galimberti, D. Giulietti, L. A. Gizzi, P. Koester, and L. Labate, T. Ceccotti, P. D’Oliveira, T. Auguste, P. Monot, and P. Martin, “Pre-pulse effect on intense femtosecond laser pulse propagation in gas,” *Phys. Plasmas* **13**, 093103 (2006).
116. C. G. Durfee III, J. Lynch, and H. M. Milchberg, “Development of a plasma waveguide for high-intensity laser pulses,” *Phys. Rev. E* **51**, 2368 (1995).

117. H. M. Milchberg, T. R. Clark, C. G. Durfee III, T. M. Antonsena, and P. Mora, “Development and applications of a plasma waveguide for intense laser pulses,” *Phys. Plasmas* **3**, 2149 (1996).
118. P. Monot, T. Auguste, L. A. Lompr, G. Mainfray, and C. Manus, “Focusing limits of a terawatt laser in an under-dense plasma,” *J. Opt. Soc. Am. B* **9**, 1579 (1992).
119. T. Hosokai, A. Zhidkov, A. Yamazaki, Y. Mizuta, M. Uesaka, and R. Kodama, “Electron energy boosting in laser-wakefield acceleration with external magnetic field $B \sim 1$ T and laser pre-pulses,” *Appl. Phys. Lett.* **96**, 121501 (2010).
120. S. P. D. Mangles, A. G. R. Thomas, M. C. Kaluza, O. Lundh, F. Lindau, A. Persson, Z. Najmudin, C.-G. Wahlstrom, C. D. Murphy, C. Kamperidis, K. L. Lancaster, E. Divall, and K. Krushelnick, “Effect of laser contrast ratio on electron beam stability in laser wakefield acceleration experiments,” *Plasma Phys. Control. Fusion* **48**, B83 (2006).
121. S. P. D. Mangles, A. G. R. Thomas, O. Lundh, F. Lindau, M. C. Kaluza, A. Persson, C.-G. Wahlström, K. Krushelnick, and Z. Najmudin, “On the stability of laser wakefield electron accelerators in the mono-energetic regime,” *Phys. Plasmas* **14**, 056702 (2007).
122. F. S. Tsung, W. Lu, M. Tzoufras, W. B. Mori, C. Joshi, J. M. Vieira, L. O. Silva, and R. A. Fonseca, “Simulation of mono-energetic electron generation via laser wakefield accelerators for 5–25 TW lasers,” *Phys. Plasmas* **13**, 056708 (2006).
123. S. Banerjee, S.Y. Kalmykov, N. D. Powers, G. Golovin, V. Ramanathan, N. J. Cunningham, K. J. Brown, S. Chen, I. Ghebregziabher, B.A. Shadwick, and D. P. Umstadter, “Stable, tunable, quasi-mono-energetic electron beams produced in a laser wakefield near the threshold for self-injection,” *Phys. Rev. ST Accel. Beams* **16**, 031302 (2013). C. Rechatin, X. Davoine, A. Lifschitz, A. B. Ismail, J. Lim, E. Lefebvre, J. Faure, and V. Malka, “Observation of beam loading in a laser-plasma accelerator,” *Phys. Rev. Lett.* **103**, 194804 (2009).

124. S. P. D. Mangles, A. G. R. Thomas, M. C. Kaluza, O. Lundh, F. Lindau, A. Persson, F. S. Tsung, Z. Najmudin, W. B. Mori, C.-G. Wahlstrom, and K. Krushelnick, “Laser-wakefield acceleration of mono-energetic electron beams in the first plasma-wave period,” *Phys. Rev. Lett.* **96**, 215001 (2006).
125. S. M. Wiggins, R. C. Issac, G. H. Welsh, E. Brunetti, R. P. Shanks, M. P. Anania, S. Cipiccia, G. G. Manahan, C. Aniculaesei, B. Ersfeld, M. R. Islam, R. T. L. Burgess, G. Vieux, W. A. Gillespie, A. M. MacLeod, S. B. van der Geer, M. J. de Loos, and D. A. Jaroszynski, “High quality electron beams from a laser wakefield accelerator,” *Plasma Phys. Control. Fusion* **52**, 124032 (2010).
126. K. Schmid, A. Buck, C. M. S. Sears, J. M. Mikhailova, R. Tautz, D. Herrmann, M. Geissler, F. Krausz, and L. Veisz, “Density-transition based electron injector for laser driven wakefield accelerators,” *Phys. Rev. ST Accel. Beams* **13**, 091301 (2010).
127. B. Hidding, M. Geissler, G. Pretzler, K.-U. Amthor, H. Schworer, S. Karsch, L. Veisz, K. Schmid, and R. Sauerbrey, “Quasi-mono-energetic electron acceleration in the self-modulated laser wakefield regime,” *Phys. Plasmas* **16**, 043105 (2009).
128. B. S. Rao, J. A. Chakera, P. A. Naik, M. Kumar, and P. D. Gupta, “Laser wakefield acceleration in pre-formed plasma channel created by pre-pulse pedestal of terawatt laser pulse,” *Phys. Plasmas* **18**, 093104 (2011).
129. S. Amoruso, R. Bruzzese, N. Spinelli, and R. Velotta. “Characterization of laser-ablation plasmas,” *J. Phys. B: At. Mol. Opt. Phys.* **32**, R131 (1999).
130. R. K. Singh, O. W. Holland, and J. Narayan, “Theoretical model for deposition of superconducting thin films using pulsed laser evaporation technique,” *J. Appl. Phys.* **68**, 233 (1990).
131. T. Matsuoka, C McGuffey, M. Levin, S. S. Bulanov, V. Chvykov, G. Kalintchenko, S. Reed, P. Rousseau, V. Yanovsky, A. Zigler, K. Krushelnick, and A. Maksimchuk,

- “Self-guided laser wakefield acceleration using ablated plasma targets,” *Plasma Phys. Control. Fusion* **51**, 095003 (2009).
132. B. R. Walton, S. P. D. Mangles, Z. Najmudin, M. Tatarakis, M. S. Wei, A. Gopal, C. Marle, A. E. Dangor, K. Krushelnick, S. Fritzler, V. Malka, R. J. Clarke, and C. Hernandez-Gomez, “Measurements of forward scattered laser radiation from intense sub-ps laser interactions with underdense plasmas,” *Phys. Plasmas* **13**, 113103 (2006).
 133. R. M. G. M. Trines, C. D. Murphy, K. L. Lancaster, O. Chekhlov, P. A. Norreys, R. Bingham, J. T. Mendonça, L. O. Silva, S. P. D. Mangles, C. Kamperidis, A. Thomas, K. Krushelnick, and Z. Najmudin, “Photon acceleration and modulational instability during wakefield excitation using long laser pulses,” *Plasma Phys. Control. Fusion* **51**, 024008 (2009).
 134. M. Chen, E. Esarey, C. B. Schroeder, C. G. R. Geddes, and W. P. Leemans, “Theory of ionization-induced trapping in laser-plasma accelerators,” *Phys. Plasmas* **19**, 033101 (2012).
 135. J. Y. Mao, L. M. Chen, X. L. Ge, L. Zhang, W. C. Yan, D. Z. Li, G. Q. Liao, J. L. Ma, K. Huang, Y. T. Li, X. Lu, Q. L. Dong, Z. Y. Wei, Z. M. Sheng, and J. Zhang, “Spectrally peaked electron beams produced via surface guiding and acceleration in femtosecond laser-solid interactions,” *Phys. Rev. E* **85**, 025401 (2012).
 136. T. Nakamura, S. Kato, H. Nagatomo, and K. Mima, “Surface-magnetic-field and fast-electron current-layer formation by ultra-intense laser irradiation,” *Phys. Rev. Lett.* **93**, 265002 (2004).
 137. M. Chen, Z. M. Sheng, J. Zheng, Y. Y. Ma, M. A. Bari, Y. T. Li, and J. Zhang, “Surface electron acceleration in relativistic laser-solid interactions,” *Opt. Express* **14**, 3093 (2006).

138. A. G. Mordovanakis, J. Easter, N. Naumova, K. Popov, P. E. Masson-Laborde, B. Hou1, I. Sokolov, G. Mourou, I. V. Glazyrin, W. Rozmus, V. Bychenkov, J. Nees, and K. Krushelnick1, “Quasi-mono-energetic electron beams with relativistic energies and ultra-short duration from laser-solid interactions at 0.5 kHz,” *Phys. Rev. Lett.* **103**, 235001 (2009).
139. W.M. Wanga, L.M. Chen, J.Y. Mao, K. Huang, Y. Ma, J.R. Zhao, L. Zhang, W.C. Yan, D.Z. Li, J.L. Ma, Y.T. Li, X. Lu, Z.Y. Wei, Z.M. Sheng, and J. Zhang, “Collimated quasi-mono-energetic electron beam generation from intense laser solid interaction,” *High Energy Density Phys.* **9**, 578 (2013).
140. P. A. Norreys, M. Santala, E. Clark, M. Zepf, I. Watts, F. N. Beg, K. Krushelnick, M. Tatarakis, A. E. Dangor, X. Fang, P. Graham, T. McCanny, R. P. Singhal, K. W. D. Ledingham, A. Creswell, D. C. W. Sanderson, J. Magill, A. Machacek, J. S. Wark, and R. Allott, “Observation of a highly directional γ -ray beam from ultra-short, ultra-intense laser pulse interactions with solids,” *Phys. Plasmas* **6**, 2150 (1999).
141. D. F. Cai, Y. Q. Gu, Z. J. Zheng, T. S. Wen, S. T. Chunyu, Z. B. Wang, and X. D. Yang, “Experimental study for angular distribution of the hot electrons generated by femtosecond laser interaction with solid targets,” *Phys. Plasmas* **10**, 3265 (2003).
142. A. Zhidkov, A. Sasaki, T. Utsumi, I. Fukumoto, T. Tajima, F. Saito, Y. Hironaka, K. G. Nakamura, K. I. Kondo, and M. Yoshida, “Pre-pulse effects on the interaction of intense femtosecond laser pulses with high-Z solids,” *Phys. Rev. E* **62**, 7232 (2000).
143. A. Giulietti, A. Macchi, E. Schifano, V. Biancalana, C. Danson, D. Giulietti, L. A. Gizzi, and O. Willi, “Stimulated Brillouin backscattering from underdense expanding plasmas in a regime of strong filamentation,” *Phys. Rev. E* **59**, 1038 (1999).
144. <http://www.physics.nist.gov/PhysRefData/XrayMassCoef/>

145. A. G. Mordovanakis, P. M. Laborde, J. Easter, K. Popov, B. Hou, G. Mourou, W. Rozmus, M. G. Haines, J. Nees, and K. Krushelnick, “Temperature scaling of hot electrons produced by a tightly focused relativistic-intensity laser at 0.5 kHz repetition rate,” *Appl. Phys. Lett.* **96**, 071109 (2010).
146. F. Borne, D. Delacroix, J. M. Gele, D. Masse, and F. Amiranoff, “Radiation protection for an ultra-high intensity laser,” *Rad. Prot. Dosimetry* **102**, 61 (2002).
147. R. J. Clarke, D. Neely, R. D. Edwards, P. N. M. Wright, K. W. D. Ledingham, R. Heathcote, Mc Kenna, C. N. Danson, P. A. Brummitt, J. L. Collier, P. E. Hatton, S. J. Hawkes, C. Hernandez-Gomez, P. Holligan, M. H. R. Hutchinson, A. K. Kidd, W. J. Lester, D. R. Neville, P. A. Norreys, D. A. Pepler, T. B. Winstone, R. W. W. Wyatt, and B. E. Wyborn, “Radiological characterisation of photon radiation from ultra-high-intensity laser–plasma and nuclear interactions,” *J. Radiol. Prot.* **26**, 277 (2006).
148. *Ionising Radiations Regulations* 1999 (London: HSE Books) (ISBN 0-7176-1746-7).
149. Y.T. Li, J. Zhang, L.M. Chen, Y.F. Mu, T.J. Liang, Z.Y. Wei, Q.L. Dong, Z.L. Chen, H. Teng, S.T. Chun-Yu, W.M. Jiang, Z.J. Zheng, and X.W. Tang, “Hot electrons in the interaction of femtosecond laser pulses with foil targets at a moderate laser intensity,” *Phys. Rev. E* **64**, 046407 (2001).
150. J. MacFarlane, I. E. Golovkin, and P.R. Woodruff, “HELIOS-CR – A 1-D radiation-magneto-hydrodynamics code with inline atomic kinetics modelling,” *J. Quant. Spectrosc. Radiat. Transf.* **99**, 381 (2006).
151. V. Arora, P. A. Naik, J. A. Chakera, R. A. Khan, and P. D. Gupta, “Study of 2ω and $3\omega/2$ harmonics in ultra-short high-intensity laser plasma interaction,” *Pramana* **75**, 1175 (2010).

152. W. L. Kruer, “*The Physics of Laser Plasma Interactions*,” (Addison-Wesley, New York, 1988).
153. J. Yu, Z. Jiang, J. C. Kieffer, and A. Krol, “Hard x-ray emission in high intensity femtosecond laser–target interaction,” *Phys. Plasmas* **6**, 1318 (1999).
154. S. Bulanov, N. Naumova, F. Pegoraro, and J. Sakai, “Particle injection into the wave acceleration phase due to nonlinear wake wave breaking,” *Phys. Rev. E*, **58**, R5257 (1998).
155. H. Suk, N. Barov, J. B. Rosenzweig, and E. Esarey, “Plasma electron trapping and acceleration in a plasma wake field using a density transition,” *Phys. Rev. Lett.*, **86**, 1011 (2001).
156. H. Suk, C. Kim, G.H. Kim, J. U. Kim, I. S. Ko, H. J. Lee, “Energy enhancement in the self-injected laser wakefield acceleration using tapered plasma densities,” *Phys. Lett. A* **316**, 233 (2003).
157. C. -T. Hsieh, C. -M. Huang, C. -L. Chang, Y. -C. Ho, Y. -S. Chen, J. -Y. Lin, J. Wang, and S. -Y. Chen, “Tomography of injection and acceleration of mono-energetic electrons in a laser-wakefield accelerator,” *Phys. Rev. Lett.* **96**, 095001 (2006).
158. C. G. R. Geddes, K. Nakamura, G. Plateau, Cs. Toth, E. Cormier-Michel, E. Esarey, C. Schroeder, J. Cary, and W. Leemans, “Plasma-density-gradient injection of low absolute-momentum-spread electron bunches,” *Phys. Rev. Lett.* **100**, 215004 (2008).
159. D. Umstadter, J. -K. Kim, and E. Dodd, “Laser injection of ultrashort electron pulses into wakefield plasma waves,” *Phys. Rev. Lett.* **76**, 2073 (1996).
160. E. Esarey, R. Hubbard, W. Leemans, A. Ting, and P. Sprangle, “Electron injection into plasma wakefields by colliding laser pulses,” *Phys. Rev. Lett.* **79**, 2682 (1997).

161. H. Kotaki, S. Masuda, M. Kando, J. K. Koga, and K. Nakajima, “Head-on injection of a high quality electron beam by the interaction of two laser pulses,” *Phys. Plasmas* **6**, 3296 (2004).
162. G. Fubiani, E. Esarey, C. B. Schroeder, and W. P. Leemans, “Beat wave injection of electrons into plasma waves using two interfering laser pulses,” *Phys. Rev. E* **70**, 016402 (2004).